THE USE OF PACKED SPHERE MODELLING FOR AIRFLOW AND HEAT EXCHANGE ANALYSIS IN BROKEN OR FRAGMENTED ROCK

by

Sidney Schafrik

A thesis submitted in partial fulfillment

of the requirements for the degree of

Doctor of Philosophy (PhD) in Natural Resources Engineering

Faculty of Graduate Studies

Laurentian University

Sudbury, Ontario, Canada

THESIS DEFENCE COMMITTEE/COMITÉ DE SOUTENANCE DE THÈSE
Laurentian Université/Université Laurentienne
Faculty of Graduate Studies/Faculté des études supérieures

Title of Thesis Titre de la these	THE USE OF PACKED SPHERE MODELLING FOR AIRFLOW AND HEAT EXCHANGE ANALYSIS IN BROKEN OR FRAGMENTED ROCK
Name of Candidate Nom du candidat	Schafrik, Sidney
Degree Diplôme	Doctor of Philosophy

Department/Program Département/Programme	Natural Resources Engineering	Date of Defence Date de la soutenance	December 17, 2014

APPROVED/APPROUVÉ

Thesis Examiners/Examinateurs de thèse:

Dr. Dean Millar (Supervisor/Directeur de thèse)

Dr. Lorrie Fava
(Committee member/Membre du comité)

Dr. Marty Hudyma
(Committee member/Membre du comité)

Dr. Helen Shang
(Committee member/Membre du comité)

Dr. Sukumar Bandopadhyay
(External Examiner/Examinateur externe)

Dr. Graeme Spiers
(Internal Examiner/Examinateur interne)

Approved for the Faculty of Graduate Studies
Approuvé pour la Faculté des études supérieures
Dr. David Lesbarrères
M. David Lesbarrères
Acting Dean, Faculty of Graduate Studies
Doyen intérimaire, Faculté des études supérieures

ACCESSIBILITY CLAUSE AND PERMISSION TO USE

Abstract

Airflow and heat exchange characterizations through large bodies of fragmented rock in mines, such as those at Creighton and Kidd Creek Mines, reveal them to be still fundamentally only empirical in nature. Analysis of the accepted methods for the design and understanding of geometric properties such as the heat exchange area or the length or shape of airflow passages known to affect heat transfer in, for example, heat exchanger design do not appear in the 'design' equations for those bodies of broken rock. This thesis couples a method of discontinuum porous media modelling (referred to as a packed sphere model, abbreviated PSM) with a computational fluid dynamics (CFD) code to develop a proxy methodology for analysis of porous media that incorporates variables of airflow, heat transfer, and geometry (including porosity and tortuosity). Material property values for equivalent continuum fluid dynamics models are established and are found to follow formulations for airflow branches used in mine ventilation network analysis. Laboratory experiments of airflow and heat transfer with the PSMs were compared to CFD results for the same models on a 1:1 scale, to verify the approach and CFD results. Three separate approaches were investigated for the scaling of the results of the PSMs for use in large scale ($\sim 1 km^3$) CFD simulations of industrial situations. The result of the work presented in this thesis is a verified methodology for establishing CFD airflow and heat transfer parameters for large bodies of broken and fragmented rock from knowledge of the particle size distribution parameters or the body porosity. The application of the methodology is illustrated with reference to the so-called Natural Heat Exchange Area at Creighton Mine, Sudbury, Ontario.

Keywords

Porous media, Equivalent continuum, Airflow, Heat exchange, Packed Sphere Modelling, PSM, Natural Heat Exchange Area

Table of Contents

List of Tables

List of Figures

List of Abbreviations

APD - Automatic Parameters Definition

ASTM - American Society for Testing and Materials

ARD - acid rock drainage

BST - Breakaway Support Technology

CAD/CAM – computer aided design or computer aided manufacture

CDF - Cumulative distribution function

CFD - Computational fluid dynamics

CT scan - Computerized tomography

DEM – Discrete element method

EC – Environment Canada

In-situ Conversion Processes (ICP)

LNCR - Narrow channels refinement level

LSSF - Small solid feature refinement level

Ltol - Tolerance refinement level

LINEST – linear statistics function (EXCEL)

MGS - Minimum gap size

MWT - Minimum wall thickness

MW_e – Megawatt of electricity

Ngap - number of cells per channel width

NHEA - Natural Heat Exchange Area

PSM - packed sphere model

PFC - particle flow codes

PG – Point Goal

PDF – probability distribution function

Re - Reynolds number

RRL - Result Resolution Level

RPM – revolutions per minute

RR - Rosin Rammler distribution

.stl - Stereo Lithography format

SP – Static pressure

(Cp/Cv) - Specific heat ratio

2SWF - Two-Scale Wall Functions

SST - Soluble Support Technology

S-T - Steinhart-Hart equations

SG – Surface Goal

TP – total pressure

UPS – uninterruptible power supply

VP - velocity pressure

VG – Volume goal

List of Nomenclature

A = Cross sectional surface area used for flow (m^2)

A = area through which q passes (m^2) [conduction]

A = heat transfer area of the surface (m^2) [convection]

A = surface area of the emitting body (m^2) [radiation]

A_1 = surface area of rock 1 or emitting surface [view factor]

A_2 = surface area of rock 2 or receiving surface [view factor]

c_p = specific heat in (J kg^{-1} K^{-1}) [Prandtl number]

c_p is the heat capacity (J K^{-1}) [Steady State Energy Equation]

c = shape factor that accounts for the shape and tortuosity of channels (Kozney - Carman)

D = duct diameter (m)

d_C = the characteristic size of the fragments of interest [Rosin Rammler]

$\bar{d}$ = the mean diameter of the fragments of interest [Rosin Rammler]

D_h = hydraulic diameter (m)

dP = change in pressure across two points (Pa)

$d\theta$ = change in temperature (°C)

dF – degrees of freedom (From LINEST function)

dx = distance between isotherms (m)

$\Delta\theta$ = temperature difference between the surface and the bulk fluid (K or ^oC) [convection]

D_R = the specific weight = the density of solid over the density of water [Kozney – Carman]

μ = dynamic viscosity (Nsm^{-2})

e_t = tunnel wall absolute roughness (m) [Atkinson's]

ε_1 = emissivity of emitting surface 1 [view factor]

ε_2 = emissivity of receiving surface 2 [view factor]

ε_t = dimensionless relative roughness [Atkinson's]

e = void ratio (porosity) [Kozeny – Carman]

$\int_1^2 Vdp$ = flow work (J kg^{-1}) [Steady State Equation]

F_{ev} = emissivity and view factor

g = gravity (m/s^2)

δ_{ij} = Kronecker delta function [Navier-Stokes]

GW_{th} - Gigawatt Thermal

H = enthalpy, J kg^{-1} [Navier-Stokes]

h = thermal enthalpy J kg^{-1} [Navier-Stokes]

h_c = convective heat transfer coefficient (W/m^2K)

h_R = radiative heat transfer coefficient $(W/m^2 °C)$

ΔH = difference in height or head (cm) [Darcy's]

k = thermal conductivity in (W m^{-1} K^{-1}) [Prandtl]

k = hydraulic conductivity (cm/s) [Darcy's]

k = gas permeability (m^2) [Darcy Gas]

k = hydraulic conductivity (l/s) [Kozeny-Carman]

k = Atkinson's friction factor (Ns^2/m^4 or kg/m^3).

k = a constant of proportionality, the thermal conductivity (W m^{-1} C^{-1})

$k =$ resistance vector of porous media [Navior-Stokes]

L = flow path length or the length of a sample section in the direction of flow (m)

m = the mass flow rate through the body (kg/s)

n = spread factor [Rosin Rammler]

O = Perimeter length of a section of a sample (m) [Atkinson's]

ΔP = Pressure drop across a sample (Pa) [Atkinson's]

$P_t =$ total pressure at a point in the wind tunnel (Pa) [Bernoulli]

$P_s =$ static pressure at a point in the wind tunnel (Pa) [Bernoulli]

$P_v =$ velocity pressure at a point in the wind tunnel (Pa) [Bernoulli]

Q = flow rate (m^3/s) [Atkinson's]

q = The rate of heat transferred (W) [conduction]

q = heat transferred per unit time (W) [convection]

q = heat transfer per unit time (W) [radiation]

q = heat added to the system J kg^{-1} [Steady State equation]

$q_i =$ the diffusive heat flux (W/m/s) [Navior-Stokes]

$Q_H =$ is a heat source or sink per unit volume (W/m^3) [Navior-Stokes]

R = Atkinson resistance of the duct (Ns^2/m^8)

R^2 – correlation coefficient

R = resistance measured (ohms)

ρ = density in (kg/m^3) [Reynolds number]

ρ_a = the air density in (kg/m^3) [Atkinson's]

$S_i =$ mass distributed external force per unit mass due to a porous media resistance (N/kg) [Navior-Stokes]

$S =$ specific surface (m^2/kg of solids) (Kozney – Carman])

θ_1 and θ_2 = temperature of the two solid surfaces ($^\circ C$ or $^\circ K$) [Radiation]

T = temperature °Kelvin

$\tau_{ij} =$ the viscous shear stress tensor (Pa) [Navior-Stokes]

μ_a = absolute viscosity (Pa s^1) for kinematic viscosity [Navior-Stokes]

μ = gas viscosity (Pa*s) [Darcy gas]

$\mu_w =$ the dynamic viscosity of water (N s/m^2) [Kozney – Carman]

u_1 and u_2 = velocity at input/exhaust in m/s [Steady State Equation]

$u =$ fluid velocity (m/s)[Navior-Stokes]

fluid velocity V (m/s) [Reynolds number]

ν_a = the kinematic viscosity of air

v_m = mean velocity of airflow (m/s) [Atkinson's]

W = work added to the system, J kg^{-1}[Steady State]

Y = The mass fraction of a body of fragmented rock, passing a sieve size, d [Rosin Rammler]

Z = elevation from point of reference (m) [Steady State Equation]

1 Introduction to the Packed Sphere Model workflow

Analysis of the accepted methods for the design and understanding of airflow and heat exchange through large fragmented rock bodies in mines, such as those at Creighton and Kidd Creek Mines, reveal them to be still fundamentally only empirical in nature (Rutherford, 1960); (Western Miner, 1982; Envers, 1986; Stachulak, 1991; Acuna *et al.* 2010). In these methods, none of the key geometric variables known to affect heat transfer in, for example, heat exchange design, appear in the design equations, such as the heat exchange area and the length or shape of passages. In contrast, equations used in heat exchanger design such as those of Muralikrishna and Shenoy (2000) require such geometric parameters to be defined at the outset. The embedded empiricism of prior methods cannot support the re-engineering of such assets to extend their duties or capacities. The intent of this research was to better understand how discontinuous porous media problems could be modeled more realistically to overcome these engineering challenges. The work has applications in the engineering of large scale regenerative heat stores, as at Creighton Mine, improved process control via temperature regulation in heap leaching and possibly a further understanding of the performance of tailings embankments (Auer, Rosenberg and Whitney, 1996), among other potential heat transfer problems in porous media.

There are essentially two approaches to the analysis of fluid flow and heat transfer in fragmented rock:

i. An equivalent continuum modelling approach where the entire porous medium is considered as a whole, and the demands for specification of geometric parameters are minimal.

ii. Discontinuum models where the internal geometric characteristics are faithfully represented, but where the baseline information on this geometry is difficult to obtain.

In order to investigate the hypothesis that a proxy experimental procedure can be used to help re-engineer large scale problems currently using strictly empirical methods, this research develops a methodology to permit specification of geometric parameters for discontinuum models. Packed Sphere Models (PSM) are renderings of fragmented rock bodies that are produced by means of caving, collapse, or consolidation dynamics embedded with so called "particle flow codes" (Itasca, 2013). These codes use spheres to represent rock fragments and simulate the natural collapsing of a rock mass by applying Newtonian dynamics to the ensemble. The link with real fragmented rock bodies is that these particle ensembles can be synthesized so that their particle size distribution is the same as the real object being modelled. The methodology could be adapted to utilize other geomechanical tools that are able to model progressive damage in rocks, such as ELFEN (Rockfield, 2014). The approach was evaluated using a CFD tool: Flow Simulation (Dassault Systèmes, 2013), which is part of the Solidworks CAD/CAM software suite; however the method could have adopted other CFD codes such as COMSOL multiphysics (Comsol, 2014) or FLUENT (ANSYS, 2014). The Packed Sphere Method was tested to verify the basic technique, in advance of attempted verification in large scale engineering applications.

1.1 Thesis research questions

Overall, the research aimed to answer the following questions:

i. Does the determination of geometric parameters for the discontinuous porous medium lead to improvements in accuracy, precision, or computational efficiency in modelling and understanding of heat transfer and flow properties for real-world applications involving fragmented rock bodies (e.g. ice stopes, geothermal energy reservoirs, permafrost thaws)?

ii. Which of the approaches explored leads to the best characterization of heat transfer phenomena in these materials?

iii. Can PSM be used to calibrate large scale equivalent continuum models to reduce computational time and increase accuracy for problems of a spatial scale of relevance to the mining industry, which may be in the tens to thousands of meters (as shown from the laboratory scale of Figure 1 to the engineering scale of Figure 2)?

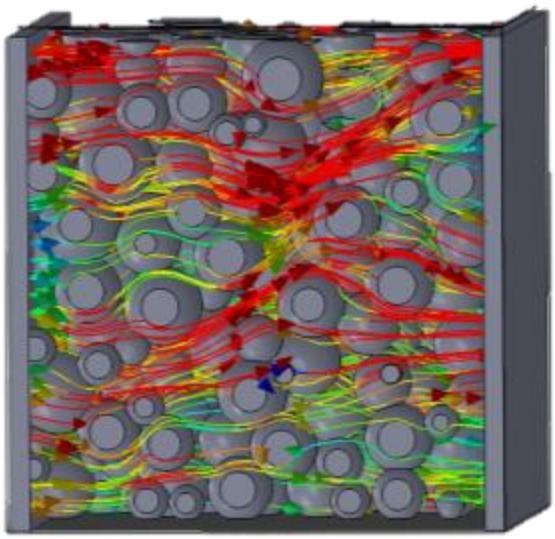

Figure 1: Schematic rendering of a PSM with airflow moving from left to right. The PSM shows a base representative elemental volume in this methodology that may be adapted to the larger problem as in Figure 2. The size of the sample is 7.62cm in each direction.

Figure 2: Thermal storage system at Creighton mine in Sudbury, Ontario. The broken rock pile is not fully represented by just a surface image because the reservoir extends at least 250m below this porous media interface, which directly influences airflow. The distance across the pit to the other side is 850m. Modelling of this porous media problem is a primary objective of this methodology, since the Creighton system is currently only analysed by empirical methods.

1.2 Research hypothesis

It is hypothesised that improvement of the equivalent continuum model for analysis and design can be examined first on a discrete level with PSMs coupled with CFD or experimental results. This information can then be used to develop fluid flow and heat transfer characteristics that may be inputted into equivalent continuum techniques to model large scale problems.

1.3 Outline of the approach used in this thesis

To test the hypothesis described above, a discrete "porous medium" equivalent based on Rosin Rammler particle size distributions was formed to produce the so called "Packed Sphere Model" or "PSM". The technique was then physically replicated in a laboratory environment to verify the predictions made by the Fluid Flow Simulation tool. This was done by means of a 3D printer manufactured discrete model that was used to measure airflow, pressure, and temperature in two separate physical experimental rig experiments. The PSM technique then used CAD techniques to establish values for the low level geometric parameters used in fluid flow and heat exchange and also to measure or proxy difficult numerical parameters such as the tortuosity of the discrete model. Once the technique was developed, questions about the discrete model behaviours in accordance with Kirchhoff's Laws for behaviour of fluids in series and parallel ducts were examined. Beyond this, practical issues such as repeatability, scaling, representative elemental volumes, and technical issues such as the effects of computational meshing were also examined. Finally, the use of the discrete PSMs to create continuum equivalent models was tested and verified for airflow within a massive porous medium constituting a thermal reservoir at a mine in Northern Ontario, through another physical experiment.

1.4 Workflow details of the thesis

Contained within this section is the workflow of this thesis. The detailed breakdown is as follows:

Chapter 2. Background and literature review of thesis – This component reviews the background information for the PSM technique. Areas covered include: porous media modelling, industrial applications, heat transfer theory, computational fluid dynamic codes and their verifications, Rosin Rammler classification of porous media, and large scale experimental techniques drawn upon later in the thesis, including for example, the variations of the constant head pressure test.

Chapter 3. PSM CFD simulation workflow – This chapter details the workflow required for the creation of the packed sphere models and their analysis for fluid flow.

Chapter 4. Experimental setup (Resistance testing) – This chapter covers the contribution of the wind tunnel rig verification experiment for airflow created based on the PSM Rosin Rammler distribution derived and geomechanically consolidated CFD model. The manufacturing of a complex 3D discontinuum porous media model for verification of airflow and thermal performance in a direct one to one scale model is detailed. The remaining portion of this chapter deals with the further characterisation of the physical wind tunnel experiment. The experiment set up and equipment adopted is also described.

Chapter 5. Airflow performance (Resistance) – In this chapter, the method of verification of the CFD code in modelling PSM is detailed and results are presented. This verification is based on the comparison of pressure and flow rate values from the CFD model with those of the physical wind tunnel experiment detailed in Chapter 4.

Chapter 6. CFD mesh sensitivity and repeatability – In this chapter, the sensitivity of results of PSM for airflow resistance are tested using five different PSM renderings with the same Rosin Rammler distribution. The common factor between these 5 replicates is that the Rosin Rammler and porosity values are the same. The specific geometries of the particle ensembles are very different. The second section of this chapter deals with the geometric mesh sensitivities in CFD simulations of PSMs.

Chapter 7. PSM derived estimates of Atkinson's resistance and friction factor – The work reported in this chapter examined whether or not it was possible to geometrically interrogate a PSM so that the detailed geometric parameters known to affect flow and heat transfer could be determined. The contribution in this chapter is a method of geometric interrogation of the PSM that produces the exact perimeter lengths, cross-sectional areas, and true length of fluid motion within a volume known as the tortuosity. These parameters are then used for the calculation of the Atkinson's resistance and friction factor, assuming that PSM flow behaviour can be represented by an airflow duct, as used in mine ventilation network modelling.

Chapter 8. Heat transfer performance of PSMs – The focus of this chapter is on the thermal performance of physical experiments and corresponding parameters of the PSM, as well as

verification of CFD simulations of PSM using results from a physical wind tunnel. The method uses a PSM with known geometry and thermal properties, although the latter are not rock properties. Nevertheless, this enables verification of the approach and technique. Results are compared at 1:1 scale.

Chapter 9a. Scaling of PSMs and creation of equivalent continuum models – The work represented in previous chapters dealt with 1:1 scale comparisons between CFD simulations of experiments conducted at laboratory scales. The engineering structures the work considers are at least 6 orders of magnitude larger than this. Thus, a key matter of concern is how to scale the relations between fragmented rock geometry that have been determined at lab scales to engineering scales. In this chapter, three distinct approaches to scaling airflow and heat exchange behaviour are explained. The first approach, which is detailed within this section, is a self-similar scaling of the PSMs. Self-similar scaling in this case means that all components of the PSM (spheres and containment boxes) are scaled directly by a scaling factor to see if the airflow and resistance values change for the same geometries. The scaling factor of 10 was used first in this examination.

Chapter 9b. Representative elemental volume of PSM – The second method of scaling is explored within this section by use of sub-samples of a large PSM. A given Rosin Rammler distribution was tested in the CFD simulator to determine whether equivalent airflow behaviour was recovered when testing smaller elements of the larger bulk sample. Each sub-sample has a particular geometric configuration of particles that may be expected to change the airflow characteristics of the relative sub-samples. Given the fact that the statistical description of the

particle ensembles were known to be the same, the key question investigated was whether these each led to the same bulk qualitative airflow resistance characteristic. An independence test of the Atkinson's friction factor and a power law theory relation between the volume of a sample and airflow resistance is presented.

Chapter 9c. Scaling through branch behaviour of PSMs – As a third method to scale up a PSM, this section examines whether branch behaviour using Atkinson's Law is reasonable for application to series and parallel behaviour. This information could then be used to scale up a PSM further, in an alternate manner of PSMs.

Chapter 10 and 11. Modelling an approximately 1 km^3 thermal regenerator – These chapters illustrate the application of the research to the analysis of a large scale seasonal thermal regenerator. The model in these chapters utilize an airflow resistance characteristic determined from CFD simulation of a PSM and then applies scaling rules to produce an airflow resistance characteristic applicable to the mesh size of a CFD model of the large scale structure. The scaling process was guided by pressure difference observations across the large scale structure. The methodology and equipment used to gather this data are also explained in this chapter.

The thesis 'roadmap' is shown in Figure 3. This flow chart presents the different PSMs designed and tested to examine certain behaviours. The first model is the 3D printed model that was used in the laboratory experiments for both the fluid flow and heat transfer verification of the CFD code. The second set of PSMs was created to test whether the principles of equivalent geometry of the Rosin Rammler distribution held. That is, when the same Rosin Rammler distribution of

particles (for all geometric characteristics such as surface area and volume) is consolidated in different ways, do the airflow characteristics differ? The third set of models also consists of three different PSM that were used to examine the scaling issues of PSMs. The first PSM deals with direct scaling and the creation of equivalent continuums, the second with representative elemental volumes, and the third with series and parallel behaviour. For the methodology aspects, the verification model was used to test and design the geometric dissection techniques while the scaling models were used in synthesis for the verification of the thermal reservoir porous media problem.

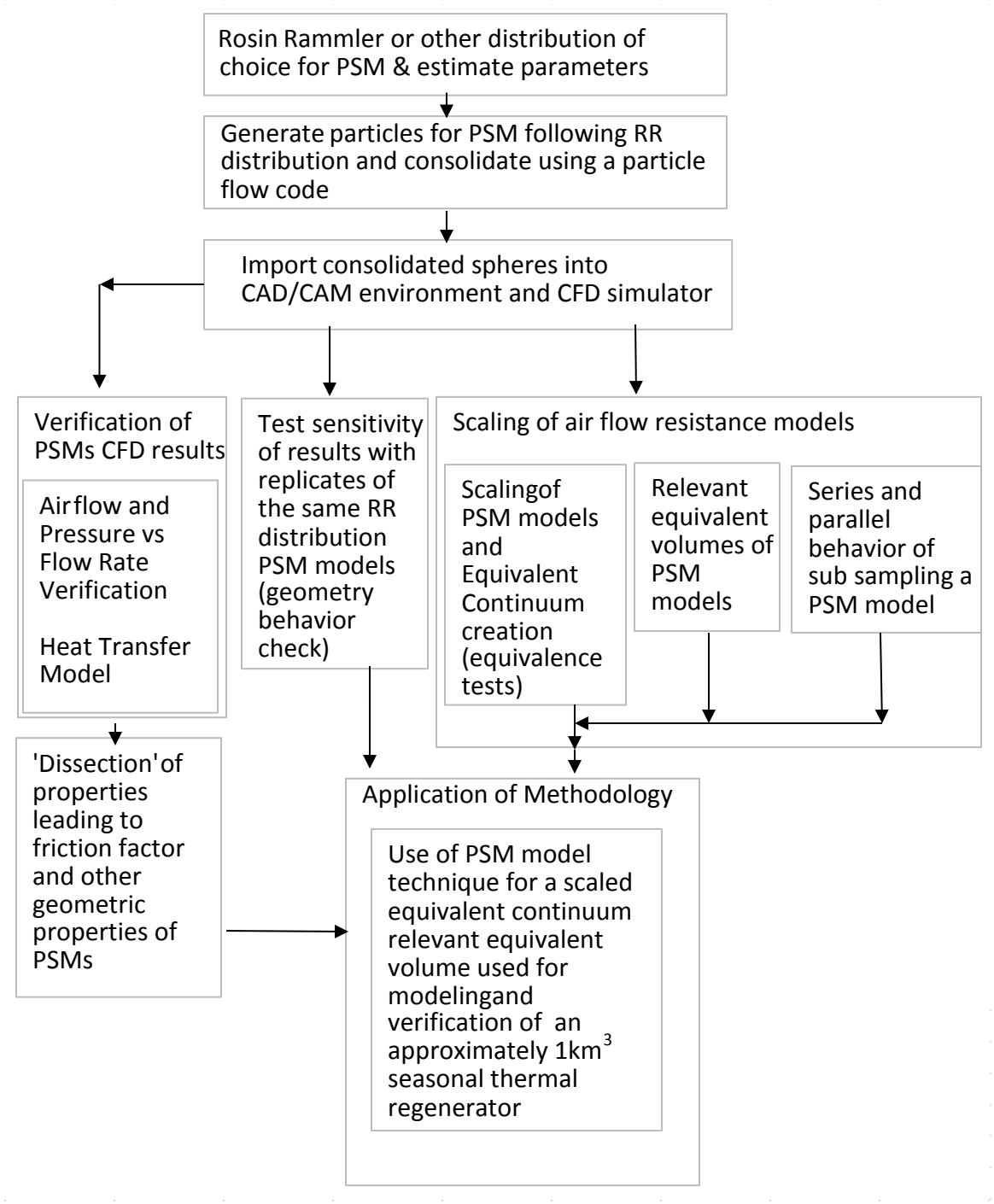

Figure 3: Thesis 'roadmap'

2 Background and review of porous media

2.1 Modelling approaches of porous media

Overall there are two general ways to characterize the geometry of broken and fragmented rock. The first is to investigate it as an equivalent continuum of a permeable geomaterial; the second is to look at the problem as an ensemble of broken rock components with airways formed from the interstitial spaces between the fragments and treat them either individually or as a bulk sample of discrete branches.

Method 1: Discrete branches (including Packed Sphere Model)

The discrete branch method used in ventilation practice uses the characteristic of resistance to define a branch. The advantage of this method is that normally with ventilation circuits, the geometry of the system including the length in the direction of flow, cross sectional area perpendicular to the flow, perimeter, and the friction factor are all known. In terms of porous media, this is not the case. The Atkinson's equation defines the resistance of an individual airway and is represented by:

$$R = k\frac{LO}{A^3} \tag{1}$$

where:

R = Atkinson resistance of the duct (Ns^2/m^8),

L = flow path length or the length of a sample section in the direction of flow (m),

O = Perimeter length of a section of a duct or sample (m),

A = Cross sectional surface area available for airflow (m^2), and

k = Atkinson's friction factor (Ns^2/m^4 or kg/m^3).

If this equation is multiplied by the flow rate squared Q^2 (m^3/s) then the pressure drop (Pa) across the length L is known. The Atkinson's resistance can also be defined as the following total resistance of a combination of one or more airways:

$$\Delta P = R_T Q^2 \quad (2)$$

Where R_T = Total Atkinson's Resistance (Ns^2/m^8) (for one or multiple branches)

Q = flow rate (m^3/s)

This means that by measuring the pressure drop and the flow rate, the Atkinson's Resistance can be calculated. An illustration of an individual discrete branch is shown in Figure 4.

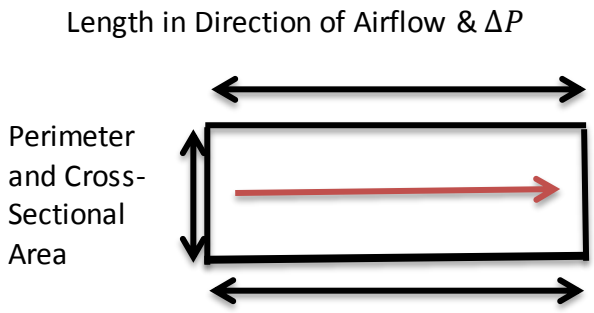

$$R = k \frac{LO}{A^3} \qquad \Delta P = R_T Q^2$$

Figure 4: One ventilation branch with a resistance and pressure drop.

Series and parallel behaviour of multiple ducts can be examined similarly to the relationships that follow for the total resistance R_T according to Kirchhoff (McPherson, 2007):

For series behaviour:

$$R_T = R_1 + R_2 + \ldots R_N \quad (3)$$

The rule for series behaviour of two ducts that are the same size is that if the same flow rate and resistance is in the two ducts, the pressure drop is doubled.

For parallel behaviour:

$$\frac{1}{\sqrt{R_T}} = \frac{1}{\sqrt{R_1}} + \frac{1}{\sqrt{R_2}} \ldots\ldots + \frac{1}{\sqrt{R_n}} \quad (4)$$

The rule of parallel behaviour of two ducts of the same size is that if the same pressure drop across both ducts is the same, then the flow rates sum up. An illustration of this is shown in Figure 5. As a bulk value for the whole system, the total resistance can again be used.

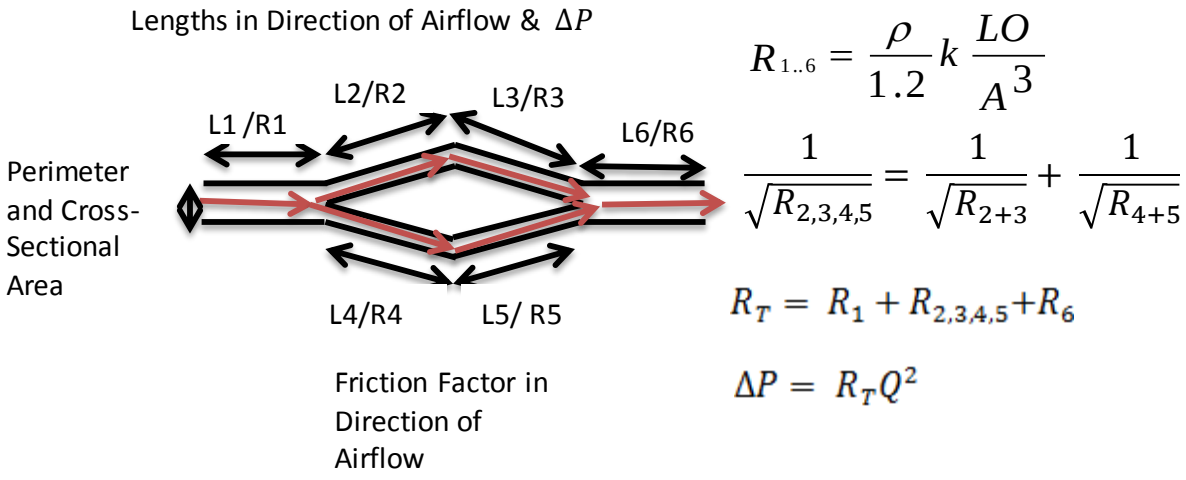

Figure 5: Series/Parallel representation of several airflow branches. The pressure losses and resistances of these systems can be reduced into a single airway through Kirchoff's current and Ohm's laws

The PSM technique uses the measurement of airflow and pressure drop to determine the total Atkinson's Resistance of the discontinuum ensemble. The reason for this is that the discrete branches cannot be easily geometrically interpreted at this time. In Chapter 4 a new method will be presented. A schematic form of the PSM is shown in Figure 6.

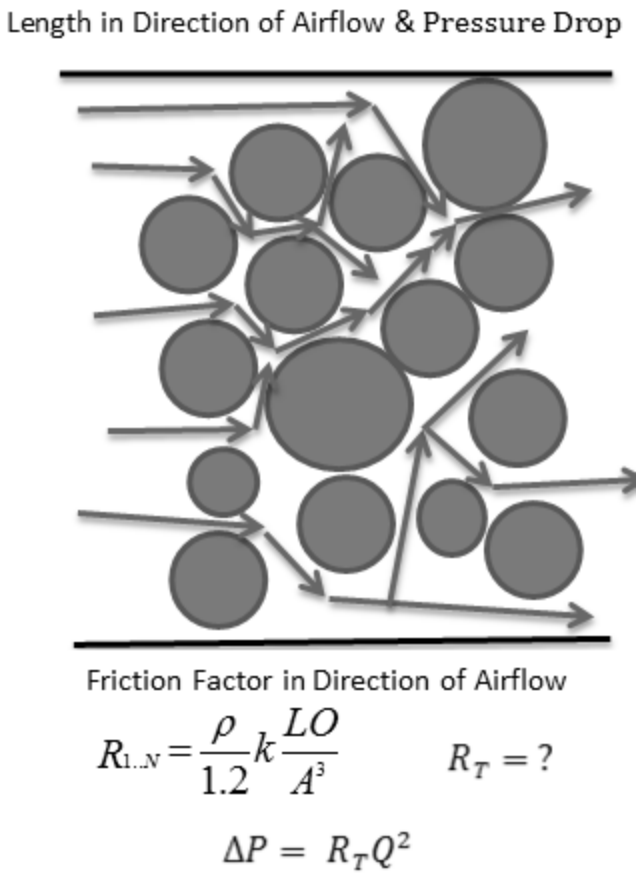

Figure 6: PSM discontinuum model representation. The resistance of the model is found by measuring the flow rate and pressure drop across the ensemble. Using a dissection technique in Chapter 4, the low level geometric parameters can then be calculated by using the resistance

The airflow characteristics of PSM are extremely difficult to obtain unless a tool such as computational fluid dynamics (CFD) is used. An experimental approach can be used to determine the flow rate, but it generally then requires a destructive test in which the geometry of the system is lost. The PSM (Figure 7) technique therefore is a proxy method to obtain these observations and make the geometric dissection possible by using synthetic modelling. The method of discrete branches is typically abandoned for equivalent continuum modelling techniques due to not being able to properly gather this information. In contrast, a PSM represents this information and allows it to be recovered digitally. The PSM also provides the

possibility of translating its data into an equivalent continuum model, as seen in the direct scaling section of Chapter 9.

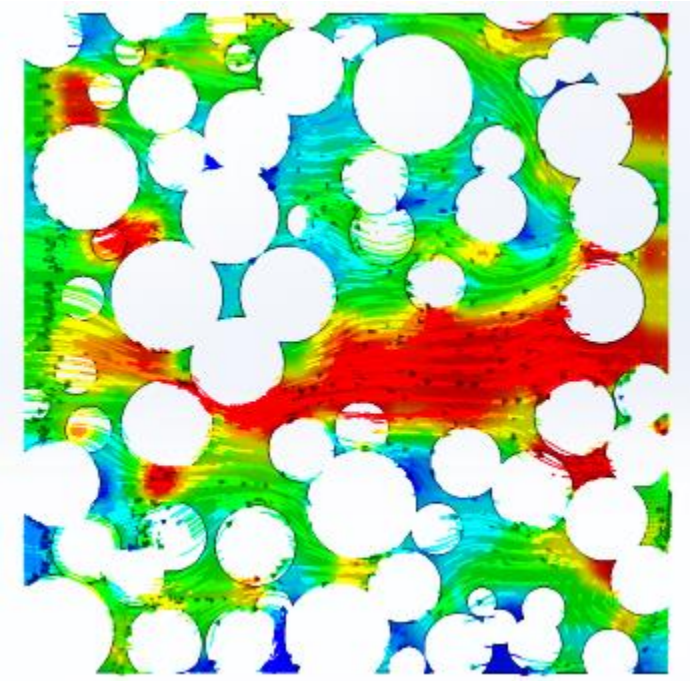

Figure 7: PSM detailing velocity field and flow trajectories around particles in the ensemble. The red colours have higher velocities in this state.

Method 2: Equivalent Continuum

An equivalent continuum representation of a flow material contains no internal geometry, only the cross–sectional area and the length of the sample. The pressure loss can also be described by the Atkinson's resistance which is identical to the branch model, but the variables required for this technique are not easily obtainable and it is difficult to ensure representativeness, repeatability and accuracy. The main benefits of this model type are the computational efficiency and the ability to scale series and parallel behaviour as discussed above. A schematic representation of an equivalent continuum model is shown in Figure 8.

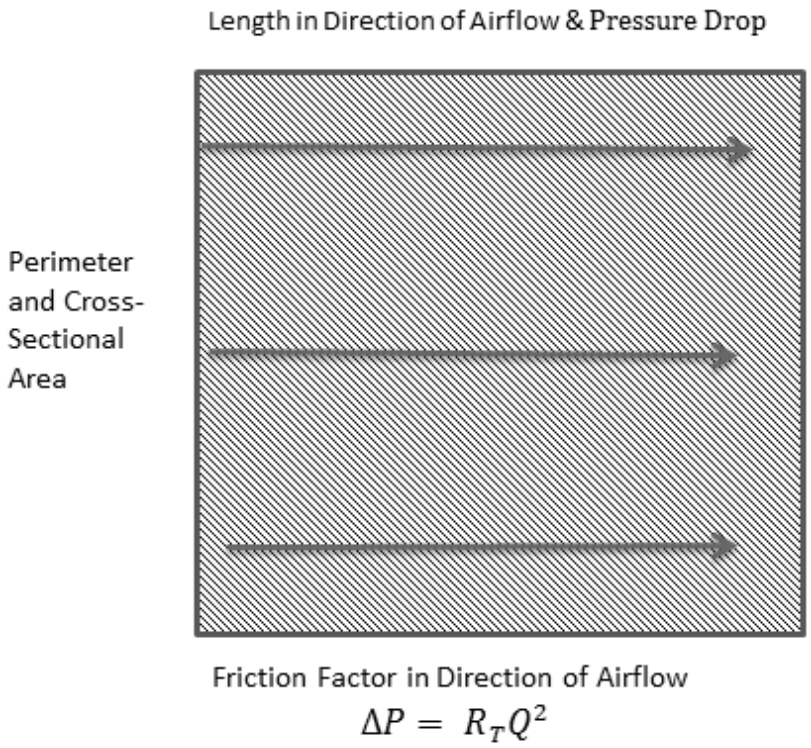

Figure 8: Equivalent continuum model schematic of an individual ventilation branch.

The standard directional characteristics of a porous medium for both equivalent continuum and discontinuous continuum are defined as follows (Daussalt, 2013):

1. isotropic (i.e., the medium permeability is independent of direction)

2. unidirectional (i.e., the medium is permeable in one direction only)

3. axisymmetrical (i.e., the medium permeability is fully governed by its axial and transversal components with respect to a specified direction)

4. orthotropic (i.e., the general case, when the porous medium permeability varies with direction and is fully governed by its three components determined along three principal directions).

Within this thesis, each sub-sample is assumed to have orthotropic behaviour, unless proven otherwise.

2.2 Industrial applications involving porous media

The following section provides examples of industrial situations where a porous medium analysis may be adopted, and thus also reflects the potential application areas for the research in this thesis. The engineering problems briefly outlined include:

i. surface air intake climate control

ii. geothermal energy

iii. ground freezing

iv. tailings management facility control

v. heap leaching

2.2.1 Surface intake climate control areas

One of the applications requiring evaluation of fluid flow and heat flow of broken and fragmented rock is the surface intake climate control systems used in the mining industry. The three main sites that have used this technology include Vale's "NHEA" (Natural Heat Exchange Area) at Creighton Mine, Glencore's Kidd Creek "Cold Stope Intake" (Hardcastle *et al.* 2008) and at their, now closed, Falconbridge Mine (Partyka, 2003). The technique originates from open pit or underground mines close to surface (that typically have used sub-level stoping or sub-level caving mining methods) that have finished producing and are then modified by having the underground bottom of the pit turned into ventilation system surface intake, via re-engineering of former production openings.

The early original works by Inco Limited used psychrometric property calculations of a single airway to approximate the performance of the Creighton Mine NHEA as a whole (Rutherford, 1960; Western Miner, 1982; Envers, 1986; Stachulak, 1991; Sylvestre, 1999, and Golder Associates, 1980). The relative complexity of the system meant that to isolate the characteristics of the porous media itself was practically impossible. This is because the system consists of surface intake, which is a section of caved and subsided rock, and an air outlet system of over 100 slusher trenches and production drifts. With time and improvements in sensing, the analysis of the individual slusher trenches system became possible and can be seen with model calibration and optimization approaches using genetic algorithms (Acuna *et al.* 2010). Other similar works involve general airflow through broken media with more straightforward inlet and outlet geometries (Johnson, 2006; Hardcastle *et al.* 2008). Johnson and Hardcastle provide evidence that porous media problems can be examined in a similar way to ventilation airway networks, and can also characterize properties of heat transfer as well as airflow. This simplification was possible because of the relatively simple geometry adopted with one inlet and one outlet, but the same approaches would be challenged with complex geometries involving multiple inlets or outlets. In the latter circumstances, although behaviour and performance of the asset can be characterized, current evaluations of the multiple outlet problem are done largely empirically, which may be appropriate for operational description, but presents difficulties in manipulation when re-engineering the asset for increased duty.

2.2.2 Geothermal energy

A second application area for this work involving fluid flow and heat transfer in fragmented rock bodies is geothermal energy. Worldwide in 2010, about 10,715 MW_e of geothermal power was

produced from 67,246 GW_{th} across 24 countries (Holm, *et al.* 2010). Hydraulic fracturing is used to stimulate the heat transfer performance between the geomaterial and the geothermal brine used for thermal energy abstraction (M.I.T, 2006) by increasing the average permeability for the latter. Hydraulic fracturing increases the relatively narrow flow apertures in the geothermal reservoirs, and thus the PSM method would require some development to become suitable to this application. Hamm and Sabet (2010) have used the FLUENT software (Fluent Inc., 2010) to conduct heat transfer analysis to evaluate whether thermal energy in flooded coal mines in France can be used for district heating purposes. Problems highlighted in that work include the lack of accurate results for the heat transfer surface area that affects permeability, which made the heat transfer calculations conservative. The work reported herein may provide an alternative method of characterization of fluid flow and heat transfer to permit progress to be made.

2.2.3 Ground freezing

Artificial ground freezing has been used for over 150 years and is extensively used for shaft sinking purposes through aquifers, being first proposed by Poetsch (1863). One of the current notable uses for freezing has been proposed by Echo Bay Ontario, Ltd (Layne Christensen Company, 2006). A frozen earth barrier will be constructed around the perimeter of the proposed Aquarius open pit gold mine in Timmins, Ontario. The frozen barrier, created by converting the groundwater to ice, has been determined to be an environmentally acceptable technique to prevent groundwater inflows into the mine excavation (Layne Christensen Company, 2006). Understanding the resistance of the porous media for water may result in better freeze wall design capability. Another ground freezing process to which this work may be applicable is from the oil and gas industry, through Shell's research into *In-situ* Conversion Processes (ICP) (Shen

et al; 2010), which are very similar to the technique described above. In ICP, a square 'box' is constructed by freezing in the porous medium of interest. Within the 'box', electrodes are used to heat the porous medium to release the oil contained inside. With some development, the research presented herein may assist with design controls of processes for the freezing wall.

2.2.4 Control of Tailings Management Facilities

Regarding the analysis of fluid flow and heat transfer in broken and fragmented rock, studies have been executed by solving coupled problems using the finite element method (Arenson *et al.* 2006). One such example is the software program GeoStudio Beta 2006 (GeoSlope International Ltd. 2007). Geostudio Beta (Geoslope, 2014) software uses an equivalent continuum approach in the finite elements to model the volume of rock. It explicitly does not consider the airspace as void through which flow occurs. Klassen *et al.* (2007) and Pham *et al.* (2008), conducted research at Rio Tinto's Diavik mine using a similar implementation to model the cooling of a series of tailings piles. Their model was validated against results from Nield and Bejan (1999); Goering (2003); Sun *et al.*(2005); Goering and Kumar (1996); Lai *et al.* (2003a); Lai *et al.* (2003b); and Yu *et al.* (2004), each of which applied to the structural degradation of highway embankments. While the meshing element representations of the Diavik pile themselves were good, analysis of the temperatures in the Diavik test pile showed the importance of i) the air intake geometry through the side slopes and ii) heterogenous permeability throughout the pile. It is hypothesized that by using the PSM technique set out herein, better characterisation of the process may be possible.

In the control of tailings embankments for acid rock drainage (ARD), Wels *et al.* (2003) adopted a slightly different model of heat flow / heat transfer evaluation. The numerical simulations of waste pyrite bearing rock piles were carried out with an equivalent continuum within TOUGH AMD developed by Lefebvre (1994, 1995a, 1995b) with the option of using FIDHELM developed by the Australian Nuclear Science and Technology Organization (ANSTO) (Pantelis, 1993). This has been applied to theoretical as well as field problems (e.g. Pantelis and Ritchie, 1991; Pantelis, 1993; Kuo and Ritchie, 1999). The TOUGH AMD program (Lefebvre *et al.* (2001a, 2001b)) has been adapted to the modelling of acid rock drainage. With adaptation to two phase CFD codes, PSM could serve as an alternative to these forms of analysis with the benefit of geometric parameters.

In the context of acid rock drainage control of tailings of the Diavik minesite, Blowes *et al.* (2006) undertook hydrology, geochemistry, temperature, and biogeochemistry tests of the waste rock piles over time. Subsequently, the objective was to model the acid rock drainage problem in tailings piles by examining the oxygen content of the waste pile. The concept underlying the design of the test piles followed from earlier work at the Cluff Lake mine in northern Saskatchewan (Smith and Beckie, 2003; Nichol *et al.* 2005; Wagner *et al.* 2006). To aid in the design of the instrumentation system within the test piles and to gain initial insight to the thermal evolution of the test piles, preliminary modelling was conducted using a modified version of the two-dimensional finite difference model SULFIDOX (Brown *et al.* 2001; Linklater *et al.* 2005). This model incorporates gas and water transport, kinetically controlled sulfide oxidation (and associated heat generation), heat transfer, ice formation and melting. Simulations were based on biotite schist averaging >0.08 wt. % sulphur material, as it is associated with the greatest

potential for heat release and acid generation at this site. This approach also takes an equivalent continuum approach to the problems of heat transfer, but does not explicitly consider internal surface area or other geometric properties of the tailings pile, as is the case with the PSM approach.

2.3 Review of heat transfer theory for fragmented rockpiles

In this investigation of surface area, length, circumference and other geometric properties relevant to heat exchange, the formulae in the design of heat exchange can be used to develop understanding of discrete discontinuum models that are the main conceptualisation of this work. For heat transfer, conduction, convection, and radiation mechanisms can be evaluated. Heat transfer due to phase change is known to be an important mechanism in mine air climate simulation, but is not considered in this work.

2.3.1 Conduction for a single airway

Fourier's Law is used frequently to represent the process of conduction. In this equation, heat transfer is proportional to both the surface area, A, orthogonal to the heat flux, and also to the temperature difference, $d\theta$, which drives the heat flow. The heat transferred is also inversely proportional to the distance, dx, between isotherms (McPherson, 1986). In one dimension, Fourier's Law is:

$$q = -kA\frac{d\theta}{dx} \tag{5}$$

Where:

q = The rate of heat transferred (W)

k = a constant of proportionality, the thermal conductivity (W m^{-1} C^{-1})

A = area through which q passes (m^2)

dx = distance between isotherms (m)

$d\theta$ = change in temperature (° C)

Conduction is a key premise in many investigations due to the need to try and quantify the amount of heat transferred from the broken rock to the adjacent air or liquid flow.

Most problems only use 2D solvers for porous medium problems. Since it will be shown to be possible to dissect the geometry in 3D (Chapter 7), it is also relevant to provide the equation in three dimensions (McPherson, 1986):

$$\frac{\partial \theta}{\partial t} = \alpha \left(\frac{\partial^2 \theta}{\partial x^2} + \frac{\partial^2 \theta}{\partial y^2} + \frac{\partial^2 \theta}{\partial z^2} \right) = \alpha \left(\theta_{xx} + \theta_{yy} + \theta_{zz} \right) \quad (6)$$

where the thermal diffusivity is: $\alpha = \frac{k}{c_p \rho}$

2.3.2 Convection for a single airway

In the absence of phase changes, the heat transfer mechanism that may dominate, in the principal application area considered, is forced convection. Forced convection is defined by Newton's

Law of Cooling but has been modified to include the parameters associated with the laminar, transitional and turbulent flow regimes (Incropera, DeWitt, 2006):

$$q = h_c A \Delta\theta \tag{7}$$

where:

q = heat transferred per unit time (W)

h_c = convective heat transfer coefficient of the process (W/m^2K)

A = heat transfer area of the surface (m^2)

$\Delta\theta$ = temperature difference between the surface and the bulk fluid (K or ^oC)

There are three general cases of forced convection: laminar, transitional, and fully turbulent flows. In comparison to conduction, the areas referred to are different; this is because whereas the conduction area is typically internal to the body, the convection areas are between the surfaces of the rock and the fluid.

2.3.3 Radiation for a single airway

The area of heat exchange can also be found in the radiation equations of heat transfer. The linearized formula for radiative heat is as follows:

$$q = h_R \cdot A \cdot (\theta_1 - \theta_2) \cdot F_{ev} \tag{8}$$

Where:

q = heat transfer per unit time (W)

h_R = radiative heat transfer coefficient ($W/m^2 °C$)

A = surface area of the emitting body (m^2)

θ_1 and θ_2 = temperature of the two solid surfaces (°C or °K)

F_{ev} = emissivity and view factor, where:

$$F_{ev} = \frac{1}{\frac{1}{\varepsilon_1} - \frac{A_1}{A_2} \cdot (\frac{1}{\varepsilon_2} - 1)} \quad (9)$$

and:

A_1 = surface area of rock 1 or emitting surface

A_2 = surface area of rock 2 or receiving surface

ε_1 = emissivity of emitting surface 1

ε_2 = emissivity of receiving surface 2

The h_R remains fairly constant in mining applications at 6 $(W/m^{2\circ}C)$ (Partyka, 2003) but can be calculated by:

$$h_R = 4.62\left[1 + \frac{t_1 + t_2}{546.3}\right]^3 \quad (10)$$

With particles of rock greater than 10mm, the influence of thermal radiation becomes significant because the effective thermal conductivity increases considerably with particle diameter (Marie-Helene, 2011).

2.3.4 Reynolds number

One of the potential methods of calculating the friction factor is through the Reynolds number, which is commonly used for representing the flow regime of a fluid system and is thus relevant to the convective heat transfer mechanism. The Reynolds Number is a dimensionless number that is a ratio of the inertial forces to the viscous shear forces in the field. The Reynolds number

uses the density ρ in (kg/m^3), the mean fluid velocity V in (m/s) of the air in a duct, the duct diameter D (possibly modified by a shape factor) in (m), and the dynamic viscosity μ in (Nsm^{-2}). The characteristics of the flow are either laminar or turbulent and are distinguished by the Reynolds number:

$$\mathrm{Re} = \frac{\rho V D}{\mu} \tag{11}$$

With $\mathrm{Re} < 2500$ the flow is laminar, $2500 \leq \mathrm{Re} \leq 6000$ yields transitional flow, and $\mathrm{Re} > 6000$ is turbulent flow. In particular conditions (such as at an inlet or outlet CFD boundary condition), the Reynolds number is calculable.

2.3.5 Prandtl number

The Prandtl number Pr is a dimensionless number approximating the ratio of momentum diffusivity (kinematic viscosity) to thermal diffusivity and can help define the conjugate flow regime in a PSM. It is readily displayed in Flow Simulation software (Dassault Systèmes, 2014). The Prandtl number is defined as:

$$\mathrm{Pr} = \frac{c_p \mu}{k} \tag{12}$$

where:

c_p = specific heat in (J kg^{-1} K^{-1})

k = thermal conductivity in (W m^{-1} K^{-1}). Commonly for air in laminar flow Pr = 0.7-0.8 and for ideal turbulent flow = 1, but averages between 0.8 – 0.9.

μ = dynamic viscosity in ($\frac{\mathrm{N \cdot s}}{\mathrm{m}^2}$)

2.3.6 Laminar and turbulent airflows

The faster the flow rate of the fluid, the more heat can be exchanged. This is due to the nature of the convective heat transfer coefficient. This coefficient is dependent upon the thickness of the boundary layer, which in turn is dependent upon the Reynolds number. The boundary layer is small when the fluid flows at high velocity. In practice this means that the heat transferred by convection increases when, for example, the velocity of the air flowing in a pipe is increased. The properties of heat flux, heat capacity, Reynolds number and viscosity for a given streamline all change when moving from laminar to turbulent flow. As a consequence, the Navier–Stokes equations for turbulent flow change and the Reynolds-averaged Navier–Stokes equations become valid. In these terms, the Reynolds stresses can enhance the heat and mass transfer (Rogers and Mayhew, 1992).

2.3.7 Airflow field

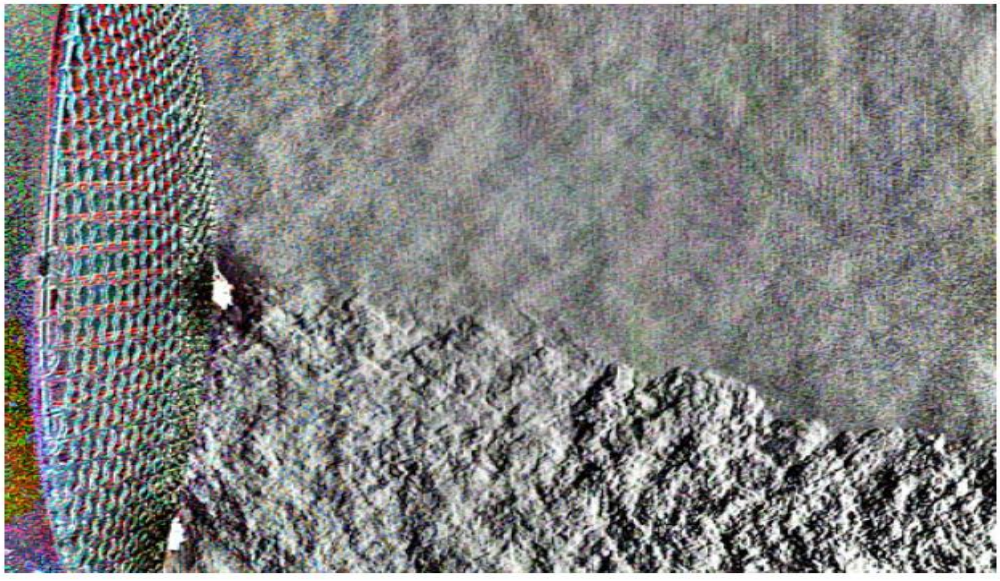

Figure 9: Schlieren infrared image of heated air passed through a fan (Jong and Luxbacher, 2010)

The airflow field is the distribution of velocity over a given area, as seen in the infrared image in Figure 9. Turbulent, laminar and transitional flow properties have a great influence on how heat transfer across a given control volume is calculated. According to Papakonstantinou *et al.* (2000), in most civil engineering applications, there are two popular methods to predict airflow fields; the first is the model experiment, and the second is numerical simulation.

2.3.8 Atkinson's friction factor

John J. Atkinson defined his friction factor in 1862. He defined it as a measurement of the resistance to airflow in a duct. Calculation of the Atkinson friction factor k, for both turbulent and laminar flow can be carried out as described by Montecinos and Wallace Jr. (2010). First, the Reynolds Number and relative roughness factors must be calculated.

$$\varepsilon_t = \frac{\mathrm{e}_t}{\mathrm{D_h}} \tag{13}$$

$$\mathrm{Re} = \frac{\mathrm{v}_m D_h}{\nu_a} \tag{14}$$

where:

ε_t = dimensionless relative roughness

e_t = tunnel wall absolute roughness (m)

D_h = hydraulic diameter (m)

v_m = mean velocity of airflow (m/s)

ν_a = the kinematic viscosity of air, defined as:

$$\nu_a = \frac{\mu_a}{\rho_a} \tag{15}$$

where μ_a = absolute viscosity (Pa s^1) and ρ_a is the air density. The following equation permits calculation of density at an elevation different than the air density at a given elevation (origin ρ_0) where the temperature is T_0:

$$\rho_h = \rho_0 0.9^h \tag{16}$$

where h is in km, and according to relation of a perfect gas:

$$\rho_a = \rho_0 \left(\frac{\rho_h}{\rho_0} \frac{T_0}{T_a} \right) \tag{17}$$

The absolute viscosity can be calculated using the following formula that applies in the following conditions:

Absolute Pressure <737.6 kPa

233 K < T_a <573 K

T_e = 273.16 K

C_e = 100 K

T_a = temperature of the mine air

$$\mu_a = \frac{23.36 \times 10^{-6}}{1 + \frac{C_e}{T_a}} \sqrt{\frac{T_a}{T_e}} \tag{18}$$

The friction factor, $f_t = \mathrm{F}(\mathrm{Re}, e_t / D_h)$ and can be found from charts as done by Montecinos and Wallace Jr. (2010).

The Atkinson friction factor is then found as in Hartman (1986):

$$k = \frac{f_t}{8} \rho_a \tag{19}$$

The use of Atkinson's friction factor traditionally in mine ventilation is as follows:

$$R = k\frac{LO}{A^3} \tag{20}$$

where

R = the so called Atkinson resistance of the duct (Ns^2/m^8),

k = Atkinson's friction factor (Ns^2/m^4 or kg/m^3).

L = flow path length or the length of a sample section in the direction of flow (m),

O = Perimeter length of a section of a duct or sample (m),

A = Cross sectional surface area available for airflow (m^2)

2.3.9 Steady flow energy equation

The steady flow energy equation is the basis for calculation of several ventilation parameters when there is additional heat or work added to the system. The steady flow energy equation is a total energy balance. Any frictional effects will reduce the mechanical energy terms and increase the internal energy but will have no influence on the overall energy balance. McPherson's (2007) interpretation of the steady flow energy equation is shown in Figure 10, but in the case of broken and fragmented rock, there is no extra fan work added to the system. The heat input to the system between points 1 and 2 is shown.

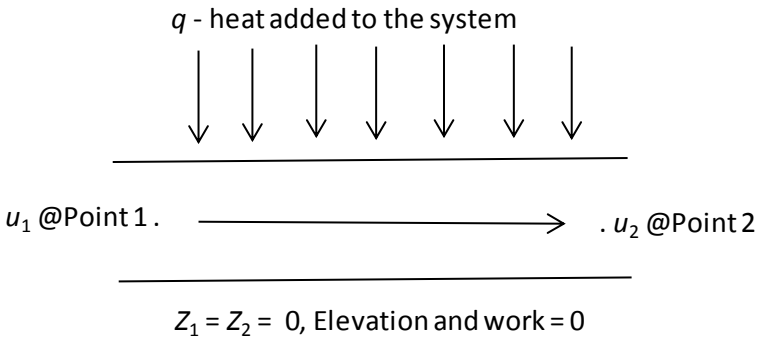

Figure 10: Diagram of steady state energy equation

$$\int_1^2 Vdp + F_{12} = \left(H_2 - H_1\right) - q_{12} \quad {}^{J}\!/_{kg} \tag{21}$$

$$\frac{u_1^{\,2} - u_2^{\,2}}{2} + \left(Z_1 - Z_2\right)g + W_{12} = \int_1^2 Vdp + F_{12} = C_p\left(T_2 - T_1\right) - q_{12} \quad {}^{J}\!/_{kg} \tag{22}$$

In these equations:

u_1 and u_2 = velocity at input/exhaust in m/s (Figure 10)

Z = elevation from point of reference (m)

g = gravity (m/s^2)

W = work added to the system, J kg^{-1}

H = enthalpy, J kg^{-1}

$\int_1^2 Vdp$ = flow work (J kg^{-1})

q = heat added to the system J kg^{-1}

T = temperature K

C_p is the heat capacity (J K^{-1})

These sets of equations describe the potential and kinetic energy, work, friction loss, enthalpy and heat transfer terms for steady (non-transient) flow.

2.4 Computational fluid dynamics models of airflow

2.4.1 'Flow Simulation' code in the context of porous media

In general, the Favre-averaged Navier-Stokes equations (Dassault Systèmes, 2013) are used within the CFD tool for most applications, where time-averaged effects of the flow turbulence on the flow parameters are considered. Other large-scale, time-dependent phenomena are taken into account directly in the CFD tool. Through this procedure, extra terms known as the Reynolds stresses, appear in the Navior-Stokes equations. The Navier-Stokes equations, however, require additional information. Most importantly this includes the turbulent kinetic energy and its dissipation rate as in the k-ε model (Launder & Spalding, 1972 and Wilcox, 1994). The conservation laws for mass, angular momentum and energy in a Cartesian coordinate system rotating with angular velocity u about an axis passing through the coordinate system's origin can be written in the conservation form as follows:

Mass continuity:

$$\frac{\partial \rho}{\partial \mathrm{t}} + \frac{\partial}{\partial \mathrm{x_i}} (\rho \, \mathrm{u_i}) = 0 \qquad (23)$$

Conservation of angular momentum:

$$\frac{\partial \rho u_i}{\partial t} + \frac{\partial}{\partial x_j} \left(\rho u_i u_j\right) + \frac{\partial \rho}{\partial x_i} = \frac{\partial}{\partial x_j} \left(\tau_{ij} + \tau_{ij}^R\right) + S_i \; with \; i = 1,2,3 \qquad (24)$$

Conservation of energy:

$$\frac{\partial \rho H}{\partial t} + \frac{\partial \rho u_i H}{\partial x_i} = \frac{\partial}{\partial x_i}\left(\mu_j\left(\tau_{ij} + \tau_{ij}^R\right) + q_i\right) + \frac{\partial \rho}{\partial t} - \tau_{ij} + \tau_{ij}^R \frac{\partial u_i}{\partial x_j} + \rho\varepsilon + S_i u_i + Q_H \quad (25)$$

$$H = h + \frac{u^2}{2} \quad (26)$$

where:

$u =$ fluid velocity (m/s)

$\rho =$ fluid density (kg/m^3)

$h =$ thermal enthalpy J kg^{-1}

$Q_H =$ is a heat source or sink per unit volume (W/m^3)

$\tau_{ij} =$ the viscous shear stress tensor (Pa)

$q_i =$ the diffusive heat flux (W/m/s)

$S_i =$ mass distributed external force per unit mass due to a porous media resistance (N/kg)

The mass distributed force due to porous media resistance consists of:

$$\left(S_i^{porous}\right) + \text{buoyancy } \left(S_i^{gravity}\right) + \rho g_i + \text{ a systems rotation } \left(S_i^{rotation}\right)$$

where:

$$S_i^{porous} = -k\delta_{ij}\rho u_j \quad (27)$$

with:

$\delta_{ij} =$ Kronecker delta function

$\rho =$ fluid density

$u_j =$ fluid velocity

$k =$ resistance vector of the porous media

For an equivalent continuum problem to be fully specified some constants need to be determined to specify the porous medium resistance to fluid flow: vector k, defined as $k = -grad(P)/(\rho \cdot V)$, where P, ρ , and V are fluid pressure, density, and velocity, respectively. It is calculated according to one of the following formulae that are obtained from the discrete model geometric and fluid flow parameters (Dassault Systèmes, 2013):

1: $k = \Delta P \cdot S/(m \cdot L)$, where ΔP is the pressure difference between the opposite sides of a sample parallelepiped porous body, m is the mass flow rate through the body, S and L are the body cross-sectional area and length in the selected direction, respectively. ΔP can be specified as a function of m, whereas S and L are constants. Instead of mass flow rate one can also specify volume flow rate, v. In this case, Flow Simulation calculates $m = v \cdot \rho$. Of these values, only the resistance, k, do not specify the porous body for the calculation, and is used by the flow simulation tool to scale the material properties defined. This is key for Chapters 9 and 11.

2: $k = (A \cdot V + B)/\rho$, where V is the fluid velocity, A and B are constants and ρ is the fluid density. Here, only A and B are specified, since V and ρ are solved for in the formulation.

3: $k = \mu / (\rho \cdot D^2)$, where μ and ρ are the fluid dynamic viscosity and density, D is the reference pore size determined experimentally. Here, only D is specified, since μ and ρ are calculated.

4: $k = \mu / (\rho \cdot D^2) \cdot f(Re)$, differing from the previous formula by the $f(Re)$ factor, yielding a more general formula. Here, in addition to D, $f(Re)$ as a formula dependency is specified.

The parameter k can be determined from PSMs. To obtain this coefficient in general practice, physical testing must be performed, but the PSM enables a proxy technique for the gathering of this porous media constant by using the discrete model form.The k factors in this thesis are

obtained from technique 1 because all of the parameters are known and can also be obtained easily from experimentation. Method 2 requires an interpretation of experimental results which cannot easily be determined with agreement on the interpretations of the coefficients. Method 3 requires the parameters to be determined experimentally or approximated as an average pore diameter size, which is not an improvement to current techniques. Method 4 can be determined on a bulk sample but the geometric calculations required for the Reynold's number depend on the porous media geometry, and are and not easily verified.

2.4.2 Flow Simulation meshing structure for discontinuum porous materials

Within this section, a description of the immersed boundary condition and meshing structure within the Flow Simulation code is given. The immersed boundary conditions are important for many reasons including the calculation of boundary conditions between the fluid and solid medium for flow and heat transfer. Wall conditions for PSM and equivalent continuum models are also covered for the concept of thick and thin boundaries.

The flow simulation tool uses a structured cartesian octree mesh structure to discretize the finite volumes used in the calculations. What this means is that each component of the mesh is cubic, square in 2D, and to refine the volumes for calculation, smaller cubes are placed in divisions of two to properly capture the problem geometry, as illustrated in Figure 11 and Figure 12.

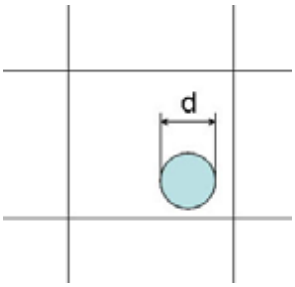

Figure 11: Example of how a solid is surrounded and meshed in the CFD tool without refinements (Dassault Systèmes, 2013)

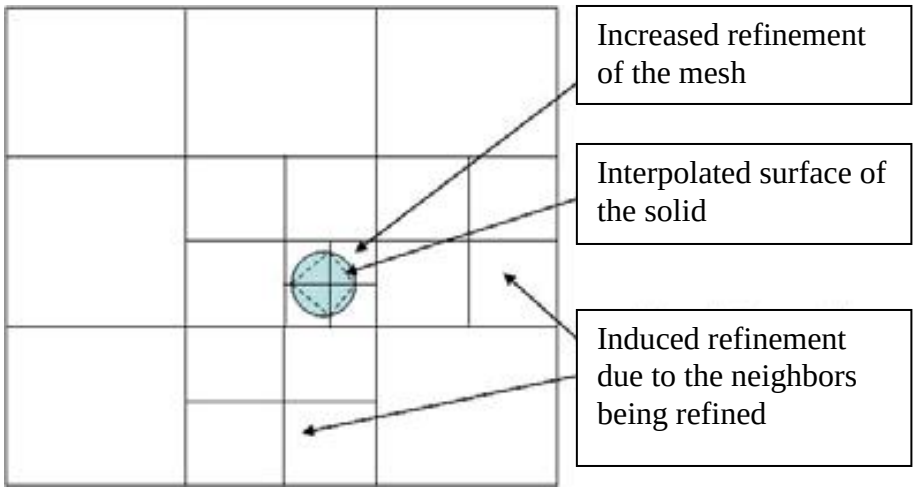

Figure 12: Same solid as Figure 11, meshed with refinement resolution increased to level 2 (Dassault Systèmes, 2013)

According the Solidworks technical manual (Dassault Systèmes, 2013), approximation errors (Local Truncation Errors) caused by the spread of intermodal distances (mesh irregularity) is greatest for unstructured meshes. A loss of computational robustness is caused by secondary fluxes at skewed faces. These secondary fluxes increase the degree of schemes specific geometry and, as a result, decrease the diagonal dominance of the difference operators and are an issue in other types of meshing.

The flow simulation octree mesh generator uses a system of refinement criteria, each with their own values and refinement levels as shown previously for the immersed solid. Patented procedures have been integrated into the code which they call Automatic Parameters Definition (APD) technology.

The main idea of the APD technology is to define both the base mesh and refinement settings from the definition of the model's fluid domain and boundary conditions. The defining of any simulation must have values for the following characteristics:

1. Problem type (Internal or External, Compressible or Incompressible Flow, 3D or 2D)
2. Minimum gap size (MGS) dgap – the smallest size of all flow openings or faces where solution goals have been specified to control convergence of the solver
3. Minimum wall thickness (MWT) dwall – the smallest size of all solid objects or faces where solution goals have been specified to control convergence of the solver represented in the fluid domain
4. Level of initial mesh or Result Resolution Level (RRL) – The control mechanism for the resolution of the mesh relative to the fluid domain
5. Computational model bounding box (which is the same for PSM internal conditions) – the outside numerical limits of the computational domain
6. Fluid region bounding box (which is the same for PSM internal conditions)
7. Symmetry settings applied to the computational domain boundaries, ie: the number of cells created in the Y-axis relative to the X-axis, for example

8. Middle size of the computational model – the center point numerically of the computational domain

9. Wind direction for external flows

The APD output comprises:

1. Base mesh

    a. Computational domain box x,y,z

    b. Key planes sets for x, y, z direction and cell ratios at these planes

    c. Number of cells for x, y, z direction: Nx, Ny, Nz

2. Refinement settings

    a. Small solid feature refinement level LSSF – This is a mesh resolution setting used as a capturing tool for smaller CAD objects. This resolution level is used to capture smaller objects than the resolution of the mesh, which calls for the cell to become refined or decreased in size

    b. Tolerance refinement level Ltol and tolerance dtol – geometric length tolerance used for generating the refined mesh structure

    c. Narrow channels refinement level LNCR and the number of cells per channel width Ngap

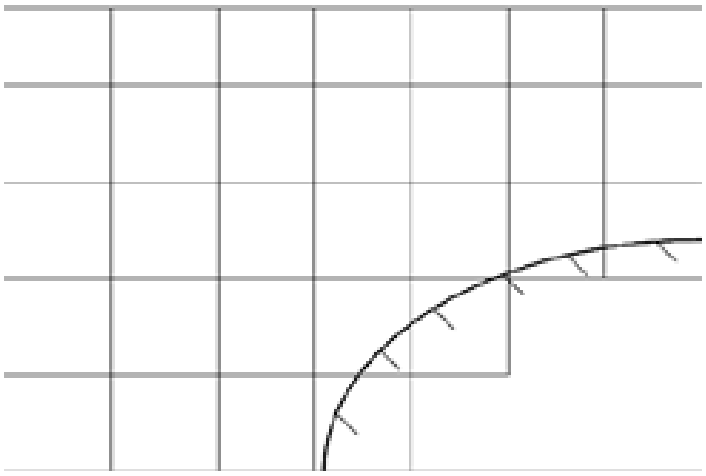

Figure 13: Structured Cartesian immersed-body mesh (Dassault Systèmes, 2013)

To solve the Navier-Stokes equations with a two-equation $k - \varepsilon$ turbulence model without resolving the near-wall fluid (Figure 13) boundary layer would require a very fine computational mesh. Due to this problem, a "wall function" approach had been proposed by Launder and Spalding (1972, 1974) to reduce mesh sizes. According to this approach, the fluid wall frictional resistance and heat fluxes from the fluid to the wall are used to calculate the wall boundary conditions for solving the Navier-Stokes equations. The main domain flow physical properties will be those of the boundary layer's external boundary conditions.

In Flow Simulation, Van Driest's (1956) universal profiles are employed to describe turbulent boundary layers and two approaches (called "Two-Scale Wall Functions," denoted 2SWF in the literature) have been devised to fit a fluid's boundary layer profile relative to the main flow's properties:

1) when the fluid mass centers of the near-wall mesh cells are located inside the boundary layer, i.e., the physical fluid flow boundary layer is thick; and

2) when the fluid mass centers of the near-wall mesh cells are located outside the boundary layer, i.e., the physical fluid flow boundary layer is thin.

These two approaches allow the flow simulation tool to overcome the traditional CFD code restriction of having to employ a very fine mesh density near the walls in the calculation domain, and to use immersed boundary Cartesian meshes for all geometries (Kalitzin and Laccarino, 2002).

It is because of this immersed boundary that the simulations executed within this thesis were possible in a reasonable (less than a day) time. If the resolution at all of the boundary and wall conditions had to be implemented in a very fine mesh structure, many hours, if not days or weeks, would have been necessary to complete the various computations.
The mesh characteristics of the PSM can substantially affect the results as shown later (Chapter 4). At any point, either a 2D or 3D mesh representation can be shown for the user to determine if they wish to change or create local mesh conditions to improve the accuracy of the models or troubleshoot potential boundary errors.

Besides the octree mesh structure used in the Flow Simulation tool for this thesis, there are several other types of mesh configurations that are used in other CFD codes and research. These include

Comsol Multiphysics

The Comsol solvers use a hybrid method of meshing in an unstructured form as shown in Figure 14. Initially the mesh is either tetrahedral or hexahedral in nature, but the shapes can deform throughout the calculation process. Calculation times are large with this mesh structure (Dassault Systèmes, 2013).

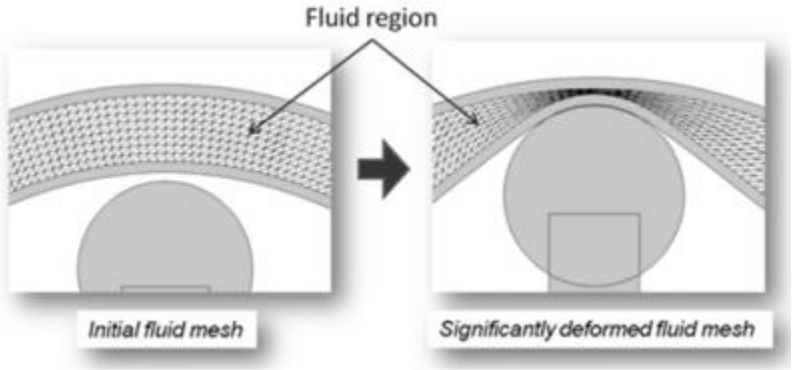

Figure 14: Structural coupled fluid domain problem using Comsol Multiphysics deformable mesh (Comsol Multiphysics, 2014)

Flac 4.0

Flac 4.0 software from Itasca software has the option of using either an octree, tetrahedral or hexahedral mesh structure in an unstructured form. The mesh elements sizes may vary in a similar refinement option as the Flow Simulation tool used in this work as seen in Figure 15.

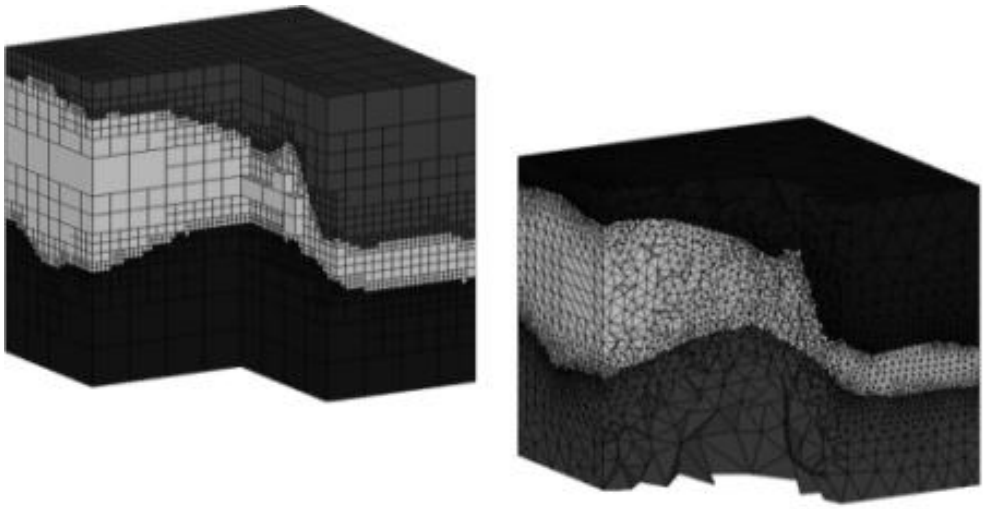

Figure 15: Mesh structure options in Flac 4.0 (Itasca Houston, 2014)

Fluent

Fluent (Ansys, 2014) is software that contains an unstructured mesh system that has the options for an octree, tetrahedral or hexahedral mesh structure (the latter as seen in Figure 16). Refinement capabilities are similar to the other programs mentioned.

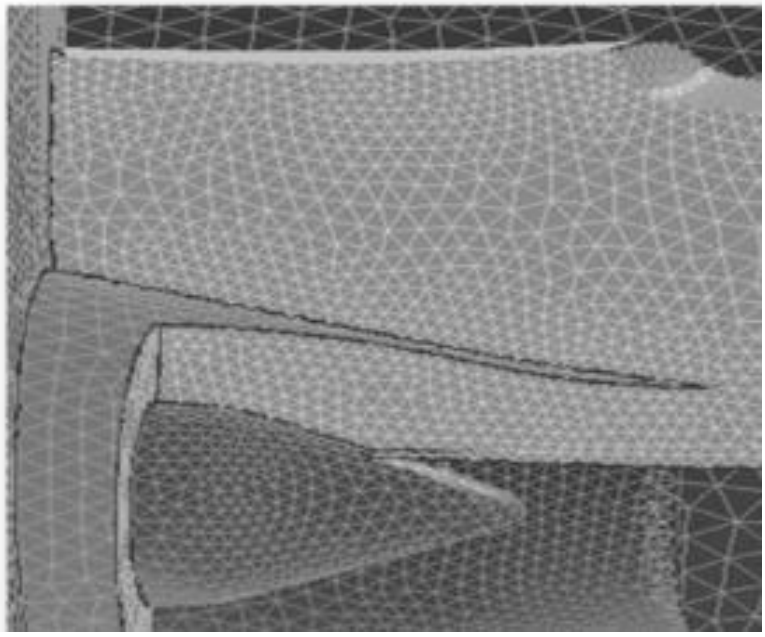

Figure 16: Mesh structure option used in FLUENT models (ANSYS, 2014)

2.5 Fluid flow code tool validation examples

In the following section, CFD simulations by Dassault Systèmes presented in whitepapers published in 2013 were used to compare the code with various experimental results. The relevant CFD files are provided with all Flow Simulation licenses and are detailed here for the problems relevant to this thesis.

2.5.1 Direct measurement of incompressible turbulent three dimensional flows

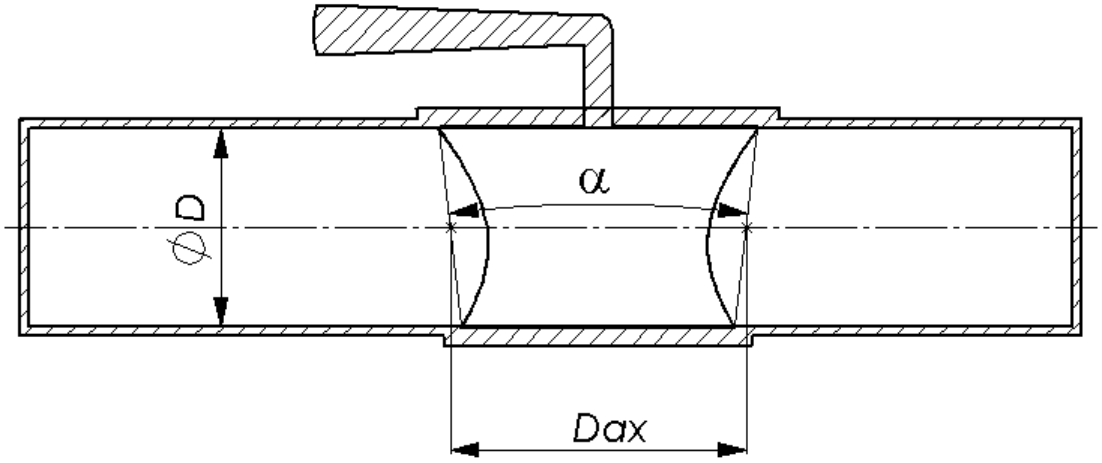

Figure 17: The cone valve under consideration: D = 0.206 m, Dax = 1.515D, α = 13°40'. (Image courtesy of Dassault Systèmes, 2013)

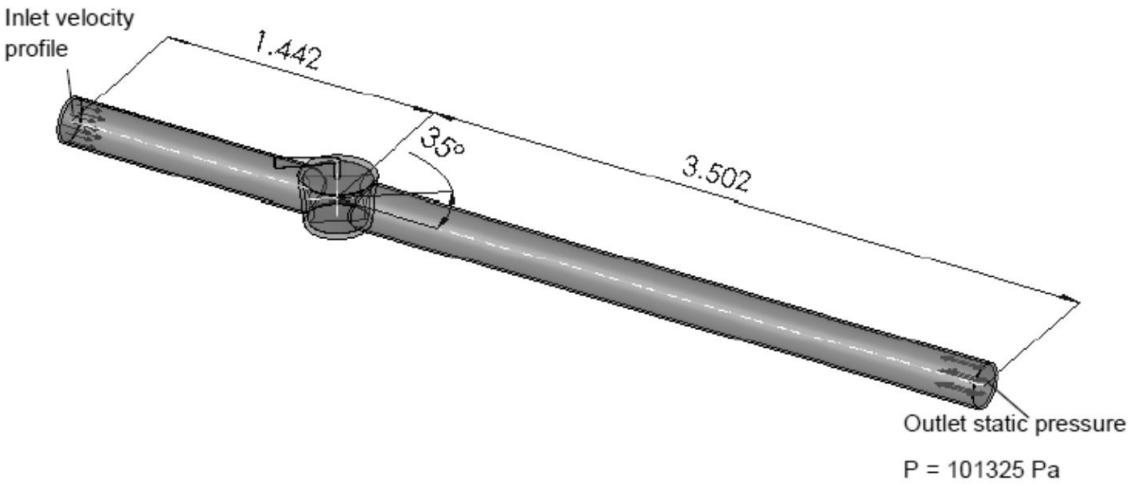

Figure 18: Rendering of the cone valve simulation in the CAD/CAM environment

The analytical solution of 3D flow through a cone valve from Idelchik in 1986, Yanshin in 1965 and Yu and Joshi in 2002 was used to test the Flow Simulation tool cone valve system as shown in Figures 17 and 18. This work used the measurement of hydraulic resistance through a pipe to compare the measurements with CFD solutions. The meshing conditions in the model were manually set to be the minimal cross-sectional area of flow within the valve. In the verification model, boundary conditions of an outlet pressure of 101325 Pa and an inlet profile of mass-average velocity of 0.5 m/s were used. The angle of the valve ranged from 0 to 55°. The hydraulic drag was calculated by taking the inlet and outlet pressures along with velocity squared and the density as follows:

$$\delta = \frac{P_{inlet} - P_{outlet}}{\frac{\rho U^2}{2}} \tag{28}$$

This value was compared with the hydraulic drag, which was also compared experimentally through the work of Idelchik and Yu in 2002.

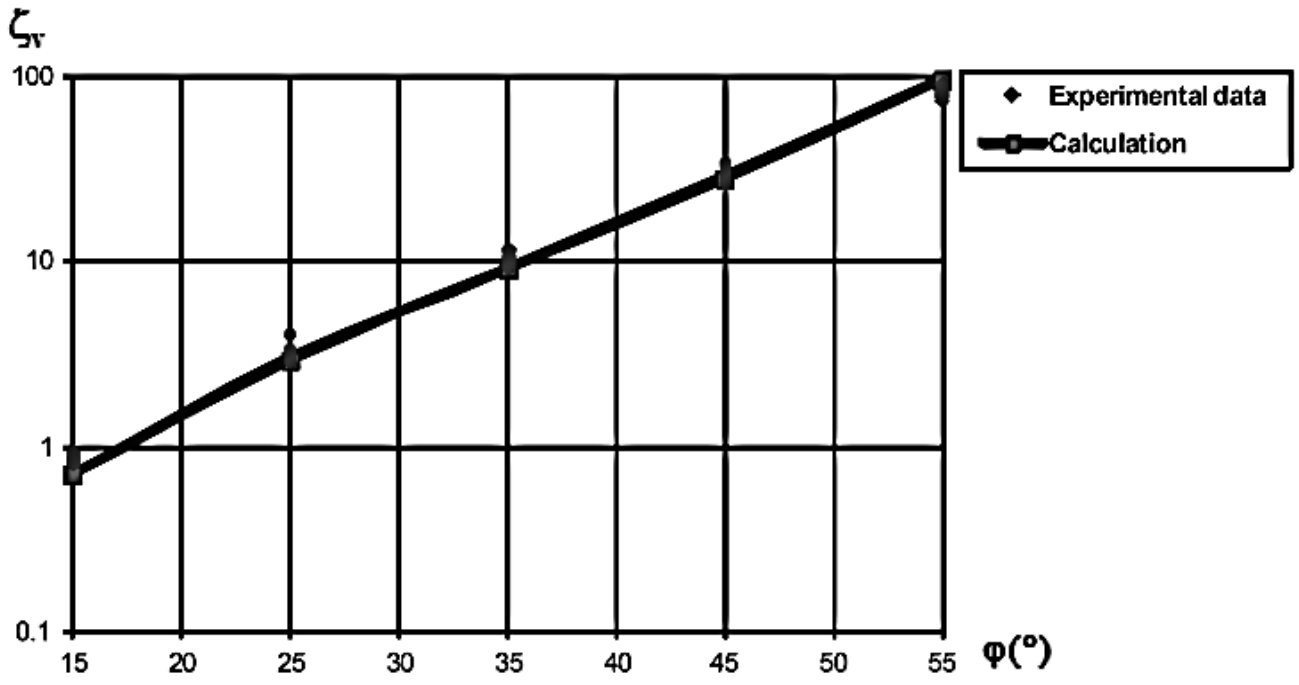

Figure 19: Comparison of Hydraulic Drag vs angle of Ball Valve experimentally (Idelchik, 1986) and CFD (Dassault Systèmes, 2013). The calculated values from Dassault Systèmes have the line through them as compared to the experimental data which consists of points.

As seen in Figure 19, the values corresponded quite well between the experimental methods and the CFD simulations.

2.5.2 Laminar and turbulent flow through a 3D pipe

The flow through a 3D pipe was compared with Schlichting, (1979), Idelchik, (1986), and White, (1994) and is shown in Figure 20. The CFD model was sensed at the inlet and outlets, as well as along the inside surface of the model for pressure loss. Velocity boundary conditions were assigned to the inlet.

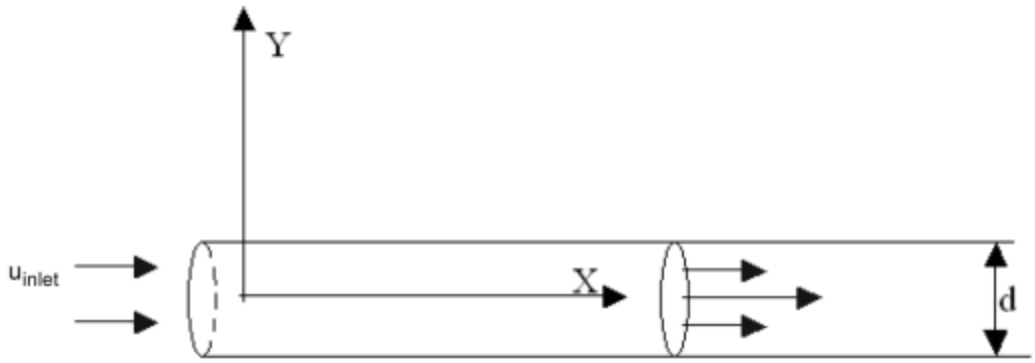

Figure 20: Schematic of the CFD model (Dassault Systèmes) used to verify the work of Schlichting, Idelchik, and White

The parameters examined for the smooth pipes were the pressure and velocity while the rough pipe added the friction factor, which is defined as:

$$f = \frac{\Delta P}{\rho u_{inlet}^2} \frac{d}{L} \tag{29}$$

While the smooth pipe simulations compared well (Figures 21 and 22), the rough pipe calculations had an error of up to 13% as shown in Figures 23-25. The reason for this error may be due to how the pressure is sensed within the CFD code. In the CFD environment, a bulk average pressure at the inlet and outlet areas is measured. Within the real life experiments, a spot or point measurement through a manometer or barometer is used. In other words, this means that the difference in averaging of the CFD boundary condition surface may be the cause of the error.

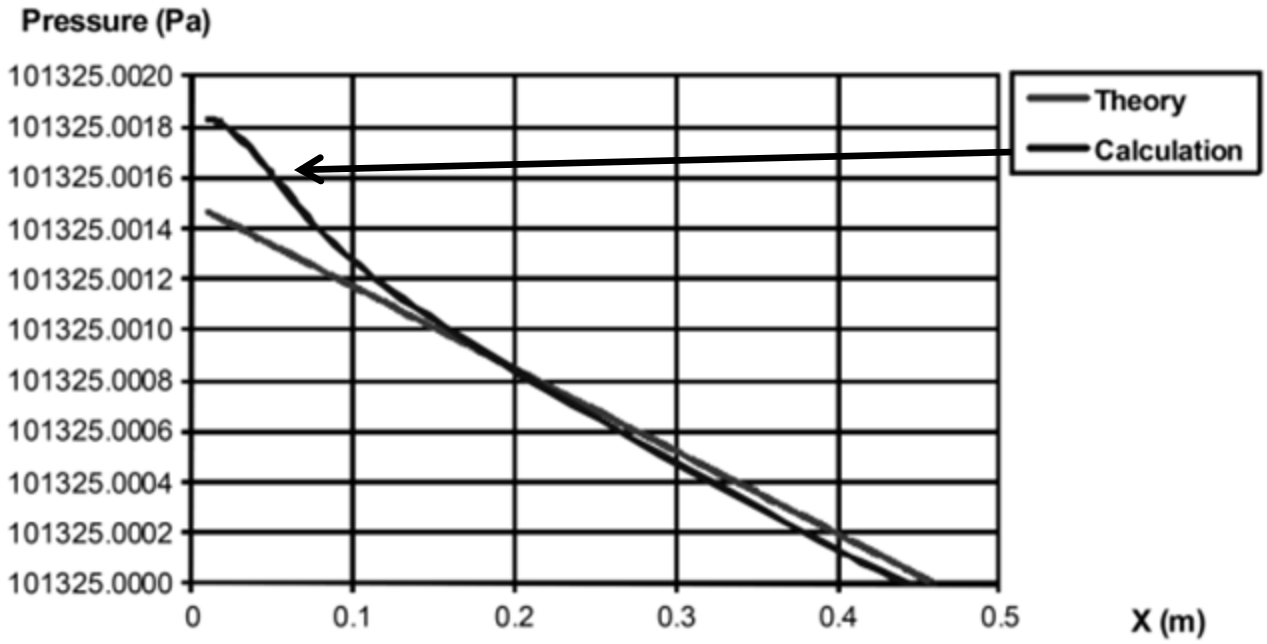

Figure 21: CFD (Dassault Systèmes) results of longitudinal pressure change compared with the work of Schlichting, (1979) at a Re number of 100

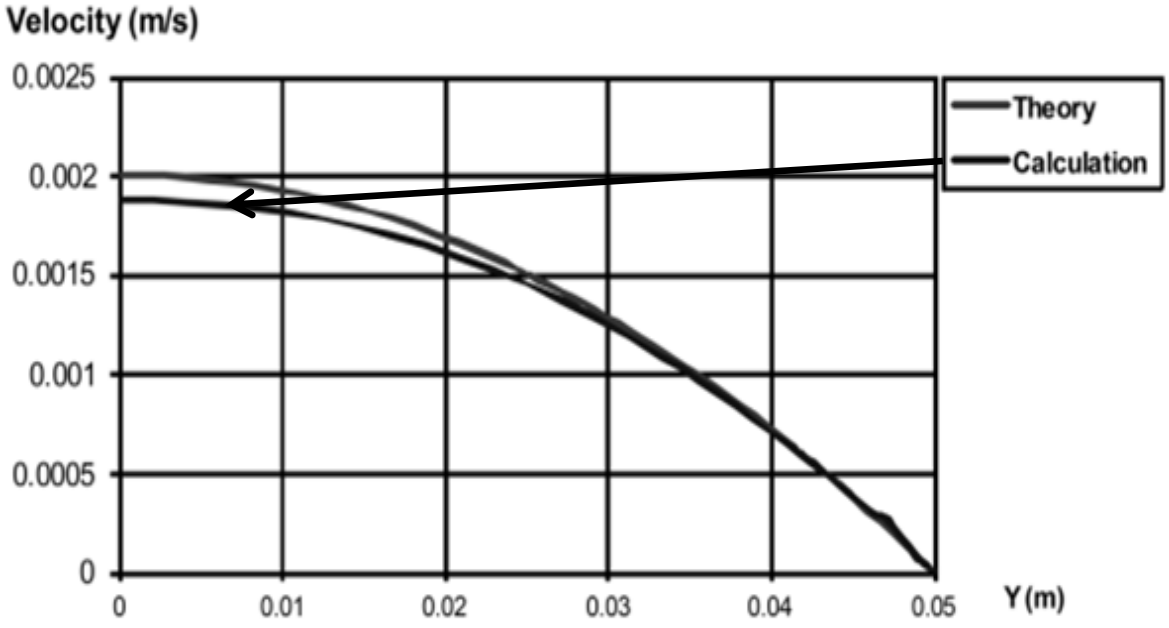

Figure 22: CFD (Dassault Systèmes) fluid velocity profile for the outlet at a Re of 100 compared with Schlichting, (1979)

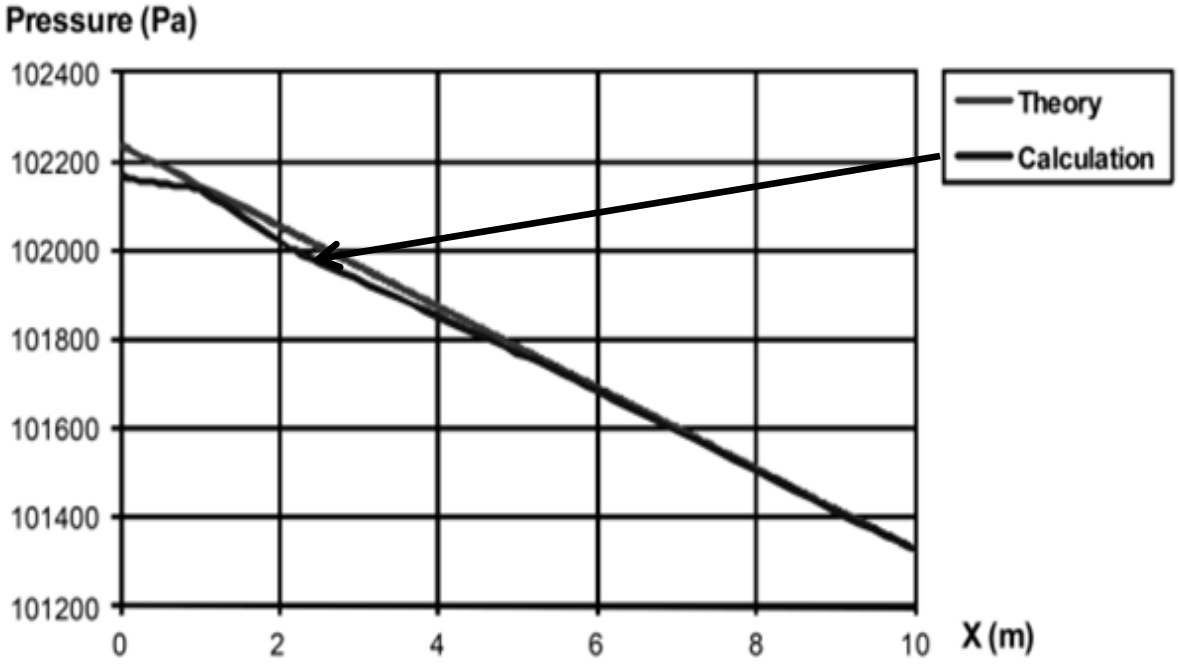

Figure 23: CFD (Dassault Systèmes) longitudinal pressure change along the pipe at Re = 100000 compared with Schlichting, (1979)

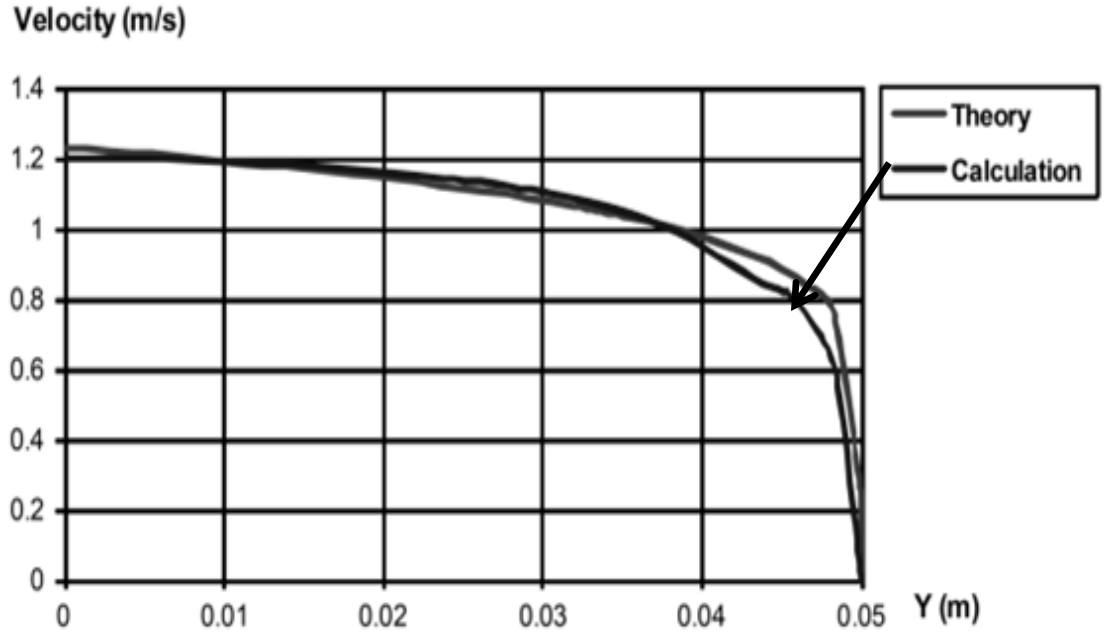

Figure 24: CFD (Dassault Systèmes) fluid velocity profile at the pipe exit at a Re = 100000 compared with Schlichting (1979)

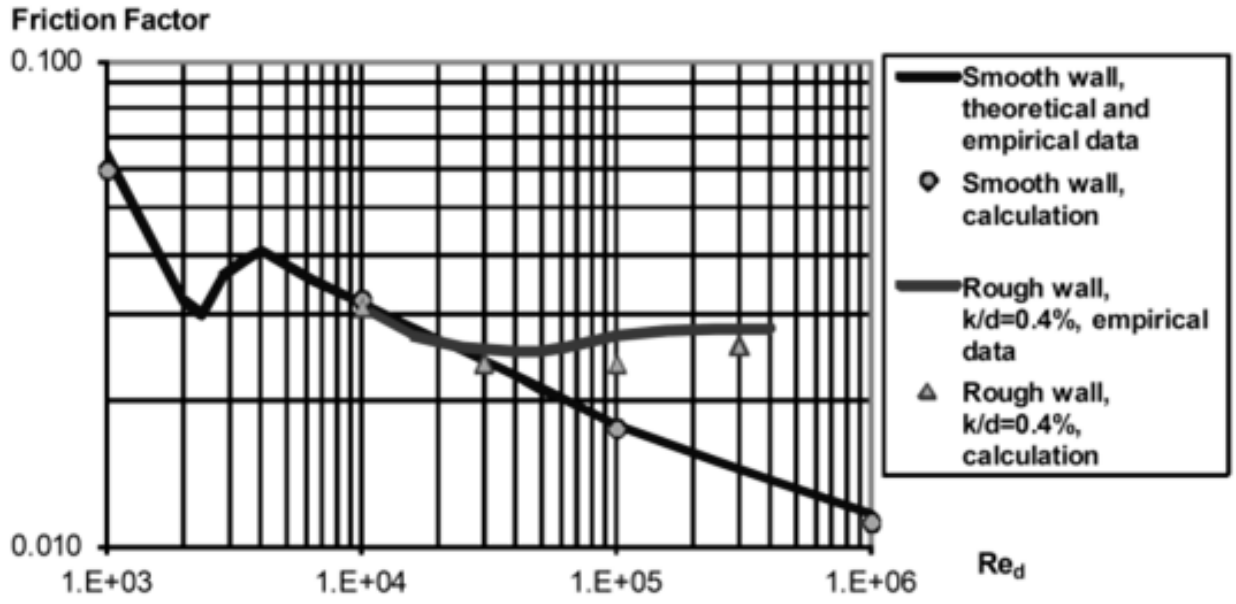

Figure 25: Comparison of smooth and rough wall pipes in 3D by Dassault Systèmes with the works of Schlichting, (1979), Idelchik, (1986), and White, (1994)

2.5.3 Porous screen in a non-uniform stream

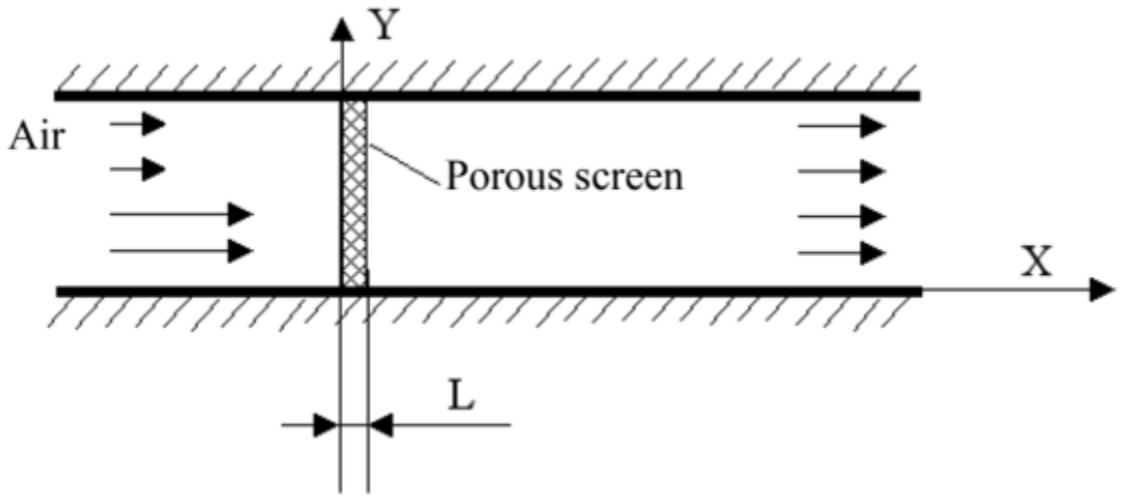

Figure 26: Schematic of the analytic and experimental CFD verification of a porous medium in an air tunnel compared with Idelchik (1986)

The purpose of this work was to compare a Dassault Systèmes CFD simulation of cold airflow between two plates and a porous screen, with the work of Idelchik (1986). The flow conditions were set as a step to prove the levelling effects of the screen illustrated in Figure 26. This profile staggering can be seen with the velocity boundary conditions shown in Figure 27. Several velocities were also chosen to do a thorough comparison with the calculated values of hydraulic drag from the physical experimentation and CFD modelling.

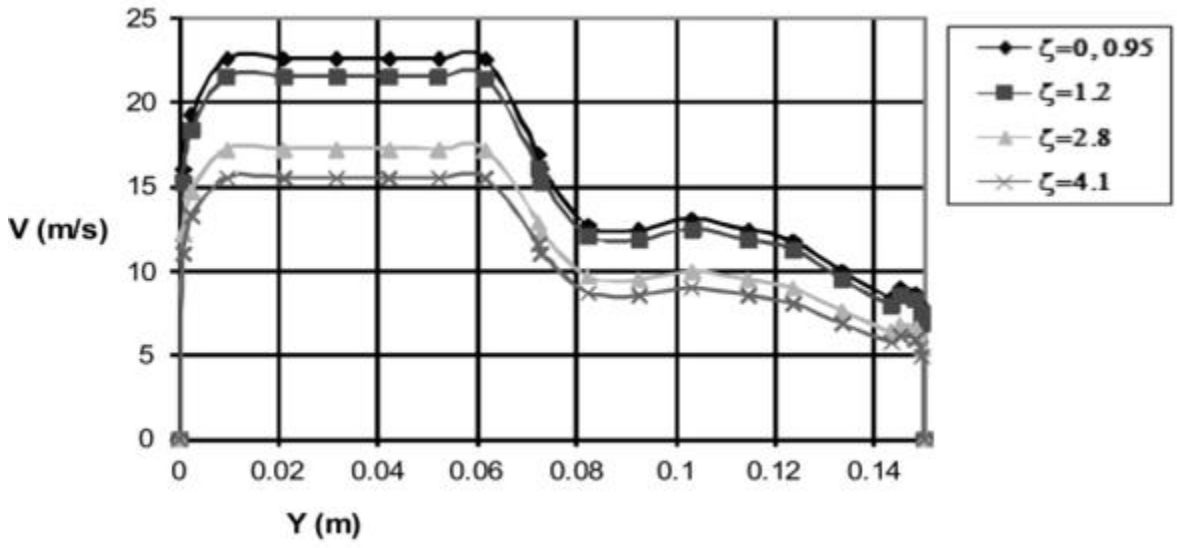

Figure 27: Inlet velocity profile used in the CFD verification model by Dassault Systèmes from the work of Idelchik (1986)

This is only a two dimensional flow simulation and the screen sizes vary for several experimental runs. The sensing for the dynamic pressure was done at a distance of 0.3m past the porous screen. When compared with no screen and just a duct, the errors are relatively small; the screen settings produced errors of up to 30% when comparing the experimental and simulation pressures with different gauge sizes, which use a calculated drag coefficient and an input porous resistance. The drag coefficient was calculated as follows:

$$\delta = \frac{2\Delta P}{\rho V^2} \tag{30}$$

The porous medium resistance for flow simulation is defined from page 34:

$$k = \frac{-gradP}{pV} \tag{31}$$

The porous screen calculation of resistance with the length of screen *L* was defined:

$$k = \frac{V\delta}{2L} \tag{32}$$

and finally, they defined the porous material in the form:

$$k = \frac{(AV+B)}{\rho} \tag{33}$$

By using this procedure, the values for A = 57, 72, 168, and 246 $\frac{kg}{m^{-4}}$ were calculated and used in the simulations. The direct comparison of the dynamic pressure vs distance from the boundary in both the physical experiment and CFD calculation is shown in Figures 28-32, with Figure 28 being with no screen to Figure 32 with the highest value hydraulic drag for the porous screen.

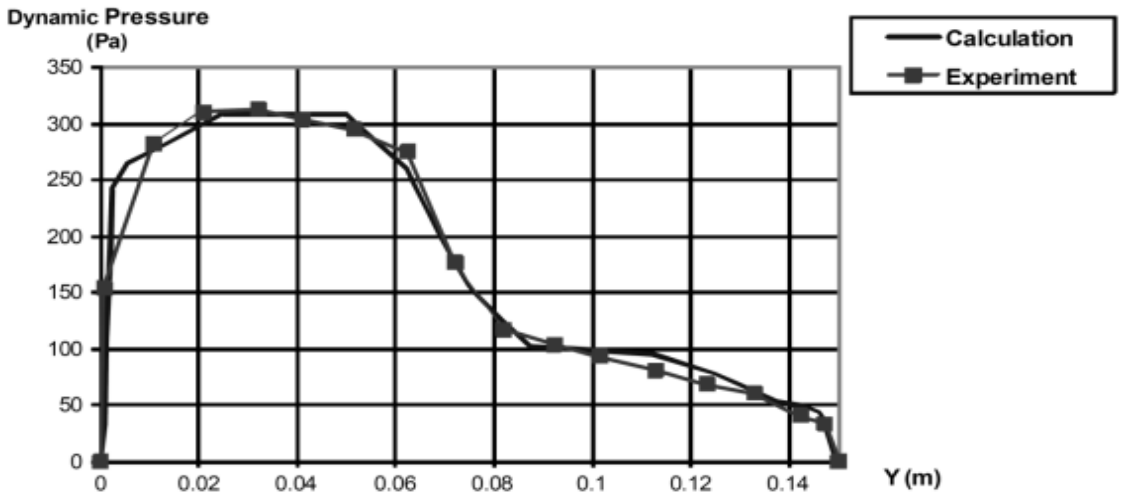

Figure 28: Dynamic pressure at a distance of 0.3m with no porous screen from Dassault Systèmes

The results in the case without a screen in Figure 28 turned out well but there was a sign of error at the profile point 0.11m. This error could come from how the step profile for the velocity was configured either in the CFD code or the physical experiments.

Once the screen was put in place, as in Figure 29, the errors begin to increase along the profile. The error in this simulation is an exaggeration of the profile errors from Figure 28, showing that there is a problem either with how the coefficients of the porous medium were calculated, or as a result of the geometry of the plate not being well represented in the equivalent continuum model.

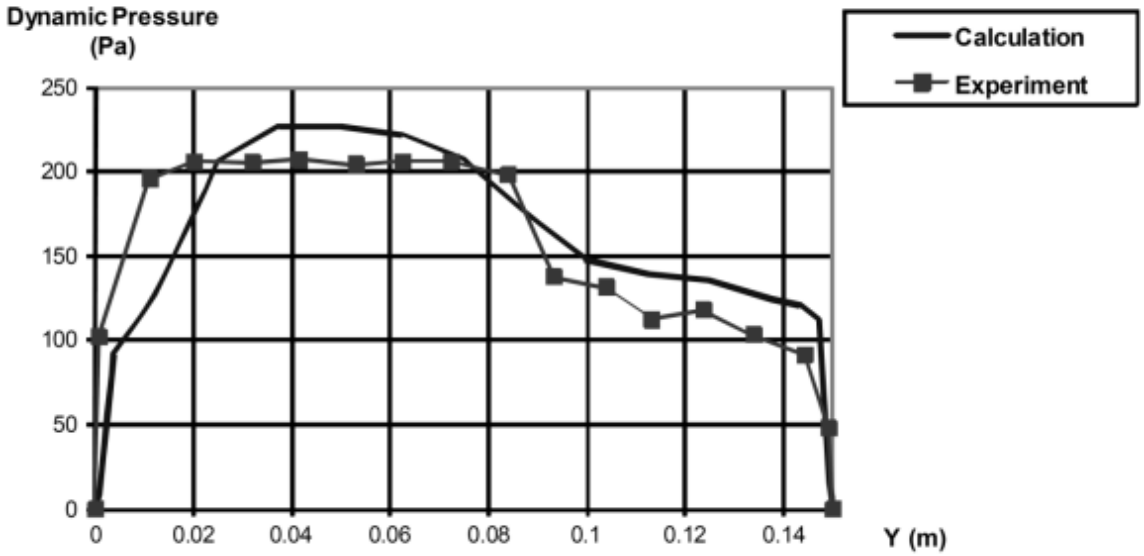

Figure 29: Two plates with a porous screen and a drag coefficient of 0.95 compared with Idelchik (1986) experimental data (Dassault Systèmes, 2013)

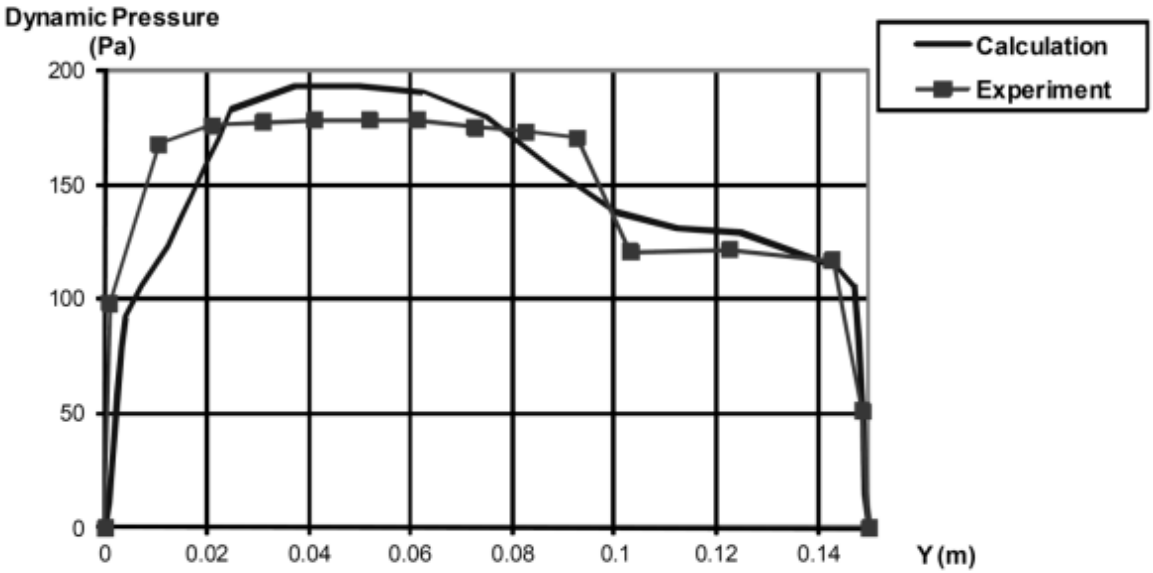

Figure 30: Two plates with a porous screen and a drag coefficient of 1.2 CFD model (Dassault Systèmes) compared with experimental data from Idelchik (1986)

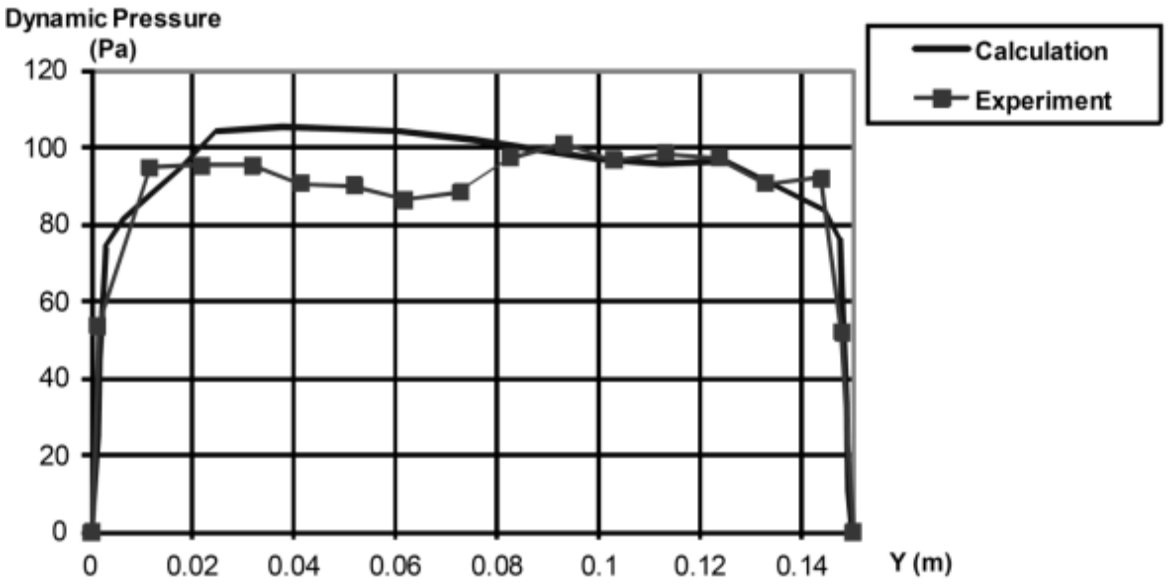

Figure 31: Two plates with a porous screen and a drag coefficient of 2.8 (Dassault Systèmes) compared with Idelchik (1986)

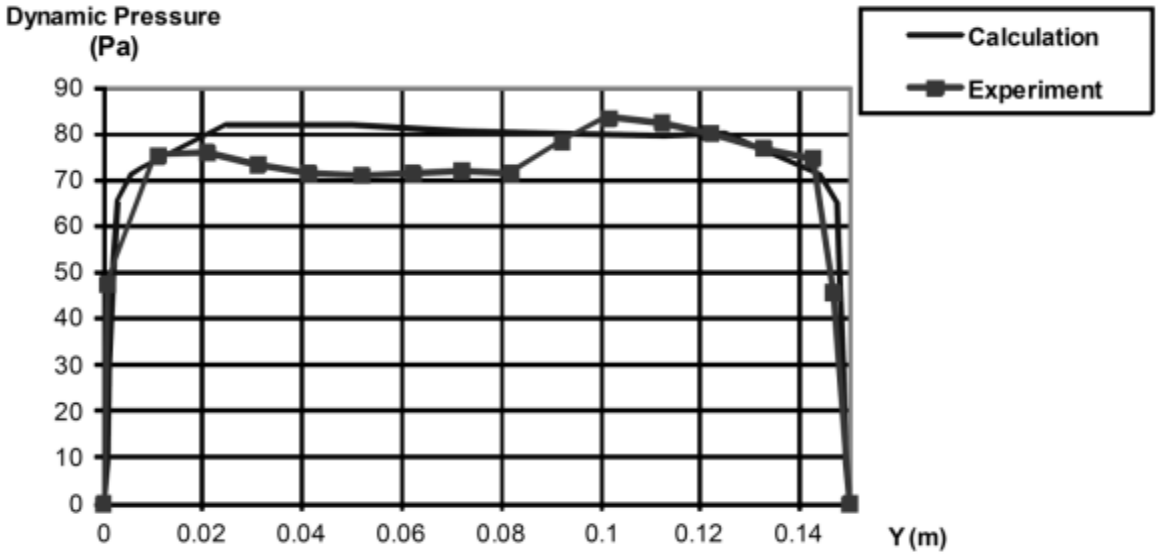

Figure 32: Two plates with a porous screen and a drag coefficient of 4.1 compared with Idelchik (1986) by Dassault Systèmes

Referencing Figures 30-32, the resistance to the porous medium used in those simulations may have been the cause of an unacceptable amount or error, up to 30%, for a fairly straightforward problem. The reason for this error may have its roots in how the resistance coefficients were

defined for the porous medium. The dynamic pressure may also be the cause of error in the simulations, due to the profiles used if the velocity boundary conditions were substantially different from those of the experimental procedure. The reason for stating this is a relatively constant error band between 0.02 to 0.08m on the profile, which is consistent with the velocity profile simulation boundary conditions.

2.5.4 Unsteady heat conduction in a solid

To validate heat conduction in a solid (i.e., a conjugate heat transfer), Dassault Systèmes used the analytical work of Holman (1997) to compare with their CFD model. To compare the flow code predictions with the analytical solution from Holman, a one-dimensional problem was solved for a warm solid rod. This rod had a specified initial temperature of 350 $°K$ and then in the simulation and in experiment, the heat-insulated surface suddenly becomes, and stays, cold (at a constant temperature of T=300 K). The rod inner temperature evolution was studied using time - based monitoring for the profile of the rod as shown in Figure 33.

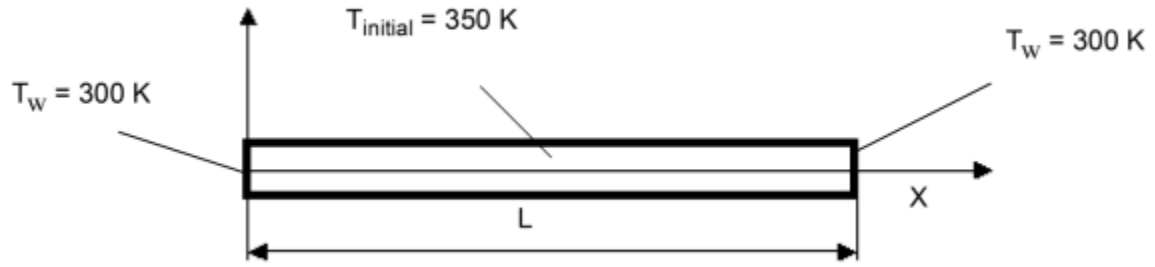

Figure 33: Rod used in Dassault Systèmes's validation example and compared with Holman (1997)

The evolution of maximum rod temperature, predicted with Flow Simulation and compared with theory from Holman, is presented in Figure 34. The Flow Simulation prediction has been performed at result resolution level 5. The flow code coincides with the theoretical curve. This shows that the temperature profile along the rod is well represented by the code.

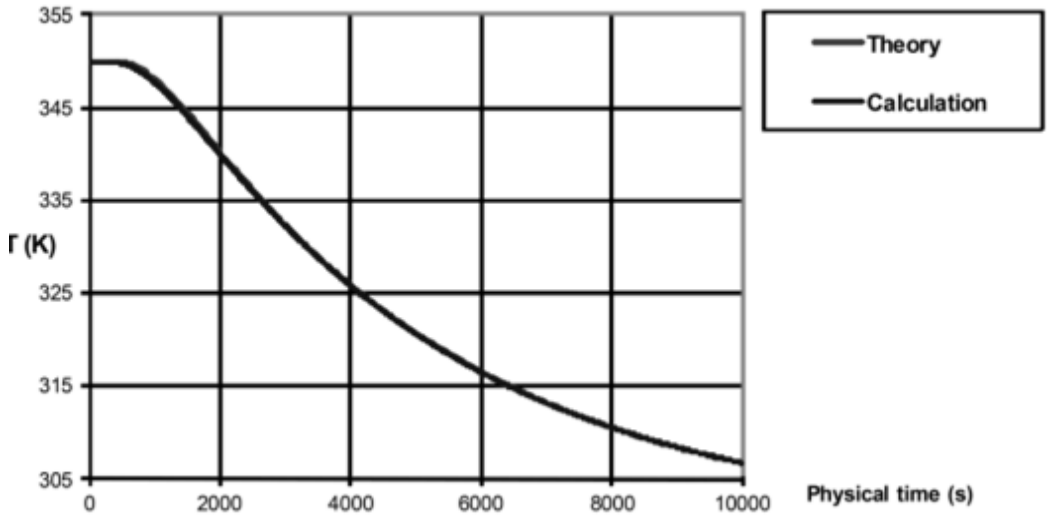

Figure 34: Temperature graph confirming the results of the CFD code by Dassault Systèmes

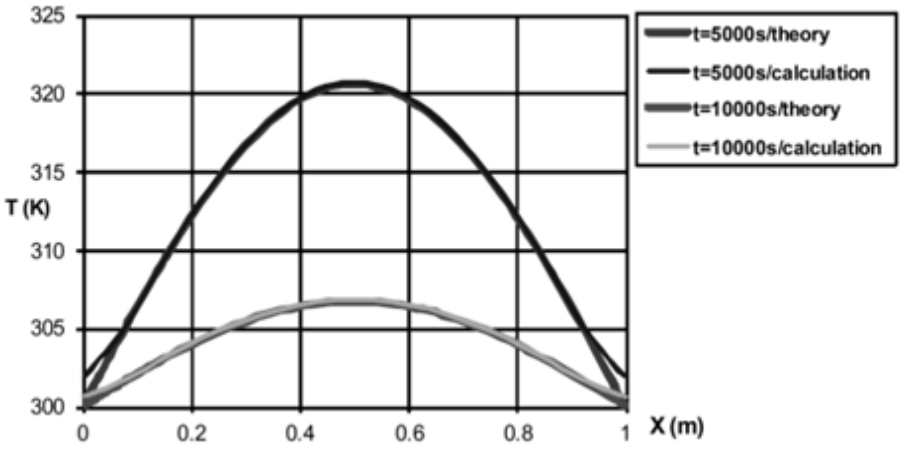

Figure 35: Graph from Dassault Systèmes confirming Fourier series thermal calculations as compared with Holman (1997)

The temperature profiles along the rod taken from Fourier series analysis and compared with temperatures taken from the CFD code are shown in Figure 35. The maximum prediction error not exceeding 2K occurs at the ends of the rod and is likely caused by calculation error in the theoretical profile due to the truncation of the Fourier series used in the analytical work. This is a good confirmation that the tool is acceptable for use for heat transfer problems as a base and can be used in the PSM experiments to validate a more complicated problem.

2.6 Rosin Rammler distribution for fragmented rock grading

Within this section, a summary will be given for one of the key distributions used in the characterisation of broken and fragmented rock, the Rosin Rammler distribution (Rosin and Rammler, 1933), which was chosen to be used extensively throughout the Packed Sphere Modelling process. The Rosin Rammler distribution was first applied by Rosin and Rammler to model the particle sizes for coal fine, but was originally identified by Frechet (1927). In 1951, the statistician and mathematician Wallodi Weibull fully described the distribution functions (Weibull, 1951). For purposes of fragmentation, the Kuz-Ram model was created by Cunningham (1983, 1987) and uses a combination of the Rosin Rammler distribution, Kuznetsov equations (Kuznecov, 1980) and uniformity index equations for prediction of rock fragmentation for open pit and underground blast design (Cunningham 2000, 2005). This technique is still frequently used in mining practice to this day and is also commonly used throughout many different forms of civil engineering, such as powder size analysis (Gonzalez-Tello *et. al*, 2008), cement processing and manufacture (Mejeoumov, 2007), as well as fluid mechanics and computational fluid dynamics (Alfredsson, 2010) for the size characteristics of water droplets. In

engineering geology, the distribution is used for characterising various aspects of shear zones fills (Masin, 2002) as well as general characterisation of baseline materials.

The Rosin Rammler distribution works on two levels, the first being the theoretical mass retained in specified diameter bins, or sieve sizes, as set out by particle size analysis standards (e.g. ASTM C136 – 06). The second way this distribution is used maintains the same process of sieving, but then fits the data from an unknown particle size distribution tested, back to the Rosin Rammler parameters as in blasting fragmentation assessment (Cunningham, 1983; (Doucet, 2005; Strelec *et al.* 2011) as well as many programs that use visual techniques for fragmentation such as WipFrag (WipWare, 2013).

2.6.1 Forms of the Rosin Rammler distribution

The conventional Rosin Rammler probability distribution function is described by:

$$Y = e^{-\left(\frac{d}{d_C}\right)^n} \tag{34}$$

where:

Y = the mass fraction of a body of fragmented rock, passing a sieve size, d

n = spread factor, a parameter of the distribution

d_C = the characteristic size of the fragments of interest, also a parameter of the distribution.

This is the base formula used for one particular bin size or diameter of interest within a distribution of broken and fragmented rock. The cumulative probability distribution is then as follows:

Cumulative Probability Distribution Function Type 1:

$$Y = 100e^{-\left(\frac{d}{d_c}\right)^n} \tag{35}$$

where:

Y = the percent mass fraction of a body of fragmented rock, passing a sieve size, d

n = spread diameter, a parameter of the distribution

d_c = the characteristic size of the fragments of interest, also a parameter of the distribution.

Another way of looking at how the particle sizes range is through a mean diameter and requires another form of the Rosin Rammler distribution, which is as follows:

Cumulative Probability Distribution Function Type 2:

$$Y = 100e^{-.693\left(\frac{d}{\bar{d}}\right)^n} \tag{36}$$

where:

Y = the percent mass fraction of a body of fragmented rock, passing a sieve size, d

n = spread diameter, a parameter of the distribution

$\bar{d}$ = the mean diameter of the fragments of interest, also a parameter of the distribution.

To tie the two forms of the distribution together there is a substitution: $Y = 0.5$ and $d = \bar{d}$ which leads to:

$$d_c = \left(\frac{\bar{d}}{.693^{\frac{1}{n}}} \right) \tag{37}$$

The probability distribution function for the Rosin Rammler is derived by integration of the form of interest. For case 1, the probability distribution function is as follows:

$$Y = -\left(\frac{n}{d}\right)\left(\frac{d}{d_c}\right)^n \left(e^{-\left(\frac{d}{d_c}\right)^n}\right) \tag{38}$$

2.6.2 Distribution parameters

The Rosin Rammler distribution is dictated by two parameters: the characteristic diameter of interest, d_c , and the distribution shape factor, n. Of the two parameters, it is the spread factor which varies the distribution to mimic many different possible forms and shapes characteristic of other distributions. In mining, generally the second formula is used, and typically the spread factor can range between values of 0.5 to 2 (Cunningham, 1987, 2005). However, it is known that much higher values of up to 5 to 10 can be obtained, depending on individual rock conditions or specific requests to make a particular d_c size during blasting operations. The spread factor being above 5 means that there is almost a uniform distribution of rock fragments at a particular size of interest, but this size distribution may be what is requested from later crushing and grinding requirements. The range of how the CDF function changes with shape factor n is shown in Figure 36.

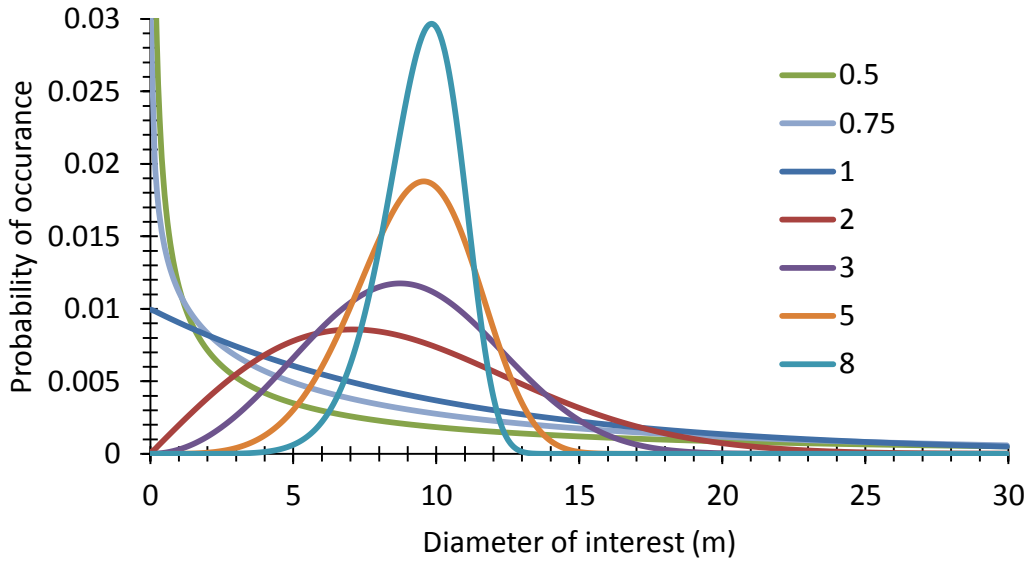

Figure 36: PDF function sensitivities to n: dc = 10. The high peaked curves are for high values of n while the lower numbered n values of 0.5 and 0.75 have a 1/x curve shape. The value at one has a peaked curve but is focused to the left of the characteristic diameter and as n increases the curve peaks closer to the dc value.

It is important to note that the smaller the spread variable, the more the chance that extreme values (meaning very small and very large values) can occur if the sample is randomly distributed. A small spread factor means that it has a very large range around the diameter of interest (i.e. 10 in the distributions shown above). A small spread factor may have a value of n = 0.5. The implications of this are that the rock fragments, which range from 0.5 – 2, tend to have a broad distribution of size from very small particles to very large particles. The cumulative distribution function, which shows this trend by a final percentage retained, is shown in Figure 37. The remaining 30% of mass for n = 0.5 can be physically explained as one large fragment above the 30mm diameter chosen here for examination.

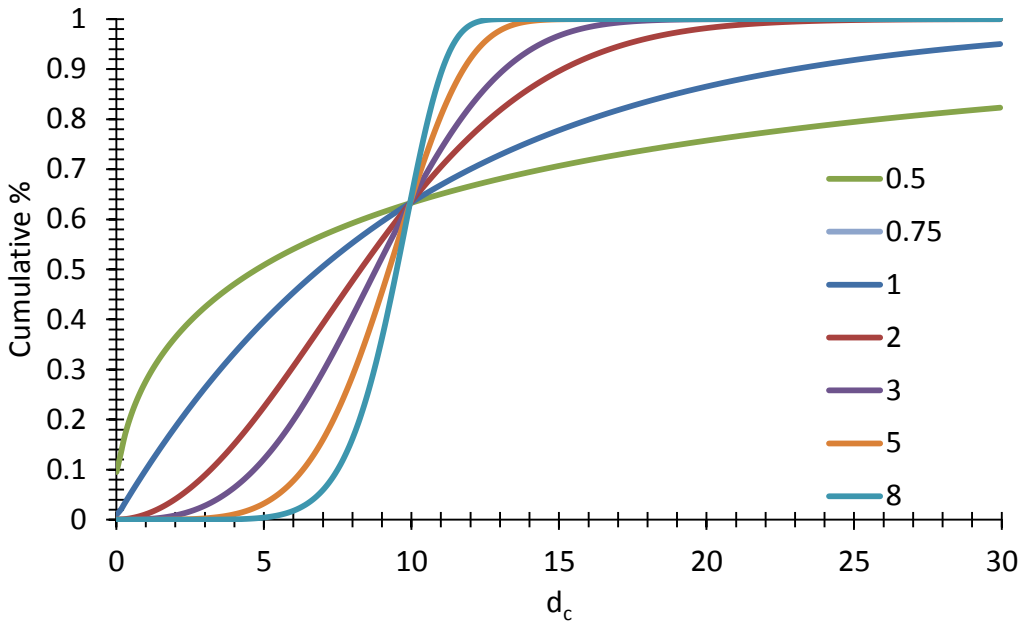

Figure 37: CDF Function Sensitivities to n: d_c = 10. The lower values of n have an arc shape that never approach 100%, while as the values of n increase, the curves focus around the d_c value in a steep fashion

2.6.3 Parameter values for mining applications

Cunningham utilized the Rosin Rammler distribution for blast fragmentation design in 1987. Since then, the Kuz-Ram model has been utilized commonly for blast design practices of all methods of mining activity (open-pit, drift rounds, caving techniques, and others such as cut and fill). One of the performance characteristics of blasting that can be measured and compared with this model, is the particle size distribution of the resulting muckpiles, some using the Rosin Rammler distribution as the performance standard due to the uniformity index *n* which is a key element of the Kuz-Ram model. While it is expensive, time consuming, and sometimes difficult to do, there have been several cases investigated experimentally using sieving of blasts to develop photographic scanning techniques for muckpiles to eliminate the need for sieving and this additional cost, e.g.Wipfrag (WipWare, 2013). With scanning techniques developed, the

information can be gathered in real-time so that particle size information in the distribution can be used in process control (Maerz *et al.* 2007) of the feed to the mill.

2.7 Particle flow codes

Particle Flow Code 3D (PFC3D) software, developed by Itasca, is used for various geomechanical purposes; however only its particular application relevant to this research is summarized here. PFC3D is a discontinuum code that represents rock masses as an ensemble of spheres that may have deformable contacts that can be bonded with other spheres in the ensemble. The ensemble is subject to Newtonian dynamics, initial loading and confinement conditions and mechanical boundary conditions. The interactions between spheres are used to represent exhibit large-strain and/or flow of solid materials. Figure 38 illustrates some of the physics of the interactions between spheres.

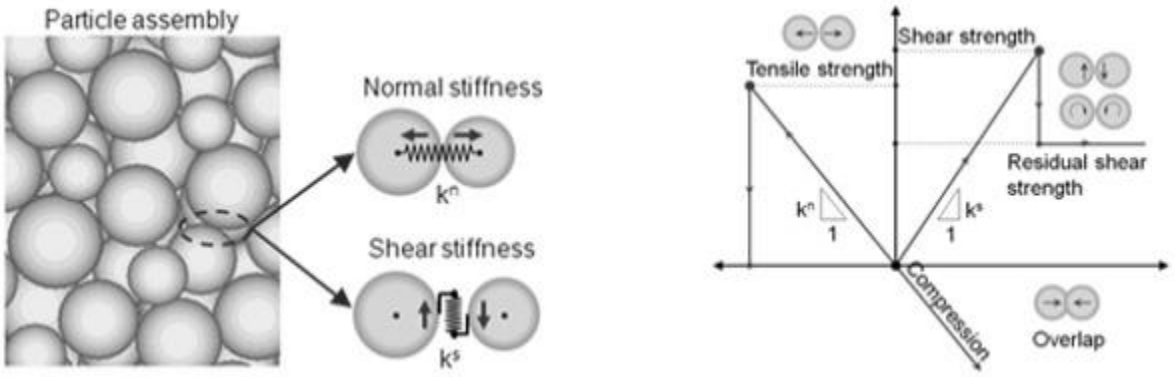

Figure 38: Particle Flow Code and mechanical characteristics of flow codes (NGI Laboratories, 2014)

According to Itasca (2010), in PFC3D, materials may be modeled as either bonded (cemented) or unbonded (granular) assemblies of particles within the code. Spherical particles are used by

default. More complex particle shapes representing irregular rock block shapes may be defined through use of a so-called “clump logic” as shown in Figure 39.

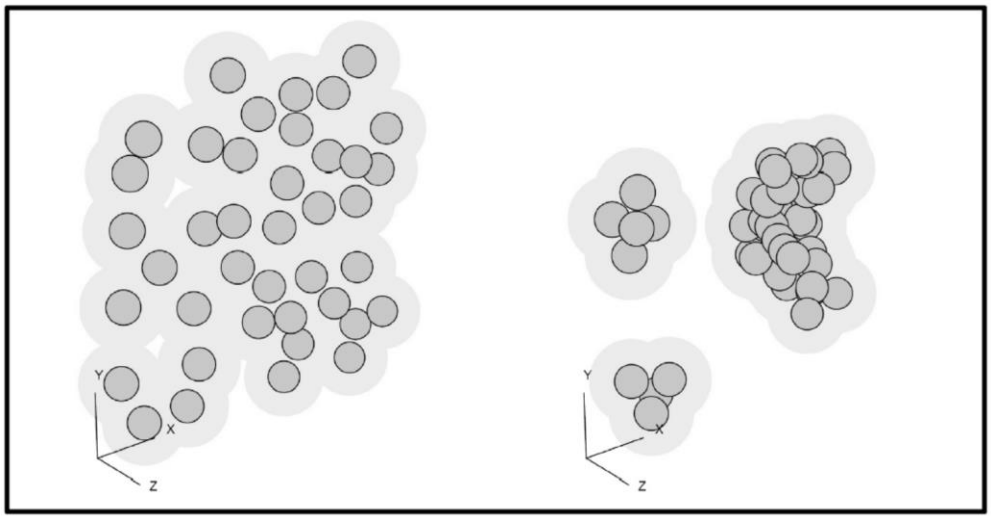

Figure 39: PFC3D Particle clumping to form representations of rock blocks in PFC3D (Itasca, 2010)

When particles are clumped together, there are no internal contact forces. The clump as a whole maintains the creation of contact forces between the consolidated clumps and wall bodies. The outside boundaries of the clumps are deformable while internally the bodies act rigidly. The advantages of clumping in PSMs are that different geometric shapes can be represented, but it must be insured that if this is the objective, there are enough styles of random clumping or the problem will become a uniform distribution of one particular clump type.

2.7.1 PFC3D case study 1: Porosity and tortuosity prediction

In one of the uses of this particle flow tool that is similar to this research, Sobieski *et al.* (2012) tried to calculate the potential tortuosity of air through a packed bed sample of spheres. The authors used mathematical models and CT scans of packed beds, along with the software, and developed a lowest tortuosity value, which is the shortest distance between the spherical particles

from the inlet to outlet boundary condition. The visualisation of their work is shown below in Figure 40. The main difference between their work and the research presented in this thesis is that the particles are not being consolidated in the same fashion and the flow conditions are just an optimal geometric result rather than the result of a full flow simulation.

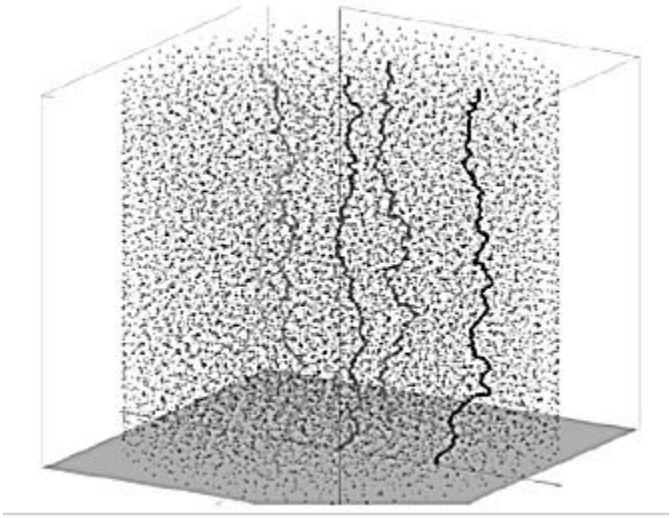

Figure 40: Visualisation of PFC3D model used by Sobieski *et al.* (2012) with the mathematical shortest distance calculations

The CT scan method that was mentioned can also be applied to the PSM method for the CFD code analysis and compared in similar ways as the models presented in this thesis. This would only be due to the geometric breakdown of the PSM technique described in Chapter 7.

2.7.2 PFC3D Case study 2: DEM analysis of soil fabric effects on behaviour of sand

The principles behind this area of research are similar to the consolidation method used in PSM with details of the behaviour of sand (Yimsiri and Soga, 2010). While the fluid flow component is also not introduced in this research, the method of consolidation is similar to the technique

adapted in this work for creation of PSM geometry, through mechanical consolidation, as shown in Figure 41. The research in this paper is also similar to fluidized bed modelling, in which the particles are dynamic in nature and not static. As the particles have dynamic motion, it does not fully represent the porous media for the cases used in this thesis, which are static in nature. The ability of the spheres to move affects the property of tortuosity, which is also, therefore, dynamic in nature.

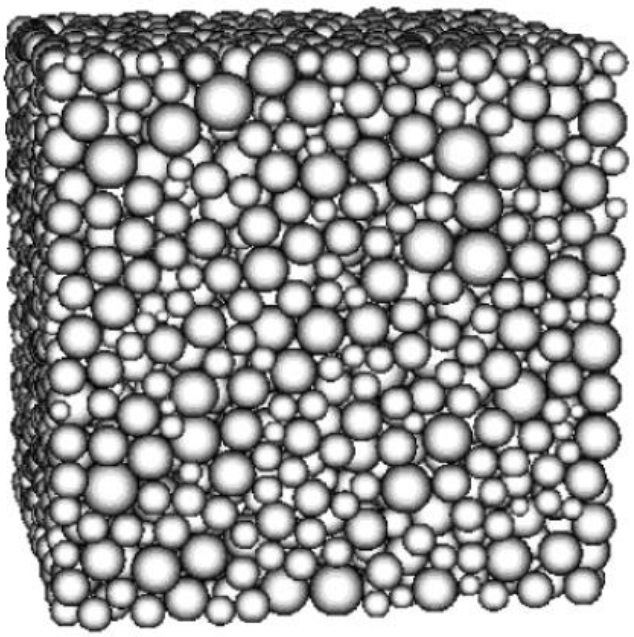

Figure 41: PFC consolidated model as created by Yimsiri and Soga (2010)

2.7.3 PFC3D case study 3: Liquefaction of saturated and loose soils

Another important research direction somewhat similar in nature to this research was started by Zeghal and Shamy in 2008. Within their work, which was focused on soil motion due to earthquakes, Navior-Stokes equations were coupled with a discrete element method for the particles. This research is the closest in nature to the research contained within this thesis pertaining to the idea that a continuum model can be developed from a discontinuum model, as

shown in Figure 42. However, their research was more focused on the solid particle component and not on the flow and heat transfer characteristics, which may or may not have been observable, as shown in Figures 43 and 44.

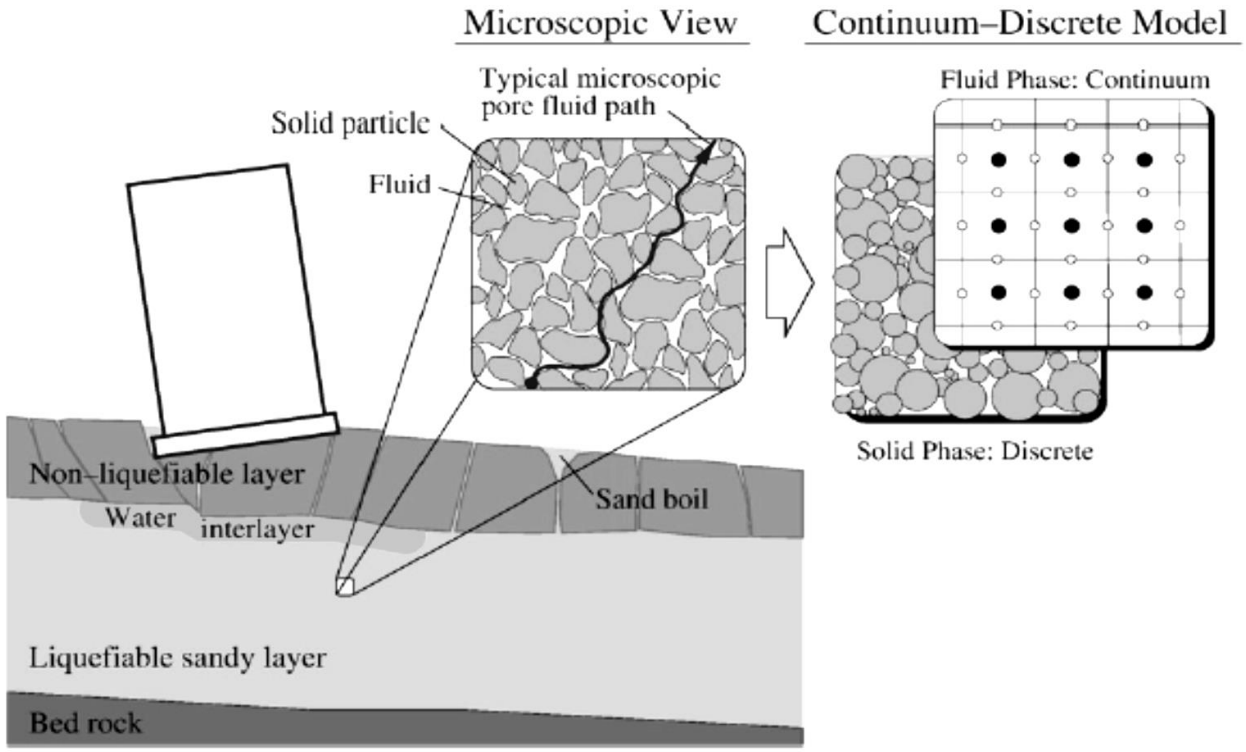

Figure 42: Schematic of approaching equivalent continuum from a discontinuous continuum model by Zeghal and Shamy (2008)

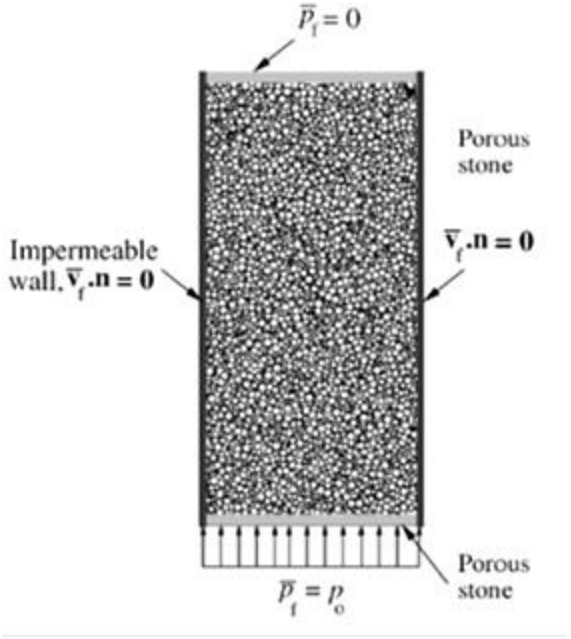

Figure 43: Modelling approach by Zeghal and Shamy (2008) of testing of solid particle flow

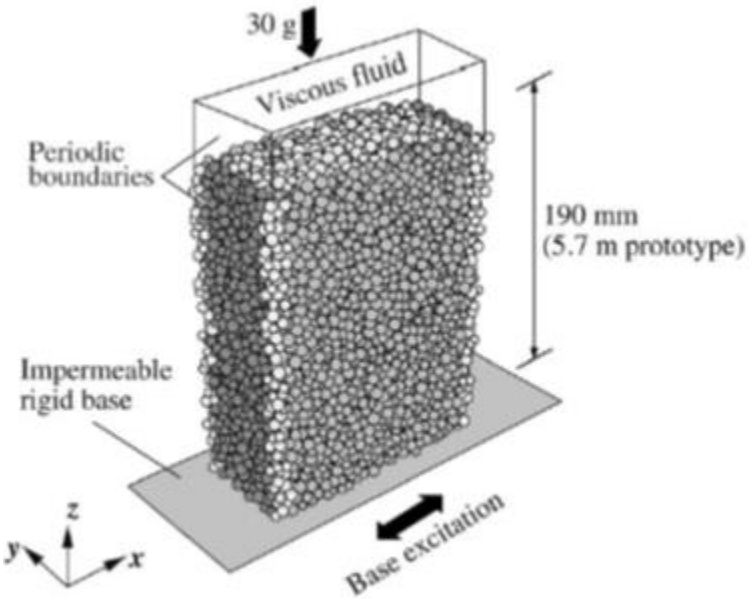

Figure 44: Viscous fluid flow simulation used for the motions of the solids during compaction by Zeghal and Shamy (2008)

2.8 A review of experimental methods and field data gathering techniques for large scale fractured porous media problems

This section describes techniques for measuring the ability of a geomaterial such as fractured rocks to transmit fluids. Also, information on how this data is collected for large scale problems is also given. This information is then used for computer modelling using the two main conceptual models described in Section 2.1. The main theory of testing for larger scale problems are forms of the Constant Head Testing Technique, and information gathered from these experiments can come in the forms of permeability, hydraulic conductivity, or porous resistance coefficients, depending upon what type of modelling technique is to be used for simulating the material.

2.8.1 Standard constant head experimental methods for liquid and gas permeability experiments

Most of the tests developed for the permeability of materials were originally developed for soils using physics developed with Darcy's Law, the Kozeny-Carman equation, and the Hagen-Poiseuille equations in standards such as ASTM D2434 - 68(2006) - Standard Test Method for Permeability of Granular Soils (Constant Head). The general assumptions for these tests are that there is a controlled pressure gradient at the inlet of the experiment and laminar flow throughout the sample. With time, modifications to this procedure have been adapted to porous media and *in situ* rock formations such as ASTM D5084 – 10 - Standard Test Methods for Measurement of Hydraulic Conductivity of Saturated Porous Materials Using a Flexible Wall Permeameter, as well as ASTM D4630 - 96(2008) - Standard Test Method for Determining Transmissivity and

Storage Coefficient of Low-Permeability Rocks by In Situ Measurements Using the Constant Head Injection Test, and ASTM D5856 - 95(2007) Standard Test Method for Measurement of Hydraulic Conductivity of Porous Material Using a Rigid-Wall, Compaction-Mold Permeameter. These tests are accepted standards and are conducted in the form described in the following.

2.8.2 Standard constant head permeameter testing apparatus and testing procedure ASTM D 2434

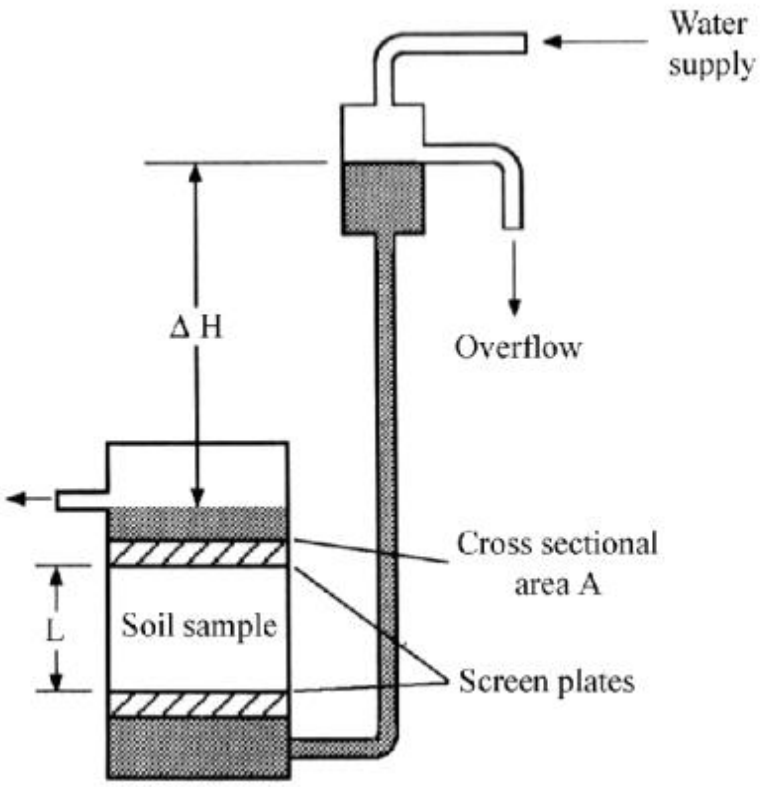

Figure 45: Standard Constant Head Permeameter Configuration (Laboratory of Ecohydrology, 2013)

The most common standard constant head pressure test experimental setup is shown in Figure 45. The ASTM standard D 2434 is referred to here as the standard procedure for receiving relevant information from this standard experimental configuration.

After following the ASTM D 2434 procedure, parameters such as the hydraulic conductivity can be calculated by using the following data to evaluate the following equation:

$$k = -\frac{QL}{A\Delta H} \tag{39}$$

where:

k = hydraulic conductivity (cm/s)

Q = constant flow rate (cm^3/s)

L = length of chamber (cm)

A = cross sectional area (cm^2)

ΔH = difference in height or head (cm)

The same constant head test can also then be configured for permeability testing with gases (air) as seen in Figure 46. The configurations are the same except measuring the pressure differences across the sample are measured instead of head difference height. This type of configuration can also be applied to a wind tunnel.

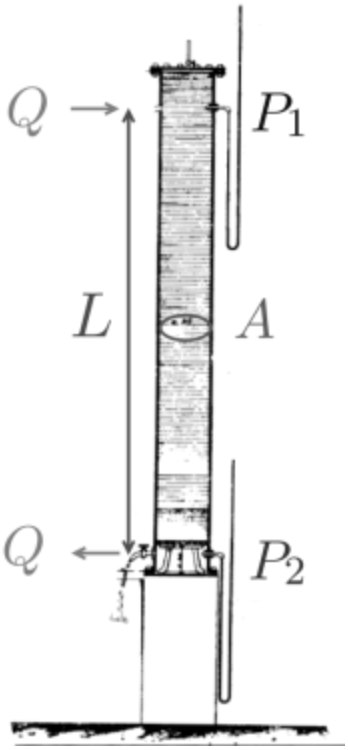

Figure 46: Constant head variation in terms of pressure loss across a sample [(Darcy, 1856) and recreated by Laboratory of Ecohydrology, 2013)]

In general, the parameter of permeability can then be calculated by the formula for Darcy's Law for gases exemplified in Tidwell (2006):

$$k = \left(\frac{2\mu Q p_1 L}{A(p_1^2 - p_0^2)}\right) \quad (40)$$

where:

k = gas permeability (m^2)

μ = gas viscosity (Pa*s)

Q= flow rate through the sample (m^3/s)

p_1 = pressure at the inlet (Pa)

L = length of the sample (m)

A = cross-sectional area of the sample (m^2)

p_0 = pressure at the outlet (Pa)

In terms of Darcy's Law, the parameters of the pressure gradient are predicated on the squared pressure owing to the compressibility of the gas (Bear, 1972).

While there are other methods of testing the permeability of porous media such as the falling head test, borehole testing techniques, and mini permeameter tests using syringes, large scale application of these techniques can be difficult and impractical. None of those techniques were used in this thesis. An explanation of how the parameters are used in analysis, that are gathered from the constant head test large scale modelling with Darcy's Law, the Kozeny-Carman equation, and PSM will now be given.

2.8.3 Darcy / permeability coefficient testing for large application

The testing method to obtain the permeability parameters of large scale porous media is derived from the constant head test described earlier. Two of the variables required in CFD simulations used to verify the results are the mass flow rates entering the porous media sample and the size characteristics of the media (rock or soils). Also, there is a need to define the porosity, from which the ratio of solid to air/ liquid capillary interfaces can be determined. One example where the permeability or hydraulic conductivity information can be gathered comes from application to aquifer reservoirs. In this version of the constant head test method, a water surface can be maintained through pumping and measurements are taken at monitoring locations in a series of wells. This method can be difficult to apply with unconfined aquifers, but that is then

transformed into a different class of testing called the falling constant head test. In Figure 47, a schematic for testing in aquifers is presented.

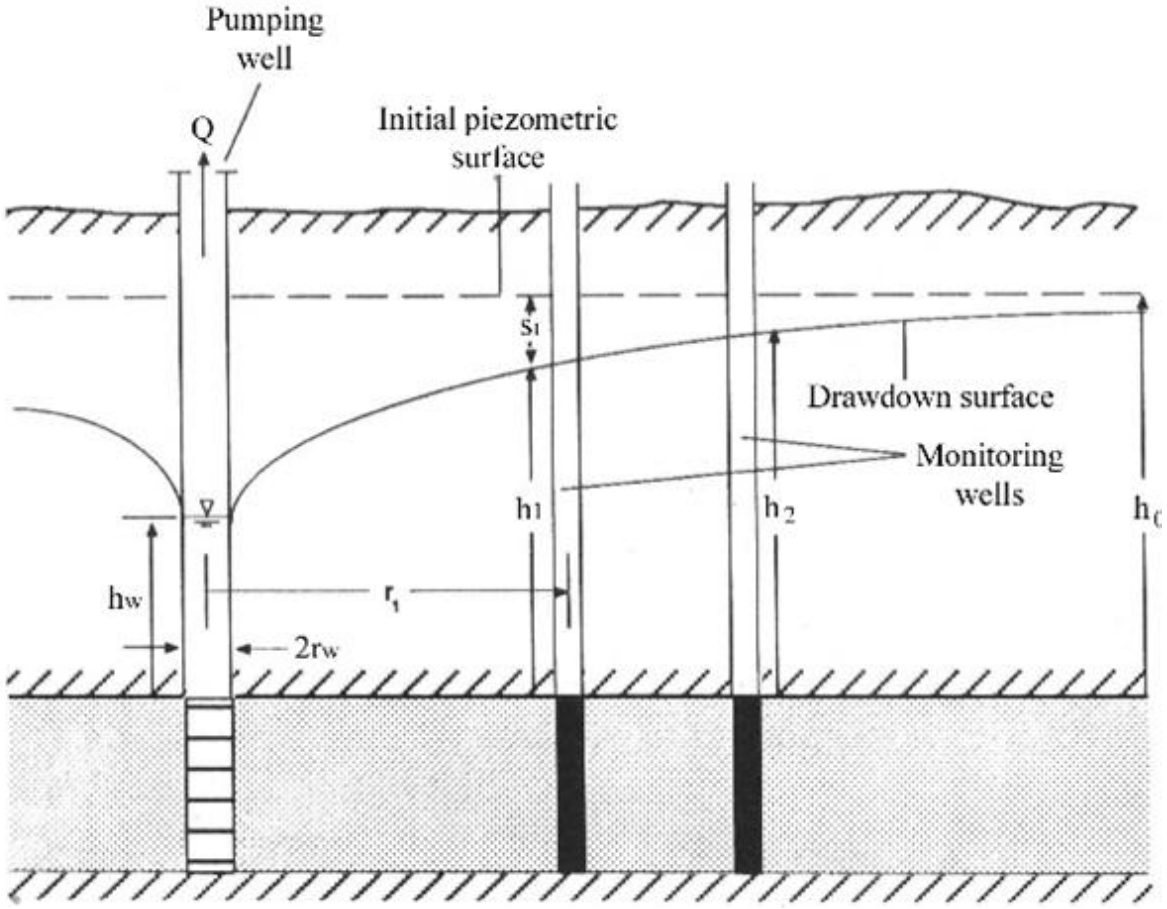

Figure 47: Version of the constant head test used in confined aquifers (Laboratory of Ecohydrology, 2013)

The analysis of the information from large scale samples can then be summarized and substituted into Darcy's Law in the following form:

$$k = -\frac{QL}{A\Delta H} \tag{41}$$

where:

k = hydraulic conductivity (cm/s)

Q = constant flow rate (cm^3/s)

L = length of well chamber(s) (cm)

A = cross sectional area of the monitoring well(s) (cm^2)

ΔH = difference in height from the initial piezometric surface (cm)

2.8.4 Kozeny-Carman variation used in full scale experimentation

The Kozeny-Carman equations are used for measuring hydraulic conductivity and values can be measured in methods similar to the constant head pressure test. Kozeny first proposed relationships between pore space sizes, flow rate, tortuosity, and connectivity in 1927 before being modified by Carman in 1937 and 1956. The prime difference between their versions and Darcy's Law is that the solid space or porous matrix can be broken down from a solid cylinder with pores or capillaries going through it into a series of solid spheres of any size to represent the solid fraction. The Kozeny-Carman formula is shown in standard form:

$$k = C \frac{g}{\mu_w \rho_w} \frac{e^3}{S^2 D_R^2 (1+e)} \quad (42)$$

where:

k = hydraulic conductivity (l/s)

C = shape factor that accounts for the shape and tortuosity of channels

g = the gravitational constant (m/s^2)

μ_w = the dynamic viscosity of water ($N\ s/m^2$)

$\rho_{w=}$ the density of water (kg/m^3)

e = void ratio (porosity)

S = specific surface (m^2/kg of solids)

D_R = the specific weight = the density of solid over the density of water

While the Kozeny-Carman equation is limited to laminar flow, some larger scale investigations have been performed to test its validity. One set of examples of concerning flow through mine tailings conducted by NRCan through papers released by L'Écuyer *et al.* (1992); Aubertin *et al.* (1993, 1996); Bussière (1993); and Monzon (1998). In these papers, fine crushed rock with the gradation of silt with little or no plasticity, along with gradation curves from empirical estimates, were modelled with the Kozeny-Carman formulation, but were found to produce substantial error in the hydraulic conductivity (Chapuis and Aubertin, 2001). Physical results were obtained for homogenized fully saturated specimens tested in either rigid-wall or flexible-wall permeameters. It was verified that both testing methods gave similar results (Chapuis and Aubertin, 2001). After a relation between the specific surface and liquid limit (Chapuis and Aubertin, 2001) was used, the variation of the Kozeny-Carman formula used in full scale experimentation by NRCan was as follows:

$$\log\lfloor k \rfloor = 1.5\{0.5 + log\left(\frac{e^3}{D_R^2 S^2(1+e)}\right)\} + 2 \quad (43)$$

where:

S = specific surface (m^2/kg of solids)

D_R = the specific weight = the density of solid over the density of water

Results of Chapuis and Aubertin's research comparing experimental tailings piles hydraulic conductivity and the values of their Kozeny-Carman equation can be seen in Figure 48.

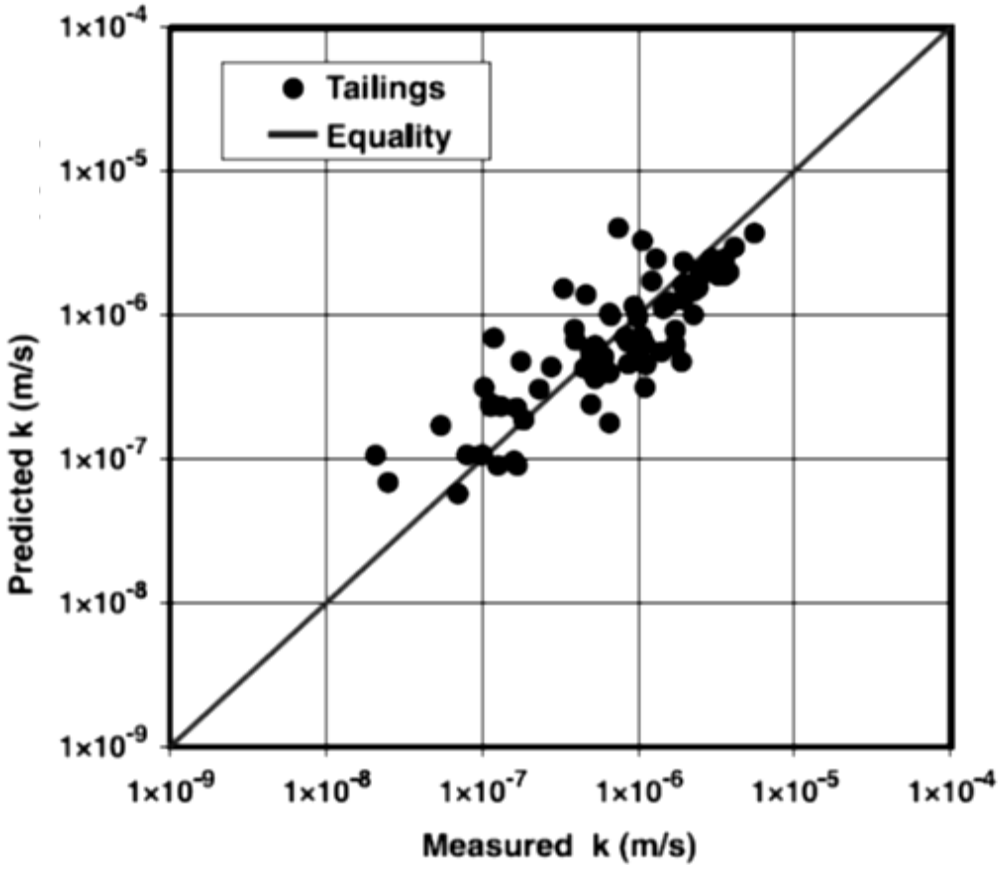

Figure 48: Predicted vs experimental hydraulic conductivity through tailings piles (Chapuis and Aubertin, 2001)

Angularity, which causes multiple values of tortuosity, as well as exothermic chemical reactions of the various materials within the tailings during the permeability tests, was assumed to be the cause of error for the experiments.

2.8.5 Ventilation network analysis data collection

While ventilation network analysis has not been directly used for large scale porous media problems previously, the concept of network analysis can be used to build up either a series of blocks, or equivalent continuum branches, to model a complex or large system. Within such models, a resistance calculation from Atkinson's equations or a friction factor model can be

developed. The scaling capability is then in the creation a series of massively parallel branch networks. The principles involved were described in detail in the previous chapter, but the data needed to verify this form of modelling can be gathered from a constant head pressure test. The resistance is a function of the pressure loss across the medium divided by the square of the flow rate. For data collection, the tools required are a flow measurement device, such as one of the forms of anemometer (hot-wire, rotating, swinging vane, or vortex types). For the pressure component, a manometer to gather the pressure difference across a sample, or for very large scale problems, two barometers that can take simultaneous observations at two locations. The cross-sectional area must also be assumed or calculated for large scale problems.

2.8.6 Packed Sphere Modelling physical data collection

While the PSM technique is a form of proxy testing for the constant head permeability test, there are some preferential characteristics required for their initial geomechanical conditions. The data needed for the PSM that cannot be simulated are the physical characterisation of the rock particle sizes. This can be done using sieve analysis for the mass distribution input into the Rosin Rammler or other distribution of choice for particles. Analysis of the sphericity and angularity can be done for a more accurate model as seen in the Figure 49. For verification purposes, a wind tunnel experiment can be undertaken (as described in the coming chapters) and requires the pressure drop across the sample as a base, and the flow rate going through the sample, as in a standard constant head test.

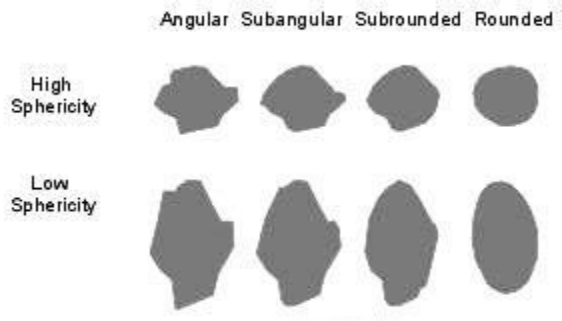

Figure 49: Shapes that can be adapted to fit into the PSM technique (Geomore, 2013)

2.8.7 Discussion of experimental methods

It can be extremely difficult to measure and gather data for large problems involving broken and fragmented rock, and this is why most experimentation for equivalent continuum modelling is done in small scale, laboratory experiments. The variation of conditions or heterogenous nature of porous materials leads to substantial difficulties in ideal analytic or empirical solutions to problems, especially at large scales due to changes in features such as tortuosity or the flow regime, which are stated as direct limitations in both Darcy and Kozeny-Carman solutions. These issues support the contributions that are possible through PSM by being able to model various real life conditions with the principle difficulty being modelling the potential distributions and shapes of the material requiring characterisation.

After investigating the properties of air and water, it was determined to use air for the PSM verification experiments. The reasons for this choice are, in particularly, due to the heat transfer characteristics of water. Air thermally much more quickly (meaning it heats up faster) than water due to a higher convective heat transfer coefficient, so signals can be measured at a much faster

rate. Also, this means that for practical wind tunnel testing, the sample could be frozen and then tested, without having the added complexity of the latent heat properties of the water.

3 PSM workflow for analysis of porous media problems

3.1 Introduction

When attempting to represent the geometric structure of porous media, characterising the internal geometry is a central challenge. If the medium is particulate, one can adopt the stance that it is the particles forming the porous ensemble that need to be characterized. If it is not particulate, such as pumice, a more appropriate approach may be to characterize the pore spaces. For particles, there are numerous geometric factors to accommodate: mass, dimensions (length, width, and breadth) angularity, surface roughness, and flake. Here, a dramatic simplification is made, namely it is assumed that the particles are all relatively smooth and spherical in shape; this allows for the investigation to proceed regarding the effects of particle size, size distribution and particle packing on the airflow resistance of porous media. As will be seen, the verification methodology proposed will permit the representation of additional geometric complexities, when data gathering can resolve them.

Adopting the simplification, one can render the internal geometry of rock piles, assuming a uniform distribution of particles, or a more complex distribution such as the Rosin Rammler distribution (Rosin and Rammler, 1933), which is currently used in practice in applications from blast design to sedimentary classification in geology. This chapter first explores a method of representation of particle ensembles that follow the Rosin Rammler distribution, and gravitationally consolidates the particles by the use of a particle flow code so that a realistic analogue of a porous geomaterial results. The second part of this chapter explains how the consolidated ensemble is rendered within a CAD/CAM environment as an intermediate step to CFD tools that can be used to establish the airflow resistance characteristics of the analogue.

Geometric thermal information can then be extracted from the analogue for use in problems dealing with the internal geometry of porous media. This chapter is effectively a summary of the backbone of the PSM technique, from sphere creation consistent with a given Rosin Rammler distribution, determination of the airflow resistance of the PSM particle ensembles through to engineering analysis of large scale problems.

3.2 Design specification of particle size distribution

To represent the particle size distribution of PSM, the Rosin Rammler distribution was adopted due to its long and frequent use for geomaterials in mining and mineral processing (Cunningham, 1983, 1987; WipWare, 2013). However, almost any distribution can be used for this process including random or clumped irregular shapes, but this is at the discretion of the individual user as the verification process is the key contribution. The Rosin Rammler distribution in the PSM is first designated and generated in the particle flow code.

3.3 Geomechanical consolidation of particles

The particle flow code adopted for this part of the work was PFC3D (Itasca, 2014). PFC3D has a macro language within it, called 'FISH' that permits specialized commands to be executed in an automated fashion. The primary FISH Command used to generate the spheres that create the defined particle geometry is as follows:

FISH Command: gen id=1, 8 rad 0.00175, 0.001925 x=0,.0762 y=0,.0762 z=-.1,0

where:

gen id = 1,n1 signifies the generation of n spheres with a numeric identifier indexing 1 through to n1. This command is called once to generate the n1 spheres required for the first size fraction bin. The process continues until n-1 to n spheres for all of the bins are generated.

rad = rad 0.00175 (lower bound for the verification example),0.001925(upper bound for the verification example) which specifies the lower bound radius(m) of spheres generated and the upper bound radius (m), for the first size fraction bin.

x= 0, 0.0762 indicates that the lower and upper bounds of initial placement of the centroids of the spheres within the particle flow code model domain in the x-direction are 0 and 0.0762 metres respectively.

The definition is similar for y and z directions. In the z-direction, greater 'headroom' is provided to permit all spheres to be placed during this initialization process.

The command above was called once for each size fraction and generated the defined number of spheres according to the particle size distribution function with parameters in the case as n= 4.5, $\overline{d}$= 0.0088m. Each sphere was randomly located within a space defined by the 6 half-spaces, with a diameter randomly sampled from a normal distribution, but constrained to be between the specific radii (size passing) limits. Smaller size fractions were processed before larger fractions, a measure that should be reversed for future implementation. The reason for placing the larger particles first during the initialization process is that the PFC3D command will not place a sphere

at a location that overlaps with the presence of a previously generated and placed sphere, which is more difficult to do if the smaller spheres are placed first rather than the larger spheres.

After the initial sphere sizes and position had been defined, all spheres generated were not in contact with any other sphere. The particle flow code dynamical logic was cycled so that inter-sphere contacts were established through the simulated application of the force of gravity until a state of mechanical static equilibrium was established. This process is called 'consolidation.' In Figure 51, a pre-consolidated model arising from the initialization procedure is shown and the same sphere in their post-consolidated condition at mechanical equilibrium is presented in Figure 52. During this process, the spheres themselves were considered rigid, such that, geometrically, inter-sphere contacts were point contacts rather than overlapping or deformed contact locations. The reason for adding the consolidation process is to settle the simulated particles instead of just having a random representation of particles, so as to more faithfully represent actual particles in muck piles and other crude representations of particle flow during caving, etc.

3.4 Verification sample ensemble of a Rosin Rammler distribution

The Rosin Rammler distribution adopted was one with an average diameter, $\bar{d}$ = .0088m and a spread diameter, n = 4.5. The distribution of spheres synthesized was passed to the consolidation process using PFC, as described previously, and then imported into the CAD/CAM environment. The expected distribution of the number of particles defined by the Rosin Rammler distribution parameters compared with the actual distribution after the PSM synthesis in PFC3D is shown in Figure 50.

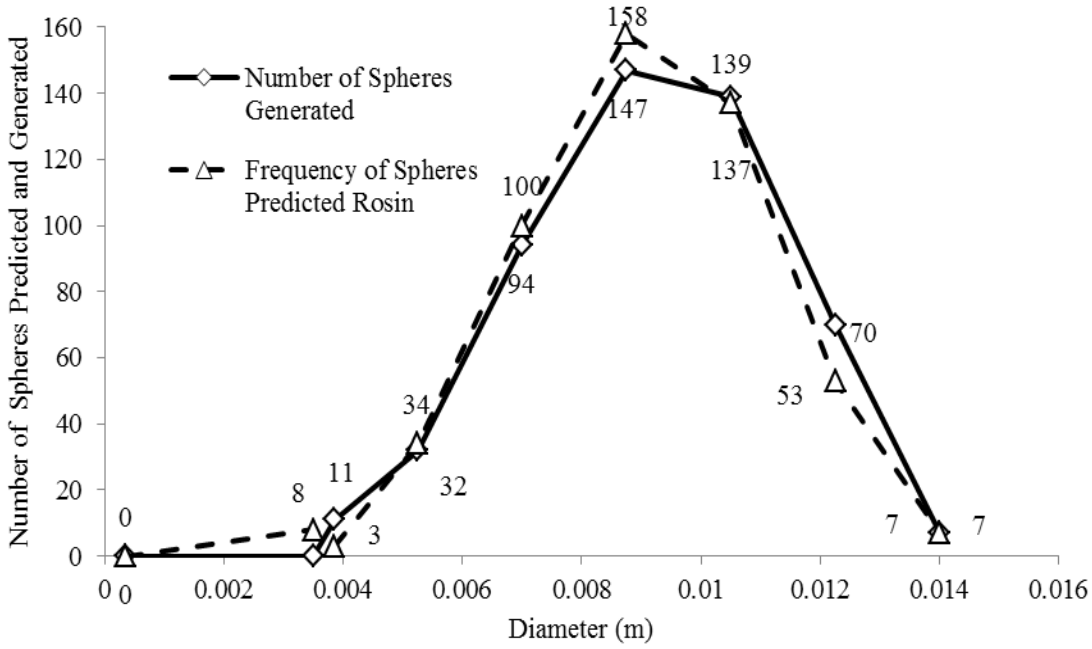

Figure 50: Rosin Rammler predicted distribution compared with spheres generated through particle flow code software. Rosin Rammler parameters are d avg = 0.0088 m, spread diameter n = 4.5. The number of particles generated not being identical to the ones predicted due to the manner in which the particles were generated using the FISH commands. This difference was corrected in future models.

A new procedure was established that recorded the radius and centroid coordinates of each sphere, resulting from the consolidation process in the particle flow code. This information was later used to automatically replicate the size and position of each and every sphere within the CAD/CAM software environment.

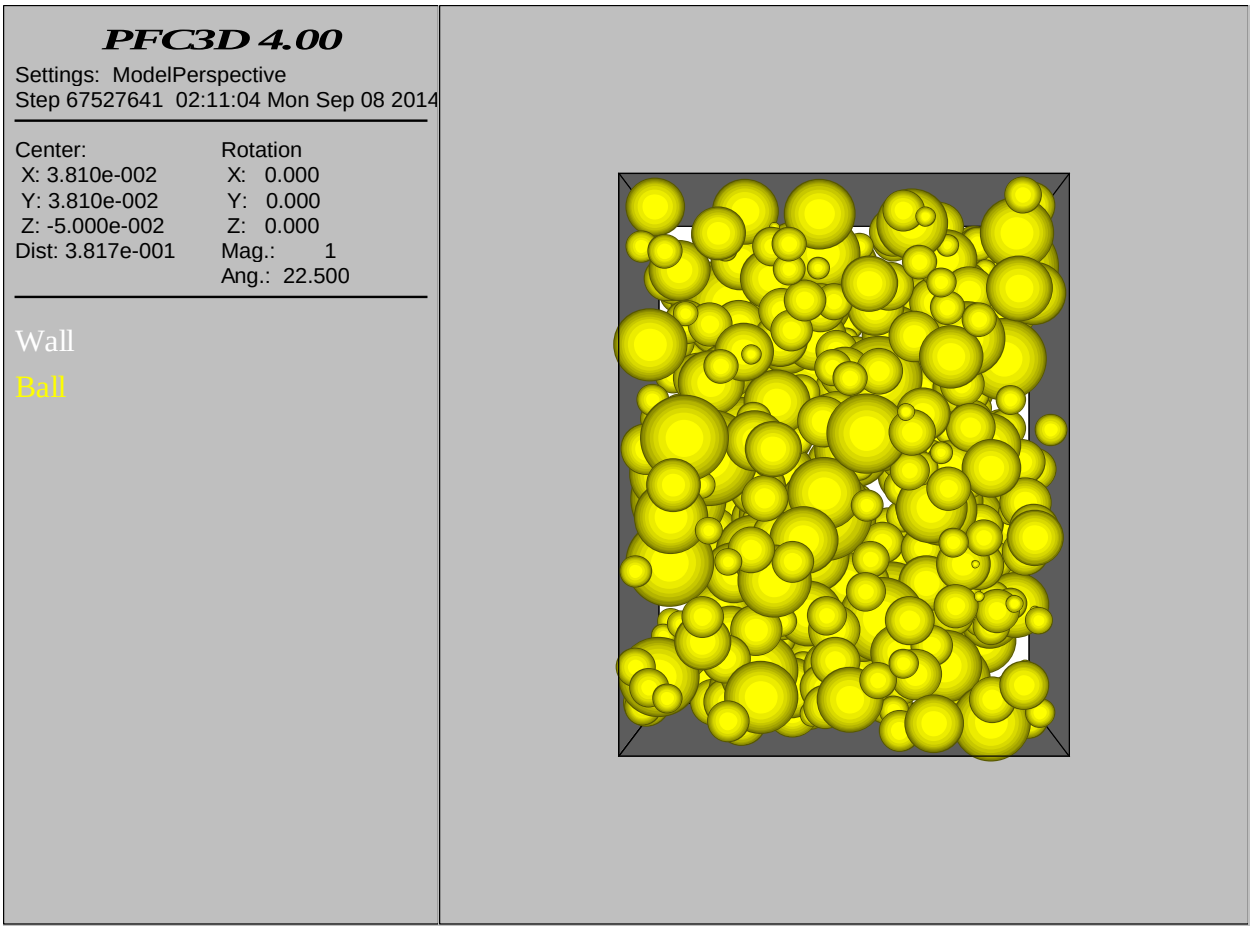

Figure 51: A PFC model as seen at the generation of spheres stage pre-consolidation

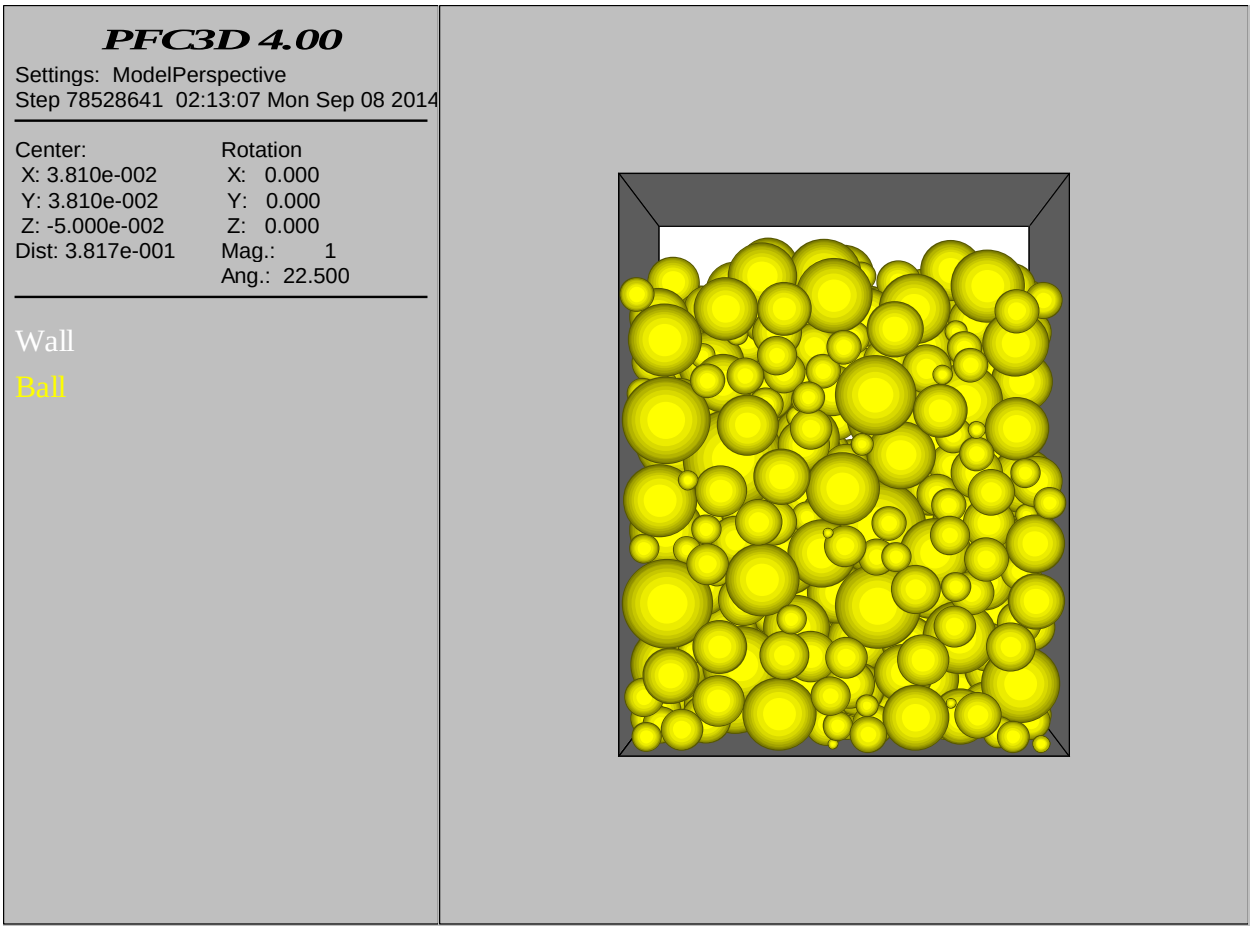

Figure 52: Same particle flow code model from Figure 51 post-consolidation

3.5 Import of PSM assembly into CAD/CAM environment

Once a model had been consolidated, a custom import program was used to exactly replicate the sphere sizes and postions relative to each other within the CAD/CAM environment. The import program is given in Appendix 1. The rendering in Figure 53 is the result of this process for the verification model.

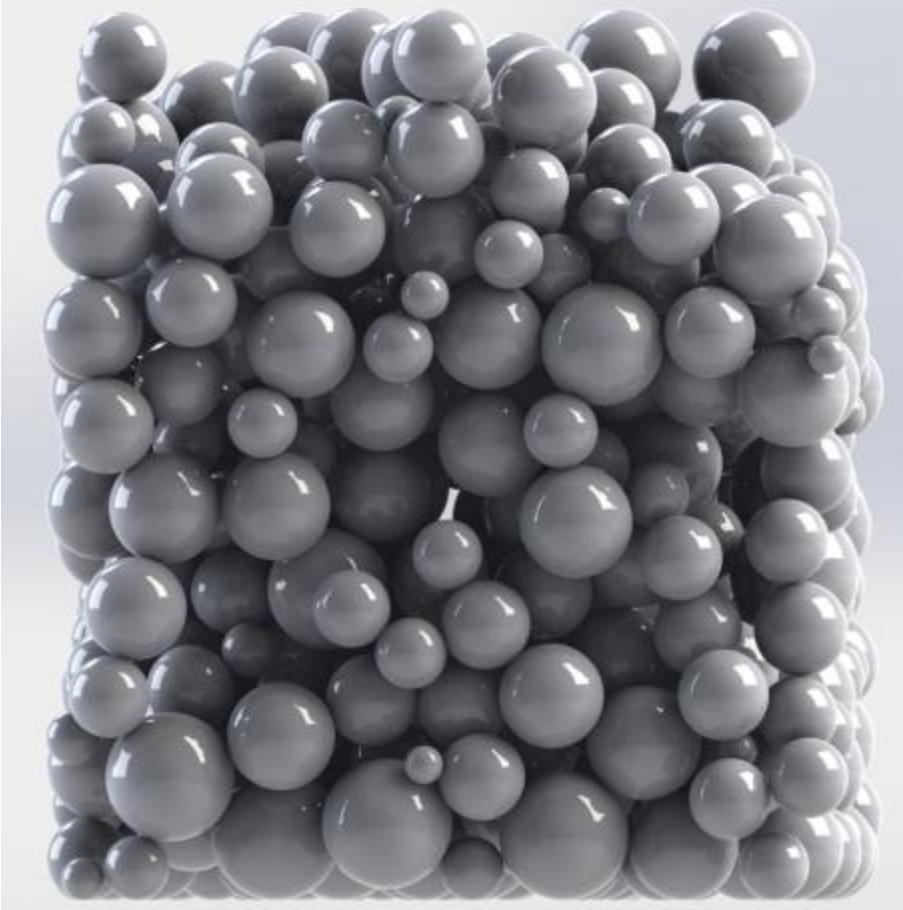

Figure 53: Full particle flow code model imported into the CAD/CAM environment before being processed for use as the verification model

3.6 'Flow Simulation' of airflow and heat transfer

Once the model had been fully imported into the CAD/CAM environment, as this was also the environment hosting the CFD analysis, the process of evaluating the airflow and heat characteristics of the ensemble could be performed. First, a square box was formed around the sample, fully surrounding it. A box was chosen for this task due to the necessary definition of porous media parameters (which are at the base level defined as boxes for octree mesh structure within the Flow Simulation solver) to create a porous equivalent. These reference parameters for the continuum model are the cross-sectional area and length of sample. Other shapes may be

used, but a square provided the most in common with how equivalent porous medium materials are defined within the Flow Simulation environment.

At this stage of the process, the key parameters that could be gathered included the size and bulk geometric values (total volume and boundary surface areas). The flow simulations were run with boundary conditions of static pressure conditions at the bulk inlet and outlets of the model as done in Section 2.4.2. With these conditions, the flow simulation can be executed and then several parameters, both locally and a bulk value can be examined.

3.7 Interpretation of results

Below is a summary of the commonly evaluated parameters used in analysis. It is important to note that while described below as a point, surface, or volume parameter that is sensed or collected from the solver, at any point in the mesh structure itself a value for the following parameter can be obtained.

3.7.1 Pressure distribution through the PSM

The user in this process defines the pressure boundary conditions at the inlet and outlet of the sample. Once the flow simulation has completed, local values of pressure either at individual points within the fluid domain, or pressure averages along any section of the domain, may be captured (Figure 54). This feature is good for examining regional features such as a particular pressure loss in an area or local features causing re-circulation within the sample.

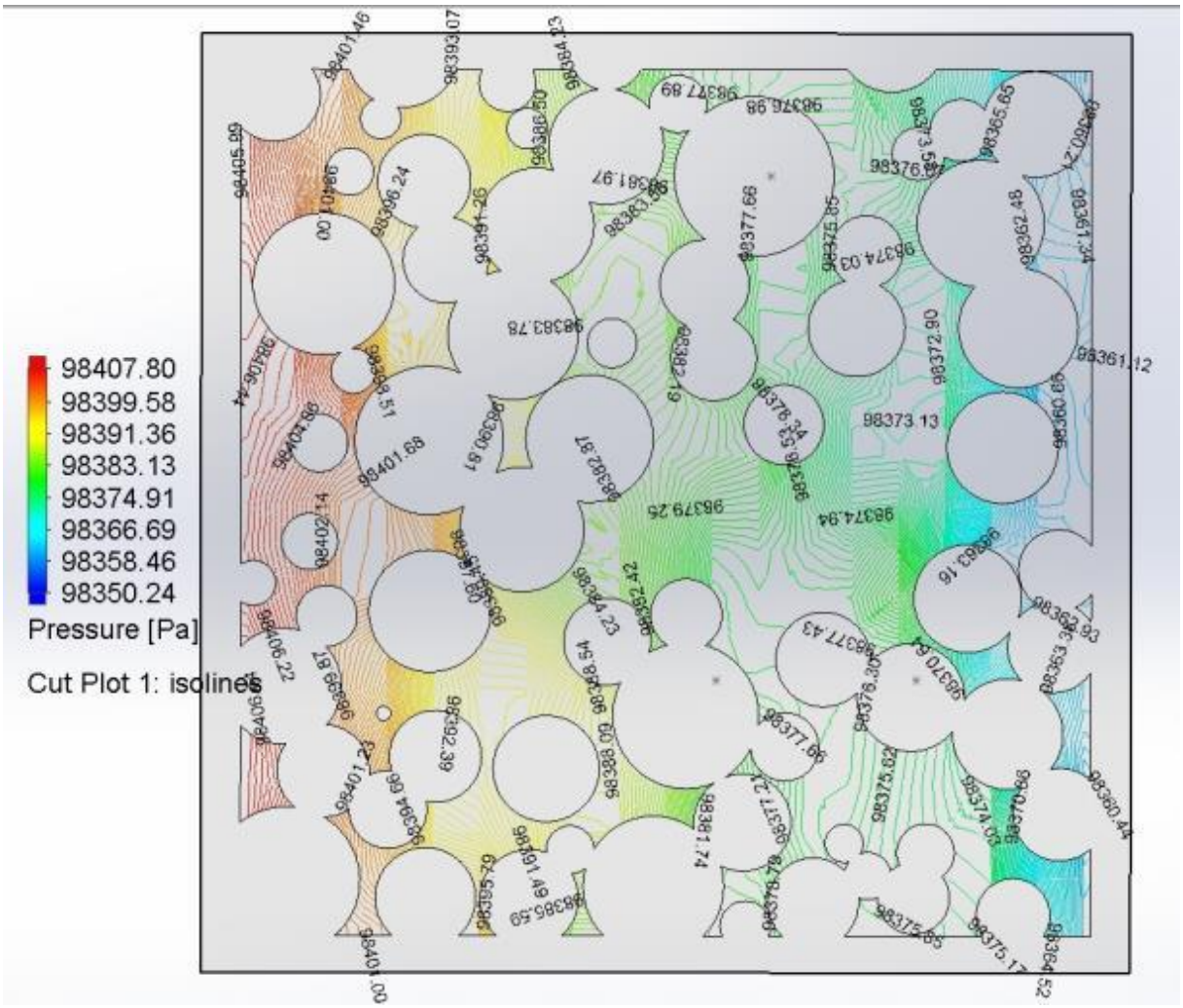

Figure 54: Pressure distribution through the PSM. Boundary conditions are a pressure difference of 57Pa across the 7.62 cm sample, and flow is from left to right.

3.7.2 Temperature distribution through the PSM

The parameter of temperature is an important feature that the PSM can generate for porous medium problems involving heat transfer. In the CFD software environment, temperatures can be evaluated either locally at points in either the solid and fluid domain or bulk temperatures can be evaluated for all of the solid material or all of the fluid domain material. Finally, temperatures over the inlet and outlet surfaces can be evaluated (Figure 55), which can be useful for

determination of the bulk (or portions thereof) parameters used in creating equivalent continuum models. In the verification example that will be presented in Chapter 8, point and surface temperature sensing were used in the simulation of the physical experiment at the locations where thermistors were used to measure the temperatures within the physical sample.

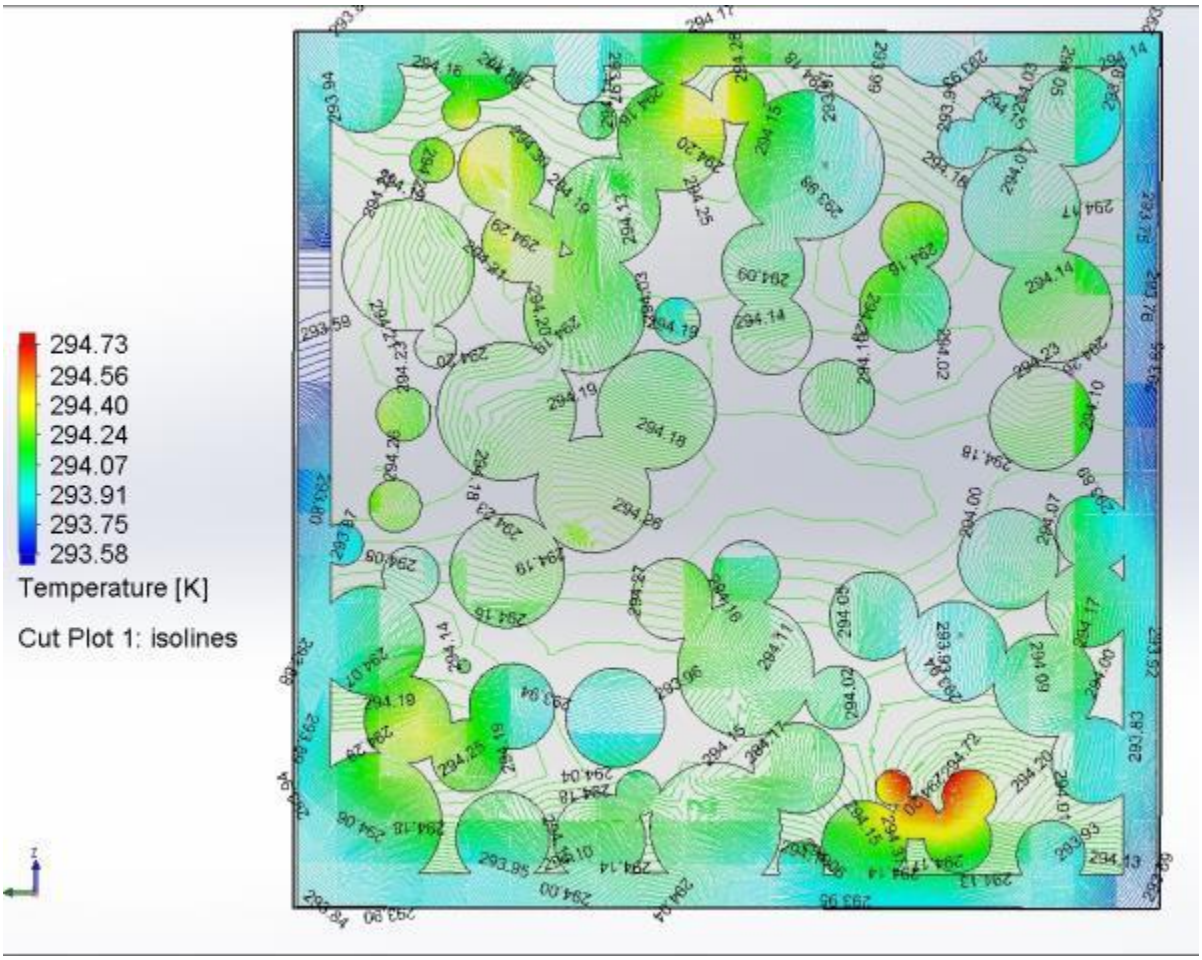

Figure 55: Temperature contours on display for both solid and fluid objects contained within the PSM. The figure above was taken during a time domain simulation and is therefore not at steady state, but a transitional one in the 7.62cm sample.

3.7.3 Density of fluid distribution through PSM

Density changes within a porous media problem can become important with large pressure differences or with auto compression, when the scale is large enough. The contour plot of density within PSM is shown in Figure 56.

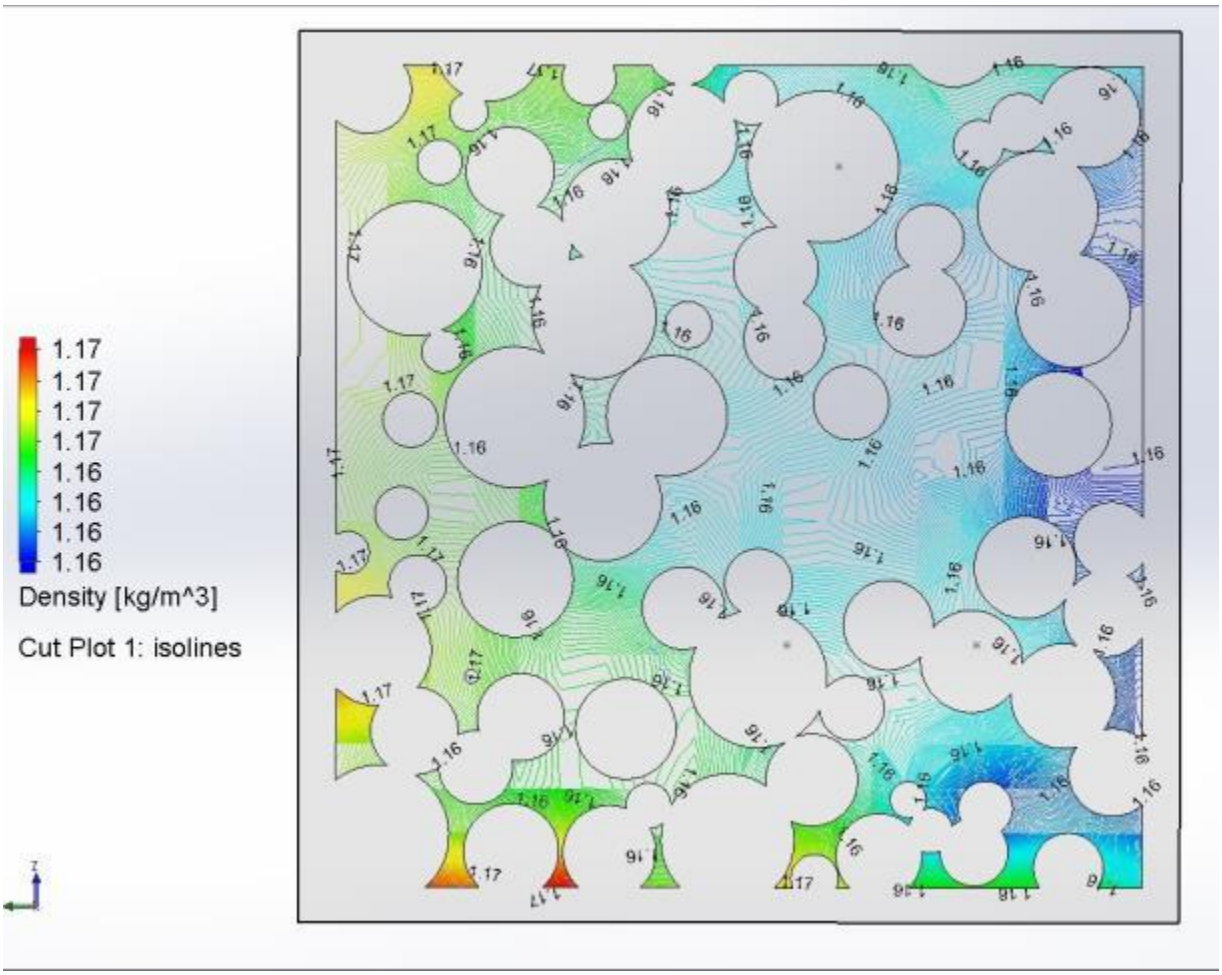

Figure 56: Density contours within the PSM verification model. Areas of different densities are caused by so called dead-end spaces that equivalent continuum models traditionally cannot calculate.

3.7.4 Velocity distribution through PSM

The velocity parameter is of primary interest in most PSM simulations. Flow rates through the sample are determined at the inlet and outlet by integrating the velocity distributions over these surfaces (Figure 57). Specific areas of interest can be investigated so that an understanding of how the fluid domain behaves during experimentation can be developed. Also, the 'dissection' of the geometry, a process explained in Chapter 7, can lead to the calculation of local Reynold's numbers, which are important in determining the flow regime and heat transfer characteristics of the sample.

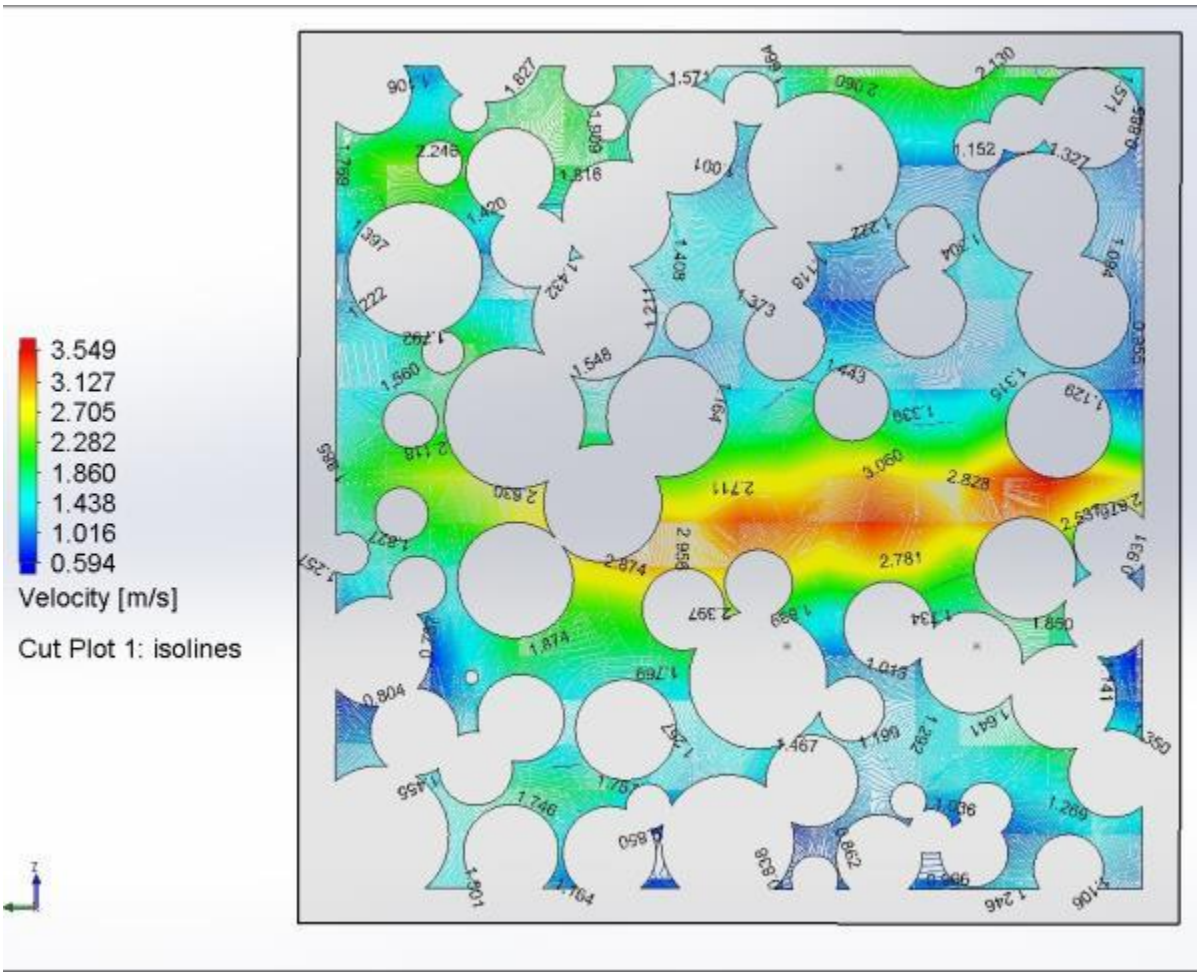

Figure 57: Velocity profile of the same section of PSM discontinuous model. Examination of flow can be more easily interpreted by evaluating the velocty profile.

3.7.5 Vorticity distribution through PSM

The vorticity contained within the PSM sample, determined by the Flow Simulation code, describes the local spinning motion of a fluid at given locations, as would be seen by an observer located at that point and traveling along with the fluid (Figure 58). Conceptually, the vorticity could be determined by marking the particles of the fluid in a small neighborhood of the point in question, and characterising their relative displacements as they move along the flow.

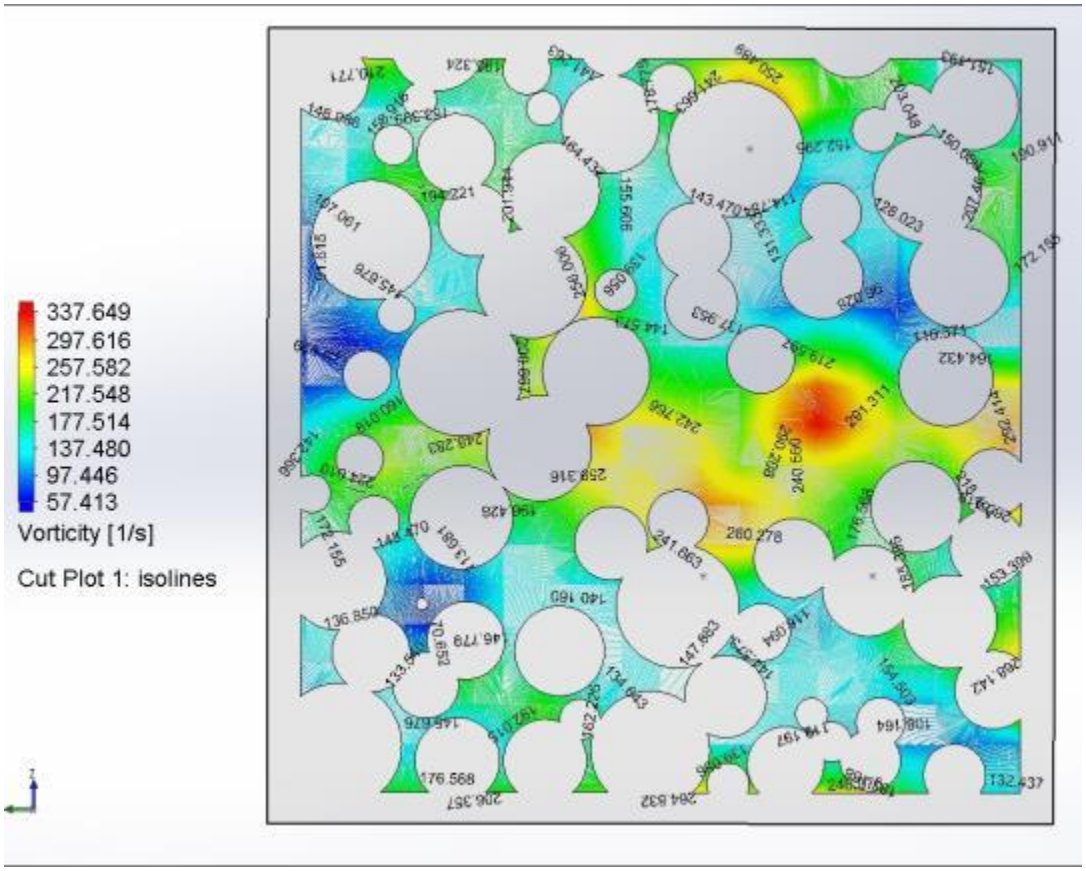

Figure 58: Vorticity of a transitional state of the PSM.

3.7.6 Prandtl Number distribution through PSM

As described earlier, the Prandtl number is important in understanding how much heat is being transferred due to convection relative to that being conducted within a sample. Specific regional areas of interest may become crucial for an evaluator's needs and is so the Prandtl can be captured at a point, profiled or integrated into a bulk parameter from the fluid flow simulation tool shown in Figure 59.

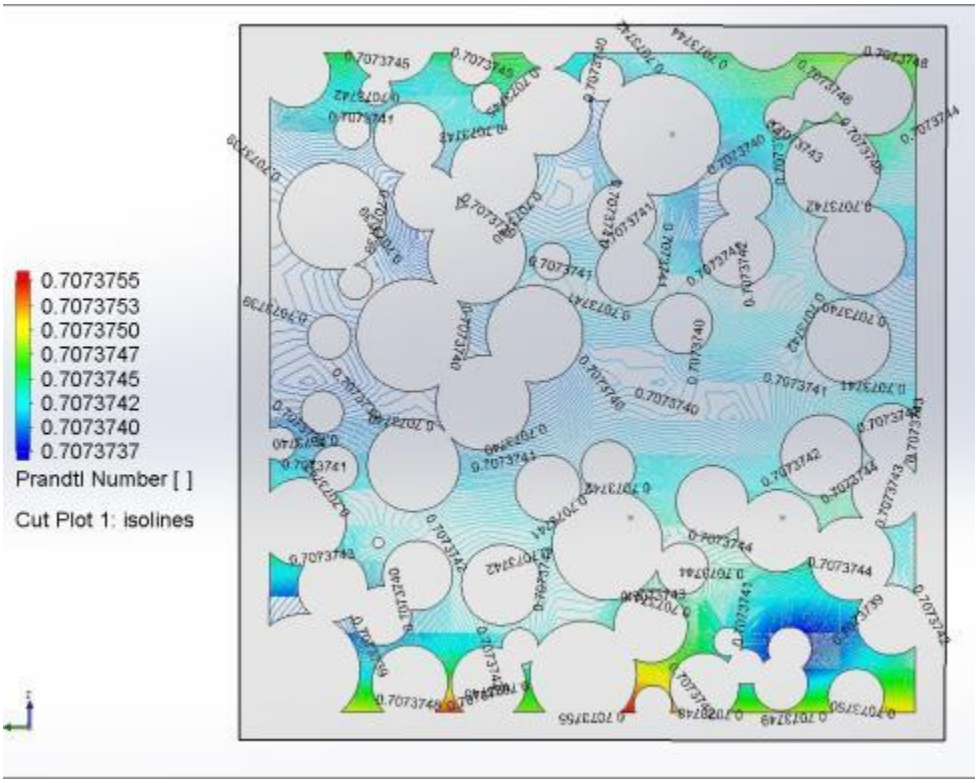

Figure 59: Prandtl number of an initial transitional temperature state of a PSM

3.7.7 Heat flux in solids

The heat flux is the rate of heat energy transferred across a given surface. As shown in Figure 60, in PSMs this parameter can identify where the heat transfer is taking place within localised

regions. This can then be used for isolating areas of thermal interaction between the solid and fluid, and the outer shell or containment area of the porous media being simulated.

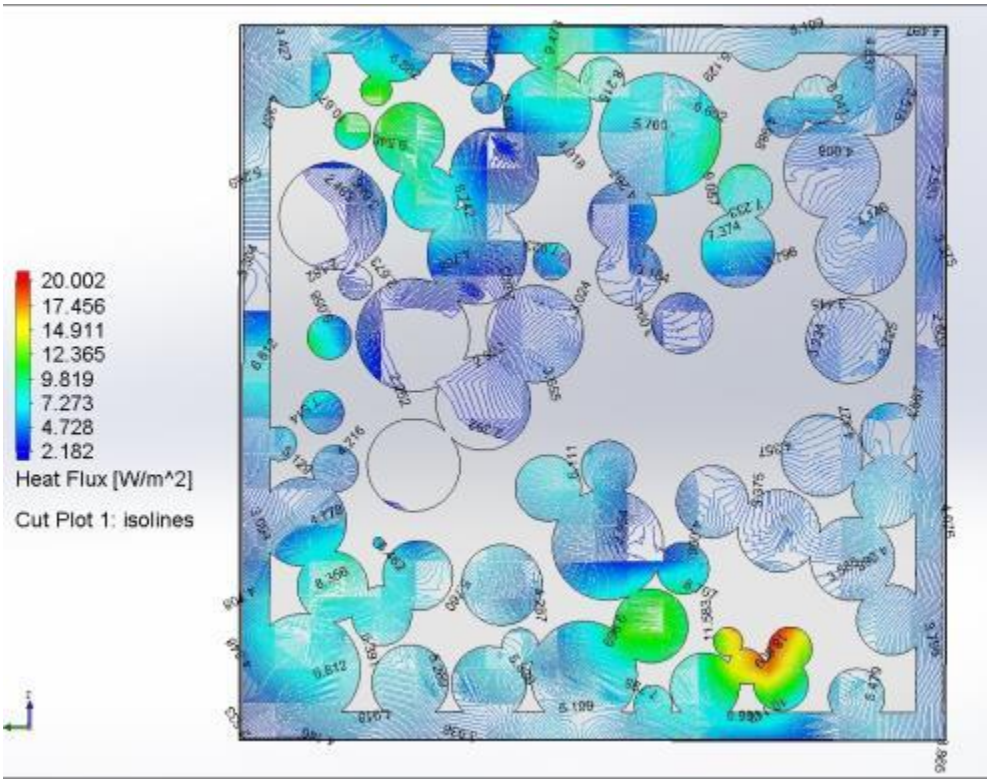

Figure 60: Heat flux contained within a transitional state PSM

3.7.8 Tortuosity within a PSM

The tortuosity, or the ratio between the actual distance travelled by a stream of fluid medium compared to the shortest distance, is a key parameter that has been examined in a theoretical way by many authors in the fluid mechanics field. From the results of these CFD analyses it is hypothesised that the tortuosity can be calculated by seeding the model with a set of sample virtual particles advected by the flow (as shown Chapter 7). The trajectories of these virtual particles can be graphically represented as vector strings and their lengths computed. If the flow field is correct within the PSM, then these calculations of the true lengths must also be correct

and reasonable estimates of tortuosity are obtainable. In Figure 61, a view from outside of a PSM is shown with such flow trajectories plotted. The redder the shade, the faster the flow is moving, and twisting and turning of the trajectories can be seen. In Figure 62, an example of flow trajectories converted into measurable strings is shown in an isometric 3D view of the same sample.

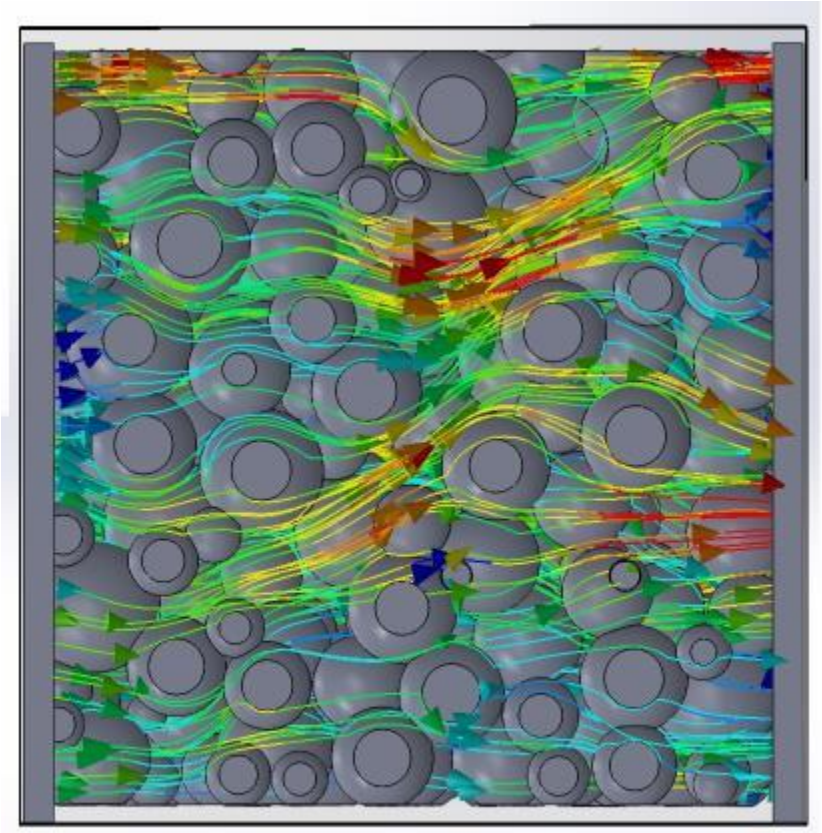

Figure 61: Flow trajectories of a seeded fluid domain as shown in one side section. These trajectories are then converted graphically into the measurable parameter of true length.

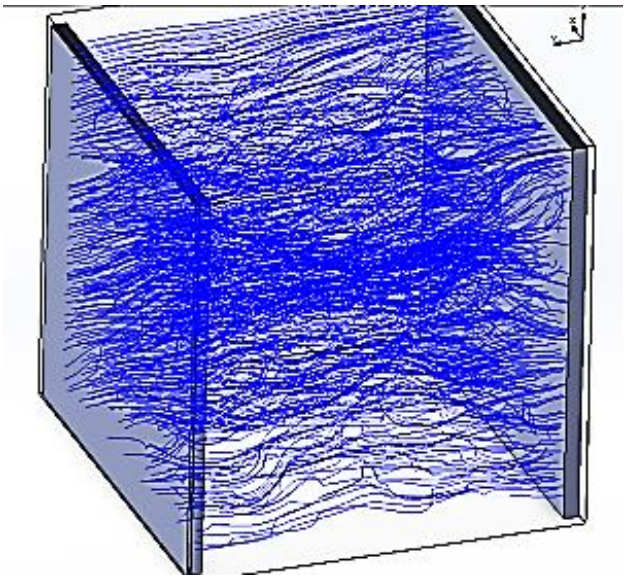

Figure 62: 3D graphic interpretation of the true lengths of airflow through the PSM

3.8 Equivalent continuum creation

The final base stage of the PSM method is to create an equivalent continuum model of the porous medium simulated with the PSM. Results of the multiple flow simulations with varying pressure differences across the specimen and flow rates are placed in the materials database of the Flow Simulation tool along with the physical characteristics of one PSM such as box size and length of the sample. Figure 63 shows how the equivalent continuum model derived from a given PSM is rendered. Computations with the equivalent continuum models are many times faster (in the magnitude from minutes to seconds, depending on the difference in internal complexity) than modelling the PSM themselves. Development of such 'equivalent continuum' models are needed in scaling studies, as described in Chapter 9.

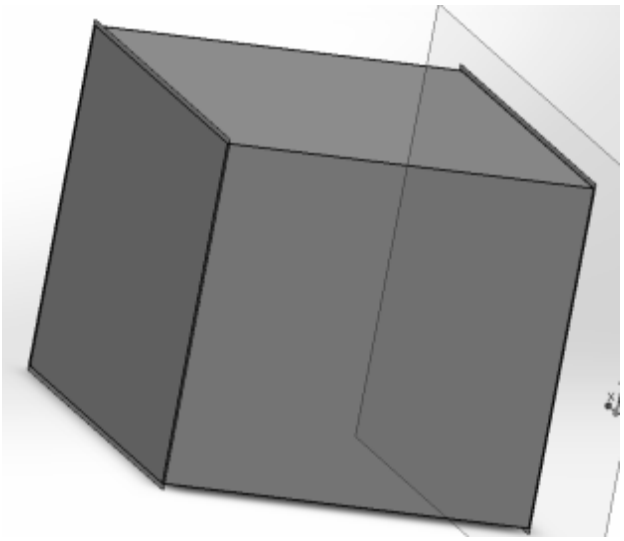

Figure 63: Equivalent continuum model representation of a box contained PSM

3.9 Application of the PSM to large porous media problems

Such a technique is useful in characterising the airflow and heat transfer behaviour of larger scale bodies of fragmented rock. For example, Figure 64 shows results of such a simulation of the NHEA at Creighton Mine that has relied on the technique to characterize airflow resistance set out in this chapter.

The NHEA application will be discussed in detail at the conclusion of this thesis. However, at this stage, it should be remembered that the equivalent continuum models of airflow resistance developed have relied entirely on the formulation of airflow physics embedded in the Flow Simulation tool, as well as the values of ancillary settings and property values prescribed. One cannot rely on the results of the CFD model in that analysis such as that illustrated in Figure 64, without first verifying that the physics of airflow in the CFD tool is appropriate and correct. This is why the verification experiments were conducted. Also, as the central topic of investigation in this thesis is the geometry of porous media and its effect on airflow resistance and heat

exchange, such a verification exercise must hold the specimen geometry as an experimental control. For natural geomaterials, obtaining this sort of control is extremely challenging. However, the PSM analogues of real geomaterials synthesized and 'tested' as explained in this chapter, due to their digital nature, have known geometry, and thus, their geometries can be held as experimental control variables as the airflow physics modelled in the CFD code is tested and verified. This will be explained in detail, in the next chapter. The 'link' of PSM analogues to real geomaterial geometries (subject to the simplification of spherical particles) is encapsulated in the known values for the Rosin Rammler distribution values, and the strength of this link will be tested subsequently too, in Chapter 6.

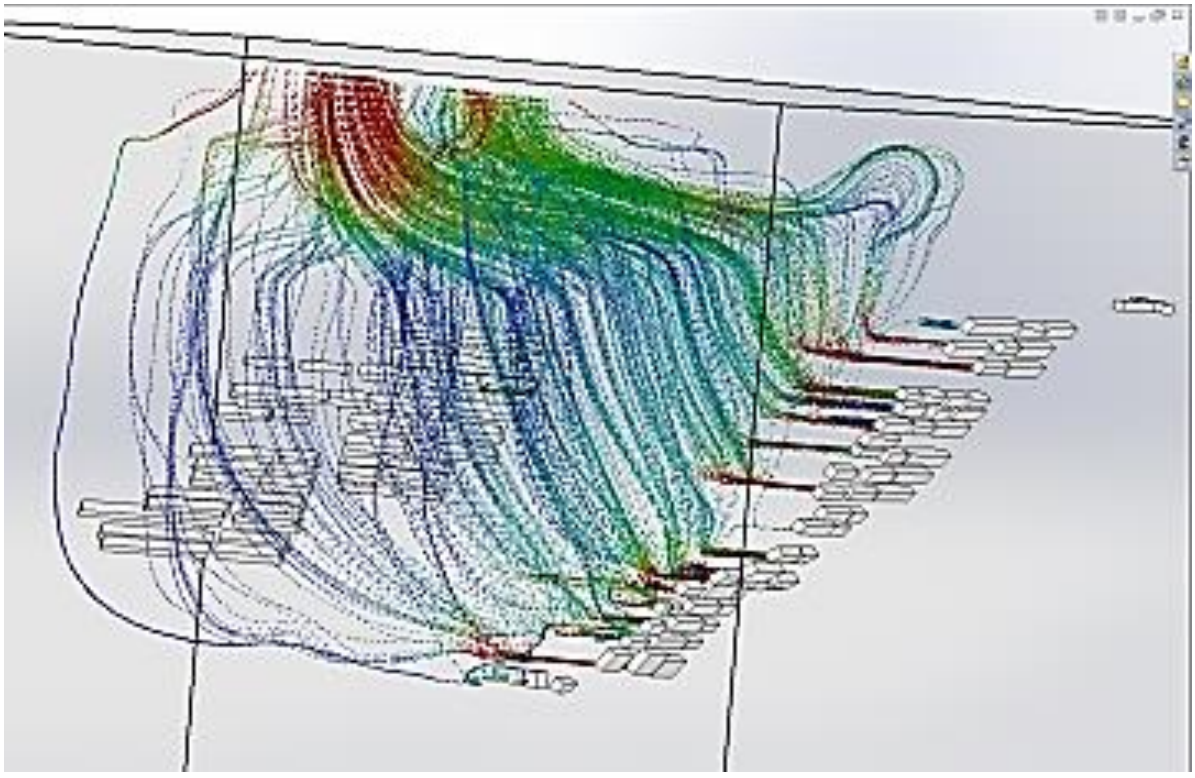

Figure 64: Thermal reservoir flow trajectories using an equivalent continuum model with resistance parameters derived from PSM. The scale of the model increased from centimeters to around 1km^3.

3.10 Discussion

This chapter has set out the process that has been developed by the author to create a PSM with known Rosin Rammler parameters and to establish estimates of the corresponding airflow resistance of the PSM analogue. First, the Rosin Rammler distribution was defined. Secondly, this distribution was rendered in the geomechanical particle flow code PFC3D; the individual size fractions of a pre-set Rosin Rammler distribution were generated directly. Geomechanical flow physics was applied to the generated spheres to consolidate the ensemble. Then, the 'consolidation' results were imported to the CAD/CAM software, which was also the environment for the Flow Simulation CFD tool, which enabled the ability for physical 3D model to be printed out in 1:1 scale, and assessed for fluid flow and thermal characteristics to later help verify the fluid flow code for this use. The most important parameters that are able to be obtained from the Flow Simulation software are the velocity and pressure fields, but particular problems may require some of the other capabilities such as temperature monitoring and heat transfer performance characteristics.

4 Experimental setup for physical PSM verification

4.1 Introduction

This verification experiment was performed to validate the use of CFD flow simulation codes for objects with complex and realistic geometries, in this case, the PSMs. While many experiments to validate the CFD tool have been performed, such as those reviewed in Section 2.8, there are numerous settings and parameter values that require verification before any results can be relied upon. For example, despite the geometry of PSMs being known, mesh generation may still affect CFD simulation results, and so these effects need to be assessed. The approach taken in this work was to physically manufacture PSMs rendered in the CAD/CAM environment and subjected to 'constant head' tests within the Flow Simulation environment, both described in the previous chapter. The PSM was manufactured, giving near perfect experimental control on the geometry. The specimen was then 'constant head' tested in a laboratory scale wind tunnel. Air resistance results were then compared with those of the CFD model.

The purpose of this experiment was to define the solid and fluid properties of a structure with known, but complex, geometry. The porosity, surface area, volume, circumference, and rubbing length (from Atkinson's) all are identical to those of the synthetic PSMs of the last chapter and are created by a 3D plotter at 1:1 scale. With good agreement on airflow resistance, CFD code or the CAD/CAM tool can be used to determine other properties from the digital solid, such as tortuosity, which can be very difficult to characterize in other ways. This chapter describes the design of a wind tunnel constant head pressure test variant used for physical verification of the CFD code.

Before 3D printing, while the centroid positions of the spheres were maintained, the diameters of the spheres were increased by 1% so that sphere contacts overlapped slightly, rather than being point contacts. This action was required so that the assemblage would not disaggregate when physically manufactured. Point contacts alone effectively would have zero tensile strength.

A limitation for the physical model was that its size could not exceed a volume envelope greater than 0.3m x 0.3m x 0.3m, as the 3D printer equipment used to manufacture prototypes cannot accommodate larger objects. Due to time and cost constraints, the selected dimensions of the extremities of the physical PSM sample were exactly 7.62cm x 7.62cm x 7.62cm. Within the CAD software, cutting planes were defined through the assemblage to trim it to these dimensions, prior to 3D printing, for all six bounding half planes.

At specific locations, 1mm diameter access ducts were formed within the digital assemblage, so that thermistors could be inserted in the manufactured object to measure temperatures of the solid portions of the spheres during testing (black ‘dot’ on CAD/CAM rendering shown in Figure 65). The CFD runs of the previous chapter were used to inform positioning of the thermistors where the temperature signal was predicted to be highest, for given initial conditions of temperature throughout the solid particles.

Figure 65: Rendering of the verification assemblage in the CAD/CAM software environment after constraints of printing size and thermal experiment preparation. Routes of insertion for one of the thermistors can be seen as a shadowed black circle. Width and height of the sample are both 7.62cm

4.2 Dimension SST 1200ES 3D printing

A Dimension 1200es (Dimension, 2013) 3D printer was used to manufacture the assemblage. This printer uses P430ABS plus material for the model material and SR-30 Soluble Support Technology (SST) or Breakaway Support Technology (BST) for the support material needed during the construction phase of the printing. The data file from the CAD/CAM environment (.SLDPRT format) was converted into Stereo Lithography format (.STL format) so the printer software could manufacture the object in the printing process. Each layer set down during the 3D printing process (as seen in Figure 66) was 0.254mm thick. For the complete object, the construction time was just over 36 hours. The fabricated PSM assembly, with its support material within the pore spaces, was then placed in a weak acidic bath, P400-SC, consisting of sodium carbonate, sodium hydroxide, sodium dodecyl sulphate, and sodiumsilicate, pentahydrate. This solution was maintained at 60°C, allowing for the support or fill material to

dissolve, leaving the assemblage structure fully constructed on a 1 : 1 scale as shown in Figure 67.

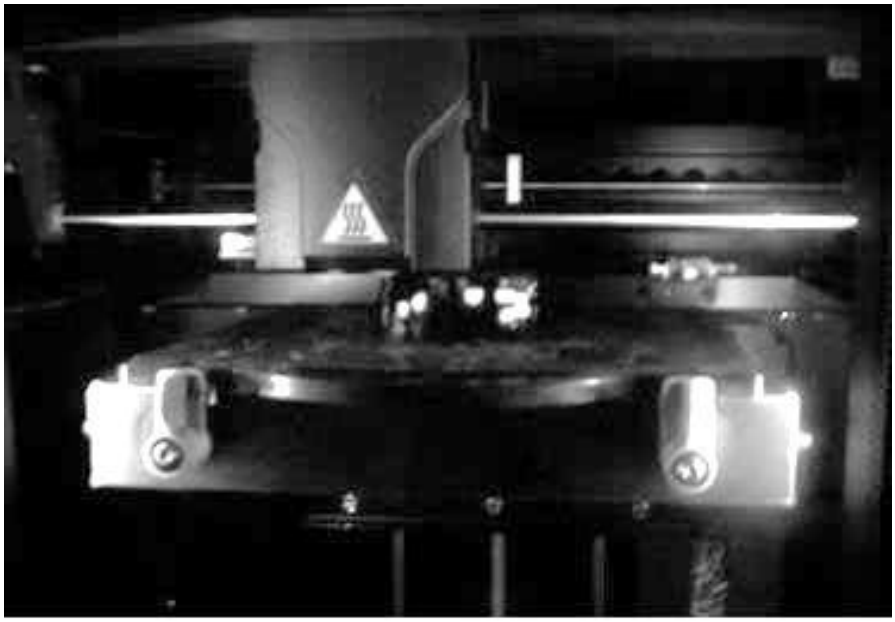

Figure 66: Assemblage being 3D printed. The light portions are the PSM spheres, the dark material is the filler which was washed away through a weak acidic bath.

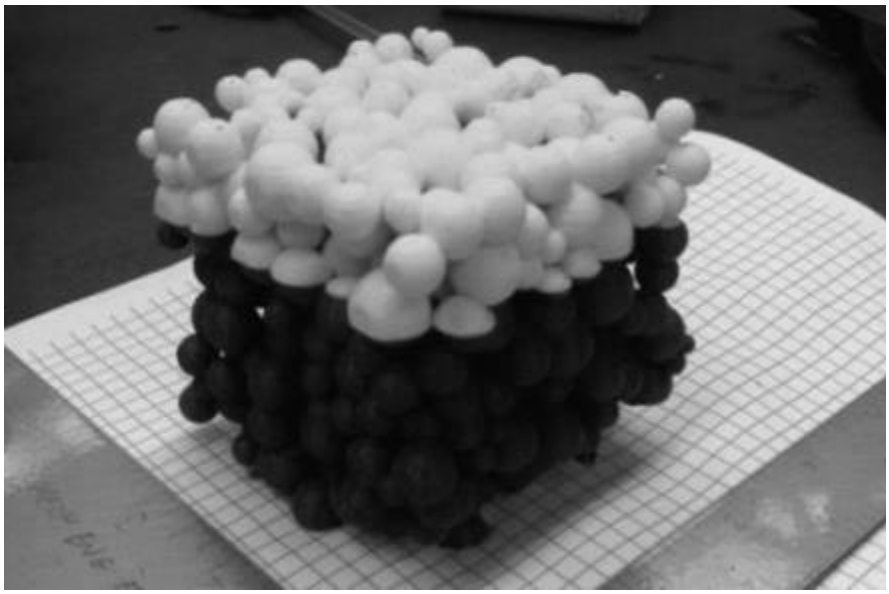

Figure 67: Completed PSM assemblage after manufacturing. Differences in color are due to two different coloured types of UBS430 plastic spools used during the printing process. The exact dimensions are 7.62 x 7.62 x 7.62cm or 3in.

A portion of the completed sample was examined under a 3D stereoscopic microscope to examine the relative roughness of the sphere surfaces of the sample after 3D printing. This was done to determine whether this roughness should be accounted for in analysis, as it could potentially influence airflow resistance results. The microscopy showed that each layer was printed approximately 0.25mm thick, as can be seen in Figure 68. The ruler in the image was marked at 1mm distances for scale. In the verification, this roughness did not seem to influence the results in a matter as such mesh conditions or how the containment box in the CFD model was created as examined later.

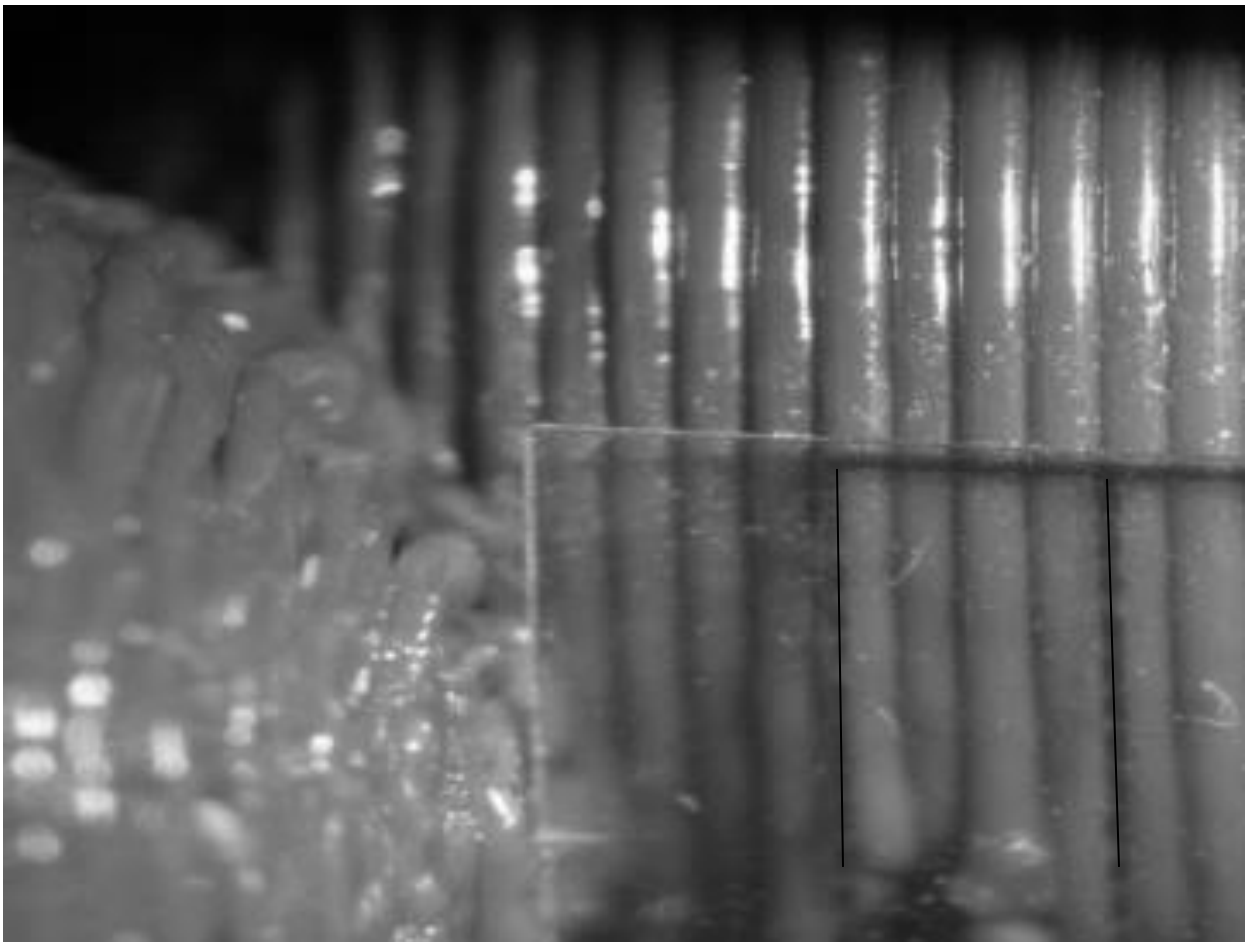

Figure 68: Sample under 3D stereoscopic microscope. The ruler is marked in 1mm increments. The resolution of the printing layers was 0.25 mm.

4.3 Experimental procedure

The intent of this verification experiment was to measure the pressure drop across and the flow rate passing through the sample. The conditions were the same as the wind tunnel simulation of a constant head test (Section 2.8) for defined settings of flow rate, set using a wind tunnel damper. This information was used to create a pressure vs flow rate curve that could be compared with the CFD model in a 1:1 scale fashion. To execute this, two methods of measuring the pressure difference were employed. The first used a micromanometer and the second used two high precision barometric standards. The flow rate was measured by an E.T.A 3000 hot wire anemometer at the centroid of the damper aperture. All equipment was calibrated within a week of experimentation and was not used until the experimental campaign. To operate the wind tunnel, various fan speeds were cycled through and allowed to settle for several minutes before the pressure and velocity observations were taken. Within the experiments, several of the speed settings were repeated to assess repeatability.

4.4 Experimental rig physical description

Components of the wind tunnel are the inlet, a uniform cross-sectional duct leading to converging and diverging ducts, the sample containment area and the outlet duct to the fan. The details of each duct are presented next.

4.4.1 Inlet and main duct

The first portion of the system is the inlet, which is composed of an aluminum diffuser that is 79cm in height and 38cm long (inner length) in the direction of airflow (Figure 69). There is then

an adjustable damper which can be set for volume flow rate control in combination with fan speed. This is the location where velocity readings were taken using the anemometer. Beyond the damper, a steel sectioned duct running a length of 800.5 cm with an approximately square profile of 38cm by 37cm leads to the specimen placement chamber.

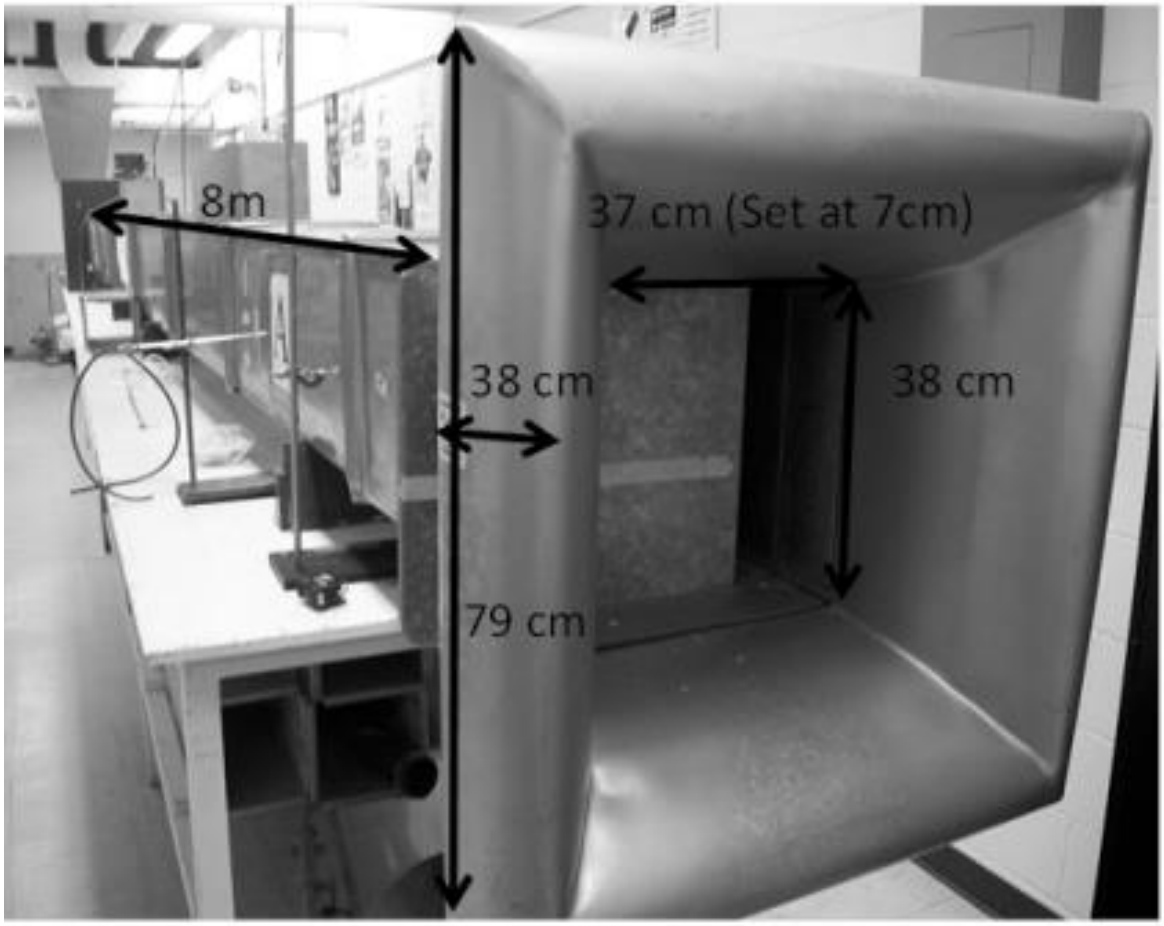

Figure 69: Experimental Rig inlet and damper

4.4.2 Diverging and converging ducts

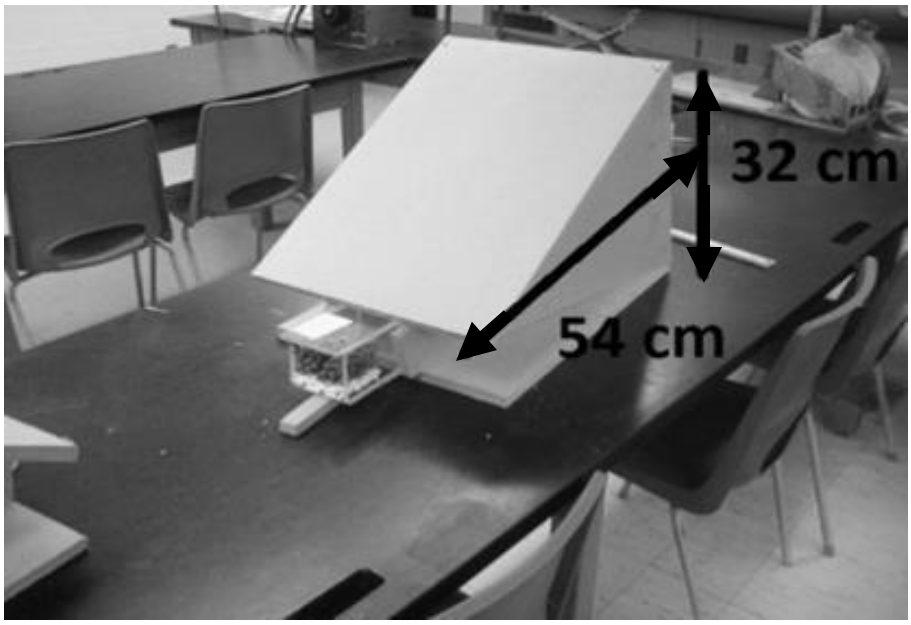

Figure 70: Converging duct before rig installation. The diverging duct is a mirror to the one shown above.

The converging and diverging ducts (Figure 70) were manufactured in plywood and mounted on both sides of the sample containment area. In Figure 71, the installed system is shown, with the addition of the acetate containing the PSM analogue and the pressure tappings.

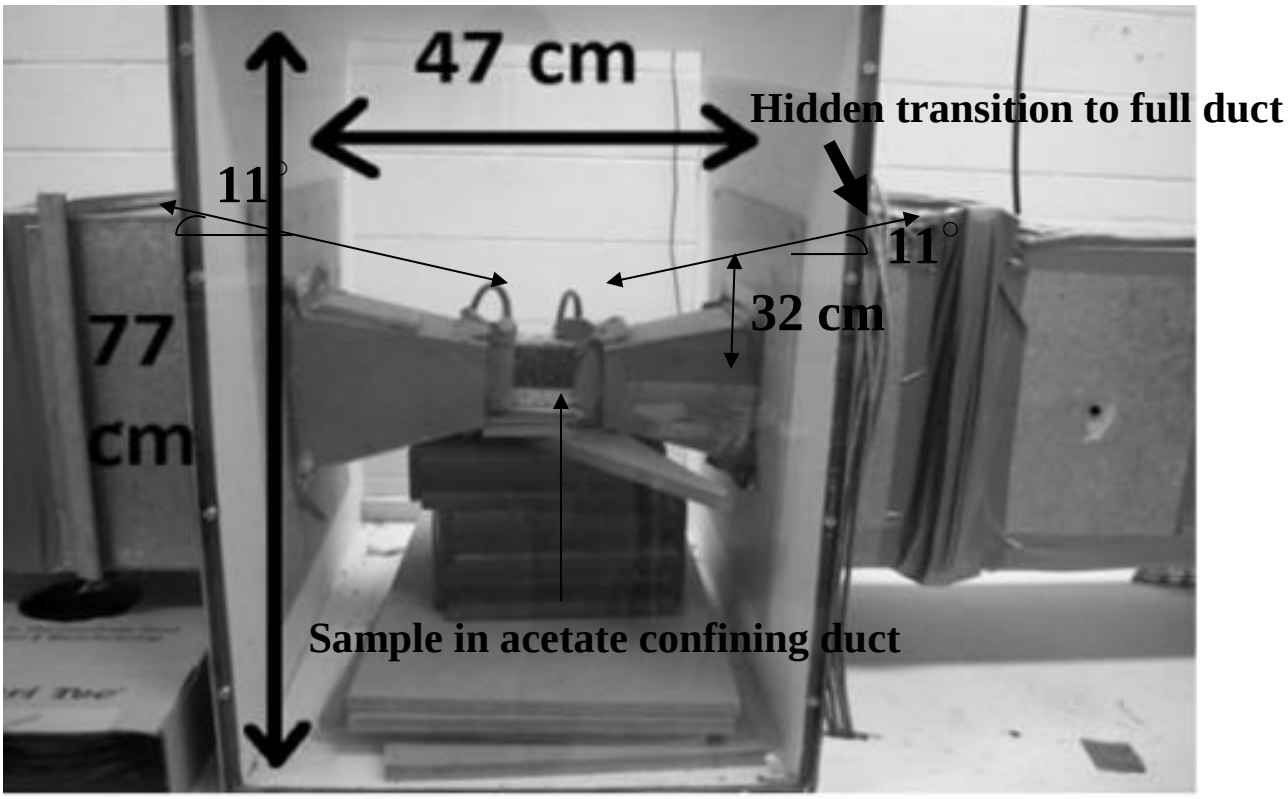

Figure 71: Installed converging and diverging ducts with sample

To reduce shock losses and minimize the introduction of turbulence, which can cause undesirable non-uniform flow at the entrance to the specimen sample, the angle of convergence of the transition duct was less than 12 degrees, as recommended by (McPherson, 2007).

4.4.3 Specimen containment section

The physical PSM was filled inside an acetate constructed box with an internal duct area of 7.62cm x 7.62cm (Figure 72) and length 10.1 cm long. This allowed for pressure tappings to be placed at locations within the duct with a uniform distribution, as was defined for the digital PSM constructed within the CFD environment. The static pressure tappings were placed across the specimen in the same locations as the CFD boundary conditions.

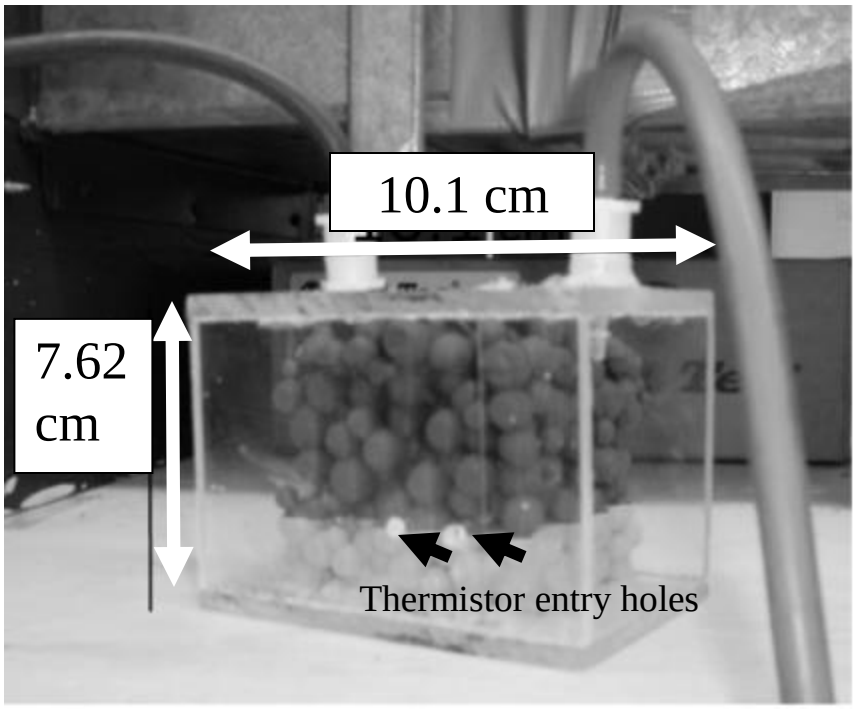

Figure 72: Sample containment duct. The holes in the perspex were for thermistor placement.

4.4.4 Post divergent duct to fan

The divergent duct takes the air back to the original 38cm by 37cm. There is then a short transitioning section (square to circle) of 40cm in length to the fan, as seen in Figure 73.

Figure 73: Post divergent duct to fan and evasee

4.5 Characterization of the wind tunnel before experimentation

The following is an analysis performed on the wind tunnel experiment using the combination of Bernoulli Equations and shock loss equations (McPherson, 2007). The analysis assumes that the flow rate Q remains constant throughout the tunnel, as well as being incompressible air. The Bernoulli results alone were not enough to verify the measured results from the experimental rig due to it only being the change of geometry, so the shock losses from the geometry changes also needed to be calculated. The procedures described in this section ensure that the velocity and pressure profiles in the duct system are well understood and characterized. Figure 74 shows a diagram of the wind tunnel apparatus with the 3 key points of geometry change within the system.

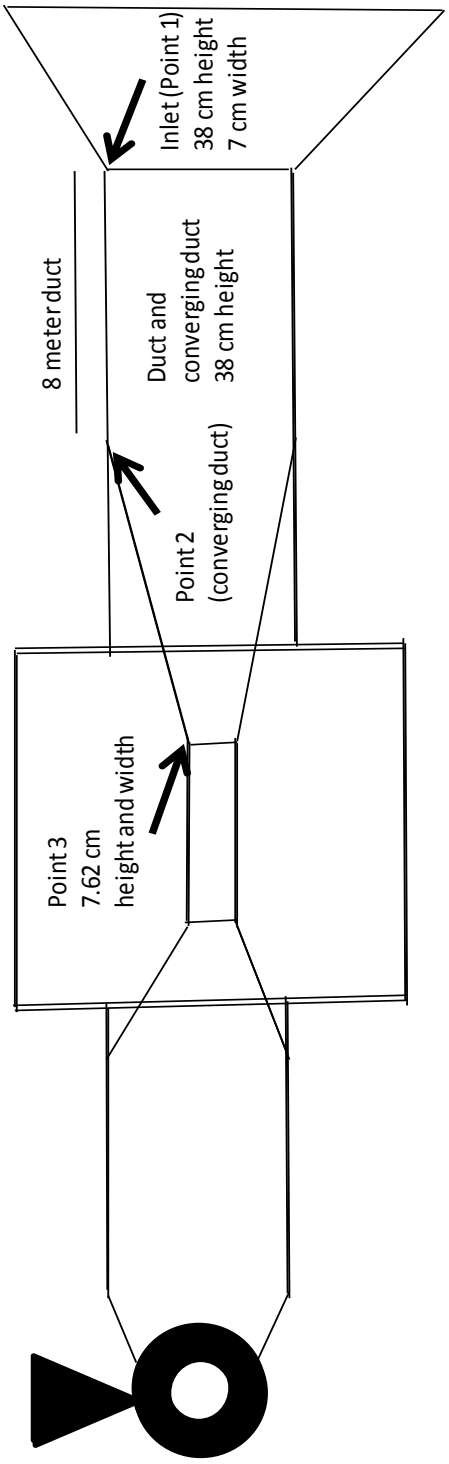

Figure 74: Diagram of the wind tunnel apparatus used in this experiment. The drawing is not to scale. A summary of the pressure loss characterisation is detailed below.

4.5.1 Part 1: Bernoulli total pressure evaluation (geometry change effects)

The flow rates for the duct and the sample were assumed to be constant throughout the experiment. The total pressure is constant throughout the wind tunnel.

The initial velocity pressure (VP) was calculated by the formula and the velocity was measured at the inlet to the wind tunnel:

$$P_v = \frac{1}{2}\rho \mathrm{V}^2 \tag{44}$$

The rig is level and there is no change in elevation along the rig, the Bernoulli equation is:

$$P_t = P_s + P_v \tag{45}$$

where:

$P_t =$ total pressure at a point in the wind tunnel (Pa)

$P_s =$ static pressure at a point in the wind tunnel (Pa)

$P_v =$ velocity pressure at a point in the wind tunnel (Pa)

The values for this calculation first begin by evaluating the static pressure, which is zero at the inlet, and measuring the velocity through the anemometer to calculate the velocity pressure. The total pressure can then be found from the relation above. Assuming continuity of the total pressure for the system, the new velocity and static pressures can then be calculated from the

geometry of the wind tunnel system. The velocities for the internal components are calculated at the points by taking the flow rate measured at the inlet and dividing them by the cross-sectional areas of the converging duct and the sample. The static pressure can then be found by taking the relationship between the total pressure and the velocity pressure. Table 1 shows the velocity and flow rate profiles at the different point locations. Table 2 shows the calculated static, velocity, and total pressures from the flow rate information.

Table 1: Velocity and flow rate at each of the evaluation point locations

Set Point	Inlet Area (m^2)	Point 1 Velocity (m/s)	Flow rate (m^3/s)	Duct Area (m^2)	Point 2 Velocity (m/s)	Flow rate (m^3/s)	Sample Area (m^2)	Point 3 Velocity (m/s)	Flow rate (m^3/s)
1	0.0228	0.2	0.0045	0.1406	0.0324	0.00456	0.0058	0.7853	0.00456
2		0.6	0.0136		0.0972	0.01368		2.3560	0.01368
3		1.02	0.0232		0.1654	0.02325		4.0052	0.02325
4		1.15	0.0262		0.1864	0.02622		4.5156	0.02622

Table 2: Static, velocity, and total pressure characteristics at each evaluated location

Set	Inlet		(Point 1)	Duct		(Point 2)	Sample		(Point 3)
Point	SP	VP	TP	TP	SP	VP	TP	SP	VP
1	0	0.024	0.024	0.024	0.023	0.000	0.024	-0.348	0.373
2	0	0.036	0.036	0.036	0.030	0.005	0.036	-3.322	3.358
3	0	0.312	0.312	0.312	0.295	0.016	0.312	-9.393	9.705
4	0	0.674	0.674	0.674	0.653	0.021	0.674	-11.662	12.336

Using the technique explained above, the static pressure loss between the inlet and sample during the set point 4 is 11.66Pa with a VP at the sample of 12.33Pa. This portion of the method used to characterize the wind tunnel was then compared with direct calculation of the Bernoulli equations between the inlet and the sample. The first step uses the equations from point 1 to 2 to calculate the pressure difference seen in Table 3, while the same procedure from the converging duct to the sample containment box is seen in Table 4.

The Bernoulli equation used for point to point pressure comparison is as follows:

$$\frac{V_1^2 - V_2^2}{2} + \frac{P_1 - P_2}{\rho} = 0 \tag{46}$$

By knowing the inlet velocity and pressure, the static pressure at point two can be calculated by either:

$$P_{sa} = \left(-1 * \left(\frac{V_1^2 - V_2^2}{2} * \rho\right)\right) - P_1 \tag{47}$$

Or in terms of loss from the change of geometry only, the change of pressure from point A to B:

$$P_{sb} = \left(\frac{V_1^2}{2}\right) * \left(1 - \frac{A_1^2}{A_2^2}\right) * \rho \tag{48}$$

Table 3: Inlet to duct pressure and velocity calculations using the Bernoulli equations

Inlet to Duct	(m/s)		(m/s)		(Pa)		A (Pa)	B (Pa)
V_1 =	0.2	V_2 =	0.03243	P_1 =	0	P_2 =	-0.024	0.024
	0.6		0.0973		0		-0.212	0.212
	1.02		0.16541		0		-0.613	0.613
	1.15		0.18649		0		-0.779	0.779

Table 4: Duct to sample pressure and velocity calculations using the Bernoulli equations

Duct to Sample	(m/s)		(m/s)		(Pa)		A (Pa)	B (Pa)
V2 =	0.032	V3 =	0.785	P2 =	0.023	P3 =	0.348	-0.372
	0.097		2.356		0.212		3.140	-3.352
	0.165		4.005		0.612		9.075	-9.689
	0.186		4.515		0.779		11.536	-12.32

To confirm the equation results in another form, a direct calculation from point 1 to point 3 was performed to test the consistency of the results as shown in Table 5.

Table 5: Direct point to point comparison from the inlet to the sample duct using the Bernoulli equations

Inlet to Sample Comparison	(m/s)		(m/s)		(Pa)		A (Pa)	B (Pa)
V1 =	0.2	V3 =	0.7853	P1 =	0	P3 =	-0.35	-0.35
	0.6		2.356		0		-3.14	-3.14
	1.02		4.0052		0		-9.08	-9.08
	1.15		4.5156		0		-11.54	-11.54

The results of this calculation show a slightly lower pressure loss of 11.53Pa from the wind tunnel inlet to the sample inlet. Since the shock losses are not calculated in this technique, method 2 of calculating the shock losses from McPherson (2007) need to be added to these pressure losses.

4.5.2 Part 2: Shock loss calculations

The following method uses the Bernoulli pressure differences resulting from the geometry previously calculated and then adds more shock loss from the technique of pressure loss across abrupt changes in a duct (McPherson, 2007). Once summed up, the total static pressure differences from the actual measurement and theory were all within 1.6Pa of the measured pressure loss from the micromanometer. In this method, 71% of the pressure loss was due to the converging duct, 4% from the damper, and the remaining 24% from the difference of geometry. The shock loss calculations and coefficients, from McPherson (2007), are shown in Table 6 from change from atmosphere to the inlet.

Table 6: Shock loss table from the damper to the duct

Change in pressure = X ρ (V^2) $X = (1/cc^2)(A_1/A_2)^2 - 1$ $cc = .48*sqrt(A_2/A_1)+.6$	Values for coefficient	Pressure loss (Pa) Shock Losses (Inlet - Damper) for the different set points
A1 =	0.1406	0.06
A2 =	0.0228	0.56
CC =	0.6100	1.64
X =	99.4923	2.09

In Table 7, the shock loss calculations and coefficients are shown between the inlet and the converging duct portion of the wind tunnel.

Table 7: Shock loss table from the converging duct to sample

Delta P = X ρ (v^2) X = $(1/cc^2)(A_1/A_2)^2 - 1$ cc = .48*sqrt(A_2/A_1)+.6	Values for coefficient	Pressure loss (Pa) Shock Losses (Inlet – Converging Duct) for the different set points
A1 =	0.1406	1.03
A2 =	0.00580644	9.29
CC =	0.600549643	26.86
X1 =	1622.974184	34.14

4.5.3 Characterisation of pressure loss in the wind tunnel experiment

In Table 8, the complete pressure characterisation of the wind tunnel experiment is shown. In this table, the shock calculation is shown, as well as the addition of the Bernoulli change of geometry effect. In general, the results turned out as expected, with the largest error being 2 Pa, which is due to the high velocities and resistance of the total system. The largest losses occurred in the converging duct sections, within the experimental set-up, which were at 71% of the pressure lost in the system. The natural change of geometry from the Bernoulli equations came up as 24% of the total losses of the system. Since the overall error in the measured to calculated pressures were low, it is assumed that this combination method fairly characterized the wind tunnel experimental rig.

Table 8: Total pressure loss table from the inlet to sample

Totals: (Pa)				
Shock Losses (inlet – damper) (Pa)	Shock Losses (Convergent duct to sample) (Pa)	Bernoulli (change of geometry) (Pa)	Total Pressure loss (calculated) (Pa)	Total measured pressure loss (Pa)
0.06 0.56 1.64 2.09	1.03 9.29 26.86 34.14	0.35 3.14 9.08 11.54	1.44 13.00 37.58 47.77	1 11 36 47
4.38%	71.47%	24.15%	% of total static pressure loss	

4.6 Instrumentation

The following section contains details of the equipment used in the two phases of the experiment (one using the micromanometer for pressure sample, while the second phase used the barometer standard). Each was calibrated the week before the experiment.

4.6.1 E.T.A 3000 hot wire anemometer

This anemometer was made by Airflow Industrial and is shown in Figure 75. This hotwire anemometer has the ability to measure up to 15 m/s or 3000 ft/min. The ranges of scale are 0-0.5 m/s, 0.5-1.0 m/s, 1.0-5.0 m/s, 5.0-10.0 m/s, 10.0-15.0m/s respectively. This anemometer was

placed at the inlet of the wind tunnel and sampling was performed for the various speed settings of the fan.

Figure 75: Airflow Industrial's E.T.A 3000 hot wire anemometer

4.6.2 Paroscientific Model 745-16B Barometric Standard

Figure 76: Paroscientific 746-16B pressure standard (Paroscientific, 2013)

Two precision barometer standards (Figure 76) were used in this experiment. They have RS-232 ports for high data logging purposes using Digiquartz software (Paroscientific, 2012). The sampling frequency within this experiment was 0.5 seconds. It has a 0.0001% resolution and

0.008% full scale accuracy according to the manufacturer calibration certification. The precision of readings provided by the instrument is 0.1 Pascal.

The manufacture's specifications for the pressure characteristics of the barometer are as follows:

19 absolute pressure ranges of 0-15 psia (0.1 MPa) to 0-40000 psia (276 MPa) with 6 gauge pressure ranges of 0-15 psig (0.1 MPa) to 0-200 psig (1.38 MPa)

4.6.3 Model 8705 DP-CALCTM Micromanometer

A TSI-made micromanometer (Figure 77) was used in the first two runs of the experiment to measure pressure across the sample. It has the following technical characteristics (TSI, 2012):

Pressure: Range: -5 to +15 in. H_2O (-1245 to 3735 Pa, -9.3 to 28.0 mm Hg)

Accuracy: 1% of reading ± 0.005 in. H2O (±1 Pa, ±0.01 mm Hg)

Resolution: 0.0005 in. H_2O (0.1 Pa, 0.001 mm Hg)

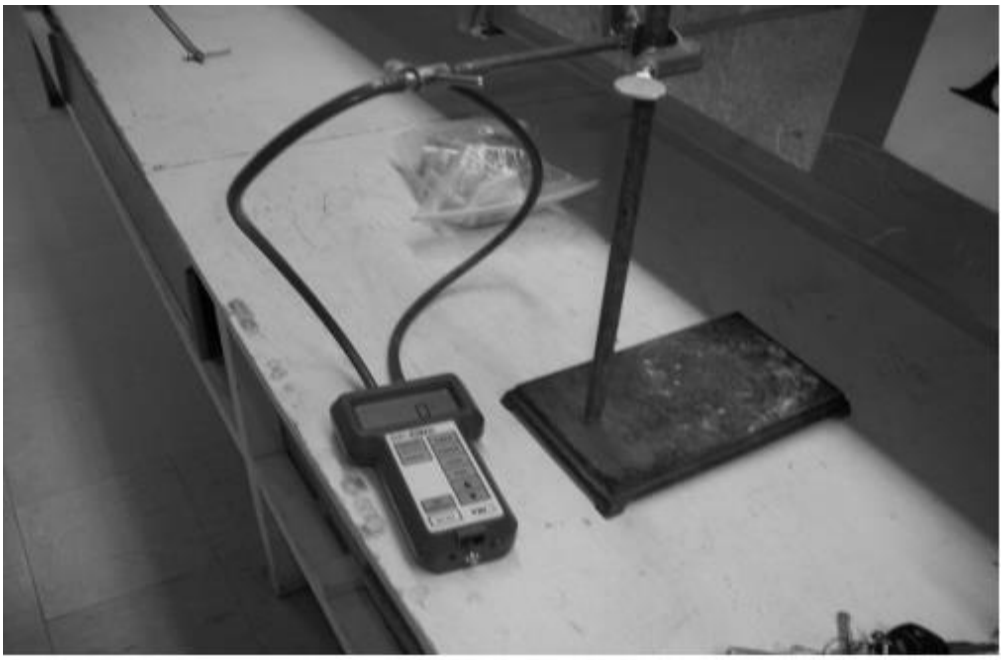

Figure 77: TSI 8705 Micromanometer used in experimentation

4.6.4 Fan and variable speed controls

The fan used in this experiment is a Buffalo Forge limit load centrifugal fan size 245 (Figure 78). This is a fan with a belted transition to an electric motor. The power supply set to a variable control box (TSP 130 Inverter) to act as a variable speed control (Figure 79). In this experiment the lowest fan speed was 517.5 rpm and the highest was 2398 rpm.

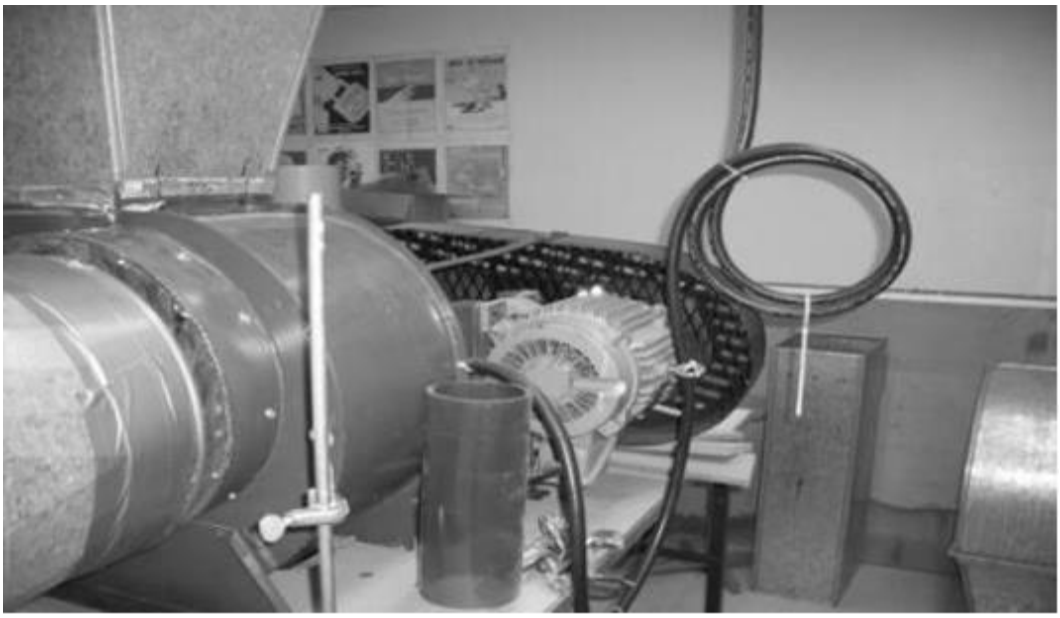

Figure 78: Buffalo Load fan belt transmission

Figure 79: Fan motor speed and power controls

4.7 Summary

This experimental section provided details of PSM manufacture and of the experimental rig used to verify PSM airflow resistance. The wind tunnel tests mimicked a constant head pressure test typically used for hydraulic conductivity determinations. These modifications included custom inlet and outlet ducts that were placed into the wind tunnel to match the exact sample containment box size, which was then identical for both the physical PSM and the digital PSM used in the CFD environment. The flow rate could then be measured at the inlet aperture and the pressure drop was measured across the sample via pressure tappings. A characterisation of the pressure profile across the entire inlet system of the rig was performed to ensure that all of the behaviour of the rig was well understood and so reliable observations would be taken with the specimen under test.

5 Airflow performance comparison

5.1 Experimental airflow resistance curve

5.1.1 Objectives

The objective of this experiment was to obtain airflow resistance data from a physical PSM so that these results could be compared with those from CFD simulations of the corresponding digital PSM. In mine ventilation studies, airflow resistance for an airflow branch (tunnel) normally follows $\Delta P = RQ^2$. Here, a relation of identical form is assumed, so that the resistance of the PSM can also be represented with an Atkinson resistance. Irrespective of whether this approximation holds, the pressure loss vs flow rate data remain comparable with PSM airflow resistance from the CFD simulations.

5.1.2 Experimental procedure

In total, five distinct experimental runs determining the airflow resistance curve were determined on the same PSM. The first two airflow resistance curves used the micromanometer for the pressure drop measurement across the sample. The fan speeds were varied in increasing levels and velocities were measured. The initial damper opening set at the inlet was 6cm and the height of the damper aperture is 38.5cm. The flow rate $\frac{m^3}{s}$ was found by taking the product of the velocity ($\frac{m}{s}$) measured at the centroid of the damper aperture and the aperture area set. Paroscientific barometers were used to monitor and log the pressures on each side of the PSM at a sampling rate of 0.5 seconds per sample for the last three experimental runs. The damper aperture was set at 6.0cm for the third test and then at 7.0cm for the fourth and fifth tests. The

two barometers collected data at 0.5s intervals but some data processing needed to be done before the airflow resistance curves could be prepared.

The data correction was needed to synchronize the timestamps of the data taken. While the barometer logger clocks were synchronised and started at times close to each other, the timestamps recorded were not synchronized. Re-sampling of the curve at ½ of the timestep (0.25s) was done to completely synchronize the datasets. It was done in this fashion to not alias the curves. As well as time monitoring corrections, there were also slight calibration differences between the barometers that affected the pressure measurements. The zero offset between the barometers was established through a sampling period of at least 3 to 10 minutes with zero flow rate when the fan was turned off. Natural peaks in the dataset made it possible to match the inlet and outlet barometers together in time during the no flow conditions.

The absolute pressure data from the barometers, now corrected, was then differenced to find the true pressure drop across the sample. The pressure difference data naturally fluctuated around a constant at the various fan set points. The average value of the pressure drop across the sample for each fan setting was thus used in the preparation of the resistance curves.

5.1.3 Manometer experimental test results

The experimental data for the first two experiments to determine the airflow resistance curve of the PSM, which were conducted with the manometer, are shown in Tables 9 and 10. In the first test, four fan set points were used to develop the resistance curve. This was increased to six set points for experiment 2.

Table 9: Results from first airflow resistance curve determination

Pressure Test 1				
Fan Rate (Set point)	Pressure Drop (Pa)	Velocity (m/s)	Area (inlet) m^2	Flow rate m^3/s
10.8 (1)	42	0.25	0.0231	0.0058
30 (2)	331	0.75	0.0231	0.0173
50 (3)	904	1	0.0231	0.0231
59.8 (4)	1309	1.2	0.0231	0.0277

Table 10: Results from second airflow resistance curve determination

Pressure Test 2				
Fan Rate (Set point)	Pressure Drop (Pa)	Velocity (m/s)	Area (inlet) m^2	Flow rate m^3/s
10.8 (1)	42	0.25	0.0231	0.0057
16 (2)	94	0.32	0.0231	0.0073
20 (3)	148	0.45	0.0231	0.0103
25 (4)	226	0.6	0.0231	0.0139
30 (5)	329	0.72	0.0231	0.0166
50 (6)	903	1	0.0231	0.0231

The procedures to determine the barometer experimental pressure and time corrections are illustrated in detail below, for airflow resistance determination. Experiment 4 and 5 are summarized in tabular format. The re-sampled and zero offset corrected inlet and outlet pressures were first plotted as shown in Figure 80.

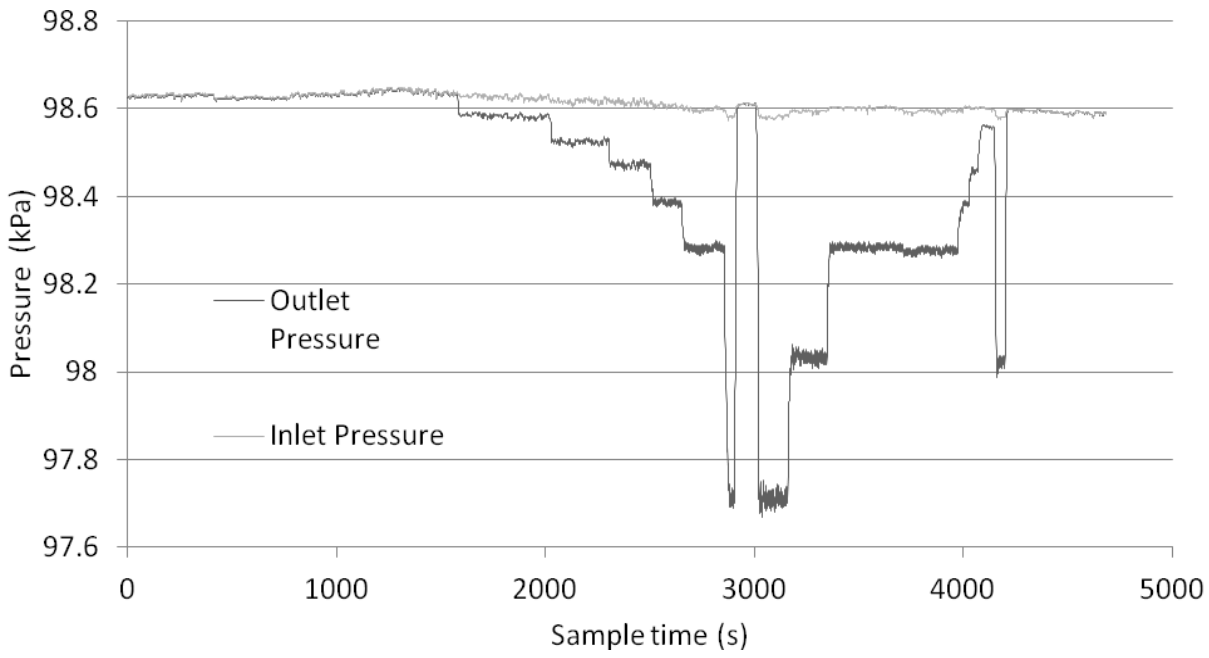

Figure 80: Airflow resistance curve determination 3 re-sampled pressure data. Fan set point setting changes can be seen in the various plateaus. At sample 3000 (1500 seconds) the fan was shut down and then restarted as part of a repeatability check. The slightly larger variations of pressure at the highest fan setting (and lowest absolute pressure) may be associated with vibration of the fan casing and the duct system that was noticed during the experiment. Close examination of the plateaus demonstrate that the apparent variability is not noise but a result of complex behaviour within the sample.

The re-sampled curve was then used to calculate the time synchronized pressure drops across the sample (Figure 81). Most of the fluctuations due to vibration disappear at this stage and show that in general, there is a consistent and constant pressure drop across the sample. A reasonable resistance could now be calculated since this is a geometric parameter and should not change very much at any flow rate that could be tested.

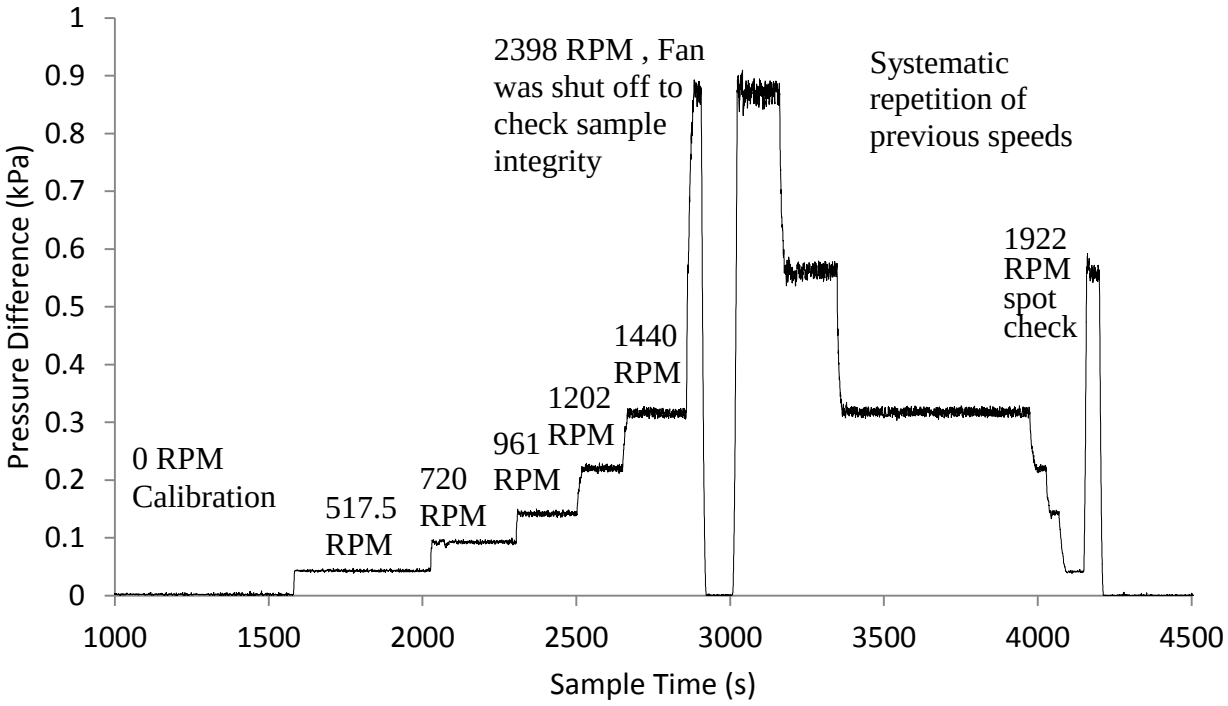

Figure 81: Pressure differences across the sample from the re-sampled and zero offset corrected data. The plateaus here show a good consistency when the difference of the two curves is shown. The seven plateaus for the pressure differences are the points used in pressure vs flow rate curves.

The summary of the determinations 3 to 5 are shown in Table 11.

Table 11: Summary of the three barometer experimental results

Fan Speed (RPM)	Pressure test 3		Pressure test 4		Pressure test 5	
	Q (m^3/s)	Average dP (Pa)	Q (m^3/s)	Average dP (Pa)	Q (m^3/s)	Average dP (Pa)
517.5	0.0057	44	0.0052	40	0.0052	45
720	0.0086	94	0.0083	77	0.0065	80.6
961	0.0115	142	0.0091	139	0.0091	144
1202	0.0138	217	0.0125	221.5	0.0104	222
1440	0.0150	309	0.0143	322	0.0143	321
1674			0.0170	427	0.0170	431
1922	0.0190	564	0.0188	557	0.0196	570
2165			0.0222	707	0.0214	720
2398	0.0231	865	0.0248	880	0.0248	889
2636			0.0274	1065	0.0261	1070
2860			0.0287	1272	0.0274	1270
3102					0.0314	1500

These data, together with those in Tables 9 and 10 can be compared to the results from testing the same PSM, in digital form.

5.2 CFD simulation of the verification model

The central purpose of manufacturing a prototype assemblage for physical testing in the wind tunnel was to verify whether or not results returned by the CFD code matched physical observations, for an object with a large degree of geometric complexity but the same geometry. This being the case, investigations on the geometric factors controlling airflow and heat transfer in similar assemblages of particles could be conducted more cheaply and rapidly with the CFD tool. Consequently, the next stage in the verification process was to conduct CFD simulations of the laboratory wind tunnel tests. The following are details specific to the CFD assemblage simulation configuration used to compare with those tests.

5.2.1 Model conditions

Flow simulation conditions – The CFD solver was configured to converge on a steady-state solution for a defined pressure differences across the sample. The CFD code uses a finite volume method for solving the Navier-Stokes equations for the convergence to a steady-state solution. For this mode of the solver, any transient behaviour observable during solution is not physically meaningful. In the simulations, the volume flow rate of air relaxes to the defined pressure difference and consequently, the flow rates constitute the principal variable used for comparison with the experimental results.

Simulation of physical boundaries – A duct structure was constructed around the assemblage to directly simulate the perspex duct of the physical experiment. The duct boundaries, where pressure was prescribed, were placed in the same locations of the CFD model as the pressure tappings of the physical model.

Boundary conditions – Pressures at inlet and outlet were assigned on planes across the duct corresponding to the locations of the pressure tappings. Velocities at solid-fluid interfaces are set at zero (non-slip) by the code. The default thermal conditions at the inlet were set to room temperature, and were considered adiabatic walls with zero roughness. Internal (non-initial condition pressure or velocity) walls also had zero roughness and were adiabatic ideal walls. Flow conditions at the inlet were assumed to be uniform, fully developed flow profiles.

Solution of model – The average length of time for a solution to the CFD simulation corresponding to a specific fan set point was 2 hrs. In these simulations, 8000 finite volume cells were used with 228 of them being fluid only cells, 222 being purely solid cells, and 7550 of the cells being partial cells (both solid and fluid properties). The flow rate values observed from the simulation at a steady state are averages computed across area of the inlet pressure boundary condition.

5.2.2 Results

The CFD PSM results are summarized in Table 12. Each test run exhibits coherence of behaviour of the assemblage in its resistance to airflow; the data consistently lie on or near a

curve determined to be, not unexpectedly, of parabolic form. The results of the CFD simulations of the wind tunnel experiments exhibit consistency with experimental results.

The fact that the correlation co-efficient of this curve is 1.00 suggests that the simulation experimental data lie on a unique curve. The co-efficient in front of the quadratic term is huge relative to that of the linear term, and thus the linear term could be neglected entirely. The resulting equation of $\Delta P = RQ^2$ where R = 1572787 Ns^2m^{-8} (computed using the excel function LINEST) of the CFD data is thus directly analogous to the Atkinson's equation which has only been applied to airway ducts. The value of airflow resistance is several orders of magnitude higher than would be typical of an airway duct in a mine ventilation network, although such comparisons are hard to establish because values of *R* are known to depend on length, cross-sectional area normal to the flow as well as surface frictional resistance.

Figure 82 presents the experimental results from the wind tunnel with the CFD simulation results. As the experimental results do not precisely agree with those from the CFD simulations, it is supposed that the variance evident must arise from random and other error associated with the experimental procedures (the numerical results were self-consistent). Examination of potential sources of experimental error suggested that the precision of wind tunnel velocity observations was the most likely source. Variations in atmospheric pressure, wind tunnel room temperature, and humidity will have an effect on the density of the air passing through the specimen, which could also contribute to the variance between experimental and simulated results for each test run as the experimental test runs were each conducted on different days.

Table 12: CFD results summary. The resistance value when fitted to a square function is 1572787 Ns^2m^{-8}

CFD Results	Q (m^3/s)	dP (Pascals)
(0.1s Timestep)	0.0024	9.979
	0.0035	19.98
	0.0051	42.17
	0.0079	99.979
	0.0093	140.855
	0.0137	299.987
	0.0142	320.813
	0.0225	799.970
	0.0228	829.279
	0.0252	1000
	0.0276	1199.996
	0.0298	1400

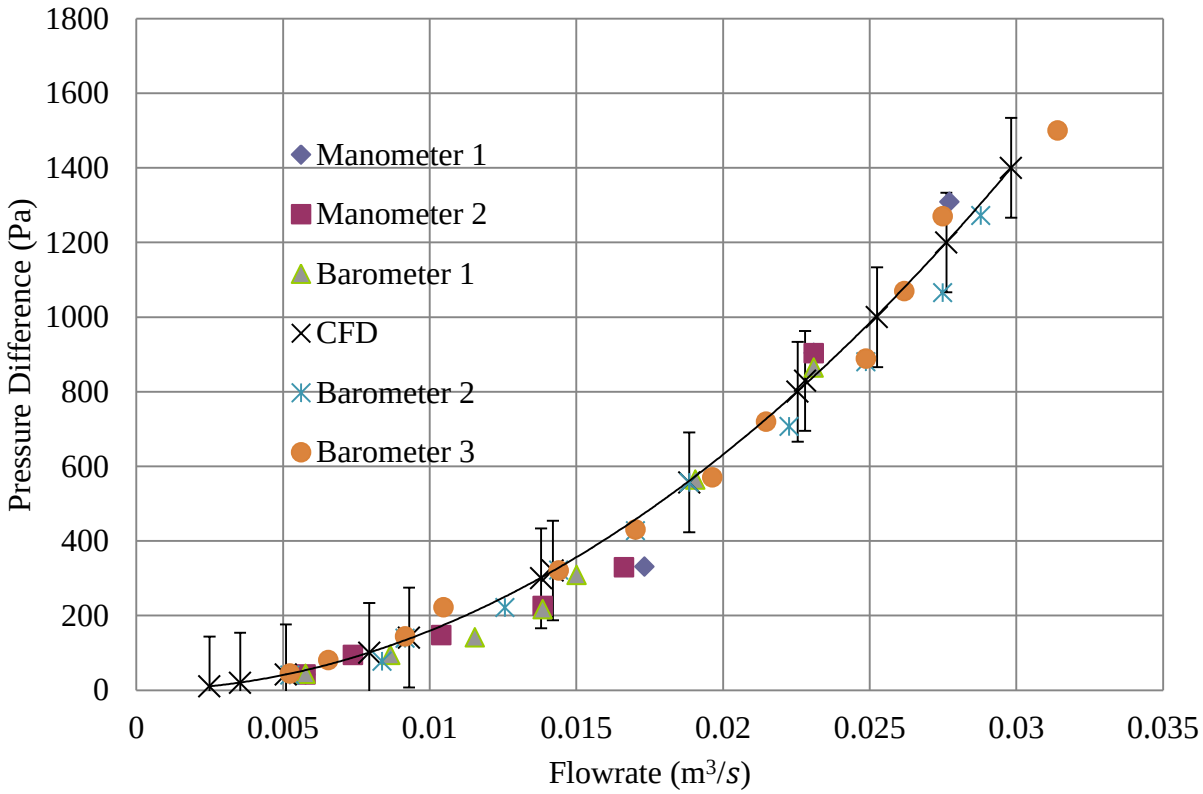

Figure 82: Pressure difference vs flow rate curves for all wind tunnel experiments and CFD simulations on the same PSM. The correlation coefficient for the CFD models is always 1 for all of the CFD results. This shows a squared law relation such as in ventilation airway resistance curves, even though the sample under test had a complex porous structure. The standard error of the CFD simulations are the error bars in Figure 89.

5.3 Resistance curve results: discussion and conclusion

The airflow resistance characteristics of each of the five sets of experimental test results exhibit a good consistency with each other and the CFD code simulations. This shows that predicted values made with the CFD code can be verified with the experimental results. The various measurements were most sensitive to the velocity readings by the hot-wire anemometer. The comparison of the CFD to the physical experiment results reveals a good agreement between the two. The standard error of the CFD code is plotted as the error bars on Figure 82 and all of the experimental results fit within the bands created. The main consideration for error is that the physical experiment has noise and experimental limits on the equipment used, while the CFD environment is a noiseless one and uninfluenced by outside sources. The results show that predicted performance of a PSM with CFD can be verified with experimental data.
The results of the CFD and experimental airflow resistance curve determination suggest:

1. That PSMs qualitatively exhibit the same airflow resistance behaviour as ventilation ducts, although they have a much higher Atkinson resistance.
2. That if the geometry of a porous particle assemblage is known, as it is with a synthesized PSM, the airflow resistance characteristics of that assemblage may be conveniently assessed using a computational fluid dynamics simulation of a ‘constant head’ test instead of requiring, or additionally requiring, a physical experiment.
3. In a methodology for determining the resistance of PSMs, only 1 CFD simulation is necessary.

These are important results that provide a foundation for the remaining work presented in this thesis. The correspondence of the PSM resistance to an Atkinson resistance leads to many questions, for example:

Can the Atkinson resistance for a PSM be ‘broken down’ in the same manner as those for air ducts? If so, can the CAD/CAM tools be used to legitimately interrogate the digital PSM geometry to obtain values for the cross-sectional area, perimeter, and lengths to establish the friction factor, *k*, as an intrinsic property of the PSM?

Can PSM Atkinson resistances be considered in series and parallel combinations, as duct Atkinson resistances can be, to consider large scale porous fragmented rock ensembles?
The work remaining to be reported in this thesis will provide answers to these questions, as well as additional results based on the fundamental results in this chapter.

6 CFD mesh sensitivity and repeatability to the Rosin Rammler distribution

6.1 Introduction

Within this chapter, an assessment of five different PSMs with the same Rosin Rammler distribution parameters will be tested to see how the pressure and flow rate characteristics change due to the consolidation process and the variation of initial ball spatial locations. This means that the same number of spheres, 500 in this case, will be consolidated in five different ways and then tested through the flow simulation tool to see whether the air flow resistance characteristics are the same or different. The question of whether the CFD results lead to the same airflow resistance curves with varying instances of synthetic ensembles that share the same Rosin Rammler distribution were then examined. This section uses a containment volume that is the same for each case. The CFD experiments were conducted in the same way as the previous chapter by having a pressure boundary across the sample and having the CFD code calculating the flow rate corresponding to that pressure drop. Also, a comparison of the fineness or coarseness of the CFD solver mesh structure was performed to compare the relative differences of the flow rates calculated by the five Rosin Rammler PSMs tested. Coarser meshing would be preferred, for computational speed, if there was convergence in the resulting airflow resistance curves.

6.2 Rosin Rammler parameters

The base Rosin Rammler parameters used were a specific diameter D_h = 0.006m and a value of n = 1.771. The Rosin Rammler distribution results used for the creation of spheres in the particle flow code are shown in Table 13.

Table 13: Rosin Rammler distribution used in the repeated consolidation process by diameter size and total mass bins

Mass Coarse	Retained	Particle % 1.90	Cumulative	# Spheres	From (Integer)	To (Integer)
0.001	0.981	98.09	0.0190	9.5	492	501
0.002	0.926	92.58	0.0550	27.5	464	491
0.004	0.735	73.49	0.1909	95.4	369	463
0.006	0.5	50.00	0.2348	117.4	252	368
0.008	0.292	29.17	0.2083	104.1	148	251
0.01	0.146	14.58	0.1458	72.9	75	147
0.012	0.063	6.25	0.0833	41.6	33	74
0.014	0.023	2.29	0.0395	19.7	13	32
0.016	0.007	0.72	0.0157	7.8	5	12
0.018	0.002	0.19	0.0052	2.6	2	4
0.02	.0005	0.04	0.0015	0.7	0	1

The numbers of balls actually generated by PFC pre-consolidation were verified during the importing process into the CAD/CAM program and are shown below in Table 14 and in the histogram of Figure 83. The information on sphere diameters and three dimensional locations of the sphere centroids were gathered through a spreadsheet application that served as a more straightforward method of conversion into the CAD/CAM environment.

Table 14: Number of spheres actually generated in PFC using the generate command

Bin	Frequency	Cumulative %
0.001	0	0.00%
0.002	9	1.80%
0.004	28	7.40%
0.006	95	26.40%
0.008	117	49.80%
0.01	104	70.60%
0.012	73	85.20%
0.014	42	93.60%
0.016	20	97.60%
0.018	8	99.20%
0.02	4	100.00%
More	0	100.00%

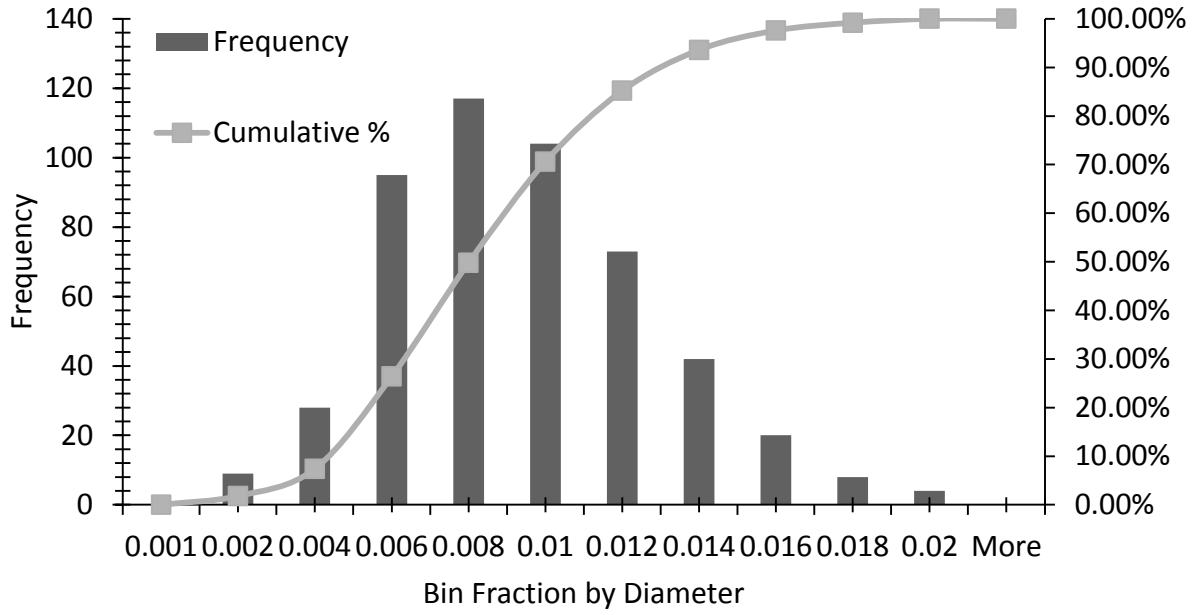

Figure 83: Histogram of the number of spheres generated in PFC pre-consolidation but double checked during the importing process

6.3 PFC Parameters used in consolidation simulation

The PFC consolidation parameters presented in Table 15 were used with the generated spheres to run the particle flow code. The geomechanical properties of stiffness, friction factor and density were all taken from the PFC 3D manual case study example of operation of the software. All the PFC models in this thesis use these default parameters except for the size of the containment boxes.

Table 15: List of PFC parameters and functions used during the consolidation simulation component of the particle flow code

PFC Parameters
Stiffness Properties (Walls) - normal and shear stiffness are assigned 10^8 N/m
wall id=1 kn=1e8 ks=1e8
wall id=2 kn=1e8 ks=1e8
wall id=3 kn=1e8 ks=1e8
wall id=4 kn=1e8 ks=1e8
wall id=5 kn=1e8 ks=1e8
wall id=6 kn=1e8 ks=1e8

Stiffness Properties (Balls)
Density of the balls = 2000 kg/m3
prop density 2000 kn 1e8 ks 1e8

Gravitational acceleration vector of 9.81 m/s^2
set grav 0 0 -9.81

Friction Coefficient (Balls)
prop fric 1.0

Box Parameters
wall id=1 face (0, 0, 0) (.0762, 0, 0) (.0762, 0 -.1) (0, 0,-.1)
wall id=2 face (0, 0, 0) (0, 0,-.1) (0, .0762,-.1) (0, .0762, 0)
wall id=3 face (.0762, 0,-.1) (.0762, 0, 0) (.0762, .0762, 0) (.0762, .0762,-.1)
wall id=4 face (.0762, .0762,-.1) (.0762, .0762, 0) (0, .0762, 0) (0, .0762,-.1)
wall id=5 face (0, 0,-.1) (.0762, 0,-.1) (.0762, .0762,-.1) (0, .0762,-.1)
wall id=6 face (0, 0, 0) (0, .0762, 0) (.0762, .0762, 0) (.0762, 0, 0)

6.3.1 Mesh density criterion

Two mesh conditions were used to compare the consolidated models in the CFD code. The CFD code meshing has density levels ranging from 0 to 10. The coarse mesh in this chapter is level 3 (minimum number of cells that the flow tool recommends) in the fluid flow code, while the fine mesh used level 8 (maximum number of cells). The mesh counts are shown in Table 16.

Table 16: Number of mesh cells used in all five models

	Coarse Mesh			
PSM	Total	Fluid	Solid	Partial
1	9579	288	621	8670
2	9579	292	607	8680
3	9593	278	600	8715
4	9579	234	630	8715
5	9593	219	644	8730

	Fine Mesh			
PSM	Total	Fluid	Solid	Partial
1	16681	41033	28839	96938
2	16721	40446	31792	94978
3	15213	35964	26930	89239
4	15559	37003	26873	91722
5	16686	39218	32062	95586

As can be seen in Table 16, the clear difference between the two mesh levels is the amount of cells used to represent the geometry. The level 3 mesh has around 10 000 cells each for the models while the level 8 meshes have between 155,000 to 167,000 cells. Figure 84 shows the level 3 mesh PSM while Figure 85 shows the same model with a level 8 mesh.

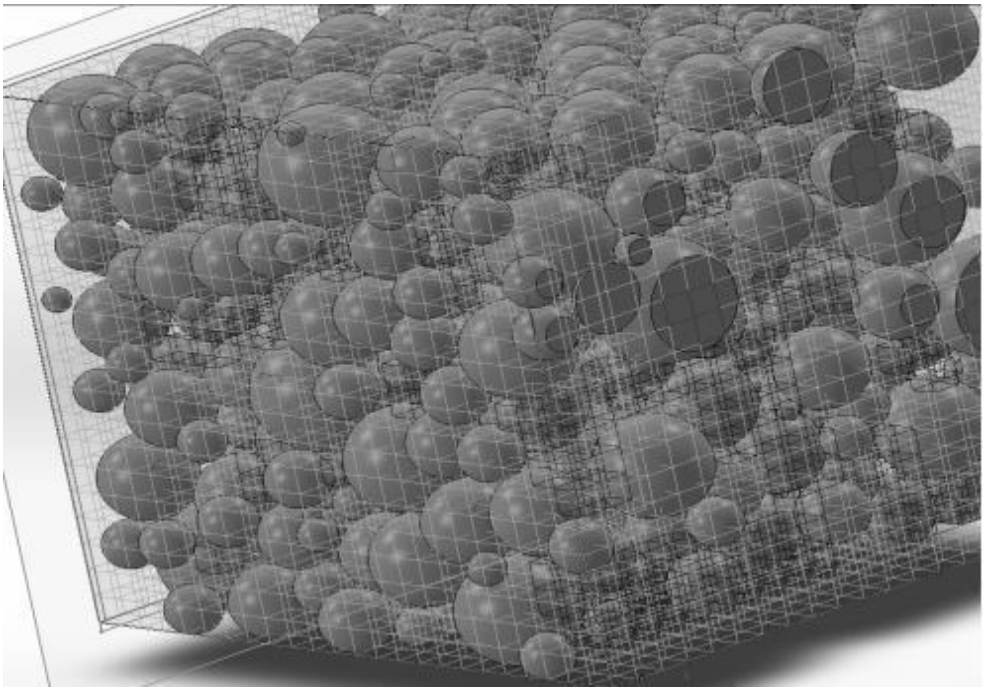

Figure 84: Image of the level 3 mesh of approximately 9579 cells for PSM #1

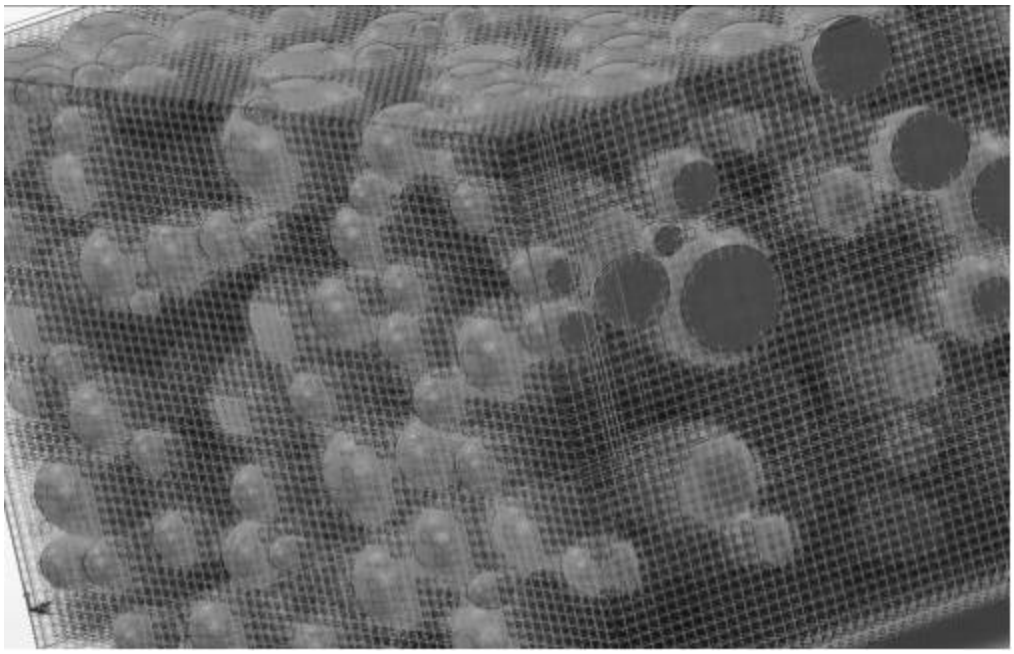

Figure 85: Image of the same model with level 8 mesh of 166810 cells for PSM #1

6.4 Containment area and geometric properties of the compared models

In the section below, the physical geometric properties were gathered during the geometric post-processing technique explained in more detail in Chapter 7. Each model had the same containment box volume as seen in Table 17.

Table 17: Dimension of the outside containment box sized used as internal simulation conditions

Height	Width	Length
74mm	74mm	88mm

Differences in the porosity were small and ranged between 50 to 51%. The 3D surface area (or true wetted area) variations are due to wall contacts of the individual models and show that the geometries are indeed the same as seen in Table 18.

Table 18: Geometric properties gathered during post processing

PSM	Volume mm^3	Volume Voids mm^3	Porosity	3D Surface Area mm^2
1	481888	245171.23	0.50877	154559.46
2	481888	247341.18	0.51328	154305.05
3	481888	246346.39	0.51121	153477.63
4	481888	245154.49	0.50874	154330.75
5	481888	245302.00	0.50904	154462.64

6.5 Flow rate results (Coarse mesh)

The flow results for the five models are summarized below. Results of the last chapter suggest that only one or two airflow simulations were required to characterize airflow resistance, as results of multiple dP vs Q tests produce a unique curve. Here, this suggestion is tested, but 3 dP settings are adopted to confirm the shape of the airflow resistance curve. In the discussion section, the direct comparisons as a ratio will be given to see the relative differences between the individual models. Table 19 contains the values of the flow rate results for the five models, while Table 20 contains the resistance calculation for each of the pressure drops tested using the LINEST function of Excel.

Table 19: Level 3 flow results for 3 different pressure drops

	Flow rates (m^3/s)					
	PSM #	1	2	3	4	5
Pressure	20	0.00388	0.00346	0.00392	0.00386	0.00375
Drop Across	500	0.01985	0.01858	0.02007	0.01972	0.01922
Sample (Pa)	1000	0.02824	0.02627	0.02833	0.02788	0.02719

Table 20: Level 3 resistance values for the various model configurations

PSM #	Resistance (Ns^2m^{-8})
1	1256894
2	1448957
3	1245044
4	1286377
5	1352833

The average value for the resistance was 1,318,021 (Ns^2m^{-8}) with a standard deviation of 84,291 and a co-variance of 0.063952. Figure 86 shows the resistance curves plotted against each other. The curve is a parabola in nature and appears to follow a square law.

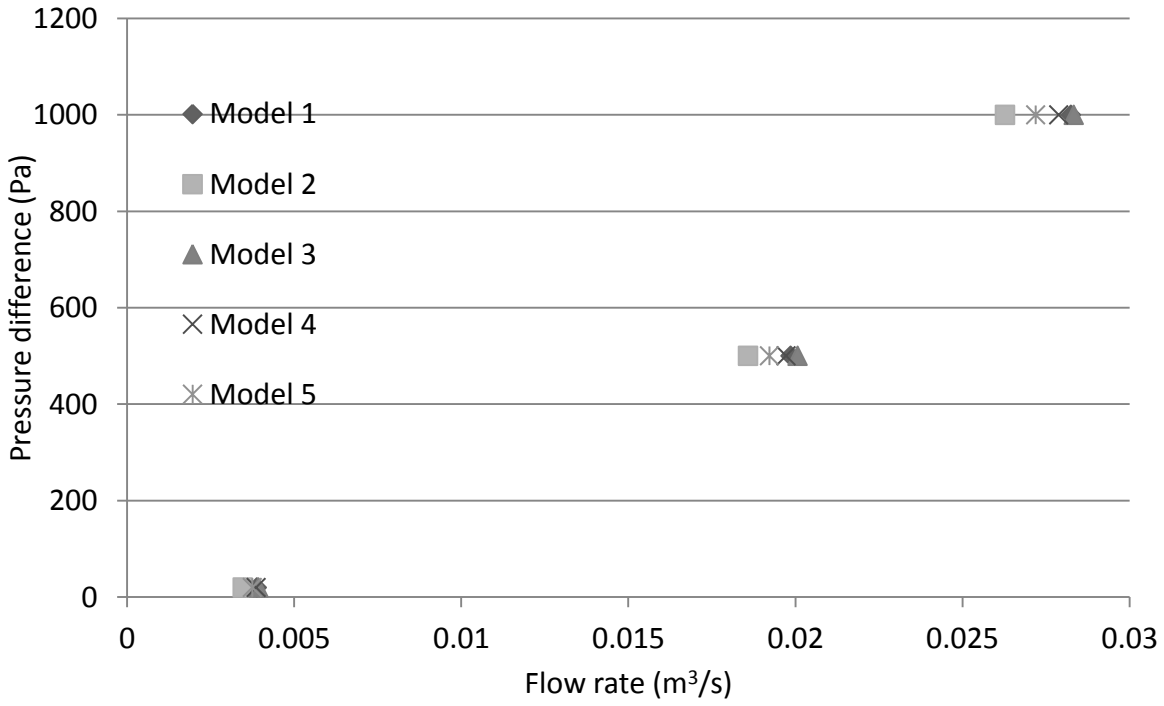

Figure 86: Level 3 Pressure difference vs Flow rate Curves. The range of resistance is 1.24 – 1.45 million Ns^2m^{-8}

6.6 Flow rate results (Fine mesh)

In this section, the flow and resistance results are presented for the Level 8 mesh settings for the same PSMs as the previous section. The flow rate results for the PSMs are in Table 21 while the resistance values are in Table 22.

Table 21: Flow rate results for the level 8 mesh

	Flow rates (m^3/s)					
	PSM #	1	2	3	4	5
Pressure Drop Across Sample (Pa)	20	0.00374	0.00362	0.00378	0.00371	0.00364
	500	0.02059	0.01914	0.02075	0.0204	0.02005
	1000	0.02914	0.02705	0.02937	0.02889	0.02837

Table 22: Level 8 resistance values

PSM #	Resistance (Ns^2m^{-8})
1	1178062
2	1366352
3	1159738
4	1198851
5	1242778

The average value for the resistance was 1,229,156 (Ns^2m^{-8}) with a standard deviation of 82,698 and a co-variance of 0.067281. Figure 87 shows the resistance curves plotted against each other. The curves again appear parabolic in nature and are assumed to follow a square law. The

resistance in this case was slightly lower than in the previous model, which is due to the wall conditions of the CFD models.

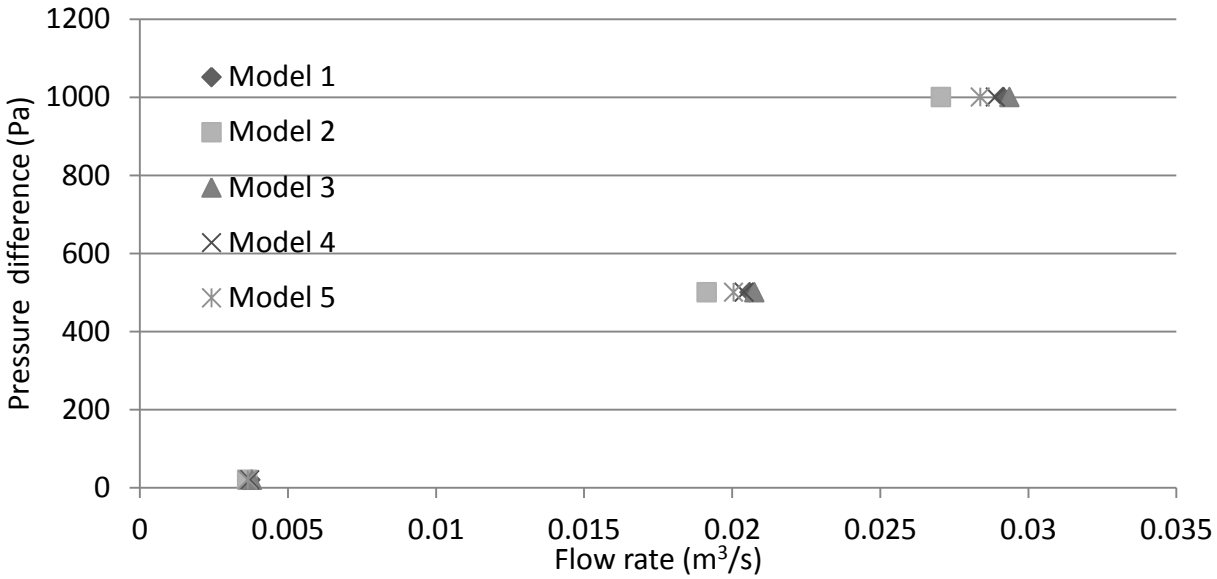

Figure 87: Level 8 Pressure difference vs Flow rate Curves. The range of resistance is 1.15 – 1.37 million Ns^2m^{-8}

6.7 Conclusions

In general for this synthetic CFD experiment of Rosin Rammler consolidated samples, the results for airflow turned out close at about a 4% difference. Overall, the results show that the level 8 mesh has a lower resistance than the level 3 mesh. This change of resistance is due to the difference between solid, partial, and fluid cells. The detail at the lower mesh level for PSM is slightly different on how it represents the outside contact between the walls and the particle flow code represented spheres. Since the partial cells have some properties of fluid, there is slightly less resistance due to the easier flow paths, as compared to truncated solid cells. In terms of relative differences of the flow rate between the samples at the same mesh level, the same ratios of airflow were generally maintained, but were closer together with the finer meshing. Less than

10% (7.2% average) differences were seen between the coarse and fine mesh setting for all five of the samples with the largest variation being sample number 5. The resistances ranged between 1.15 – 1.37 million Ns^2m^{-8} for the fine mesh and 1.24 – 1.45 million Ns^2m^{-8} for the coarse mesh. Taking this aside, this experiment set provides evidence that the parameters of airflow through porous media, if given the same surface area of particles inside, gives flow results that are very similar in nature even though the geometry of how that surface area is distributed is very different when on the same mesh density levels. The results of this study should be repeated in future work with other shaped particles besides spheres.

7 PSM derived estimates of Atkinson's resistance and friction factor

7.1 Introduction

Within this section, a methodology of analysis of PSMs will be given to produce values of Atkinson's resistance. The purpose of this chapter is to investigate what types of parameters can be obtained by geometrically 'dissecting' the PSM in the CAD/CAM environment. The primary target is the Atkinson's friction factor, but it is also important to establish whether other geometric parameters can be found. The components needed for this examination will be given in two parts. The first part is within the CFD tool for an evaluation of the property of tortuosity, while the second uses CAD methods within the CAD/CAM environment to dissect the exact wetted perimeter and cross sectional areas of the PSMs. By having this information, the hydraulic radius, hydraulic diameter and porosity can be calculated. Once all of this information has been gathered, a detailed assessments of the Atkinson's friction factor, k, can then be made.

7.2 Tortuosity

The tortuosity, or true rubbing length of airflow through a porous assemblage, is defined as the ratio of the true distance traveled by a particle compared to the direct or shortest line distance between the particle's starting and termination point, in this case, the length of the sample. The CFD code permits virtual particles to be tracked so that their flow trajectory lengths can be numerically gathered. For the study, a set of 1000 trajectory lengths were computed so that the assemblage tortuosity could be estimated from a large sample size. This set was partitioned into sub-sets with varying cardinality (10 subsets with cardinality 100, 5 subsets with cardinality 200, 2 subsets with cardinality 500, etc.) and the average trajectory length was computed for each

sub-set. This procedure was used to investigate the number of trajectory samples that would be needed to produce an estimate of the average tortuosity, with acceptable level of estimation variance. The PSM used to illustrate the methodology in this investigation is the verification model used in the wind tunnel experiments, as seen in Figure 88.

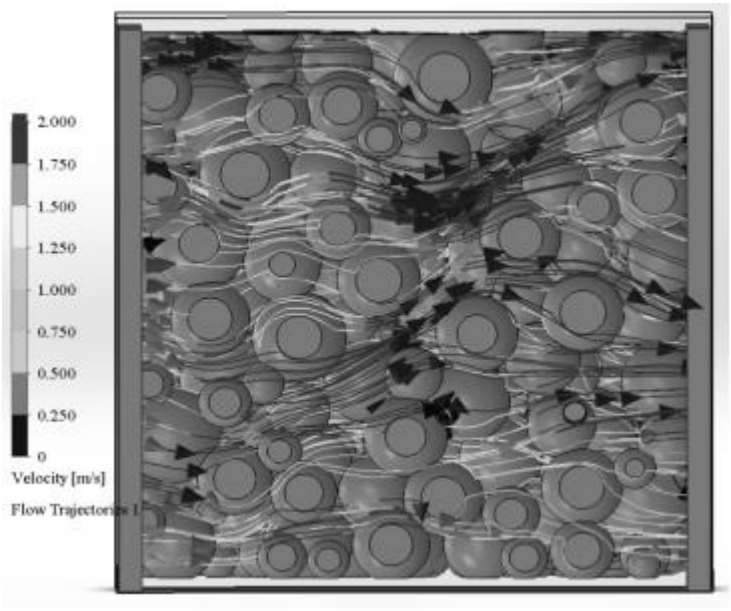

Figure 88: Flow trajectories of the velocity within the verified PSM in the CFD environment. Flow paths are coloured with the velocity at each point on the line. This rendering is the equivalent of the 1202 RPM speed setting of the wind tunnel.

To measure the tortuosity, the flow trajectories from the simulation were converted into graphical strings within the CAD/CAM environment. These graphical strings could then be used to measure the exact lengths of the sampled flow paths. An image of 1000 converted strings is shown for the PSM in Figure 89.

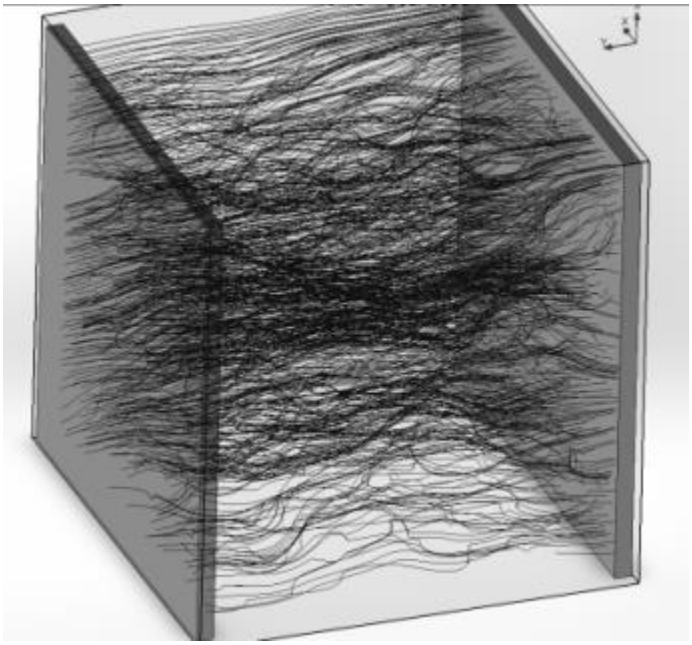

Figure 89: The same flow trajectories converted to graphic strings in the CAD/CAM environment. The length across the sample is 7.27cm.

In Table 23, the results of the tortuosity experiment are presented. The length of the containment box was 72.74mm and therefore the tortuosity is the string length measured divided by this reference length. The sample set cardinalities ranged from 1 to 1000 (which actually reduced to 993 sample trajectories due to how they were created by sampling along the inlet boundary layer) and the range of tortuosity determined was from 1.00 - 1.20.

Table 23: Sample trajectory lengths and tortuosity ratios

Sample Length (mm) 72.75	# of sample trajectories taken	Total Length (mm)	Average Length (mm)	Average Tortuosity
	1.00	81.37	81.37	1.12
	5.00	430.38	86.08	1.18
	10.00	869.53	86.95	1.20
	49.00	4063.88	82.94	1.14
	50.00	3788.93	75.78	1.04
	99.00	7214.37	72.87	1.00
	98.00	7191.63	73.38	1.01
	100.00	7797.06	77.97	1.07
	99.00	7266.29	73.40	1.01
	99.00	7427.66	75.03	1.03
	99.00	7260.08	73.33	1.01
	100.00	7401.76	74.02	1.02
	100.00	7803.59	78.04	1.07
	103.00	7551.33	73.31	1.01
	104.00	8782.03	84.44	1.16
	190.00	13905.28	73.19	1.01
	190.00	13960.03	73.47	1.01
	190.00	13957.44	73.46	1.01
	200.00	14595.09	72.98	1.00
	201.00	17205.13	85.60	1.18
	500.00	39419.87	78.84	1.08
	507.00	42102.36	83.04	1.14
	993.00	82387.37	82.97	1.14

In Figure 90, the tortuosity vs the number of samples shows that as the sample numbers are increasing, the tortuosity value approaches a bulk value of 1.14 for the sample.

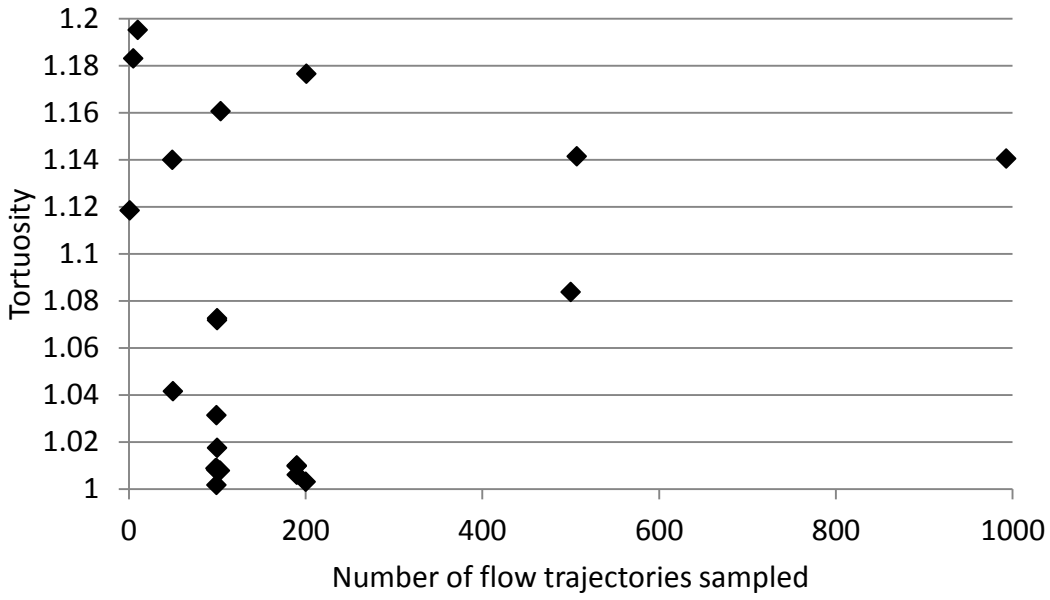

Figure 90: Average tortuosity value compared with the number of flow trajectories sampled. As the number of trajectories sampled increased, the values of the tortuosity ratio appear to converge on a value of 1.14.

7.3 Geometric dissection analysis of the PSM

The digital PSM, at this stage, can be used to establish the 'low level' geometric parameters, specifically: cross sectional area and perimeters along any direction of flow. The process of this 'dissection' is first to invert the fluid and solid domains in the model. Following this, a program created for measuring the graphic interfaces of the model was used to obtain values for the cross-sectional area and the perimeter of each section. An image of the program in use is shown in Figure 91.

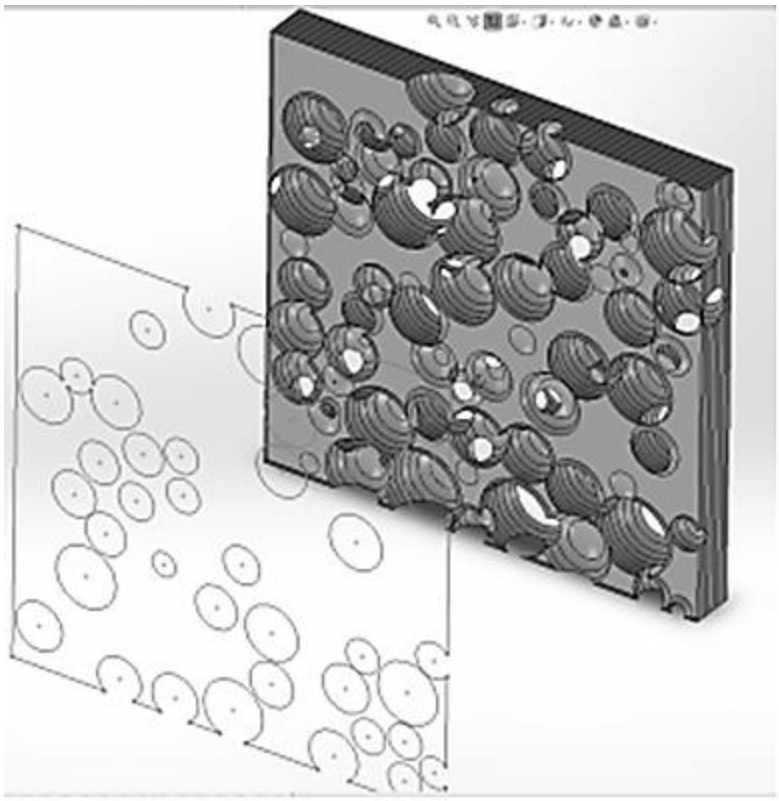

Figure 91: Inverted section of the PSM and the graphical interpretation. Measured values of cross-sectional area available for flow and perimeter can be obtained through created numerical algorithms.

7.4 Sectional geometric properties assessed by PSM interrogation

There are several physical characteristics that can be gathered from the CFD model to help extend the understanding and characterization of airflow behaviour through real assemblages of rock particles. Geometric values that can be gathered from the model include the cross sectional area available for flow, the wetted or perimeter length, the flow path length through the assemblage, the hydraulic radius and effective hydraulic diameter as well as bulk properties such as void ratio or porosity.

A plot of cross sectional area available for flow and wetted length versus section number, as seen in Figure 92, indicates that although there is clearly some variability in these quantities, values of 1.389m for the wetted length and 2680 mm^2 for the cross-sectional area available for flow may be provisionally assumed for the assemblage. The high fluid areas at both edges of the curve are due to airspace between the sample and the boundary walls; spheres have point contacts with the walls.

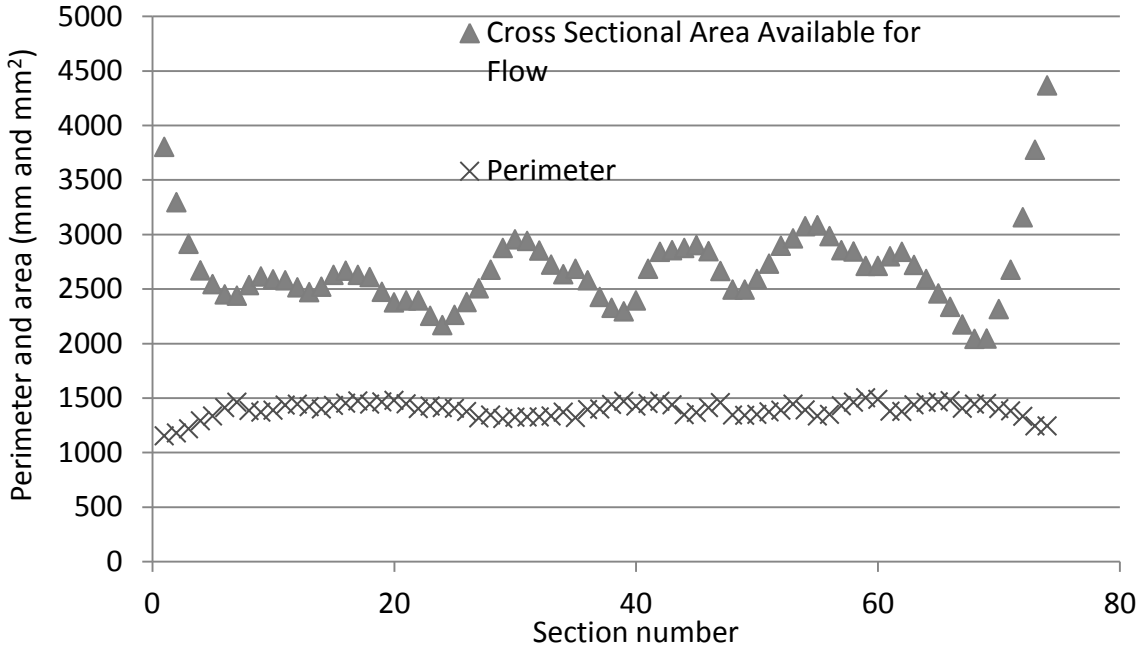

Figure 92: Plot showing the cross sectional area and perimeter for each sample slice

The next values examined were the hydraulic radius, hydraulic diameter, and porosity of the model section by section (Figure 93). To calculate these values, the cross-sectional areas and perimeter need to be used (Figure 92).

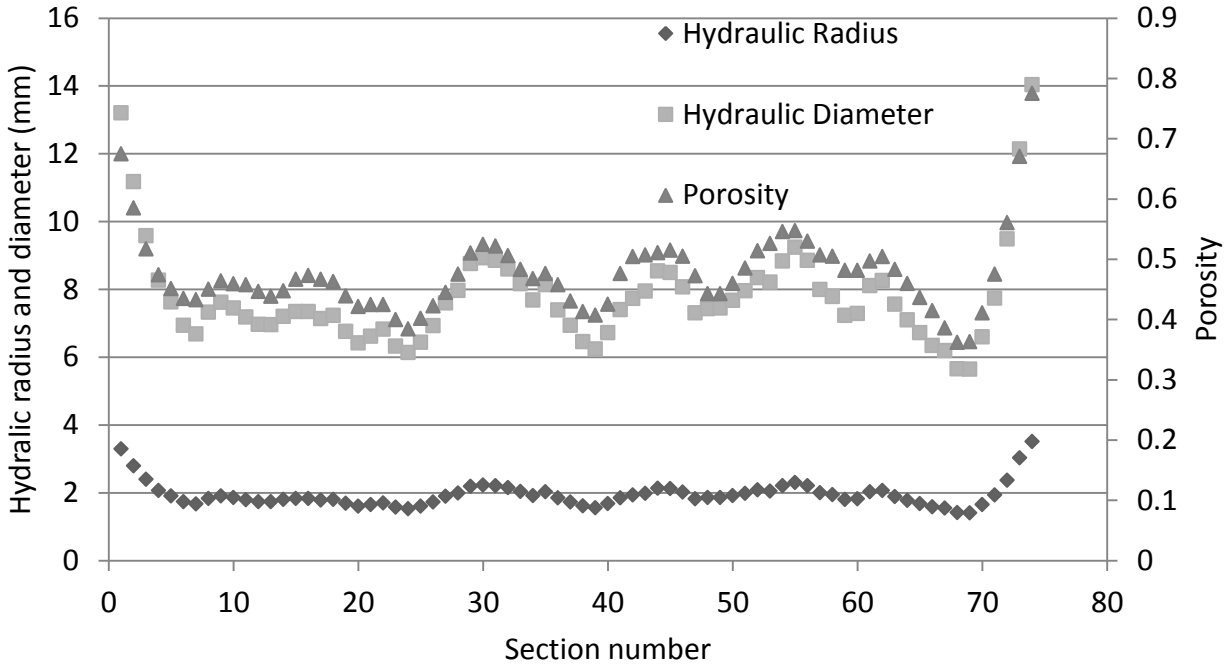

Figure 93: Plot of the porosity, hydraulic diameter and hydraulic radius of the sample. It is important to note the end effects or wall effects of the sample.

7.5 Estimation of Resistance and Atkinson's friction factor

The verification PSM results seen in Chapter 4 are consistent with an interpretation that the PSM specimens, either physical or digital, behave as a type of air duct with a given Atkinson resistance. For the digital PSM data, a value of the resistance R = 1.925 x 10^6 Ns^2m^{-8} can be obtained, which is an extremely high value in comparison for open ducts and air. Such an Atkinson resistance may be decomposed as follows:

$$R = k\frac{LO}{A^3} \tag{49}$$

where

R = Atkinson resistance of the duct (Ns^2/m^8)

k = Atkinson's friction factor (Ns^2/m^4 or kg/m^3)

L = flow path length or the length of a sample section in the direction of flow (m)

O = Perimeter length of a section of a duct or sample (m)

A = Cross sectional surface area available for airflow (m^2)

Using average values for the wetted length (1.389m), flow trajectory length (7.62 cm or the product of tortuosity) and cross-sectional area available for flow from the sections of the assemblage (2680 mm^2), an estimate of an equivalent Atkinson's friction factor, k, was found to be 0.257 Ns^2/m^4. Adopting this value of k, which would be deemed unrealistic for an actual mine airway surface, nevertheless can be considered a type of intrinsic property of the assembly, which can be used in engineering studies.

7.6 Atkinson's friction factor using 'instantaneous' cross-sectional area

Another way of calculating the Atkinson's friction factor is by using the low level geometric parameters section by section (instead of the bulk average and resistance as above) and then summing up the pressure loss across each section until the bulk pressure difference across the sample is matched. To do so, the geometric parameters are inputted in the Atkinson's equations with the bulk flow rates, and then the average k-factor generated for each section for every flow rate tested is calculated. To do this operation, the relation between pressure drop and resistance is used as shown in the Atkinson's pressure drop equation shown below:

$$\Delta P = k\frac{LO}{A^3}Q^2 \tag{50}$$

where:

ΔP = Pressure drop across a sample (Pa)

k = Atkinson's friction factor (Ns^2/m^4 or kg/m^3)

L = flow path length or the length of a sample section in the direction of flow (m)

O = Perimeter length of a section of a duct or sample (m)

A = Cross sectional surface area available for airflow (m^2)

Q = flow rate, which is constant throughout the sample (m^3/s)

The results in Table 24 show that the k-factor averaged 0.269 Ns^2/m^4 instead of 0.257 Ns^2/m^4. This form is more complex in nature but potentially more accurate due to the use of the exact geometric area and perimeter compared to an average value. The values of the k-factor are consistent in the evaluation technique for all of the pressure drops tested both digitally and physically.

Table 24: k-factor analysis using the detailed geometric breakdown of the PSM solid

Pressure Drop (Pa)	Flow rate (m^3/s)	k - factor Ns^2/m^4
9.97	0.00249	0.2718
19.98	0.00354	0.2702
42.17	0.0051	0.2746
99.97	0.00794	0.2685
140.85	0.0093	0.2758
299.98	0.0138	0.2668
320.81	0.0142	0.2695
799.97	0.02255	0.2665
829.27	0.0228	0.2702
1000	0.02525	0.2656
1199.99	0.02762	0.2665
1400	0.02982	0.2666

7.7 Atkinson's friction factor using bulk tortuosity and 'instantaneous' cross-sectional area

The final improvement to this technique can be substituting the section lengths for the tortuosity ratio lengths calculated earlier. In this example, a value of length times 1.14 (the tortuosity ratio) leads to a slightly smaller k-factor of 0.238 Ns^2/m^4. This calculation uses the most detail that can be collected from PSM. This substitution has not been done in common literature that has been reviewed for this topic. The summary of this calculation for each pressure drop is summarized in Table 25.

Table 25: *k* -factor analysis using the detailed geometric breakdown of the PSM solid.

Pressure Drop (Pa)	Flow rate (m^3/s)	*k* - factor Ns^2/m^4
9.97	0.00249	0.2384
19.98	0.00354	0.2370
42.17	0.0051	0.2409
99.97	0.00794	0.2355
140.85	0.0093	0.2420
299.98	0.0138	0.2340
320.81	0.0142	0.2364
799.97	0.02255	0.2338
829.27	0.0228	0.2370
1000	0.02525	0.2330
1199.99	0.02762	0.2338
1400	0.02982	0.2339

7.8 Conclusions

This chapter showed that some parameters that are traditionally difficult to measure or calculate for porous media, such as the tortuosity and the hydraulic radii and diameters, can be found by the 'dissection' of PSMs. For each sample layer, the porosity, fluid-solid interface surface area

and finally Atkinson's friction factors can also be determined from the geometric dissection process.

One of the key points from this chapter, which can be seen in Figure 92, is the fact that a complication that can arise in small samples is wall channeling. Wall channeling is caused by a difference between how the packing along the edges is different than that at the inner region. This can be seen in the sectioning of the sample. It is apparent in both the CFD and experimental results; thus without any geometric analysis, the channeling deficiencies would remain 'contained' within the fitted R values output by LINEST. In future PSMs, this is avoided by cutting further into the sample and correcting the lower level parameters of the wetted perimeter and cross sectional area, to produce a better bulk sample of the particles.

Although not done for a complete range of parameters, the work has shown how Rosin Rammler distribution parameters can now be examined through 'dissection' against internal fluid flow surface areas and volumes.

A concluding result is that geometric 'dissection' of consolidated PSM in the CAD/CAM environment can be used to develop estimates of the Atkinson resistance, instead of testing the materials in the CFD Flow Simulation tool. If the surface roughness is known, CFD simulations can be used to verify the value of the Atkinson resistance of the materials, if desired or necessary.

8 Heat transfer performance of PSMs

8.1 Introduction

The purpose of this chapter is to see if a physical experiment similar to the one from Chapter 4 can be modified to monitor heat transfer characteristics in a 1:1 scale PSM. This chapter details both the physical experiments, and the comparison of results from the CFD predicted values.

8.2 Coupled thermal and airflow experimental details

As a direct continuation of the previous work, thermal testing of a manufactured analogue of broken and fragmented rock has been performed to see if a coupled thermal and airflow model from the synthetic ensembles could also be experimentally verified. This procedure was done to allow for the ability to directly compare the accuracy and precision of a coupled CAD/CAM and CFD simulation model with a physical wind tunnel apparatus. The physical testing featured a series of heating tests from a sample bulk average temperature of -18°C to a room temperature of 24°C. The spot temperatures predicted with the CFD model and the experimental thermistors were compared directly at a 1:1 scale fashion similar in nature to the previous experiment, except in this case, more material properties such as the temperature and time became additional variables.

The hypothesis within this experiment is that CFD codes can be used for the evaluation of real three dimensional porous objects, or a series of objects, using spheres to approximate real physical particle geometries. If the CFD code is able to predict the thermal characteristics of the

experimental model for a material with known thermal properties and geometry, than a similar technique may be used to determine thermal characteristics for unknown materials.

8.2.1 Experimental methodology

The physical testing was conducted in the same experimental rig as the previous work presented in Chapters 3 and 4, with a modification to measure the thermal characteristics. Four 44104 series (perfluoroalkoxy alkane epoxy encapsulated) thermistor elements (Omega, 2013) with a 0.2°C interchangeability and a dissipation constant of 8 mw/°C min., or 1 mw/°C min. in still air, and 2 non-epoxy covered thermistors of the same characteristics (44004 series thermistors) were placed within the wind tunnel apparatus. The locations where the thermistors were designed into the analogue before the 3D printing, to ensure that interference from the outside environment would not be influential to the results, needed to compare with the CFD model. The thermistors use resistance as their measurement, so a switch box and digital multimeter (Mastercraft 52-0055-6) were used to log the resistance. Later, these resistance values were converted to the real temperatures using the Steinhart-Hart equations.

A fan speed of 517.5 RPM, which is the lowest setting on the variable frequency controller, was used for the experiment and this was done to extend the sample heating. This speed had a pressure drop of 44Pa, which is in the same fan set point range as the earlier experiments. The experimental procedure first involved freezing the sample in a freezer to about -18°C, and then quickly placing the sample into the sample containment section of the wind tunnel. A stopwatch was used to mark the timing of the cycle of six thermistor channels that were being monitored. The process was repeated in cycles until the experimental sample reached room temperature.

After the experiment was completed, the resistance curves were converted to temperatures using the following Steinhart-Hart Equations (Omega, 2013):

$$\frac{1}{T} = A + B\ (\ln R) + C(\ln R)^3 \tag{51}$$

where:

T = temperature in °Kelvin

A = 1.468 x 10^{-3} and is a constant

B = 2.383 x 10^{-4} and is a constant

C = 1.007 x 10^{-7} and is a constant

R = resistance measured (ohms)

An example of the conversion process is given in Table 32. It can be noticed that the resistance drastically reduces with an increase of temperature due to the fact that the curve of resistance vs temperature has a non-linear relationship.

Table 26: Table of values showing conversion of resistance to Kelvin using the Steinhart-Hart equations

Resistance Measured (Ohms)	S-H Calculated	1/ S-H	Temperature (°C)
50000	0.004173	239.5838	-33.566
46000	0.004151	240.8995	-32.250
42000	0.004126	242.3485	-30.801
38000	0.004099	243.9592	-29.190
34000	0.004068	245.7701	-27.379
30000	0.004034	247.8346	-25.315
26000	0.003996	250.2304	-22.919
22000	0.003951	253.0763	-20.073
18000	0.003897	256.5670	-16.582
14000	0.003830	261.0539	-12.096

8.2.2 Experimental rig description

The following adaptations to the experimental rig were needed for the verification of the thermal components of the PSM CFD simulations. The same 3D printed sample was used in this process.

8.2.3 Cooling apparatus

A Kenmore freezer was used to cool the sample to the initial -18°C temperature. A thermometer was placed inside the freezer to confirm this temperature and ensure that each experimental run started at the same initial temperature before placement into the wind tunnel sample containment box.

8.2.4 Specimen containment section

The PSM was placed within the same Perspex constructed box used previously that had an internal duct area of 7.62cm x 7.62cm as shown in Figure 94. The length of the specimen duct was 10.1 cm. In addition, 6 thermistors were placed in locations pre-built into the specimen sample, and the monitoring of the CFD code was also in these locations to ensure the highest degree of accuracy.

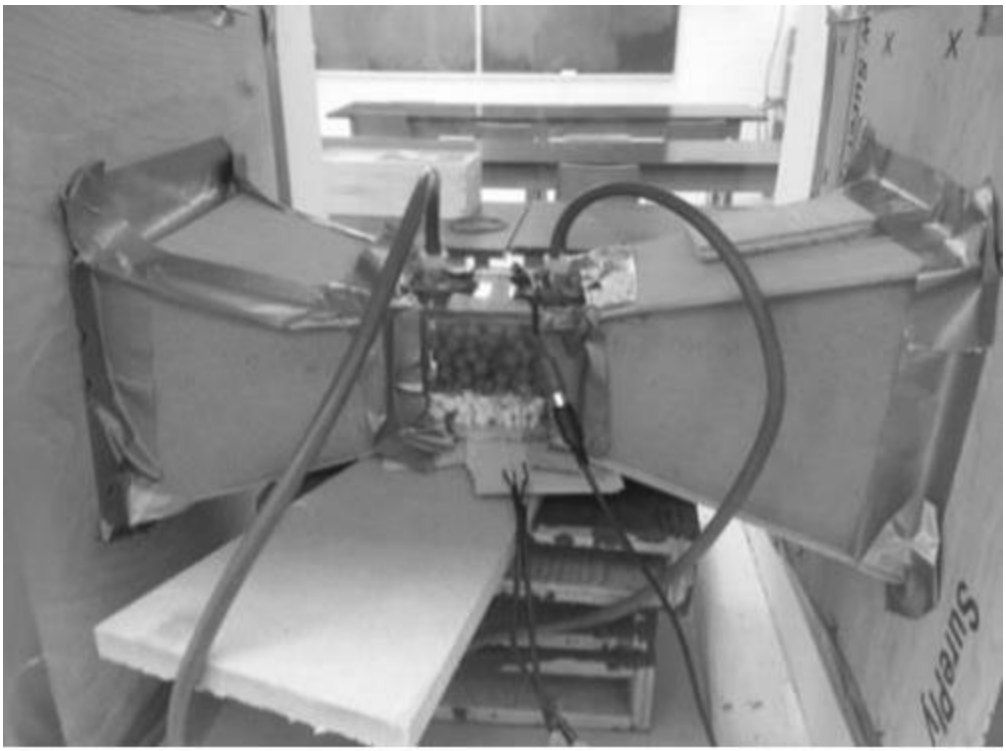

Figure 94: Thermal experiment tunnel sample configuration. The thermistors can now be seen as an addition to the previous experimental campaign.

8.2.5 Mastercraft 52-055-6 multimeter

The multimeter in this experiment was a Mastercraft Multimeter (Canadian Tire, 2014) that is shown in Figure 95, and measurements are made in the resistance mode. The ranges used were between 2000 and 20000 ohm settings. The room temperature is around 24°C, which represents a resistance of 1719 ohms.

Figure 95: Multimeter used in experiments

8.2.6 Custom switch box

To rotate between the 6 thermistor readings in this experiment, a custom switch was manufactured (Figure 96). Channels on the switch relate to the thermistors so a quick display of the resistance on each channel could systematically be recorded.

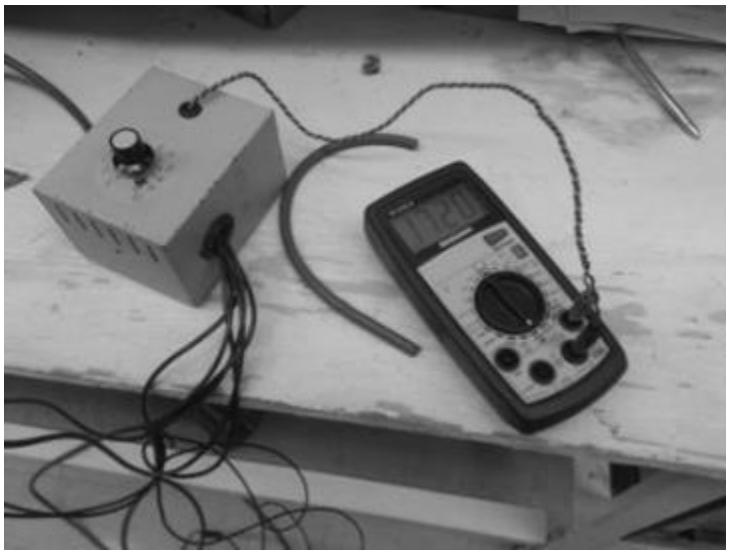

Figure 96: Switch and multimeter. The resistance of 1720 ohms represents room temperature

8.2.7 Data processing and results

The experimental results are direct measurements of the temperatures within the solid. These can be directly plotted against several different ways of sensing within the CFD code. The CFD code can evaluate the temperatures measured within the solid as a bulk value, on a surface, or at any individual point. The final physical results will be presented after the following description of the CFD simulation configurations.

8.3 CFD simulation settings

8.3.1 Mesh settings

The CFD model geometry used in this portion of the experiment was the same as that used for the verification for the pressure and flow rate previous works. This means that the number and types of cells were the same and identically meshed in terms of their geometry, which was at the coarse level 3 mesh setting used in Chapter 5 for the airflow resistance curve.

In this portion of the verification, time dependency and the thermal characteristics had to be introduced into the model with a summary of the general conditions given below:

Number of total cells within the mesh: 8000

Number of fluid only cells (air): 228

Number of solid only cells: 222

Number of partial cells (solid and fluid properties): 7550

8.3.2 Solid thermal properties

The thermal properties of the printed ABS430 plastic (Matbase, 2013) used in the manufacture of the physical PSM are now of consequence to the CFD model and are summarized in the Table 27.

Table 27: Values of ABS 430 thermal properties assigned to the CFD simulation analogue

Parameter	Value
Density	1060 kg/m^3
Specific heat	1260 J/(kg*K)
Conductivity type	Isotropic
Thermal conductivity	0.17 W/(m*K)
Absorption coefficient	0.1/mm
Refraction index	1.6
Melting temperature	500 K

The encapsulated thermistor properties also needed to be inputted into the model along the corridors that had been designed into the porous solid for the thermistor head. The properties of the thermistor casing epoxy are shown in Table 28.

Table 28: Perfluoroalkoxy alkanes thermal properties that surround thermistor elements

Parameter	Value
Density	2120 kg/m3
Specific Heat	1088.5675 J/(kg*K)
Thermal Conductivity	0.209 W/(m*K)
Absorption Coefficient	0.1/mm
Refraction Index	1.344
Melting Temperature	555.15 K

8.3.3 Additional solver settings

Additional settings for the solving controls of the CFD simulation had to be adjusted with the heat and flow coupled model, and are explained below:

Heat Conduction: On – Tells the CFD to run conduction between the fluid (air) and solid media.

Time dependency: On – This means the finite volume method translates the partial differential equations of Navier-Stokes into a series of ordinary differential equations and then solves for the transitional properties.

Radiation: On – Tells the CFD code to run with the thermal radiation properties between solid media. The radiation uses ray tracing techniques and does not combine with the conduction equations such as those found in McPherson (1986) to form an effective thermal conductivity.

The amount of time for the CFD code to simulate was equivalent to 15 minutes of real-world time, which was the length measured during the physical experiments for the temperature of the analogue to go from -18°C to room temperature. This is one way to verify that the material properties for the analogue were in the correct time-scale with the real physical experimentation, as well as how the CFD code interprets the heat transfer compared to physical experiment.

The computational time required to run these models increased from the initial 2 hrs without heat and time dependency to about 5 hrs for the entire transient heat-coupled model. The thermistor sensor locations, which also mean the CFD sensing locations, are shown in Figure 97.

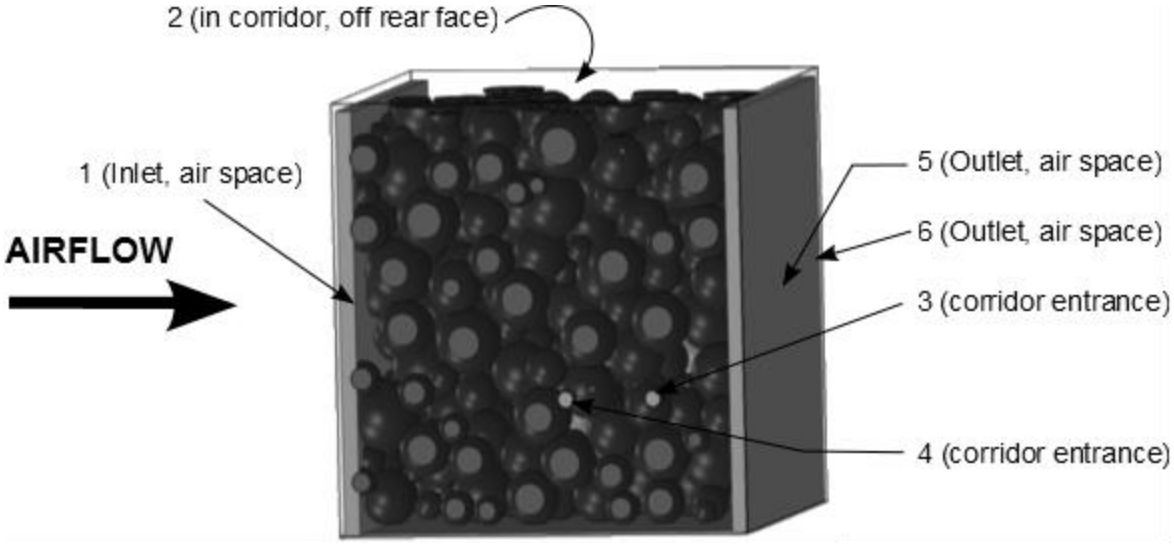

Figure 97: Schematic of thermistor locations within the PSM and the physical experiment sample

8.3.4 Boundary and initial conditions

The boundary condition set was the pressure loss across the sample measured in the wind tunnel experiments. The flow rate in the CFD simulation was calculated as a variable to check the consistency within the now heat-coupled CFD model. The inlet air temperature into the CFD model was set as the temperature measured in the laboratory at the time of physical experimentation. To mimic the physical experiment in a better fashion for the initial temperature distribution within the solid, the CFD simulation was pre-conditioned by letting the analogue also predict and verify the temperature differences caused by the time required to move the sample between the freezer to the wind tunnel rig. This second verification was done by letting the CFD model 'sit' in still air from the average temperature of the freezer to the equivalent of 300 seconds of real time that it took to move the sample and place it into the wind tunnel and turn the fan on. By letting the CFD analogue sit, the average temperature of the individual sensor locations became much closer to the real physical experiment rather than setting the entire

analogue to have an equal average temperature as an initial condition. An image from the CFD code representing the physical model at the time the fan was initiated, or when the CFD code is actually 300 seconds into the experiment, is shown in Figure 98.

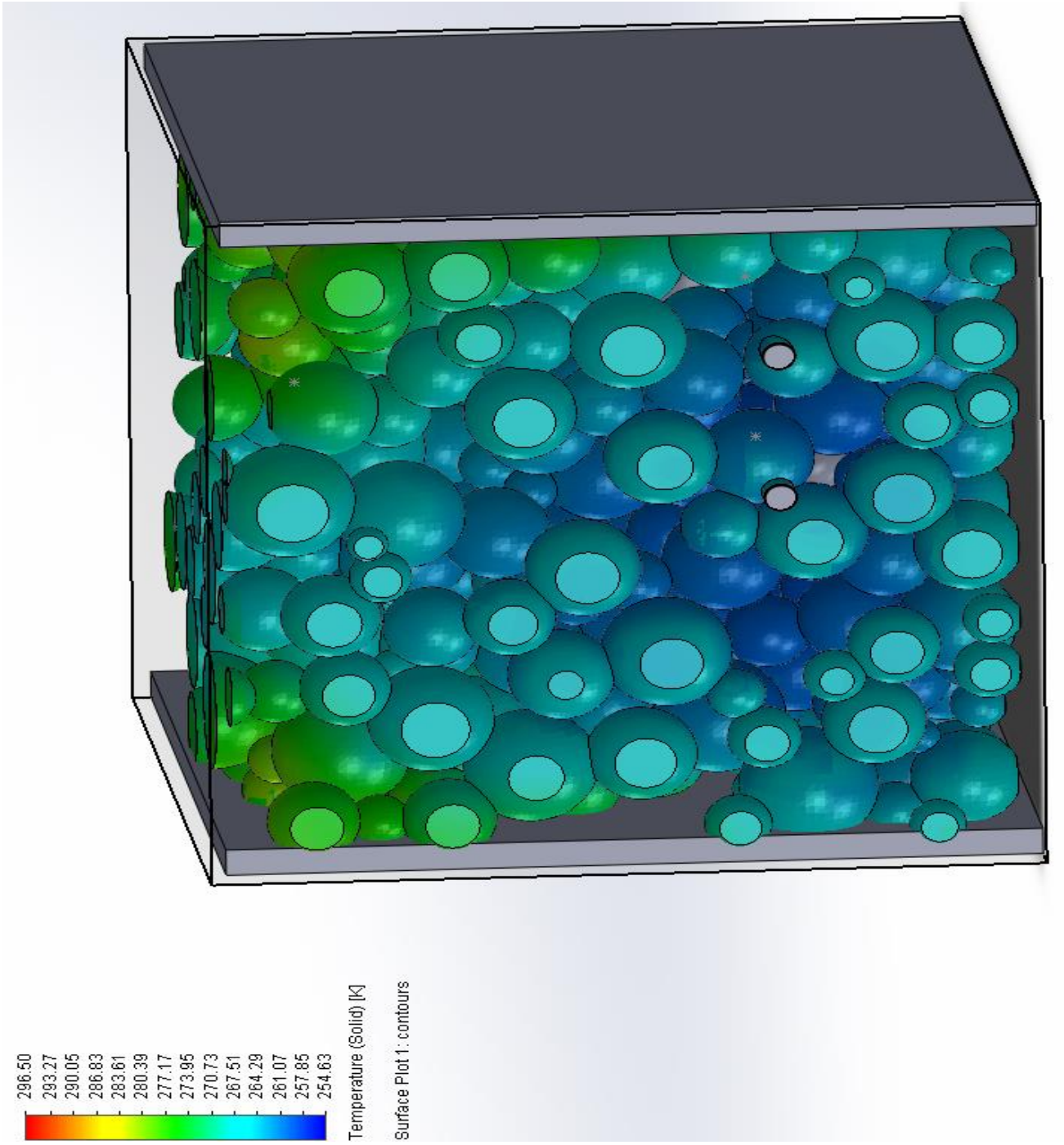

Figure 98: Rendering of initial temperatures after simulation of the 300 seconds required to install the sample into the wind tunnel apparatus and turn on the fan. This result is a second verification of the experiment due to its accuracy in predicting the conditions initial temperatures taken from the physical experiment. The darker colors are cooler temperatures of about -11 degrees Celsius.

8.4 Sensing of the CFD models

The CFD model, as described previously, has several possible ways of being sensed. In the results, the term PG = point goal location (the temperature at an exact point), SG = surface goal (the surface of the corridor where the thermistors are located) and VG = volume goal (the total bulk parameter of average temperature throughout the entire sample).

8.5 Comparison of experimental and CFD simulation results

For all three internal body thermistors, the temperatures observed from Test 1 and Test 2 lie close to one another, indicating that there is good reproducibility in the experimental observations. Each thermistor exhibits a clear transient response and converges on the same ambient temperature of ~293.5K. After installation, thermistor 1 had a physical problem, and was not used in the analysis.

The experimental data are plotted with various results produced from the CFD simulations of the same experiments. The PG temperature is the temperature predicted by the CFD simulation at the exact location at which the thermistor was expected to be installed. Maximum, minimum and average temperatures of the solid materials along the corridor alignments of each thermistor are also plotted. The maximal values can be expected to be those close to the surface of the specimen; the minimal values can be expected to be those closer to the core of the specimen. The maximum and minimum values form envelopes on each chart, within which it should be expected the experimental data are located. This is the case for all but three observations, all for thermistor 2 (which were nearly within the envelope defined anyway). For each of the three

thermistors, the average temperature of the volume of the ensemble, the average specimen temperature, is also presented and provides a useful reference across the three charts.

For Thermistors 2 (Figure 99) and 4 (Figure 101), the temperatures recorded are close to the minimum temperatures along the corridor. In other words, they are close to the end of the corridor towards the core of the specimen where the PG temperatures are sampled. As the experimental values agree well with PG and minimum temperatures, it appears that the results from the CFD simulations are consistent with the physical experiments. Such agreement is not evident for Thermistor 3. In that case (Figure 100), there is a significant disparity between the experimental curve and that of the PG from the CFD simulation.

The CFD results were produced weeks ahead of the actual experimental testing as the results were used to inform the most appropriate positioning of the thermistors. The known complications of remnant SR30 in the corridor of Thermistor 3 is thus completely consistent with these experimental observations, which are still close to the predicted average temperature of the corridor. This was further confirmed by close agreement (not presented here) between experimental observations and PG results from the CFD simulation located 3 to 5 mm closer to the surface in the corridor.

The VG shown in the plots is the CFD code prediction of the overall bulk average temperature of the entire ensemble. This is the data that would be used in creation of an equivalent continuum model representing this PSM. The point of the data in these plots is to show the fact that the bulk

values are substantially higher than any of the locations that were chosen for observation due to their predicted high signal strengths.

Sensor 2 results:

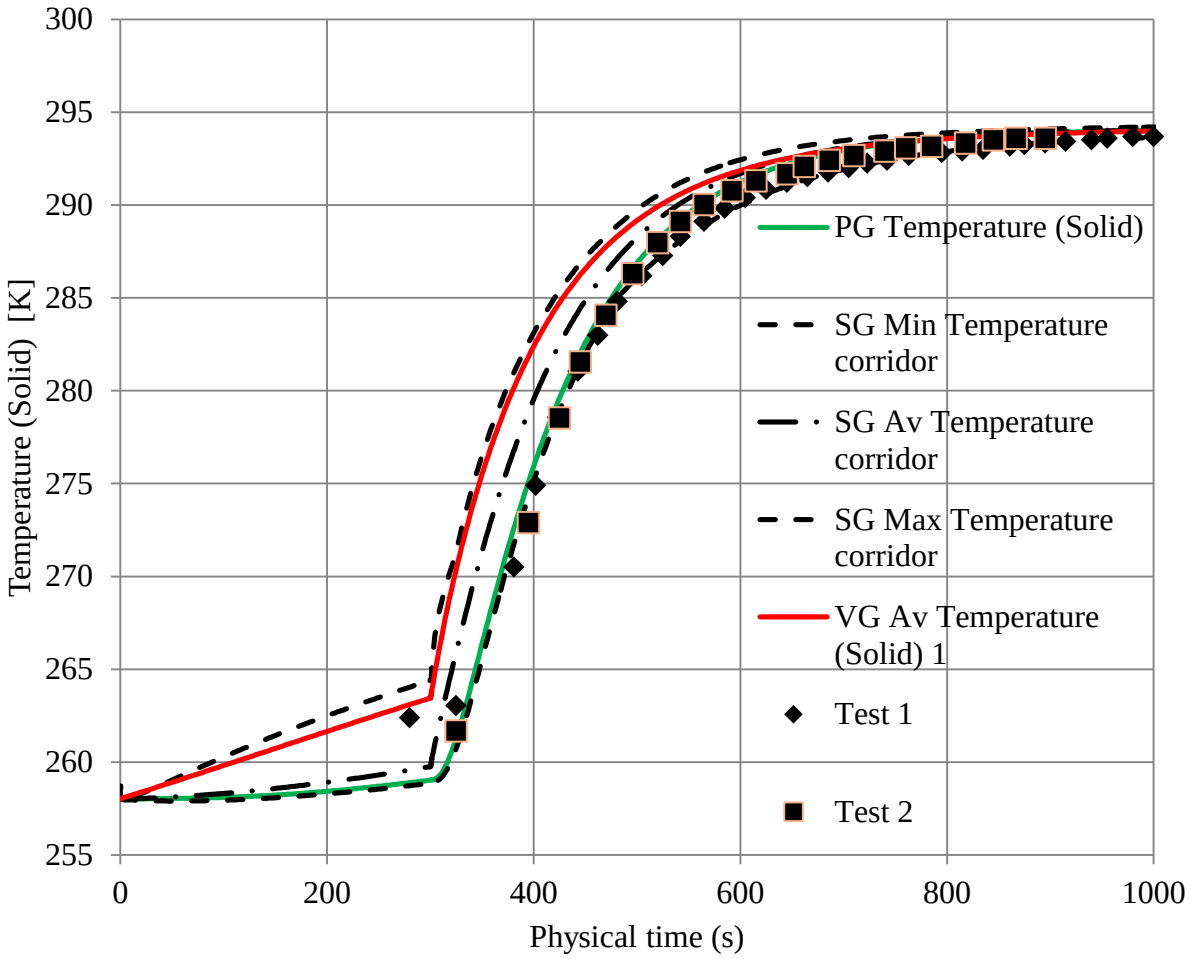

Figure 99: Sensor 2 comparison with CFD time lapse simulation

Sensor 2 (Figure 99) showed a good match of the CFD curves with the experimental data. The PG (temperature specifically at the point where the thermistor was located) showed almost a direct match to the values measured by the thermistor.

Sensor 3 results:

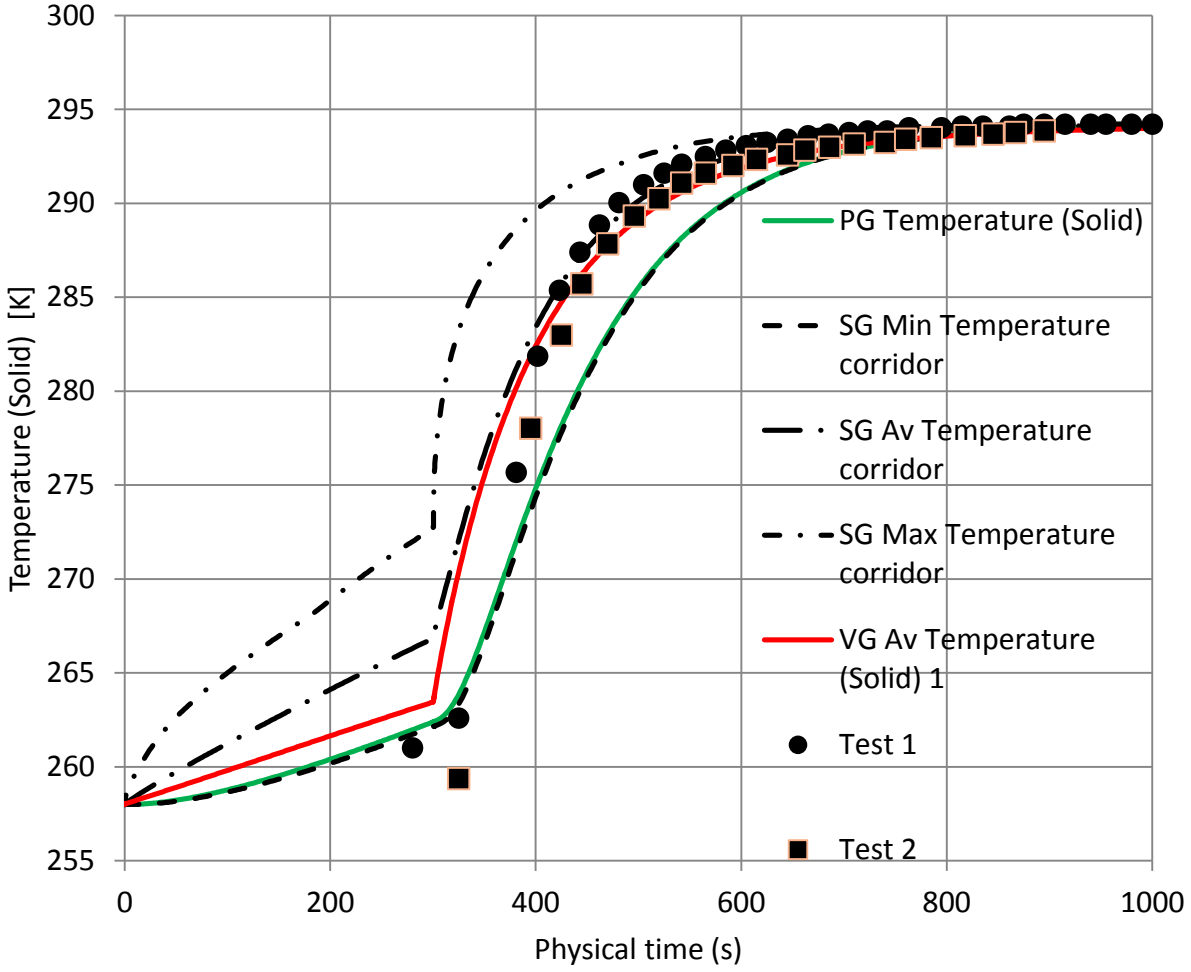

Figure 100: Sensor 3 comparison with CFD time lapse simulation

Sensor 3 (Figure 100) did not have an exact match to the point goal, but was still much lower than the maximum temperature of the internal corridor where it was placed, and it converged to the average temperature predicted for that corridor. This was further examined, and the thermistor location was not placed directly at the end of the corridor. Through examination of the results and comparison with the physical analogue, the thermistor was found to be approximately 3 to 5 mm down from the end of the corridor, which is where the CFD simulations match the temperature profile.

Sensor 4 results:

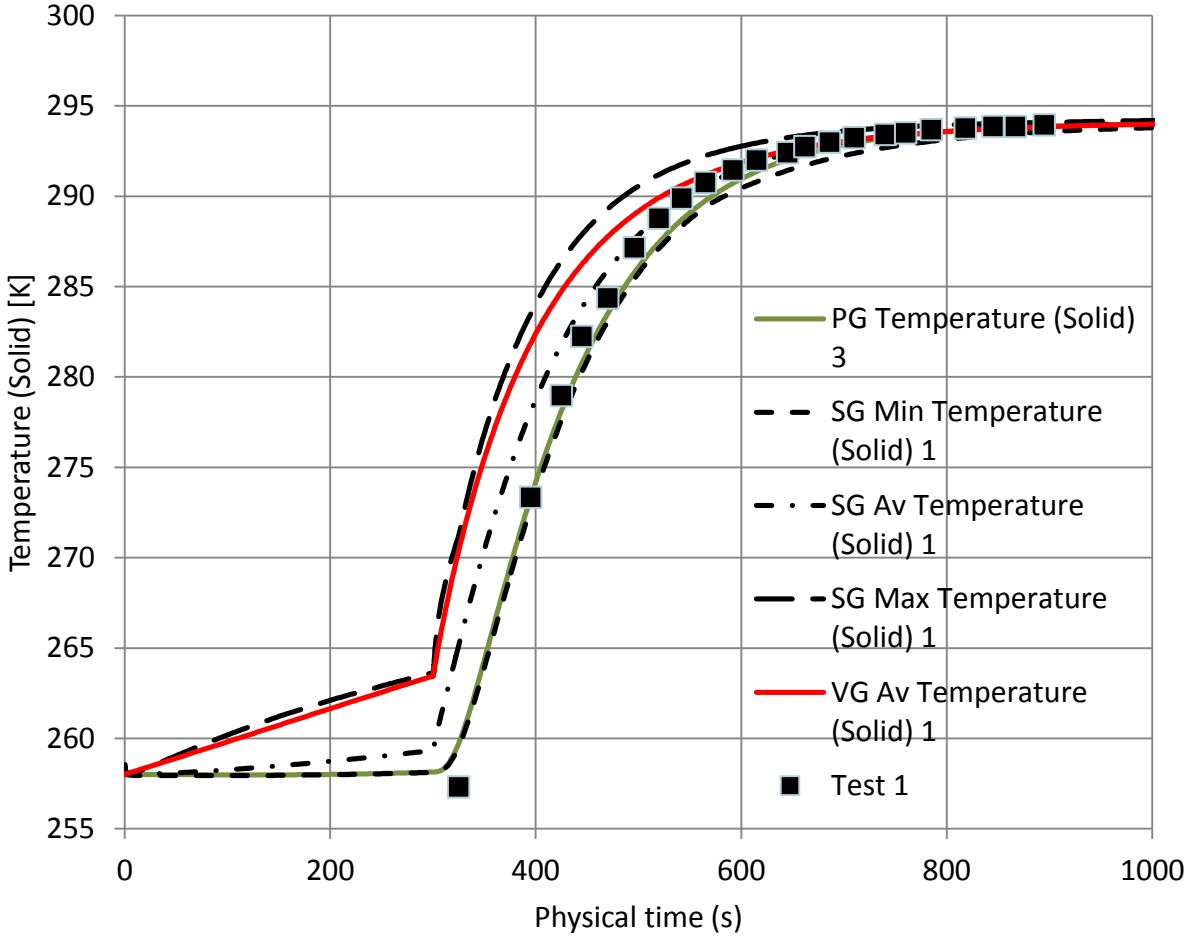

Figure 101: Sensor 4 comparison with CFD time lapse simulation

Sensor 4 showed some of the closest temperatures compared with the time-lapse and PFA epoxy modeled CFD simulation. Again, the point goal nearly matched (within 0.5°K) with the thermistor readings, indicating that the final placement of the thermistor was very close to the intended position.

8.6 Conclusions

It can be seen that when simulated with the most care to replicate the physical apparatus, the method described using a combined CAD/CAM and CFD simulation tool is capable of simulating accurately and repeatedly the heat transfer behaviour of a PSM of a porous medium. The overall conclusion drawn from this part of the verification exercise was that the CFD model was able to produce simulation results that were consistent with experimental results. This indicates that the CFD code could be relied upon as an investigative tool used to assess the thermal performance of a wider range of PSMs where the material properties represent those of rocks, rather than ABS430 plastic. The confidence gained allows the techniques to be applied for theoretical or back analysis of the performance as properties of real PSM's and other particulate porous media.

9 Scaling up for large scale mining applications

9.1 Introduction

The purpose of this chapter is to test methods of scaling PSMs for practical engineering use for large scale porous media. It will outline the three methods of scaling that were examined. The first method tested is termed ‘self-similar scaling’ of the PSM. The second method considers PSMs in series and parallel configurations to create larger sized aggregates. The third assumes that by sub-sampling a representative sample, a relation such as a power law can be developed to permit prediction of air flow resistance at other sample volumes. This work intended to answer the question of how airflow resistance changes with the scale of the problem considered. Following this, a technique implemented with the aim to uncover the representative elemental volumes associated with porous media was tested. A relationship between volume and flow resistance was then tested to see if it could be used to predict a flow rate resistance at a volume of choice. Finally, whether an equivalent continuum model has the same scaling behaviour as a discontinuum model was assessed.

The first method of scaling tested is a self-similar scaling by means of a scaling or multiplication number. In this demonstration, factors of 10 were chosen. The first objective was to see if the flow rates and resistance exhibited mathematical relations to values at alternative scales. The second objective was to establish whether or not a PSM with the same porosity but varying volume had the same air flow resistance.

9.2 ‘Self-similar’ scaling of PSMs

To further the understanding and applicability to larger problems involving porous media, scaling tests were undertaken on both the PSM and equivalent continuum models. The method for this was using a self-similar scaling on the geometry in factors of 10 and then running the fluid flow code.

The model chosen to test scaling was a uniform distribution of spheres with radius 1.269 cm. The model was generated in PFC using the porosity FISH function, and then was imported and ‘geometrically interrogated’ independently in the CAD/CAM environment. The containment box used in this model was 19.6cm x 14.7 cm x 16.3 cm, as shown in Figure 102.

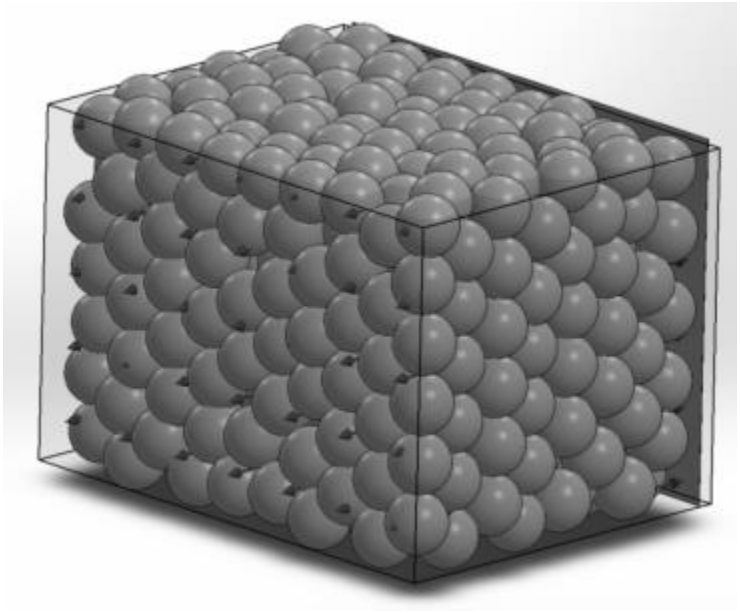

Figure 102: A model based of equivalent spheres and a controlled porosity. This was chosen to test the self-similar scaling behaviour and equivalent continuum creation. The containment box dimensions are 196mm by 147mm by 162 mm.

The flow characteristics of the original model and scaled models are shown below in Table 29 for the total of 4 samples (original plus the 10, 100, and 1000 times geometry scaled models). The boundary conditions were set pressure differences of 1000, 500, and 25Pa across the sample containment box for each pressure scenario similar to the previous 'constant head' tests. A best fit curve of the resistance was also calculated for comparison. The LINEST function within Microsoft Excel (Microsoft, 2014) was used to obtain the least squares fit value of the resistance of the PSM. While using the LINEST command, statistical characteristics such as the coefficient of determination, F statistic, and dF (degrees of freedom) were evaluated to see if the observed relationship between the dependent and independent variables occurs by chance. If the degrees of freedom are close to the F statistic, then the event may happen by chance. This was not the case for any of the results presented. The flow rate across the sample increased by a factor of the scale increase squared (ie: 10 times the size = 100 times larger) across the sample. The Q^2 value was used to determine the resistance from the pressure loss relation.

Table 29: Sample set results for the flow rate and flow rate squared used in this analysis

Sample		dP (Pa) 1000	dP (Pa) 500	dP (Pa) 25	dP (Pa) 0
1 (1X)	Q (m^3/s)	0.01006	0.00708	0.00145	0
2 (10X)		1.04905	0.74317	0.16095	0
3 (100X)		107.2	75.2848	16.2131	0
4 (1000X)		10608.7	7432.3	1571.69	0

In Table 30, the geometric dissection values for the geometry, and the results of the statistical results for the resistance fitting are given. It can be seen that even though the samples tested each have the same porosity values, different resistance values were found. The statistics show that the values for the resistance are not by coincidence, due to having the F values much higher than

the dF values, and the correlation values were all at either 0.99 or 1. This is due to the noiseless environment of the CFD code. The resistance of the sample increased by a power of four for each scale multiple of 10 times. A scale increase of 10 increases the resistance 10^4 or 10000 times. The resistance differences for each sample are at the exact same porosity. This shows there is the ability for two separate sized samples having different resistances can have the same porosity of 19.26%. The diameter of the 500 spheres in this PSM range from 0.01269m to 12.69m.

Table 30: Results of the geometric properties of the sample along with the best fit resistance

Sample	Best fit Resistance (Ns^2m^{-8})	R^2	F	df	Bulk volume (m^3)	Void volume (m^3)	Interface area (m^2)
1 (1x)	9900222	0.99	106470	3	4.67E-03	0.000898	0.66
2 (10x)	908.0201	1.00	757455	3	4.67E+00	0.898895	66.18
3 (100x)	0.087256	0.99	90560	3	4.67E+03	898.8954	6617.5
4 (1000x)	8.918E-06	0.99	48887	3	4.67E+06	898895.4	661750

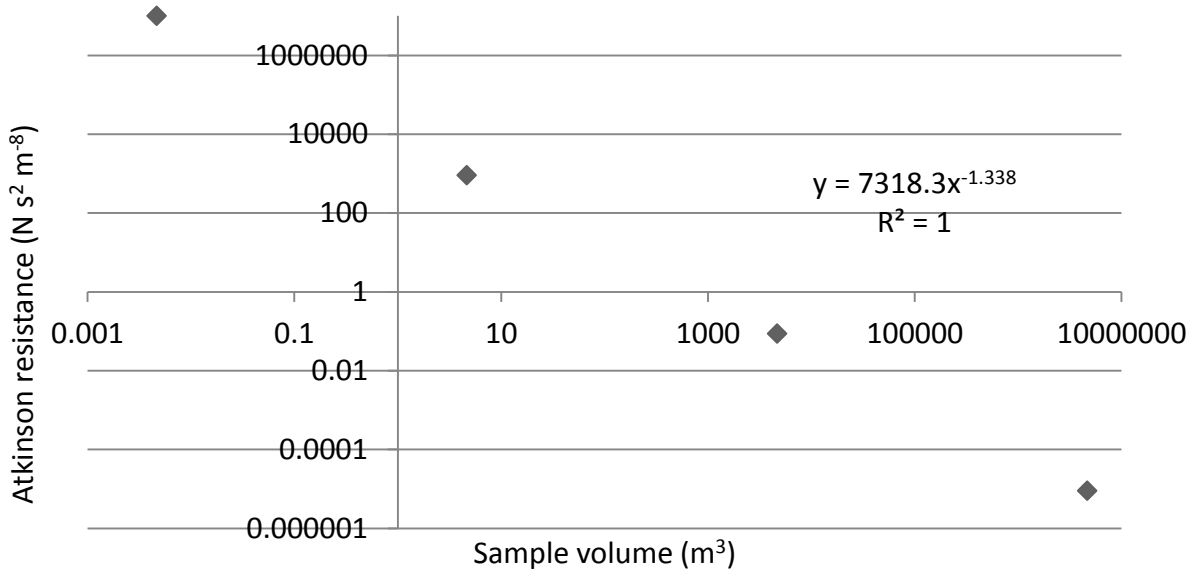

Figure 103: Log-Log plot sample bulk volume vs Atkinsons' Resistance. There is a power law relation with a 100% correlation score.

9.2.1 Discussion of results

In Figure 103, the volume of the containment box is plotted with the resistance values calculated for each sample set. There appears to be a power law relation between the two, but this will be tested in the next sub-section to see if this is the case for more than a one sub-sample model.

From examination of the sample results, it can be seen that for every scale increase of a factor 10, the subsequent flow rate increases by a factor of 100 or by 10^2. The resistance for each increasing sample reduces by a factor of 10000 or 10^4. By the use of self-similar scaling, it seems apparent that there is a relationship between flow rate, resistance, and sample size volume and the relationship behaves in predictable manners within the PSMs, in a similar fashion to

Atkinson's equation. These simulations show that the same porosity across increasing sample scale does not imply equal air flow resistance.

9.2.2 Baseline equivalent continuum model to test if PSM equivalence is possible

An equivalent continuum model was made of the original sized PSM to test the consistency between the two. Parameters needed for this are the containment box volume and an equivalent solid zone which is assigned the flow resistance curves, making it a porous medium according to the fluid flow code. To input the parameters, the fluid flow materials database was used to create the material. Input values are the box containment parameters of bulk cross-sectional area, in this case the opening area of 19.6 x 14.7 cm and the length of 16.3 cm. Also, the pressure vs flow rate characteristic from the original PSM was inputted into the Flow Simulation material database. With these values, the k parameter, which is used in the Navier-Stokes gradiant function (or porous resistance) (Dassault, 2013) shown in Chapter 2, is calculated for this block from the following formula:

$$\Delta P = km\frac{L}{A} \tag{52}$$

where:

$\Delta P =$ pressure loss across sample (Pa)

k = porous resistance (1/s)

m = mass flow rate (kg/s)

L = length of the sample (m)

A = cross sectional area of the sample

In the Flow Simulation tool, this is a piecewise function, so when inputing an air flow resistance curve to follow Atkinson's Law, more points should be used to provide a better piecewise linear approximation of the 'squared law' behaviour. Figure 104 shows the equivalent continuum of the PSM with a containment box with dimesions of 19.6 cm by 14.7 cm by 16.3 cm. The equivalent solid zone just appears as a single cell as all the 'internal geometry' of a PSM is implied in the air flow resistance characteristic; only the bulk values of porosity, the geometric size of the containment box, and the flow resistance curves are provided. This reduces the calculation time from hours to seconds and therefore it can be understood why this method is generally preferred for calculation of larger porous media problems.

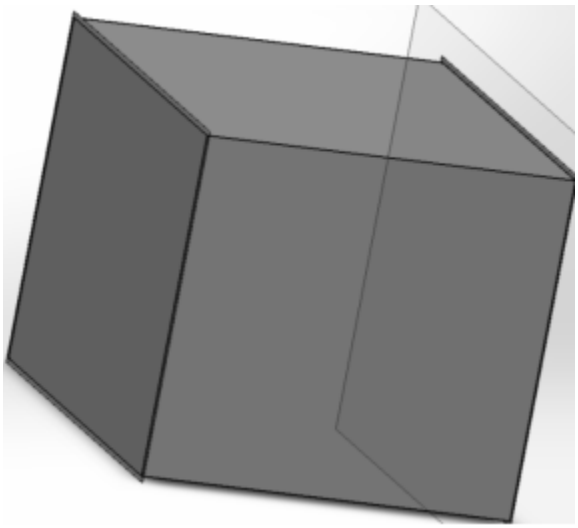

Figure 104: Equivalent continuum model representing the PSM

Table 31: Equivalent continuum model results representing the baseline PSM

Equivalent continuum model			Flow rate ratio comparison to PSM
dP (Pa)	Q (m^3/s)	R (Ns^2m^{-8})	
1000	0.01001	9979631	0.9954
500	0.00707	10013981	0.9974
25	0.00145	11893231	0.9985

In Table 31, the equivalent continuum model with almost 100% accuracy correctly simulated the same flow rates going through the model for a given pressure drop. This shows that the porous media portion of the CFD code responds in the way intended by the program, in this case, defining the material property values with the bulk PSM results.

9.3 Scaling air flow resistance for an ensemble with fixed particle size distribution using a power law

Within this section, an evaluation of how well PSM sub-samples can test for equivalence of air flow resistance is made with the aim of identifying at what scale a sub-sample behaves independently of the other samples. The second objective is to see if component blocks of PSMs can be aggregated to produce an increase in size to the point where the resistance changes very little with further increases of bulk volume.

A series of sub-sample cut sizes was compared using their resistance curves at set intervals. Three sizes were set in the containment boxes to control the samples. In Figure 105, a histogram showing all the spheres generated for the full sample is shown. The Rosin Rammler parameters

were a characteristic diameter of $d_c = 0.012$m with a spread factor of n = 4.5, which is more uniform than most mining applications.

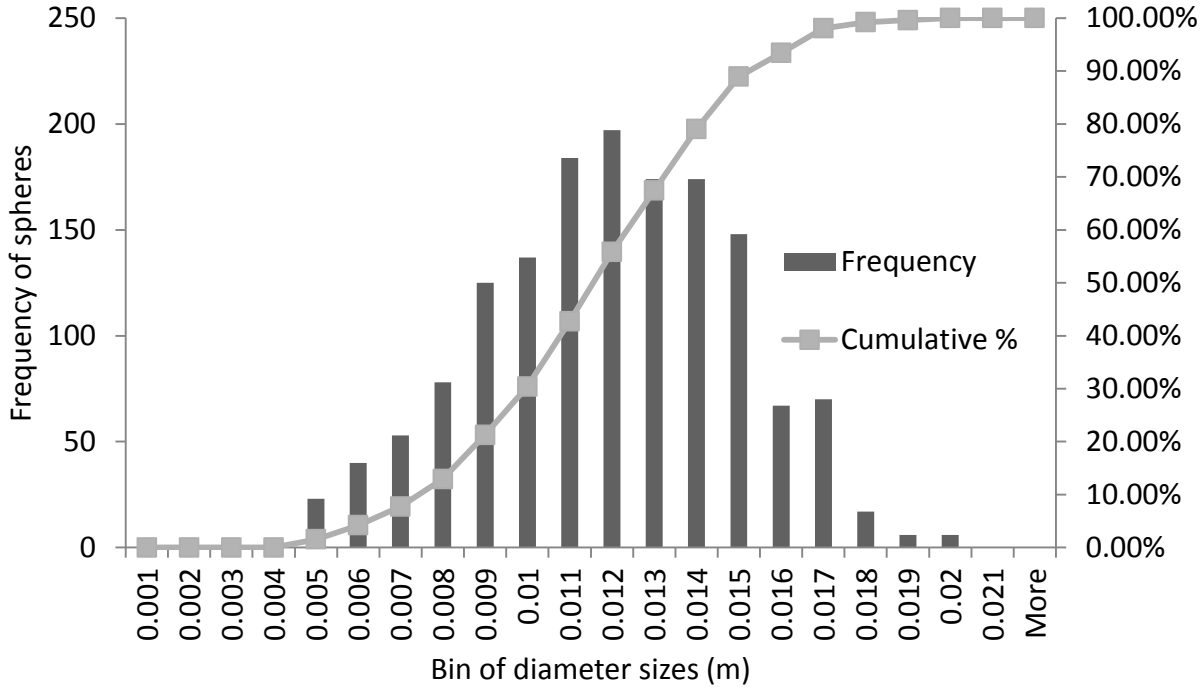

Figure 105: Histogram of the spheres that were imported into the CAD/CAM environment. The Rosin Rammler parameters are $d_c = 0.012$m with a spread factor of n = 4.5.

Not all the spheres were used in the sub-sampling campaign due to the top surface of the consolidated body not being level. This surface comes from the original consolidation during the particle flow code, as can be seen from Figure 106. The rectangular frames in the rendering are the sub-sample "cuts" used in the testing and comparison in this section.

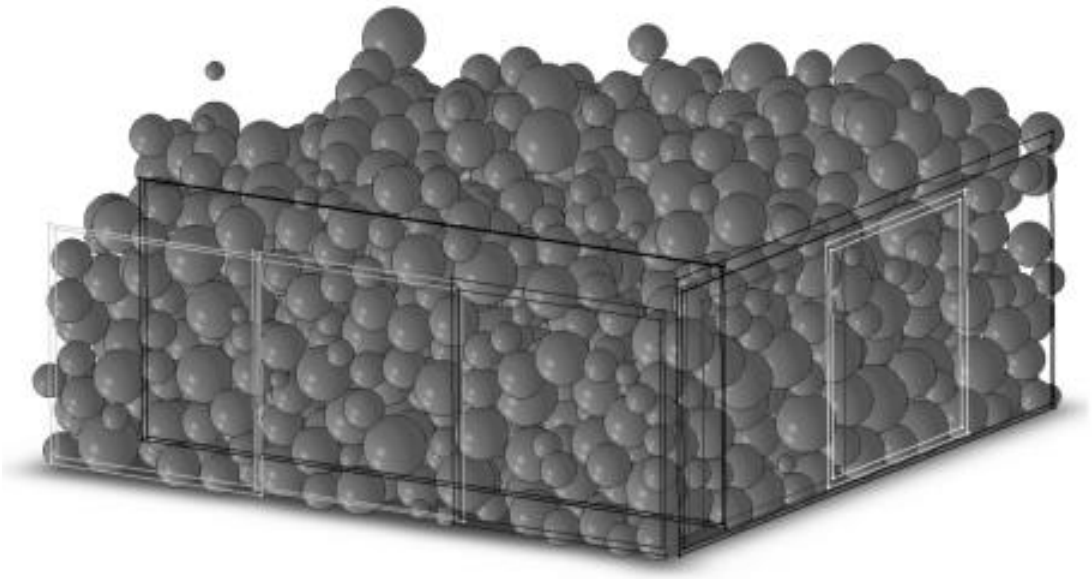

Figure 106: Rendering of the original full CAD/CAM PSM. All the sub samples are shown by the different 'shaded' containment boxes. The upper portion of the sample was deemed unusable for sampling due to the large volume of 'open space' after consolidation.

9.3.1 Simulation results

The following tables and figures are the models and resistance values arising from the campaign of simulations. Each containment box was the same in size for direct comparison of the separate sub-samples. The first set of samples was the medium size of the sets, with a width of 69.88 cm, a height of 40 cm and a length of 161.8 cm.

9.3.2 Sample set 1 results

The following tables and figures are the models and resistance values for the first set of five samples. Each containment box was the same in size for direct comparison of the separate samples. This set of samples had a height of 40cm, a width of 69.88cm and the length of sample was maintained 161.8cm.

In Table 32, the summary of the first set of sub-samples is presented. The pressures, flow rates and their statistics are shown and displayed along with the statistics and calculated geometric parameters.

Table 32: Summary of results for simulation set 1

Height (cm)	40	Width (cm)	69.88	Length (cm)	161.8
	Sample 1	Sample 2	Sample 3	Sample 4	Sample 5
Delta P (Pa)	Flow rate (m^3/s)	Flow rate (m^3/s)	Flow rate (m^3/s)	Flow rate (m^3/s)	Flow rate (m^3/s)
1000	0.0142	0.0144	0.0153	0.015	0.0154
500	0.0099	0.0101	0.0107	0.0105	0.0108
25	0.002	0.002	0.0022	0.0021	0.0022
0	0	0	0	0	0
R (Ns^2m^{-8})	4974684	4808585	4239884	4437264	4224155
R^2	0.999945	0.999951	0.9999401	0.999952	0.99993
F	54834.88	60729.59	50075.15	62332.38	45733.9
df	3	3	3	3	3
# Particles	269	315	303	295	280
Box volume cm^3	452265	452265	452265	452265	452265
Volume voids cm^3	250253	247790	285750	250606	249978
Porosity	0.55333	0.54789	0.63182	0.55411	0.55273
Surface Area (cm^2)	117852.1	120775	100696.83	114953.31	117933

The number of particles and their properties show the differences of sub-sampling the same Rosin Rammler distribution for the smallest of the volume ‘cuts’. The porosity varies about 2% throughout this sub-sample size except for Sample 3, which had a significantly larger porosity of 63%, about 8% larger than the other samples. The flow rates were approximately the same as the other samples.

Within this sample set, the largest differences in resistance were around 8% from sample 1 to (3 and 5) but had less than 2.5% in samples 3, 4, and 5. Sample 1 had the highest resistance while sample 3 had the highest porosity, lowest resistance, and had the smallest solid surface area. Sample 3 consisted most of the surface of the entire consolidated sample, and is why the porosity is higher than the other samples.

The maximum differences for relative flow rate in this set are about 8%. Sample 5 was a wall sample, and showed the most variance from the others.

9.3.3 Sample set 2 results

In Table 33, the summary of the second set of sub-samples is presented. The pressures, flow rates and their statistics are shown. The line statistics were also displayed in the resistance calculation, indicating if the results were due to chance, which they were not, due to the degrees of freedom being much lower than the F-statistic.

The geometric properties for the sub-sample are also given. When examined, the amount of particles and their properties show the internal differences of sub-sampling the larger Rosin Rammler distribution. The porosity varies about 2% throughout this sub-sample set.

Table 33: Summary of results for simulation set 2

Height (cm)	63.11	Width (cm)	61.94	Length (cm)	161.8
	Sample 1	Sample 2	Sample 3	Sample 4	Sample 5
Delta P (Pa)	Flow rate (m^3/s)	Flow rate (m^3/s)	Flow rate (m^3/s)	Flow rate (m^3/s)	Flow rate (m^3/s)
1000	0.0219	0.0215	0.0225	0.0213	0.0199
500		0.0151	0.0158	0.0149	0.014
25	0.0032	0.0032	0.0033	0.003	0.0029
0	0	0	0	0	0
R (Ns2m-8)	2074658	2165480	1965952	2208069	2526102
R^2	0.9976	0.999962	0.9991	0.99992	0.99997
F	1268.3226	79060.62	91121.629	37399.14	111852
df	3	3	3	3	3
# Particles	408	403	365	395	421
Box volume cm^3	632482	632482	632482	632482	632482
Volume voids cm^3	357418	355581	355457	357281	345824
Porosity	0.5651	0.5622	0.562	0.56489	0.54677
Surface Area (cm^2)	155780.56	153603.4	154703.11	152994.42	157407

In terms of differences between the various models for resistance, the general differences are between 4 to 12%. The biggest difference is with sample 5, which has a lower porosity, higher resistance, and increased total solid to fluid 3D surface area true rubbing length. This difference is a direct wall effect from the original geomechanical consolidation and should be noted as an influence on the flow conditions. In terms of relative particle size, the sample with the largest number of particles had the highest resistance while sample 3, which had the least amount of particles and an average surface area (of solid / fluid interface area) of the samples, had the lowest resistance.

In terms of the relative differences of flow rate, samples 5 and 3 are ‘wall’ models, meaning in the particle flow code sphere-wall contacts aligned along confining walls. This wall effect had noticeable influence on the sub-sampling results and should be noted when testing further models. The variation of flow rates were expected at this level of sub-sample due to the potential for high levels of variation in the resistance.

9.3.4 Sub-sample 3 results

The following tables and figures are the models and resistance values for the third set of two samples which encompass the largest volume of the overall samples. Each containment box was the same in size for direct comparison of the separate samples to see, at the largest scale, if there was the minimum amount of relative difference between them. This is also a test for the directionality (or isotropic behaviour) of the resistance to flow within the sample. The height of the containment box was 180.22 cm, the width was 69.88 cm and the length was maintained at 161.8 cm.

In Table 34, the flow rate, resistance and statistics are shown for the sub-sample set. This was the largest sub-sample; it encompassed all the other sub-sample sets presented earlier, and shows the most consistency between them in terms of resistance. The geometric properties are also given for the sub-sample set. The porosities and geometric properties are close in nature, but are tested in different flow directions through the sub-sample. The amounts of particles sampled differ by only nine and the general surface areas are also close in nature.

Table 34: Summary of results for simulation set 3

Height (cm)	180.22	Width (cm)	69.88	Length (cm)	161.8
	Sample 1	Sample 2			
Delta P (Pa)	Flow rate (m^3/s)	Flow rate (m^3/s)			
1000	0.067	0.0677			
500	0.0472	0.0475			
25	0.0103	0.0104			
0	0	0			
R (Ns2m-8)	222553	218264			
R^2	0.999993	0.999962			
F	408878.9	78149.28			
df	3	3			
# Particles	1138	1149			
Box volume cm^3	2037673	2037673			
Volume voids cm^3	1134103	1148151			
Porosity	0.55657	0.56346			
Surface Area (cm^2)	475468.37	481641.7			

The differences in resistance were only 1% while at the largest pressure difference of 1000Pa, the flow rates were about 2.7% different, showing a good agreement between the two largest samples.

Sample set three had the most consistent and uniform behaviour. The difference between the two cuts in terms of their ratios of resistance values were at maximum 2.7%. This is consistent in both directions of the sample for flow and can be said to be the best of the three sample sets. The resistance values are almost identical in nature. One question that comes out of these results is whether the blocks of sub-samples added together in series and parallel combination can form the larger sample. This is more thoroughly examined in the next section of this work.

9.3.5 Discussion of sub-sampling PSM

When doing sub-samples of PSMs, it can be seen that the consolidation process has an influence on the final flow characteristics, namely the wall conditions where the geomechanical code forces spheres to be packed closer together, and thus having a lower porosity in that part of the sample and thus a higher resistance value. In addition, on the other top side, the surface of the consolidated model also had an effect on the resistance. The sub-samples tended to have a higher porosity, due to extra airspace. To test the independence of the Atkinson's friction factor compared to size, the following Moody diagram comparison was made. The results indicated that there is no representative elemental volume within a PSM.

9.3.6 Atkinson's friction factor appears to be scale invariant

The Moody diagram of the three samples of different volumes from the previous section is presented in Figure 107. The following steps, used to prepare the Moody diagram, are summarized in Table 38. .

1. Sample flow rates were obtained from the PSMs.
2. The sample volumes were calculated.
3. The geometric dissection of four slices of the sample (using Chapter 7 techniques) obtained an average perimeter and cross-sectional area for flow.
4. The Atkinson's friction factor was calculated using the average geometry values and pressure drop across the PSM and the LINEST calculated resistances from the previous section.
5. The average velocity was calculated from the flow rate and average area.

6. The hydraulic diameter was calculated.

7. The Reynolds number was calculated.

8. The Darcy Weisbach friction factor was calculated by halving the Atkinson's friction factor.

9. Values 8 and 9 were plotted on the Moody Chart for the relative pipe roughness ratio.

10. Value epsilon for the asperity heights was found.

Table 35: Values for the independence of friction factor calculation

		Test 1	Test 2	Test 3
Sample flow rate	(m^3/s)	0.0219	0.014	0.067
Sample volume	(m^3)	0.4522	0.632	2.037
Average area	(m^2)	0.0023	0.002	0.007
Average perimeter	(m)	0.7092	0.5739	2.093
Atkinson's friction factor k	(kg/m^3)	0.0212	0.0232	0.0208
Average velocity	(m/s)	9.3693	8.966	9.871
Dh	(m)	0.0131	0.011	0.013
Reynolds Number		7.48E+03	6.26E+03	7.56E+03
Friction factor (Darcy)		0.0353	0.0387	0.0346
Epsilon	(m)	9.9E-05	1.1E-05	9.6E-05

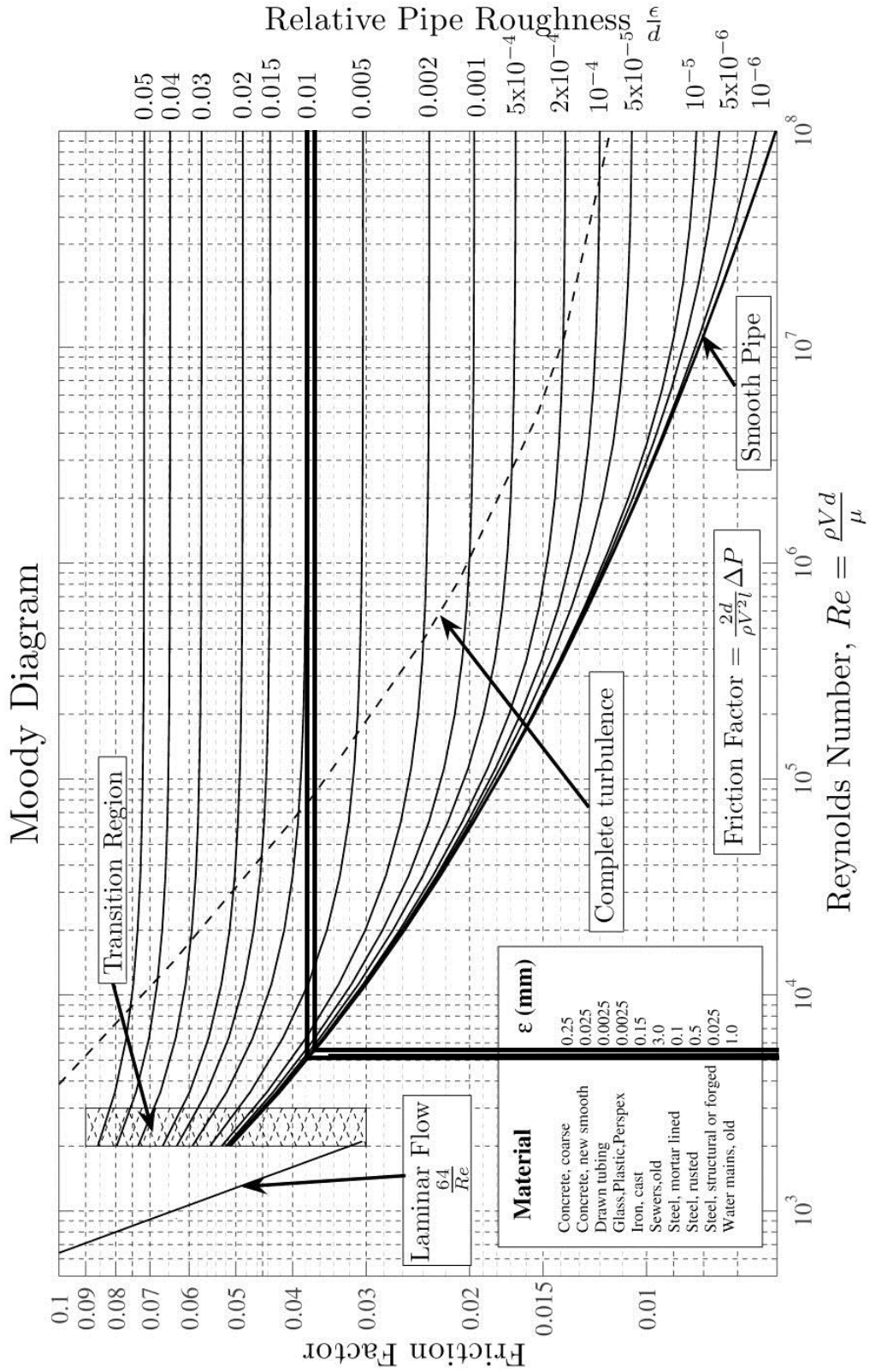

Figure 107: Moody diagram with values used to calculate the asperity height and the Re number and friction factor indicating a hydraulically smooth pipe. The heights are close to

0.1mm, which is around 0.125mm from the microscopy in section 4.2, if looked at normal to the direction of flow.

The results of this section show that the Atkinson's friction factor is truly independent of the volume of the porous sample examined. Also, the values of the Moody diagram show that the surface is hydraulically smooth, which is the case since no additional roughness was added to the material properties of the code.

The microscopy from Chapter 4 shows that the layers of the 3D-printer material are 0.25mm in size. If these layers are assumed to be spherical bulges in nature, which they appear to be visually, then when the normal direction of flow is taken into account, the true asperity height is 0.1mm, which is consistent with the results of this section.

The representative elemental volume can be assumed, with evidence from these results, to be any volume contained within a PSM. In the following section, an attempt to relate the results of the complete sampling campaign and the volume of the sample used will be tested.

9.3.7 Complete sub-sample results and power law test

The Rosin Rammler distribution that formed the assemblage had a d_c = 0.012m and a shape factor n = 4.5. The complete flow rate, resistance, and geometric properties for all of the samples are shown in Table 36.

Table 36: Complete summary of results for the entire sub-sampling campaign

Sample # (m)	Height (cm)	Width (cm)	Length (cm)	#Spheres	Resistance (Ns^2m^{-8})
1	63.11	61.94	161.8	408	2074658
2	63.11	61.94	161.8	403	2165480
3	63.11	61.94	161.8	365	1965952
4	63.11	61.94	161.8	395	2208069
5	63.11	61.94	161.8	412	2526102
6	40	69.88	161.8	269	4974684
7	40	69.88	161.8	315	4808585
8	40	69.88	161.8	303	4239884
9	40	69.88	161.8	295	4437264
10	40	69.88	161.8	280	4224155
11	180.22	69.88	161.8	1138	222553
12	180.22	69.88	161.8	1149	218264

Sample # (m)	Bulk Volume (cm^3)	Void Volume (cm^3)	Porosity	Interface Area (cm^2)	Resistance (Ns^2m^{-8})
1	632482	357418	0.5651	155780.56	2074658
2	632482	355581	0.5622	153603.35	2165480
3	632482	355457	0.5620	154703.11	1965952
4	632482	357281	0.5649	152994.42	2208069
5	632482	345824	0.5468	157406.69	2526102
6	452263	250253	0.5533	117852.10	4974684
7	452263	247790	0.5479	120775.01	4808585
8	452263	285475	0.6312	100696.83	4239884
9	452263	250606	0.5541	114953.31	4437264
10	452263	249978	0.5527	117932.72	4224155
11	2037672	1134103	0.5566	475468.37	222553
12	2037672	1148151	0.5635	481641.67	218264

9.3.8 Power law test

The hypothesis tested here is that for a specific volume chosen, the resistance can be estimated by the pressure drop vs flow rate curve in Figure 108, because the sampling campaign follows a power law relationship.

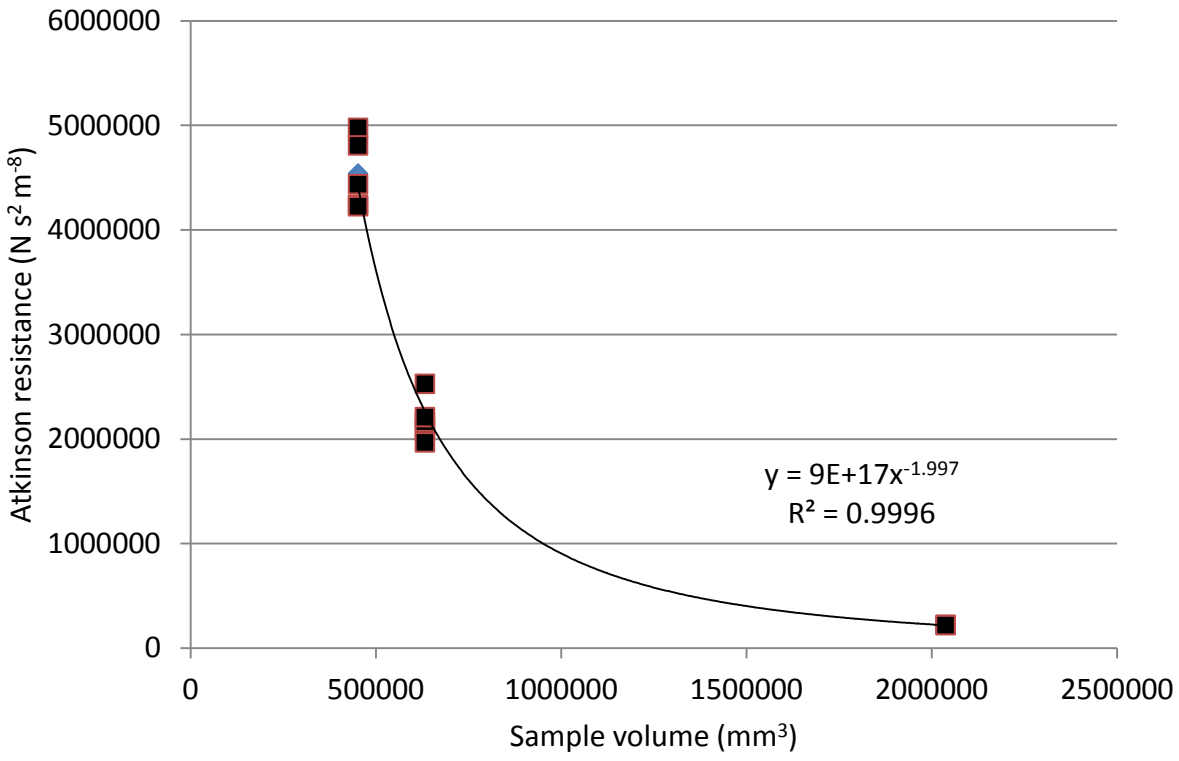

Figure 108: Volume of the containment area vs the Atkinson's Resistance

It was questioned whether the power law trendline from Figure 108 would be held if tested with a new sub-sample of 1300000 cubic millimeters. To test this theory, a containment volume of 1300000 mm^3 was tested. The sample was run through two CFD tests using the pressure drops to add two new points to the chart seen in Figure 112. Table 37 contains the results of the two chosen sub-sample sizes to test the hypothesis.

Table 37: Results of two further sampled points to see if the power law applies to the sets of curves created in the entire sample campaign

Height (cm)	Width (cm)	Length (cm)	Bulk Volume mm^3	Resistance (Ns^2m^{-8})	Volume Voids mm^3	Porosity	Surface Area mm^2
160.692	50	161.8	1299998.28	530084	691584.68	0.53199	307260.4
160.692	50	161.8	1299998.28	562923	684664.8	0.52667	312499

9.3.9 Atkinson resistance appears to follow power law scaling

From the results shown in Figure 109 with the same power law trendline overlaid, it is apparent that if a volume is chosen from the sub-sample, a power law may apply for the relationship to the Atkinson's resistance material property.

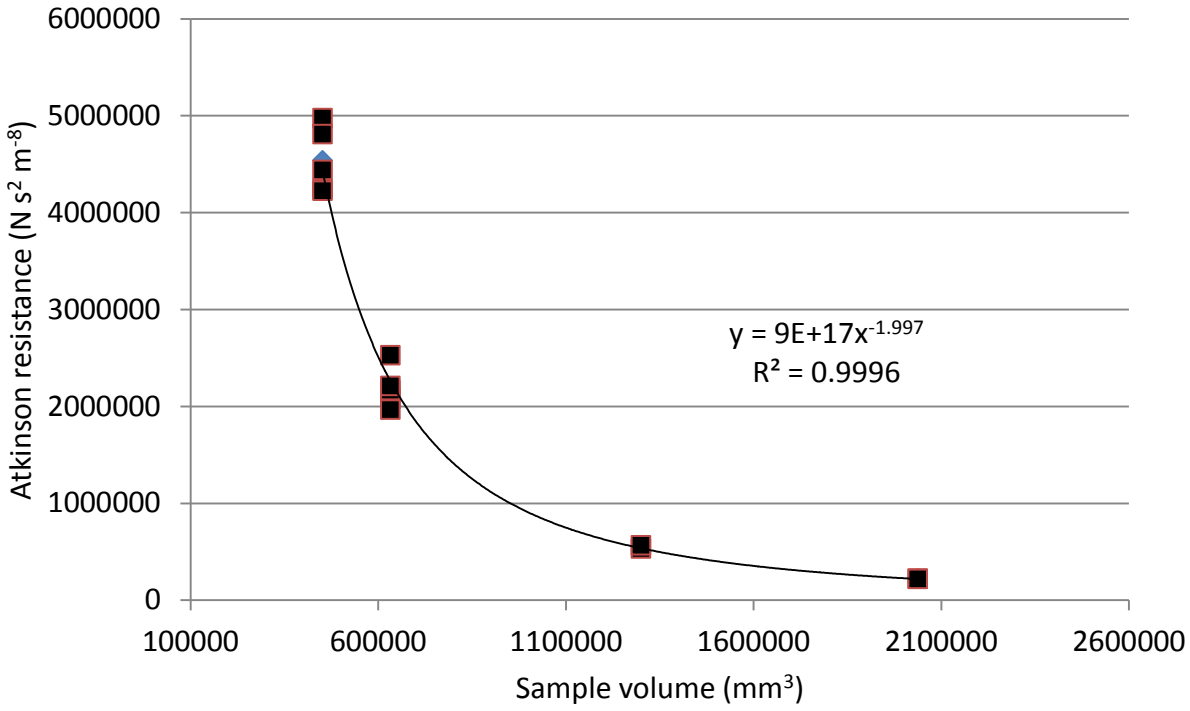

Figure 109: The complete set of sub-samples along with the newly plotted test results

The information plotted perfectly with the other results and did not change the power trendline equation at all, proving that this sub-sample set does indeed go by a power law and is predictable for a different size than was originally chosen.

9.4 Scaling air flow resistance by adopting series and parallel combinations of PSMs

Within the third scaling technique of PSMs, a sub-sampling campaign will be taken to see how homogenous the behaviour is for flow conditions in a heterogeneous sample PSM. Also, a detailed examination will be performed to see if series and parallel combination behaviours, expected for ducts obeying Atkinson's equation, can be recovered in PSMs.

9.4.1 The complete PSM used for testing

A PSM of 1500 spheres was generated, consolidated, and transferred into the Fluid Flow code. The Rosin Rammler parameters were the shape factor n = 2 and specific diameter d_c = 0.8m, which are realistic numbers taken from several mining methods such as open pit, drift, and traditional stope drill and blast techniques (Cunningham, 2005). The value of density comes from Norite rock and is typical for other igneous rocks. In Table 38, the Rosin Rammler distribution used in creating the spheres is shown.

Table 38: Rosin Rammler distribution by particles for diameter of interest = 0.8 and spread diameter n =2 used for PSM generation

	Cumulative	Conversion					
A	0.8						
n	2						
Sieve Size	Total mass (kg)	Density 2700 kg/m^3	Volume of 1 Sphere 4/3pir^3	Total Volume m^3	#balls	If 1500 spheres wanted	Integer Value
0							
0.1	1.56	2700.00	0.0005	0.0005	1.103	858.09	858.00
0.2	4.50	2700.00	0.0041	0.0016	0.397	309.41	309.00
0.3	7.06	2700.00	0.0141	0.0026	0.184	143.83	144.00
0.4	9.00	2700.00	0.0335	0.0033	0.099	77.35	77.00
0.5	10.22	2700.00	0.0654	0.0037	0.057	44.97	45.00
0.6	10.69	2700.00	0.1130	0.0039	0.035	27.22	27.00
0.7	10.47	2700.00	0.1795	0.0038	0.021	16.79	17.00
0.8	9.72	2700.00	0.2680	0.0036	0.013	10.44	10.00
0.9	8.58	2700.00	0.3817	0.0031	0.008	6.47	6.00
1	7.24	2700.00	0.5235	0.0026	0.005	3.98	4.00
2	20.77	2700.00	4.1887	0.0076	0.001	1.43	1.00

In Figure 110, the overall sample dissected is shown. The boxes are the various cuts or sub-samples used in testing how the sample behaves in terms of resistance, first from the smallest box or base unit of 1917 cm by 965.5 cm by 2000 cm. For series measurement, the length was doubled from 2000 to 4000 cm. This same study was then completed for the next level up by doubling the width of the base unit to test parallelism. This test was furthered by then doubling the widths and lengths again to get to a final block sample.

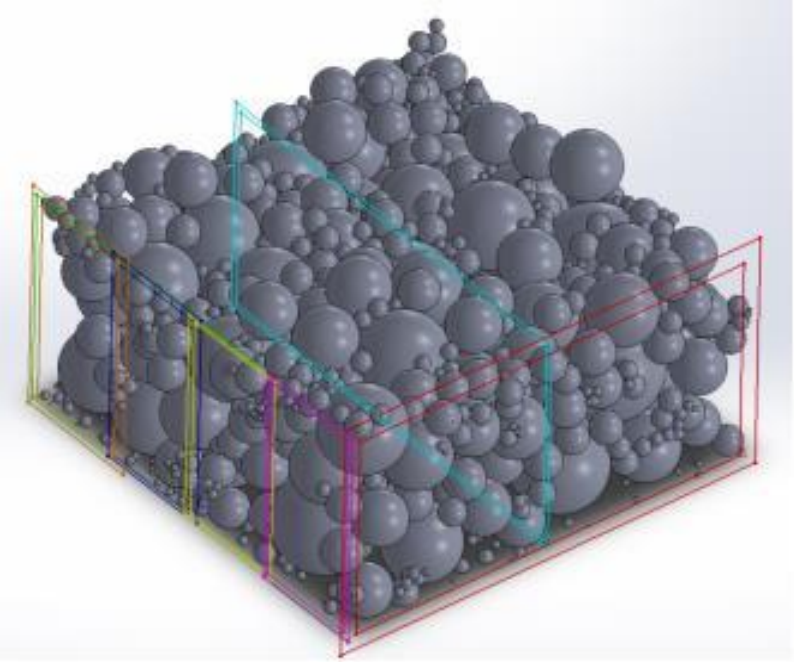

Figure 110: Total PSM inputted into the CAD/CAM environment. Boxes of different colors show the sub-sample box containment areas examined

In Figure 111, a fully rendered version of the PSM is shown. This is the first time a Rosin

Rammler distribution consistent with mining values has been shown in this fashion.

Figure 111: Full rendering of a realistic blasted rock PSM

9.4.2 Full list of cut results taken in this sampling campaign

Table 39 shows the results of each individual case sampled in this campaign in the same method as the 'constant head' test methodology used throughout this thesis. Following the listing of these results, the possible combinations of series and parallel behaviour are displayed.

Table 39: Summary of results from the sub-sampling campaign

Sample Number	Height (cm)	Width (cm)	Length (cm)	Resistance (Ns^2m^{-8})
1	1917	1931	2000	1.9
2	1917	1931	4000	4.4
3	1917	3862	2000	0.5
4	1917	3862	4000	1.1
5	1917	965.5	2000	10.8
6	1917	965.5	4000	18.2
7	1917	965.5	4000	21.1
8	1917	965.5	2000	10
9	1917	965.5	4000	20.8
10	1917	965.5	2000	11.8
11	1917	965.5	4000	28.7
12	1917	965.5	2000	12.4
13	1917	3862	4000	1.2
14	1917	3862	2000	0.6

The following relationships for series and parallel behaviour must be understood for this exercise of testing the behaviour of PSMs. They have originally derived for air flow branches using Atkinson resistance:

Series relationship:

$$R_1 + R_2 = R_t \tag{53}$$

Parallel relationship:

$$\frac{1}{\sqrt{R_1}} + \frac{1}{\sqrt{R_2}} = \frac{1}{\sqrt{R_T}} \tag{54}$$

where R_t is the total combined resistance of the combination airways or PSM blocks.

In Figure 114, a summary of how the results expected from CFD tests of larger sized PSM can be predicted from the CFD tests on a base sized PSM is presented. The base size corresponds to the members of the Set A, comprising four samples drawn from the PSM shown in Figure 111. The link between air flow resistance values of the various sets is the series and parallel combination formulae above. Hence, for example, two elements of Set A connected in series should return estimates of air flow resistance corresponding to the air flow resistances determined from CFD for elements of Set B.

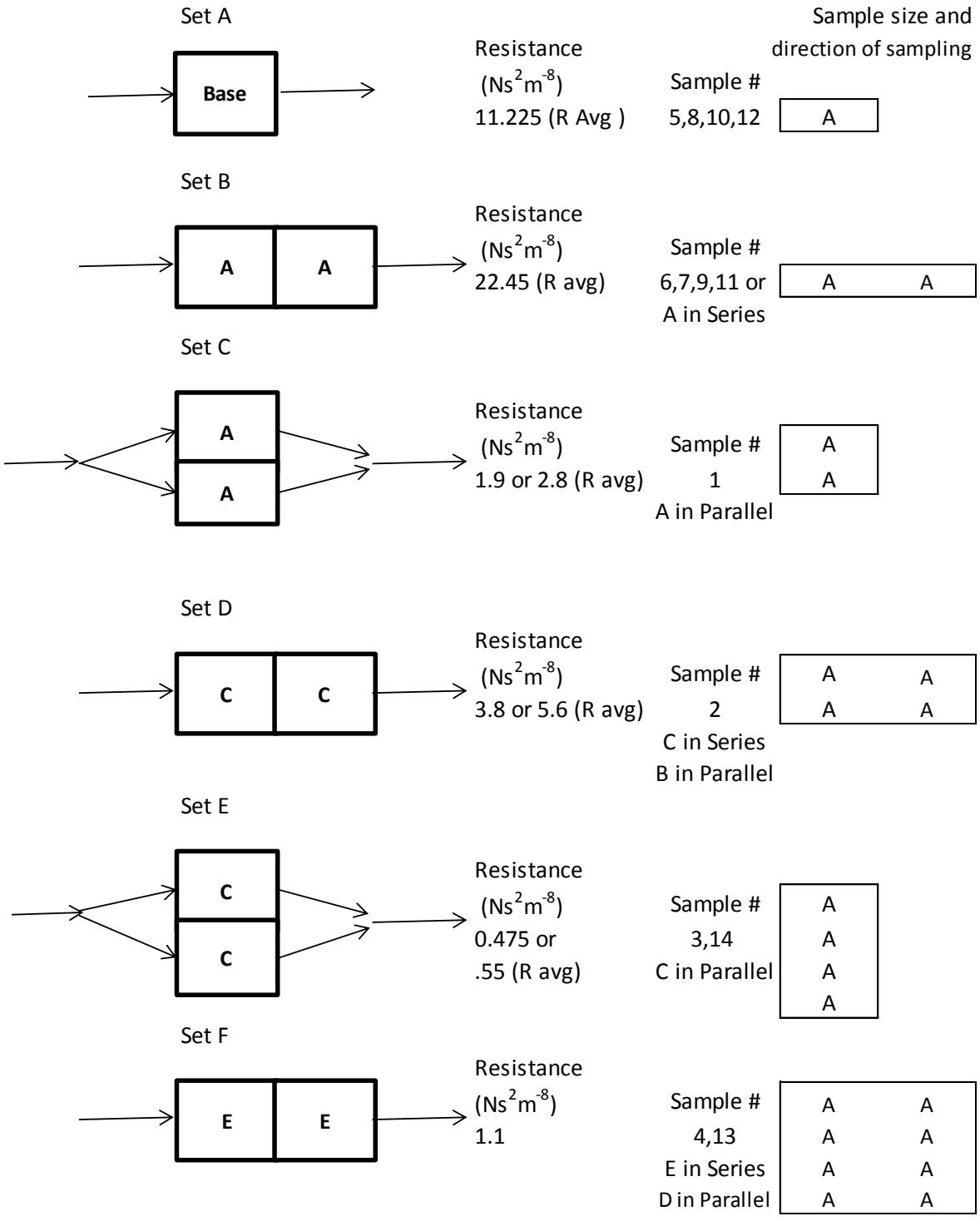

Figure 112: Diagram of how the series and parallel combinations from the base model to the largest sub-sample. The resistances are both theoretically calculated and can be compared with the individual sample sizes such as in set E, the value can be the same as sample 4 or 13.

9.4.3 Discussion and results of the sub-sampling technique

The following section is an examination of the previous results in terms of Kirchoff's rules of equivalent resistance due to series and parallel behaviour (McPherson, 2007).

9.4.3.1 Base model (A)

The Atkinson's resistance values for the first set of samples ranged between 10 to 12.4 $Ns^2\ m^{-8}$. The value of average resistance was 11.254 Ns^2m^{-8}. This is the smallest sample tested and serves as a base block for larger sample recreation.

9.4.3.2 Sample B results and discussion

The first series results compare the previous resistance levels of 10-12 $Ns^2\ m^{-8}$ in sample A to the next set of samples which was doubled in length. This means that according to Kirchoff's rules, the resistance should double to around 20-24 $Ns^2\ m^{-8}$. The average value of these sets was 22.4584 Ns^2m^{-8}. Sample 11 has the lowest porosity at 41%. In terms of the other samples in the set, its resistance is higher than the 20-24 Ns^2m^{-8} range to a value of 28 Ns^2m^{-8} although it has approximately the same magnitude. Sample 11 is also a wall sample, meaning this is where the PFC geomechanical portion of the PSM has potentially a substantial influence on the flow evaluations of the sample.

9.4.3.3 Sample C results and discussion

In this sample comparison, Sample 1 is tested or the combination of set A is taken in parallel. Since the widths are doubled in this new case, the resistance is expected to be about 2^2 or 4 times

less than the previous sample set 1 to have resistances in the 2-3 Ns^2m^{-8} range. The average resistance was 2.8 Ns^2m^{-8}¸ confirming that the series and parallel laws are taken to hold for PSMs.

9.4.3.4 Sample D results and discussion

In this sample comparison, Sample set C is placed in series. The lengths are doubled in this new case. The resistance is expected to be about 4 times greater than the previous Sample set C to have resistances in the 4.5-7 Ns^2m^{-8} range. The average of the samples was 5.6 Ns^2m^{-8}. The sample set data appears to show series behaviour with Sample C. The high potential expected resistance is again the influence of sample 11 (the wall model).

9.4.3.5 Sample E results and discussion

In this sample comparison, Sample set C is compared in parallel. The resistance is expected be in the 0.48-0.56 Ns^2m^{-8} range. The average value for the resistance of the samples was 0.55 Ns^2m^{-8}. Sample 14 as a sample equivalent is also a wall sample so the slightly higher resistance of 0.6 Ns^2m^{-8} is somewhat expected.

9.4.3.6 Sample F results

In this sample comparison, the fourth sample (the overall bulk sample), or set E, is compared in series. The resistance is expected to be about double Sample E to have resistances in the 1-1.2 Ns^2m^{-8} range. This final sample set of this chapter works both in series and in parallel to other

sample sets. This is the bulk sample that, when the correct series and parallel combinations are calculated, should be almost exactly the same. The sub-sample results of Sample 4 and 13 both show this to be the case and the capability to sum up series and parallel combinations for formation of the original sample.

9.4.3.7 Series/parallel combinations discussion

Overall, it has been shown that the behaviour of PSM can be predicted according to Kirchoff's rules of series and parallel air flow resistance combinations. This finding provides a third basis on which air flow resistance for PSM may be scaled so that small scale *in-situ* test or laboratory test results may be rendered applicable for defining the properties for large scale air and heat flow models of fractured broken rock bodies. The target scaling transformation is from laboratory scale to the size of the smallest octree equivalent continuum element of a CFD mesh. On the basis of the results in this section, Table 40 summarizes the values of Atkinson's resistance for increasing volumes of PSM with Rosin Rammler parameters $n = 2$ and $d_c = 0.8$m.

Table 40: Summary of resistance behaviour with increasing volume in series and parallel

	A	2A x 2A	4A x 4A
Height (m)	1.917	3.834	7.668
Width (m)	0.966	1.931	3.862
Length (m)	2.000	4.000	8.000
Volume (m^3)	3.702	29.614	236.911
Resistance ($N\ s^2\ m^{-8}$)	11.225	4.5	2.2

If the Atkinson's resistance of these data are plotted against sample volume (Figure 113) the following curves are obtained, which fit well to a power law on either log-log or normal scales.

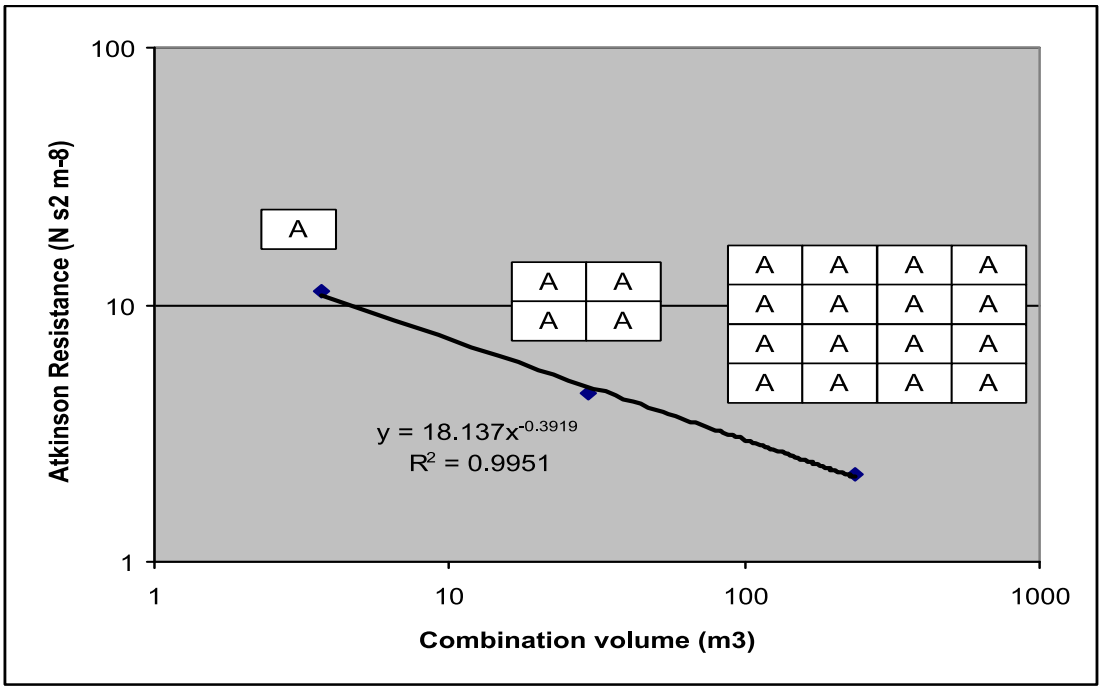

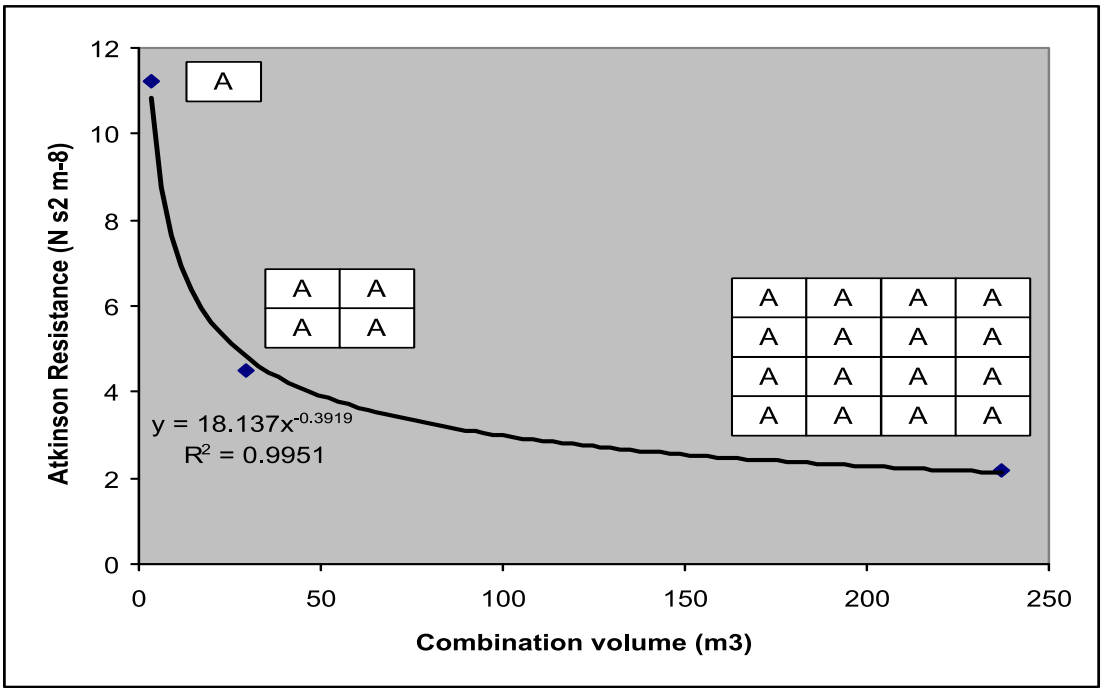

Figure 113: Plot of the sample calculation looking at the either normal or log-log scale

9.5 Conclusions

The questions asked in this chapter related to fundamental scaling behaviour patterns within PSM air flow resistance models, with a view to establishing how results from laboratory experiments of PSM can be used in applications involving much larger scale engineering problems. The three methods investigated were:

- self-similar scaling,
- scaling air flow resistance with a power law fit, and;
- series and parallel aggregation of base PSM behaviour.

The airflow and resistance curves shown in the first part of this chapter seem to follow a law of scaling, which is a power law relationship when the Atkinson's resistance is plotted against the bulk volume or containment volume of a sample. The uniform distribution PSM has a linear trend according to the power law curve fitting, while the Rosin Rammler distribution has a distinct curve to the power law relationship. This hypothesis of a power law relation was tested with a sub-sample of a volume chosen by the user and the resistances were in line with the power line approximation.

When directly compared by series and parallel adaptations of sub-sampling by the construction of discrete blocks or resistance branches, it has been shown that by constructing the smaller sub-samples by series and parallel rules used in ventilation practices, a large full sample resistance can be accurately predicted.

From the results of the last section, it may be appreciated that each of the three methods discussed are equivalent to one another. The third method has an advantage over the former two

because the basis for scaling is known physical laws governing combinations of elements, rather than reliance on empirical fitting (whether these be from physical experimental data or the results of CFD simulations). The choice of method to assume to scale laboratory scale results to the minimum element volume in a large scale CFD simulation of a fractured, porous body of rock would thus depend on the experimental information available,

A key point that was shown in the self-similar scaling section is that two separate models of similar porosity can have substantially different values of resistance due to the different particle sizes tested. In terms of airflow and heat exchange, when numbers associated in mathematical formulations involving porosity are given, a term of what size or scale relative to the low level parameters such as total surface area of the sample should also be associated with it. So, if a characteristic of resistance is stated, the parameter of the diameter of interest for the Rosin Rammler or uniform distribution must also be stated. If that number is for example 10mm, the resistance is much different at 1m, even though both samples may have the exact same value for porosity and packing arrangement.

This chapter demonstrated that with PSMs replaced by an equivalent continuum, a nearly identical (99%) value for the resistance can be found. This is the important link for being able to use the bulk parameters from the discrete, low-level geometry constraints in PSM for application of large scale problems. This method is able to keep the complex low-level design characteristics needed in geomaterial modelling while still being able to calculate a solution using mathematical reductions of bulk values. The main advantage to this method is a decrease in calculation time and processor requirements, which are substantial for PSMs.

10 Experimental data collection from an approximately 1 km^3 seasonal thermal regenerator

10.1 Introduction

The purpose of this chapter is to show how data for the calculation of the pressure drop across a large-scale porous media problem was collected using a constant head variant pressure test, and the subsequent presentation of the results. This pressure drop was then used to compare with values from a CFD tool representation of the problem, using derived parameters from PSM. This was performed to show general applicability of the technique in Chapter 11.

The site of the experiment was at Creighton Mine's Natural Heat Exchange Area (NHEA). Creighton Mine is located in the Sudbury basin and was discovered in 1856, with the first ore shipment in 1901. During the site's 113 years of production, mining methods such as open pit, shrinkage, blasthole, panel caving, square set, undercut-and-fill and vertical retreat techniques have been used (Kocsis, 2009).

During the process of mining that became the NHEA, open-pit block and sub-level caving mining techniques were used. The orebody is roughly dipping at 45 degrees, and was intersected at 90 degree angles by 96 drawpoints (Fava *et al.* 2011) which were used to feed slusher trenches for ore removal as schematised in Figure 115. The drawpoints have been classified into "Blocks" numbered 1 through 6 from south to north in direction on the eastern side of the NHEA. The surface also subsided during this time, causing a unique surface profile of broken and fragmented rock underneath leading to these drawpoints, as shown in Figure 114.

Figure 114: Creighton NHEA system looking east to west. The widths are both approximately 900m. Underneath the surface, trenches go down to a depth of approximately 450m below. (Image courtesy of Vale)

In the late 1960's and early 1970's, air flow patterns of cold air in the summer, and warm air in the winter, were noticed and built into the mine ventilation strategy. The NHEA serves as the main surface air intake and thermal regulator of the mine. In the last ten years, studies have focused on the thermal characteristics of the NHEA, with the latest estimates being in the area of $17MW_{th}$ (Fava *et al.* 2011) of cooling being provided to the now much deeper mine.

In this research, the NHEA was classified as thermal reservoir or a seasonal regenerator. This term was used because unlike previous research, the CFD code model will provide information on the temperatures of the rock, and not just the air. In the summer and winter months, the reason

for heating and cooling of the air is due to the differences between the rock temperatures and the air. The thermal energy is either gained or lost between the air and the rock, depending on the season. The cycle keeps repeating due to the changing of the seasons, and this periodicity is why the NHEA could also be termed a seasonal thermal regenerator.

The need to improve the understanding of the processes ongoing within the NHEA has led to the need to be able to model the system using modern CFD codes and techniques. Since the area had never been modelled by CFD code before, one of the types of information that could be measured physically as a performance variable was the pressure drop across the NHEA. This data collection was done by comparing the pressure difference between the surface to a level at a depth of approximately 230m below surface, known as the 800 Level.

An experimental procedure for a constant head test needed to be modified for data collection of this pressure drop. A CFD equivalent system of the experiment then also had to be created for comparison to this physical data, which is detailed in the next chapter.

10.2 In-situ observations of bulk air pressure characteristics

Within this section, an explanation of the constant head pressure experiment adapted to the NHEA is presented. The objective of this constant head pressure test is to be able to use the pressure drop across the physical pile of broken rock as a performance characteristic. The test was conducted at an elevation of 230m from the surface of the caved material shown in Figure 115.

The pressure values obtained from the experiment are from high precision barometric standard readings from two sensors. One of these sensors was located on surface next to the air intake system (broken rock) and one underground sensor at the air collector level (230m below) before the main ventilation system consisting of several sets of fans in series / parallel combinations. To assess the natural conditions of the system without the addition of work from any outside sources, this experiment was done before, during, and after a system wide electrical shutdown from scheduled maintenance.

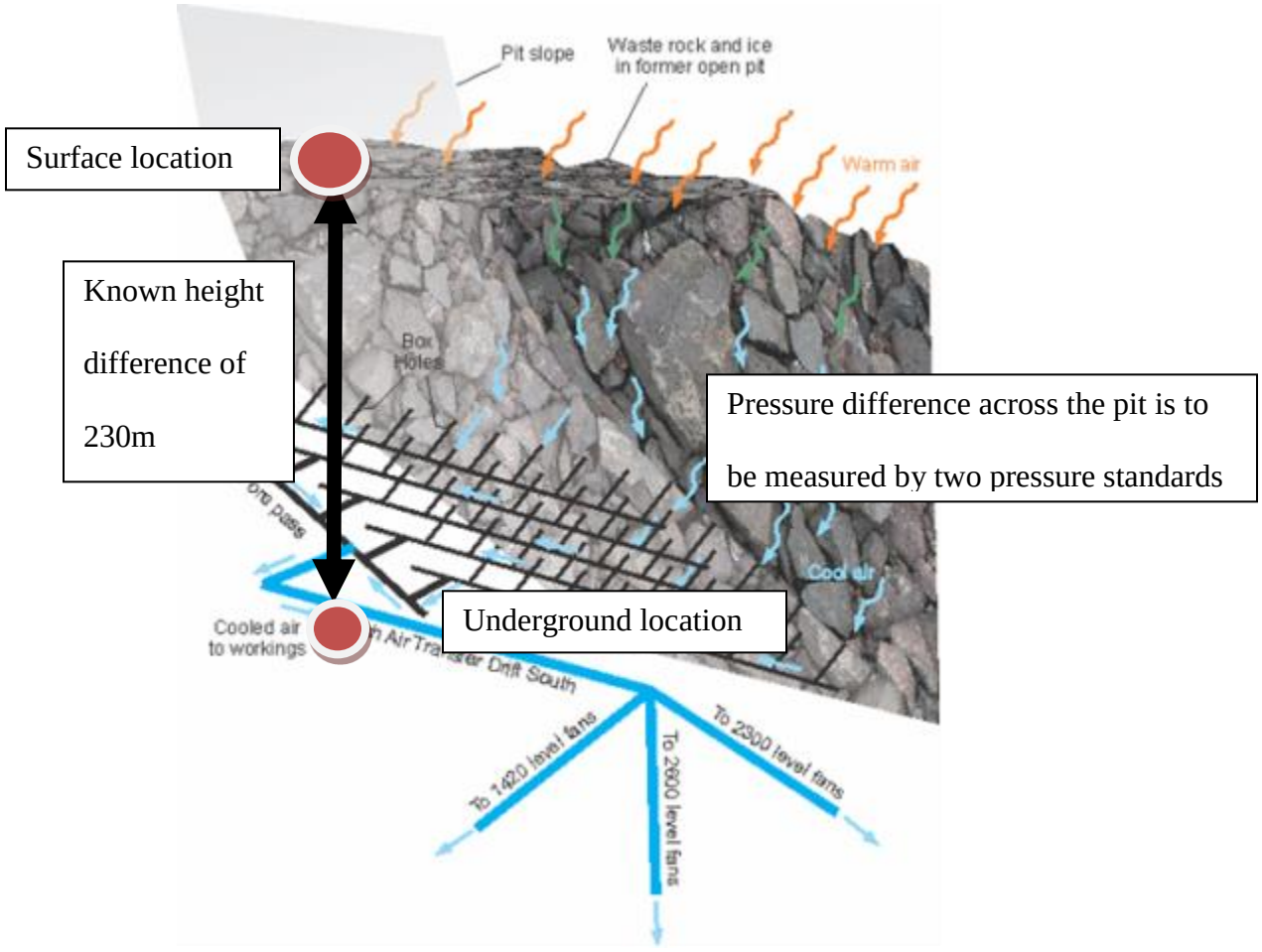

Figure 115: Conceptual NHEA modified constant head pressure test

10.3 Description of testing equipment used in kits

In this experiment, there were two set ups constructed, one that worked off normal 110V A.C power connection on the surface near the edge of the open pit, and another set on the 800 Level with both AC and DC capability to ensure continuous monitoring once the main AC power to the system was shut off. Common elements of the two set-ups were a laptop, barometer and digital monitoring software. The uninterruptable power system (UPS) also had a charger as well as an inverter within the underground monitoring station.

10.3.1 Barometers: 2 Digiquartz Parascientific Model 745-16B High Accuracy Barometric Standard

The same Barometric Standards were used as in Chapter 4.6.2.

10.3.2 Laptops

Two laptops were used, an ASUS eeePC notebook that is shown in Figure 116, as well as an HP-520 (Hewlett-Packard, 2013). The two laptops were connected through RS-232 serial connections to the barometers.

Figure 116: Asus computer used in underground monitoring station

10.3.3 Digiquartz software

Both stations used the Digiquartz Interactive 2.0 edition software (Digiquartz, 2013). This monitoring software is capable of pressure readings and then saving them to a text (.txt) file. The data was processed into Microsoft Excel (.xls) format.

10.3.4 MotoMaster Eliminator 400W inverter

In the uninterruptable power system, a 400W Inverter (Figure 117) was placed directly between the barometer and the two batteries placed in parallel for the system kit.

Figure 117: Image of inverter used in experiment (Canadian Tire, 2013)

10.3.5 MotoMaster Eliminator intelligent battery charger

In the kit system, the battery charger was placed from the extension cord on normal power to the batteries placed in parallel. Figure 118 shows the charger used in this experiment.

Figure 118: Battery charger used in experiment

10.3.6 Batteries: SureStart and MotoMaster 72 car batteries

Two batteries, shown in Figure 119, were connected in parallel for this experiment. This link in parallel was done to add the 45 Amp Hr and 20 Amp Hr capacities together for endurance

instead of in series, which just adds to the voltage. This allows the Amp Hrs to be combined for a potential 65 Amp Hrs of monitoring when the power was shut-off to the minesite.

Figure 119: Batteries used in the underground uninterruptable power station (Canadian Tire, 2013)

10.3.7 Combined kits

The kits were then placed in plastic bins for environmental protection but both had holes placed in them so that the local pressure could still be monitored without interference. These two kits, as seen in Figure 120, are the two complete sensor packages of the constant head pressure test.

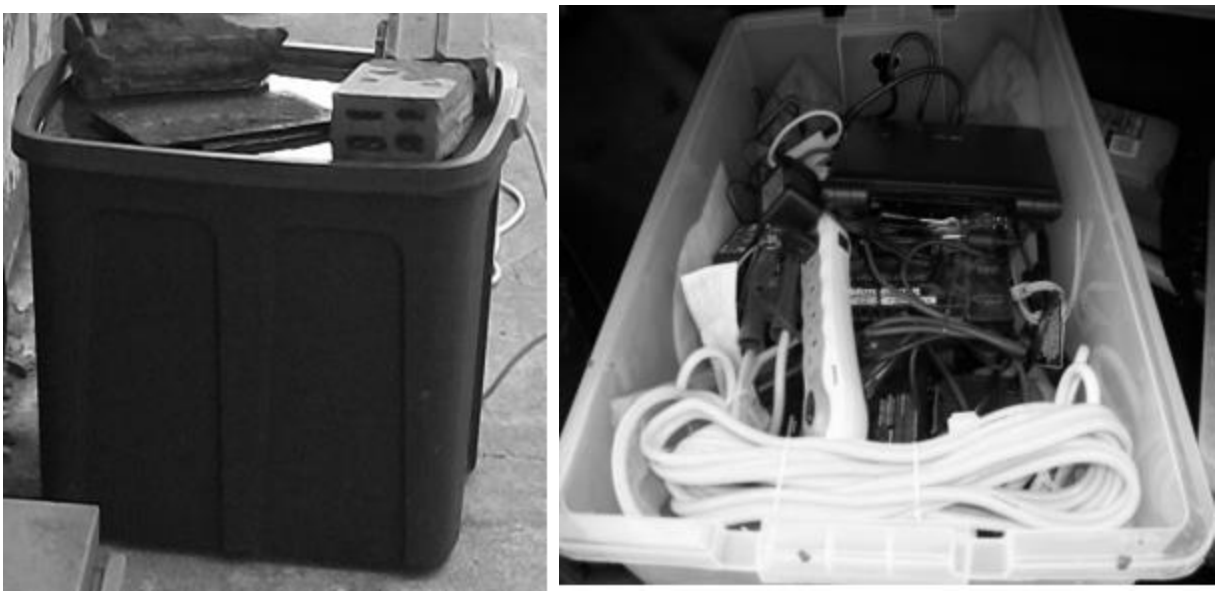

Figure 120: Both surface and underground fully constructed pressure monitoring kits

10.3.8 Description of the station location

Knowledge of the sampling locations is important to evaluate the pressure results. The surface station had to be sited at a position outside the direct zone of the pit influence (draw) and for a true reading in accordance with the CFD model described in Chapter 11. The underground location also had to be identifiable in the CFD model for sensing purposes and where the elevations were known.

10.3.9 Surface location

The surface station was located approximately 75m from the opening of the air intake system next to the building known as the 7 shaft, which is on the south side of Blocks 5 and 6 or the center to northern side of the eastern slope of the pit, as seen in Figures 121 and 122. There was a

normal AC power connection to this location only, and thus the laptop collected data for approximately 4hrs once the power was shut off due the barometer and laptop batteries.

Figure 121: View from the surface location to the pit approximately 75m away from the 7 shaft building.

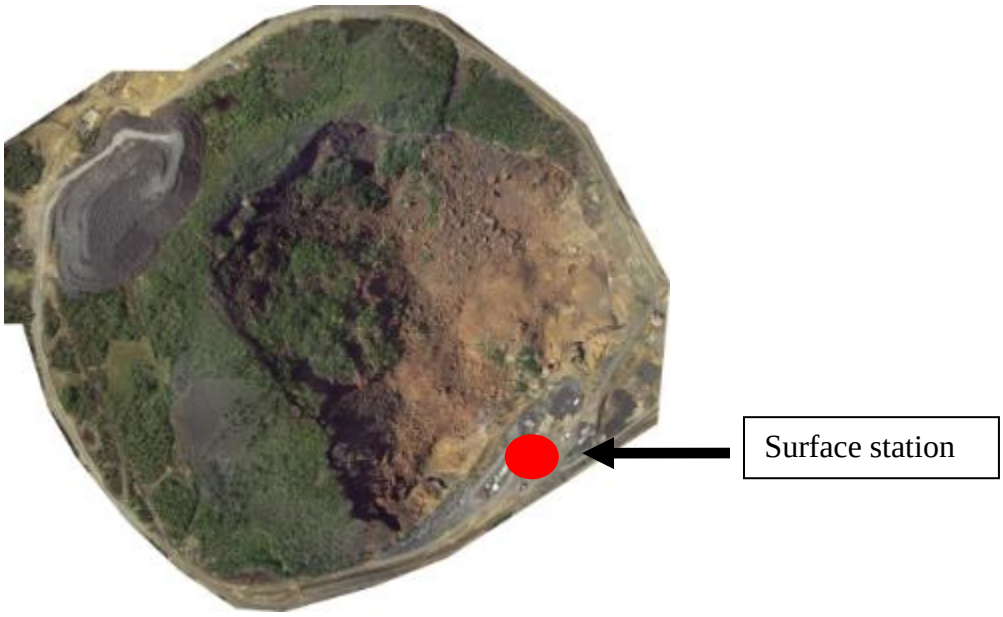

Figure 122: Surface pictures showing surface kit placement and relative distance to the surface intake (Image courtesy of Vale). This image was used to create the surface mesh file by Vale, which was later used in creation of the CFD model.

10.3.10 Underground location

The underground station was placed on the 800 Level, or collector level, for the NHEA (as schematically mapped in Figure 123 from VnetPC). There are four fresh air raises on this level, which lead to the fans on 1420, 2300, and 2600 Levels respectively. The underground sensor was in Block 2, which is represented in the transfer drift section within the VnetPC model and shown in Figure 124. The 800 Level is the main collection drift for the thermal regenerator. This location was chosen due to the ease of setting up the kit, and knowledge of the elevation.

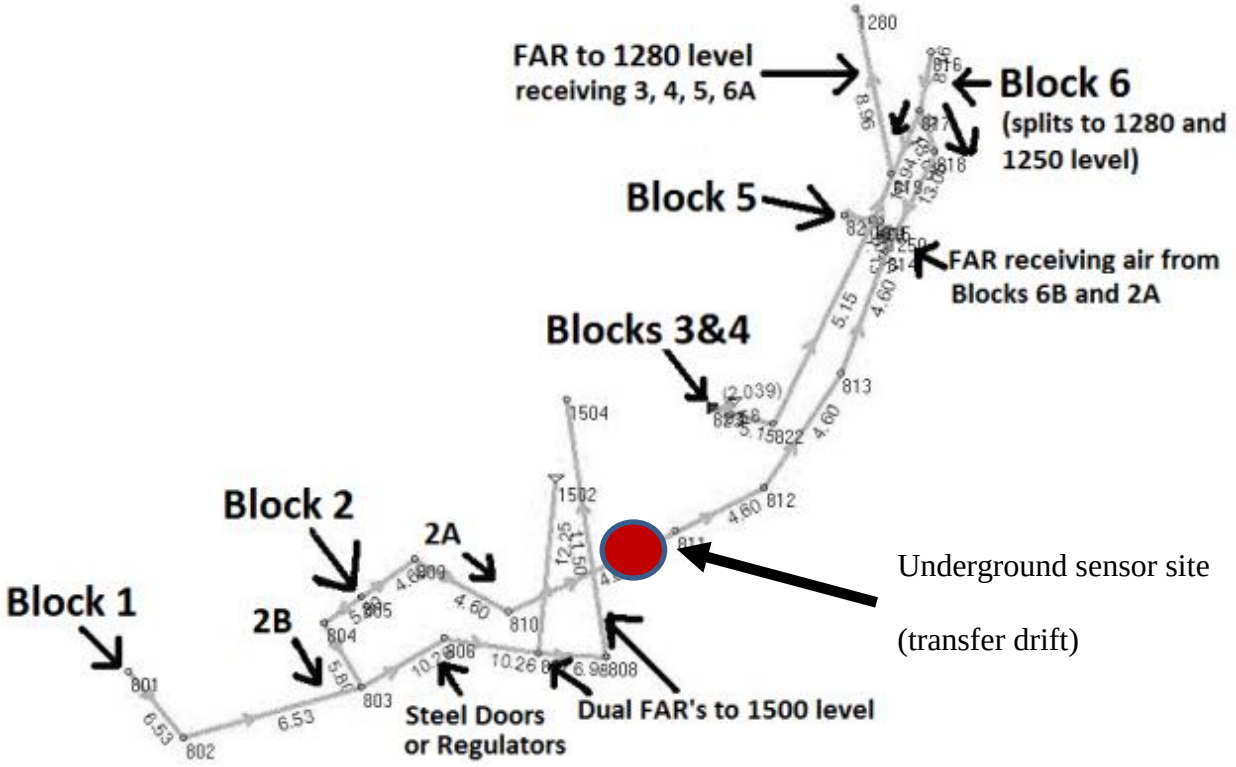

Figure 123: Plan view of 800 level from VnetPC model

Figure 124: Station near underground monitoring location on 800 Level

10.3.11 Experimental procedure

Calibration of the pressure offsets for the barometers, construction, and preparation of the laptops and equipment used in this experiment were done in the evening prior to the deployment of the monitoring systems. Deployment of the underground station was started at 8:30 AM with data collection starting at 9:04 AM on November 10th, 2011, one day before the full shut down period. The surface station was activated at 9:52 AM on the same date. Data was collected with at least one fan on in the system until approximately 8:20 AM on November 11th, 2011. Surface laptop data was collected until either the barometer or laptop battery was depleted at 11:50 AM or approximately 3.5 hrs later on the same day. Underground station data was collected until the

evening of Sunday, November 13th and the station was recovered at 10:30 A.M. on Monday, November 14th, 2011.

10.3.12 Surface data observations calibrated to Sudbury Airport data

After the mine maintenance shut down the power to the surface logger, the surface logging continued collecting data for approximately four hours on battery power. This was sufficient time to establish a correlation with data from Environment Canada for the Sudbury Airport by interpolating the data to match the timestamps. The airport station atmospheric pressure data was corrected to the elevation of the NHEA pit surface elevation by taking the differences of elevation above sea level between the two (348.4m at the airport compared to 300m at the NHEA surface). The two surface curves (the Sudbury Airport Environment Canada station and NHEA surface station) were compared and then combined (Figure 125) into one hybrid curve to show the continuity between the two for further analysis in comparing the underground station.

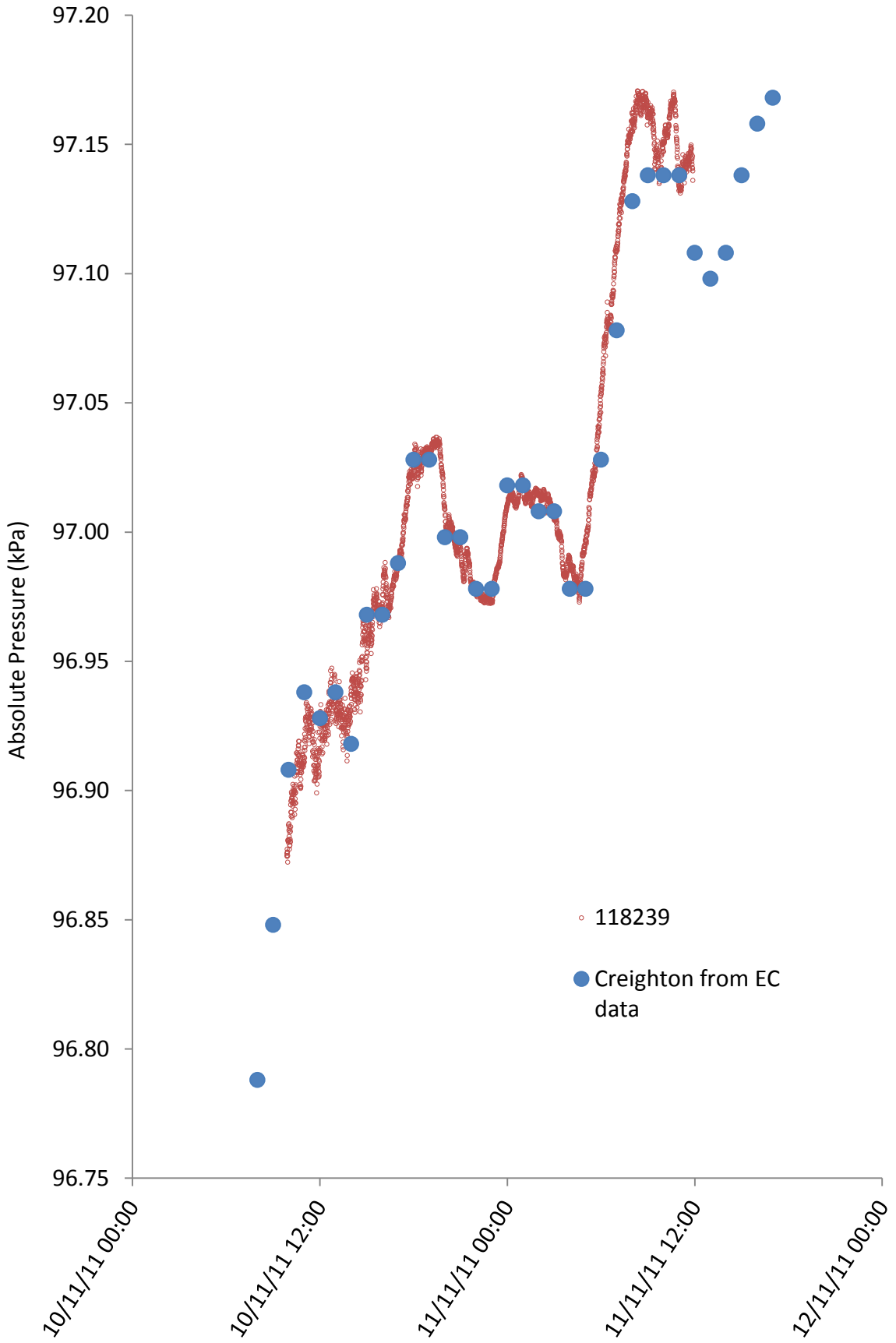
97.20
97.15
97.10
97.05
97.00
96.95
96.90
96.85
96.80
96.75
Absolute Pressure (kPa)
10/11/11 00:00
10/11/11 12:00
11/11/11 00:00
11/11/11 12:00
12/11/11 00:00
118239
Creighton from EC data

Figure 125: Environment Canada data corrected for elevation 348.4m above sea level to the surface barometer station located at the NHEA surface at 301m. This Environment Canada curve was then continued with the correction for comparison with the UG station.

10.3.13 Results of field observations and data interpretations

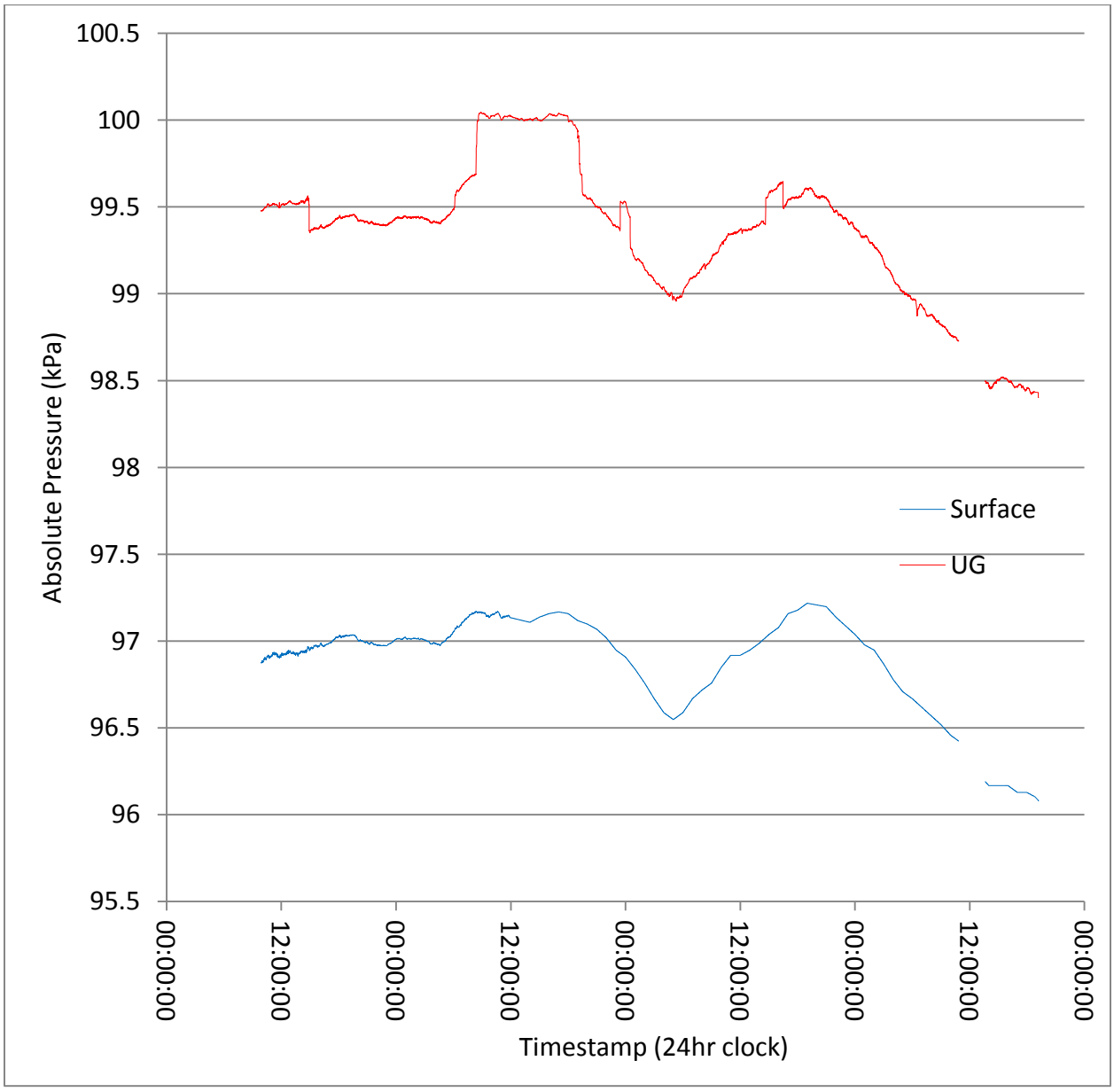

Figure 126: Absolute pressure curves of the combined surface (barometer plus Environment Canada station curve) and the underground station. These curves were monitored from November 10 – 14th, 2011.

Figure 126 shows the plotted pressure data readings collected from November 10th, 2011 through to November 14th, 2011. On the X-axis is the time stamp in 24hr clock format. Samples were taken every 30 seconds (other than the Environment Canada data which was hourly, after 11:50 AM on November 11th). On the Y-axis are the absolute pressure readings taken in kPa. The gauge pressure curves were corrected by moving the surface elevation pressure down from the 301m elevation above sea level of the surface to the 71m above sea level elevation of the floor of the 800 Level.

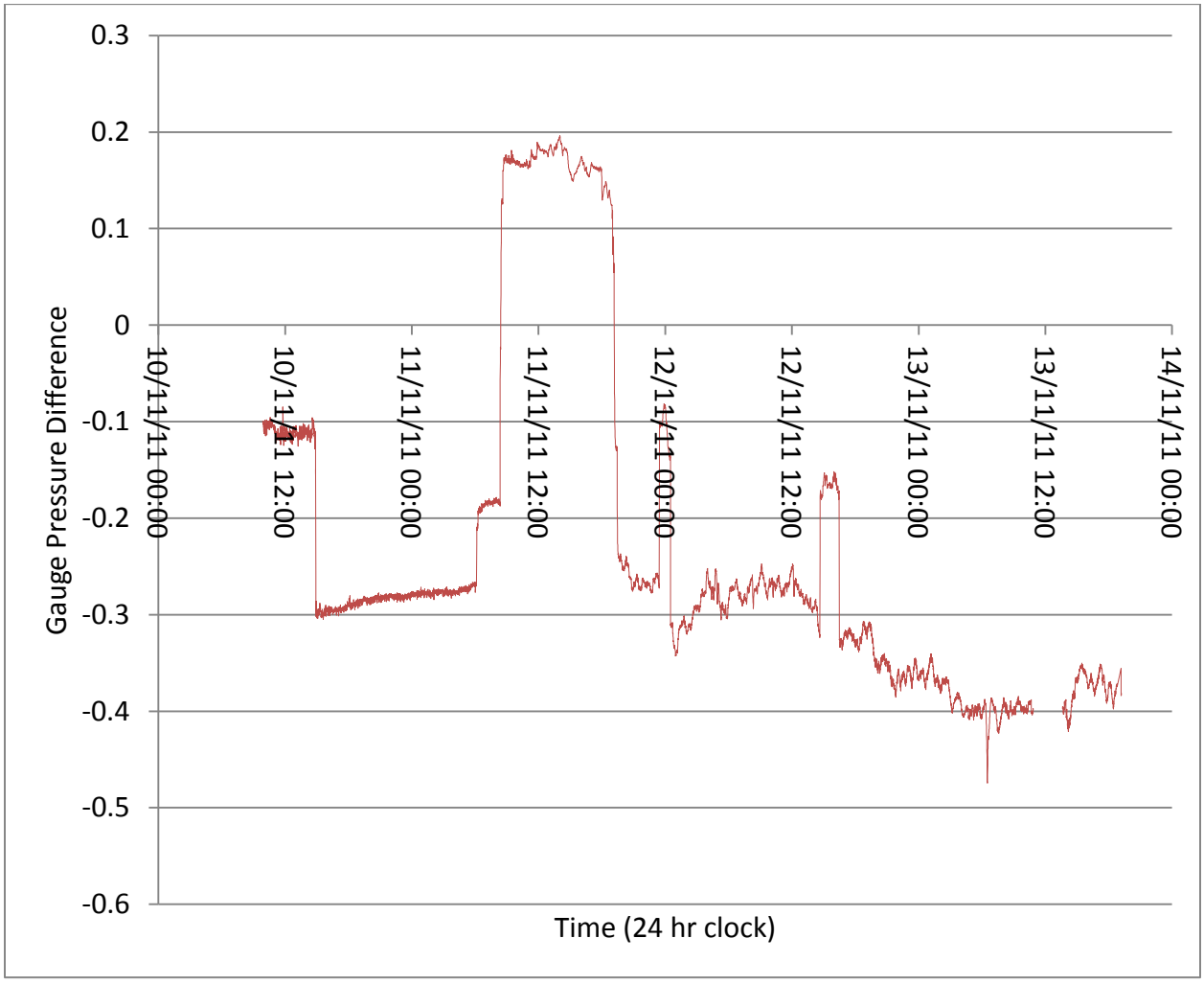

Figure 127: Pressure difference plot showing the difference in gauge pressure between surface and underground for the four days of measurement. When the fans are off, the distinct step functions in pressure can be seen. What was expected during the 11th shutdown would be a gauge pressure of near zero when all of the fans were off, but instead

a substantial increase of 360Pa (or +190Pa gauge) was seen, indicating a flow reversal, which is assumed to occur due to natural convection.

The graph in Figure 127 shows several points of interest. The first point is the apparent step functions that indicate when fans connected to the system were turned off and on (and thus the major differences of pressure). When the sampling campaign was first initiated, not all the fans were turned on and this can be seen until approximately 14:24 on the first day. At 14:24, a major set of fan(s), was taken off maintenance and put back into service. It is during this timeframe that the true difference in pressure needed for comparison with the CFD model took place. The pressure differences had slight movement to them during this time. It is assumed that this caused by a change in the density caused by change of temperature of atmospheric air or the difference in temperature between the rocks and the atmospheric air. At 6:00 of the second day, another set of fans were turned off, causing another decrease to the pressure difference before the power final was completely shut down at 8:15 on November the 11th at 6 A.M.

The pressure difference during this shutdown shows the natural difference of pressure at the different elevations of 2.89 kPa. The gauge pressure, at this time, shows a positive value of 0.18 kPa. The positive sign indicates that air flow would be leaving the NHEA at this time. The rationale behind this idea is that there is a natural ventilation pressure, of up to 0.2kPa, caused by the difference of temperature of the hot rock and the cool air entering the system. If this is truly the case, then the NHEA system is in fact a dynamic system in terms of pressure. This also means the pressure will vary by different amounts, depending on the season and the temperatures of the air and broken rock. This is the first time that this fact has been shown, although it has been discussed amongst the operator and researchers as a possibility. A smaller version of the

difference in pressure was seen during the first day, which has the highest resolution of sampling time, and the afternoon of the third day into the morning of the fourth, which only have hourly comparisons. The trend can be diurnal in nature as well, and further long-term work has begun due to the information gathered from this experiment. There were two other times fans were turned on and off during the sampling campaign, one at midnight on the third day for about three hours, and another between 2 and 4 P.M. on the same day.

The value of pressure difference that is of interest is the absolute pressure of 2.4 to 2.45kPa when all of the fans were on, and this is the value of pressure difference that the CFD representation of the NHEA will be compared with. A more thorough list of information of the time series is presented in in Table 41. The notation differences of the corrected pressure vs the absolute pressure were shown to try and isolate the pressure loss due to the flow moving through the pit, notwithstanding the density change with depth and density due to weather. This value turned out to be between 150 and 300Pa. While this is of interest to the operator, the CFD representation uses the absolute pressures differences, which ranged from 2.40 – 2.45kPa from the surface to the 230m trench depth.

Table 41: Timeseries interpretation of results

November 9th:
18:00 - Calibration exercise undertaken at 1366 Arlington
November 10th:
9:49 – One fan set turned off
14:25 – Fans turned back on
Overnight hours show an decrease in the pressure difference. This could be an indicator of difference
of temperature between the surface and underground due to an increase in density or natural convection

November 11th:
6:00 – Set of main fans turned off gauge pressure went from -.3 to -0.28kPa, Absoulte pressure = 2.4kPa
8:20 – Main or remaining fans shut off. This is also assumed when main power was turned off due to
battery life of the surface station. Gauge pressure is maximum at 0.18Pa
18-19:00 – Main power or fans back on, gauge pressure goes back to -0.28kPa
23:00 – Fan turned off for maintenance
November 12th:
0:30 – Fan from 23:00 back on
14:30 – Fan shut off for maintenance
16:30 – Fan back on
Gauge pressure drifts from -0.28kPa to -0.37kPa
November 13th:
4:30 – Possible additional fan on
7:30 – Possible additional fan off
13:30 – Final fan on
Gauge pressure remains stable at -0.4kPa
Pressure Differential (Measured):
November 10th:
Start – 15:00: The absolute difference here averaged 2.6kPa. Gauge = -0.02kPa
Evening of the 10th: The difference overnight from 2.39 – 2.44 kPa, Gauge = -0.3 - -0.28kPa
November 11th:
6:00: Difference jumped from 2.44 – 2.52 kPa, Gauge = -.08kPa
8:20: Difference jumped from 2.52 – 2.86 kPa for full shutdown, Gauge = .28kPa
18:30: Fans back on lower from 2.8kPa back to 2.45kPa, Gauge from .18kPa to -.24Pa
November 12th:
0:00-02:00: Fan shut off, Absolute pressure went to 2.6kPa, Gauge = -0.32 to -0.1kPa
14:30-16:30: Fan shut off, Absolute pressure went to 2.55kPa, Gauge = -.164kPa
November 13th:
Absolute difference of 2.35 to 2.3kPa, Gauge pressure -0.25 to -0.3kPa
Signal had logger error at 20:00

10.3.14 Discussion of the experiment

Once all power was turned off, the barometric pressure difference from the surface to the 800 Level drift was 0.18 kPa or 180 Pa after correcting for depth, which can be a conclusion that the natural ventilation resistance from the pit causes around a 0.2 kPa driven natural pressure ventilation within the system. In normal working conditions, an absolute pressure difference of 2.45 kPa can be stated as a data point of reference to the CFD NHEA due to the length of time the pressure difference was observed on both sides of the shutdown. This value of the pressure drop across the NHEA can also be assumed to be a dynamic value, which is currently being evaluated as part of the future work derived from this experiment.

It is important to note that the pressure at surface was 97kPa in absolute terms and 99.4kPa in the level drift, which is not intuitive to the concept of air moving from areas of high to low pressure. The fact is, in reality, when gravity and the distance from the surface pressure (natural compression due to elevation) are taken into account, air will move across such a pressure gradient. When worked out, the numbers with the 800 level equivalent being at 99.2 kPa, the surface pressure change would actually be around 99.4kPa. This means the right sense of direction between the two is true for the direction of airflow; it is just not immediately apparent. This is reversed when the fans are off, showing the observed reversal of flow for the first time.

11 CFD calibration of a large broken and fragmented rock problem

This chapter contains the CFD simulation, and comparison with physical experimentation described within Chapter 10. This chapter combines various elements of the thesis and can be described as the true application of the PSM technique.

11.1 NHEA geometry input and CAD/CAM model creation

The geometry used for the NHEA comes from three source files that were combined into one, all of which were in the Datamine format. The first stage of conversion was to import the files using Paraview Geo (Objectivity, 2013) as three separate files. The first file was a surface mesh (which was gathered by CAD/CAM string data from aerial surveys of the NHEA collector area). The second file was the underground or fragmented rock area (which was taken from underground surveys). The third file described the trench areas or unbroken rock areas where the airflow was being collected, and also serve as CFD boundary conditions. These files were first imported as stereolithography files (.stl). Contained within the CAD/CAM software, a conversion tool process of .stl files was used to make the "image" into a fully vectored file. The surface and underground meshes then were converted into "solids" capable of being assigned porous media properties. This enables the data for use as an equivalent continuum model. A further outside solid shell was then put in place to make the model contained, for an internal analysis, which is a condition of the CFD code. The third .stl file, the trenches, was used to cut out of the external solid shell solids, which then got converted into full trenches or boundary condition locations for the simulation code. In Figure 128, the underground portion of the porous media is shown. The .stl "image" gets converted into a manipulatable vector format native to the CAD/CAM code.

Figure 128: .stl file that was converted into a CAD/CAM solid object shell capable of being assigned porous material properties in the flow simulation tool when filled. To note, the excess image that needed to be removed from the bottom LHS is the ore deposit rising from depth.

In Figure 129, the surface portion of the thermal reservoir is shown. The file also had to be converted into a vector capable file type. The outside of the west side of the pit, which is on the top left side of the image, had to be removed due to the 1km maximum capability of the CFD code. This area is not actually part of the thermal reservoir, but rather represents a large pile of waste material and therefore has no influence on the system.

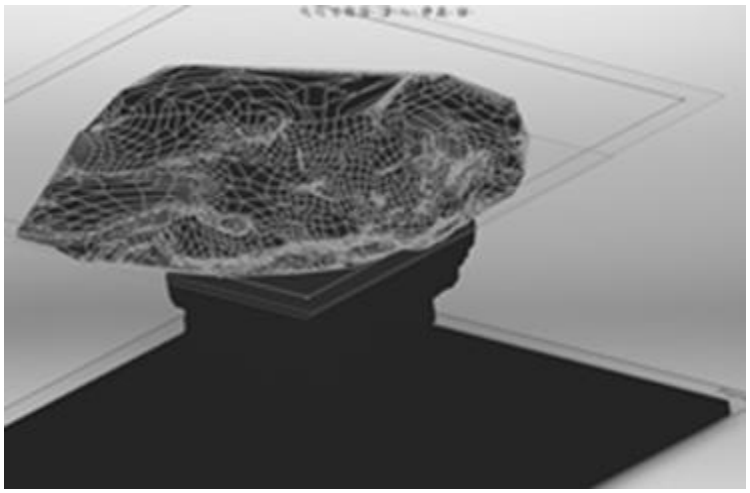

Figure 129: Overhead view of the surface .stl file during conversion process to CAD/CAM solid object

The converted file is shown in Figure 130. This is the surface of the porous medium and has a direct influence on the NHEA system. The immersed boundary conditions mentioned in Chapter 2 are essential for the meshing of this complicated structure.

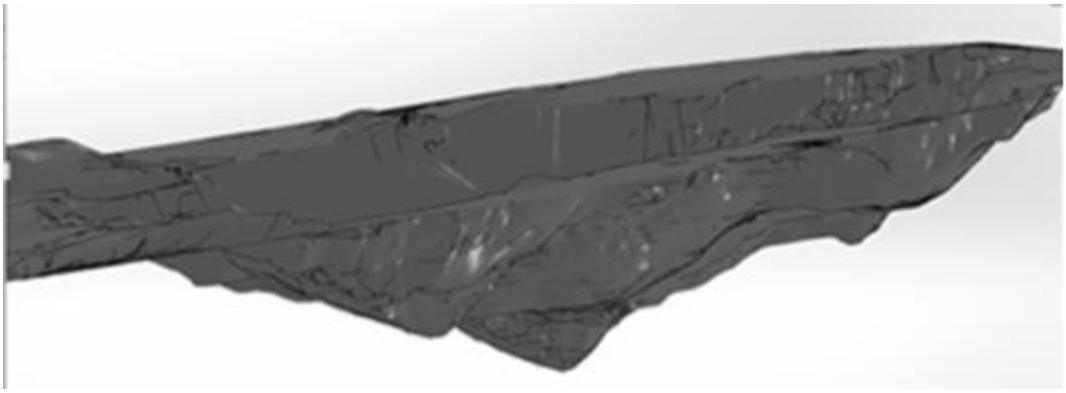

Figure 130: Surface file as CAD/CAM solid object. The gravel pile later removed is located on the left hand side of the image.

In Figure 131, all three files are shown after they were combined to form the CFD model, fully representing the thermal reservoir. The last activity to perform on this file was determining the intercepts of the porous media and the trenches to work as the boundary conditions of the CFD

code. The average width for this thermal reservoir is 950m by 900m by a depth of 500m including the outside shell.

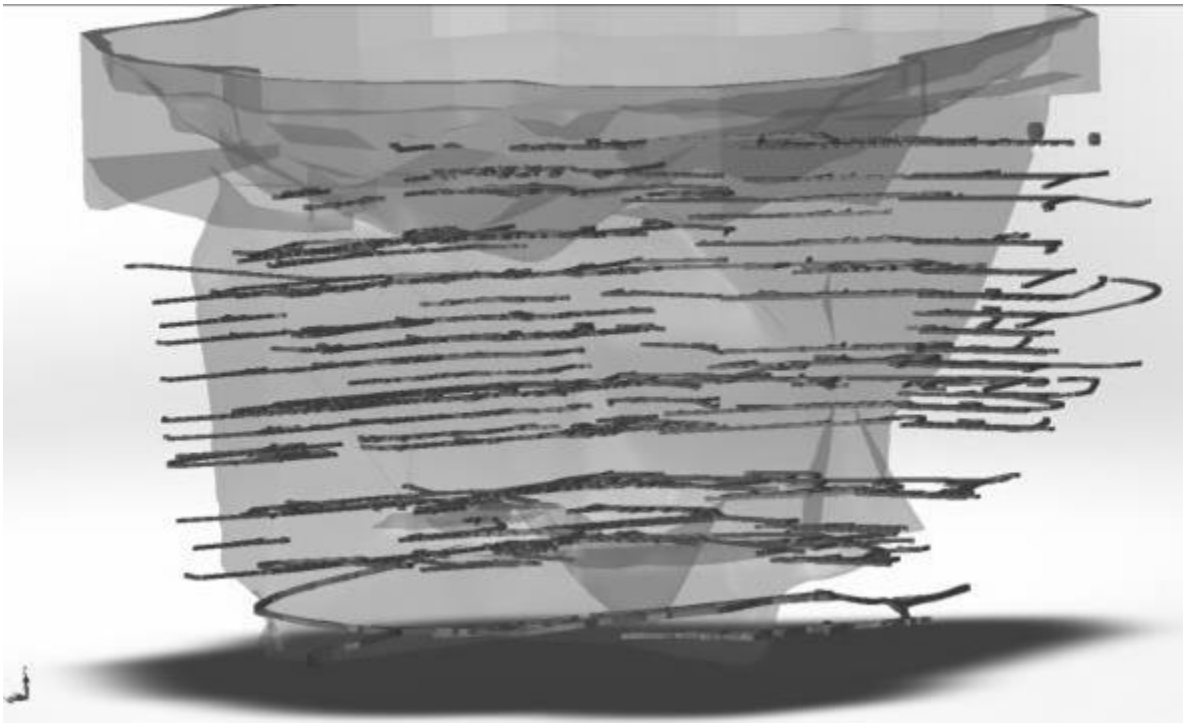

Figure 131: Combined files as a full CAD/CAM solid with CFD model characteristics

11.1.1 VnetPC model: Flow rate boundary conditions of Block 2 of the NHEA

To begin the process of calibrating the Fluid Flow Code for the problem, a ventilation software simulation was used to gather flow rate conditions to work as boundary conditions. This full minesite ventilation model, which is in the VnetPC format, is declared a verified flow model according to the local operator (Personal correspondence, 2011). The model was adjusted to use the fixed quantities of flow at the time (fans and their known flow rates) and the trench configuration for the exact same date as the physical experiment occurred. The trench configuration means that for closed trenches the resistances were set for 99999, and therefore

would have zero airflow. A summary of the flows was taken from the ventilation software results files to be used as boundary conditions for the CFD model. In terms of the physical experiment, "Block 2" was isolated and is regarded as independent of the other blocks or boundary conditions, therefore this was assumed to also be true for the CFD code. The flow rate sums for each of the blocks from the ventilation software is shown in Table 42 and are reasonable estimates for their flow at the time of the experiment.

Table 42: Flow rate sums of individual blocks

Total Flow m/s	
226.98	1 Block
274.38	2 Block
100.03	5 Block
93.96	6 Block

A detailed breakdown of Block 2 from the ventilation model is presented in Table 54 to show the boundary conditions for the CFD model. Each horizon of Block 2, which in total involves 30 trenches or drawing levels, needed to be placed as a boundary condition of the CFD model. Trench 2.10.0 south is the trench that was closest to underground monitoring station, and is on the same elevation. The flow rate assigned to this trench was 18.72 m^3/s, which was overlaid to the total area of the boundary condition, therefore representing all the slusher trenches that are the intercepts between solid intact rock and the broken and fragmented rock porous medium. In the CFD code, the pressure reading that comes as a result of the steady state solution to the trench having this flow rate is the primary performance indicator in this verification of the application of PSM. Table 43 shows the flow rates for each trench modelled in the CFD tool.

Table 43: Flow rate results for individual trenches or CFD boundary conditions

Flow rates (m^3/s)	Trench	Flow rates (m^3/s)	Trench
0.08	Trench 2.4.0S	0.08	Trench 2.11.1N
0.08	Trench 2.5.1N	0.08	Trench 2.11.1S
0.08	Trench 2.5.1S	5.03	Trench 2.12.1N
18.72	Trench 2.6.1N	0.08	Trench 2.12.1S
18.72	Trench 2.6.1S	4.31	Trench 2.13.0N
21.83	Trench 2.6.2N	10.05	Trench 2.13.0S
0.08	Trench 2.6.2S	5.17	Trench 2.13.1N
2.15	Trench 2.7.1N	3.59	Trench 2.13.1S
0.08	Trench 2.7.1S	7.18	Trench 2.14.1N
0.72	Trench 2.8.0N	18.72	Trench 2.14.1S
12.93	Trench 2.8.0S	2.51	Trench 2.15.0N
1.58	Trench 2.8.1N	5.74	Trench 2.15.0S
18.72	Trench 2.8.1S	2.15	Trench 2.15.1N
6.46	Trench 2.9.1N	5.03	Trench 2.15.1S
0.08	Trench 2.9.1S	0.08	Trench 2.15.2N
18.72	Trench 2.10.0N	8.62	Trench 2.15.2S
18.72	Trench 2.10.0S	18.72	Trench 2.16.1N
0.08	Trench 2.10.1N	45.95	Trench 2.16.1S
0.08	Trench 2.10.1S	283	Flow rate sum

In Figure 132, an image placing the 800 Level relative to the entire thermal reservoir is presented. Block 2 can be isolated into 30 trenches or boundary conditions, which are on 17 levels. The 800 Level is 10 Levels from the surface at an elevation of 230m. These drifts are represented as they are at the real facility. The average distance from the broken and fragmented rock is 10m, making a tunnel effect and minimizing the flow rate boundary effects for the CFD code. The flow rate boundary conditions can then also fit the fully developed flow criterion for the CFD code simulation.

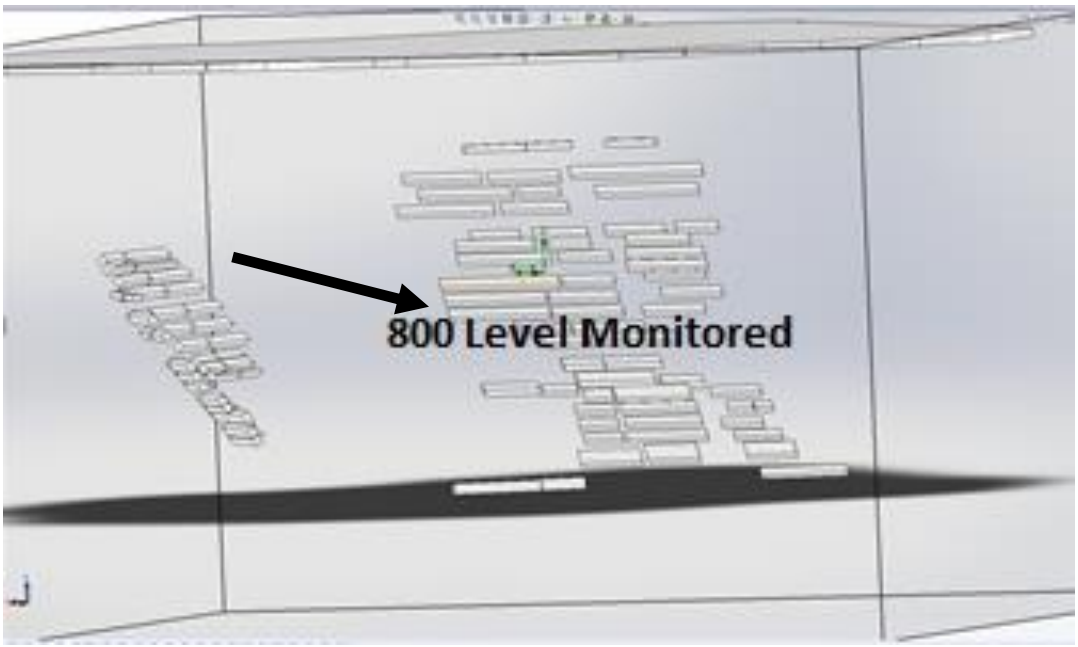

Figure 132: Image of the trenches where the pressure monitoring information was gathered to compare with the physical experimentation. The level monitored is just above the text, and is about half way up the reservoir.

11.1.2 Porous media requirements / Equivalent continuum material

For an equivalent continuum model within the fluid flow solver, a porous material with defined pressure vs flow rate tables must be installed into the model. The only information that was known about the material at the original calibration of the CFD model was the bulking factor of the porous media from the previous mining activity at the site (Personal correspondence, 2013). The bulking factor, which was estimated between 25 to 30%, leads to the calculation of the porosity of the structure by the following calculation:

Bulking factor:

$$B = \frac{V_B}{V-1} \tag{55}$$

where:

In-Situ Volume = $1m^3$

Bulked Volume = $1.25m^3$

Void Volume = $0.25m^3$

The porosity is defined as the volume of voids over total volume so the following is also true:

$$\epsilon = \frac{V_p}{V_p + V_m} = \frac{0.25}{1.25} = .2 \; or \; 20\% \tag{56}$$

This 20% porosity was the basis for how the PSM sample model was chosen and was taken from personal correspondence with the minesite operator. The Rosin Rammler parameters of the porous medium were unknown and the idea of using a uniform model was chosen to represent the PSM, which was then used to convert into an equivalent continuum model. Since the distribution of rocks within the reservoir is not known and may vary widely in the shape of the distribution, a uniform particle size was chosen instead since the one property of porosity was assumed correct and targeted by PSM. In Figure 133, the PSM that was used to create the porous resistance curves for the equivalent continuum material is shown. This is a uniform ball model, and has an average ball diameter of 1.2m, and containment area of 16.2m long. This model was chosen as a last resort, since no material properties of the porous media were known beyond the porosity. All the other materials used in previous chapters of this thesis were tested, with results either being extremely porous with too high a resistance, or too low a porosity and too low a resistance. It is known that the material of the NHEA is not of uniform structure, but it is believed that in future work, an equivalent material resistance and porosity could be manufactured using, for example, a Rosin Rammler distribution.

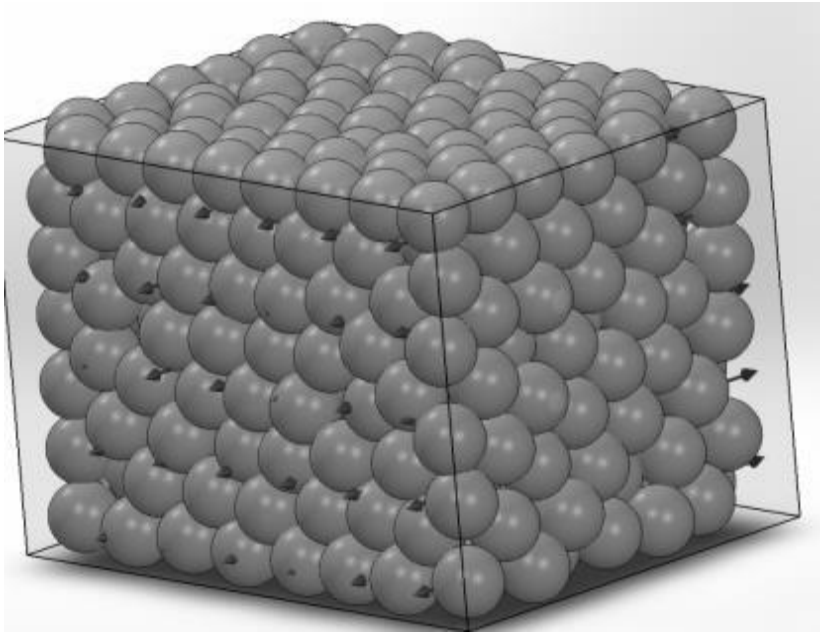

Figure 133: Model of 21.1% porosity and uniform spheres after being run through geomechanical consolidation. The height is 19.6m by a width of 14.7m and a length of 16.2m

The PSM pressure vs flow rate data was collected through CFD testing, as displayed in previous chapters. In the following sub-section, all the equivalent continuum porous media properties assigned and needed for operation of the CFD code derived from the PSM are given.

11.1.3 Porous media definitions

The following section contains the definitions used in defining the porous media of the NHEA CFD model. The parameters required are discussed in Chapter 2.4 with the APD flow simulation requirements. The essential material properties are porosity, dimensions, and the flow resistance curves that were derived from the PSM. The material properties used in the NHEA model are as follows:

Porosity: 0.211 %

Permeability type: Isotropic (meaning that the one definition for porous resistance is the same for all three primary directions, and is taken from the one resistance curve)

Resistance calculation formula: Pressure Drop, Flow rate, Dimensions – As described in Chapter 2.4.1 for use in Navier-Stokes.

Reference block length of porous medium: 16.20 m – This dimension is used in calculation of the porous resistance vector *k*, which was described in Chapter 2.4. This is how the CFD code "scales" the individual mesh sizes relative to the resistance curve inputted, independent of the scale tests in Chapter 9.

Reference block bulk cross sectional area: 288.12 m^2 - This dimension is used in calculation of the porous resistance vector *k*, which was described in Chapter 2. This is how the CFD code "scales" the individual mesh sizes relative to the resistance curve inputted, independent of the scale tests in Chapter 9.

Heat conductivity of porous matrix: No – heat transfer was not modelled in this version of the NHEA, but future work as a result of this simulation has included heat transfer properties.

Pressure drop vs. flow rate: Volume flow rate – directly derived from the PSM and shown in Figure 134. It is very important to note that the curve is deconstructed as two linear segments and

not as a parabolic form, which is how PSM resistances have been presented. This is also due to the calculation of the factor *k,* which is in a linear form and not a square law such as Atkinson's resistance, as explained in Chapter 2.

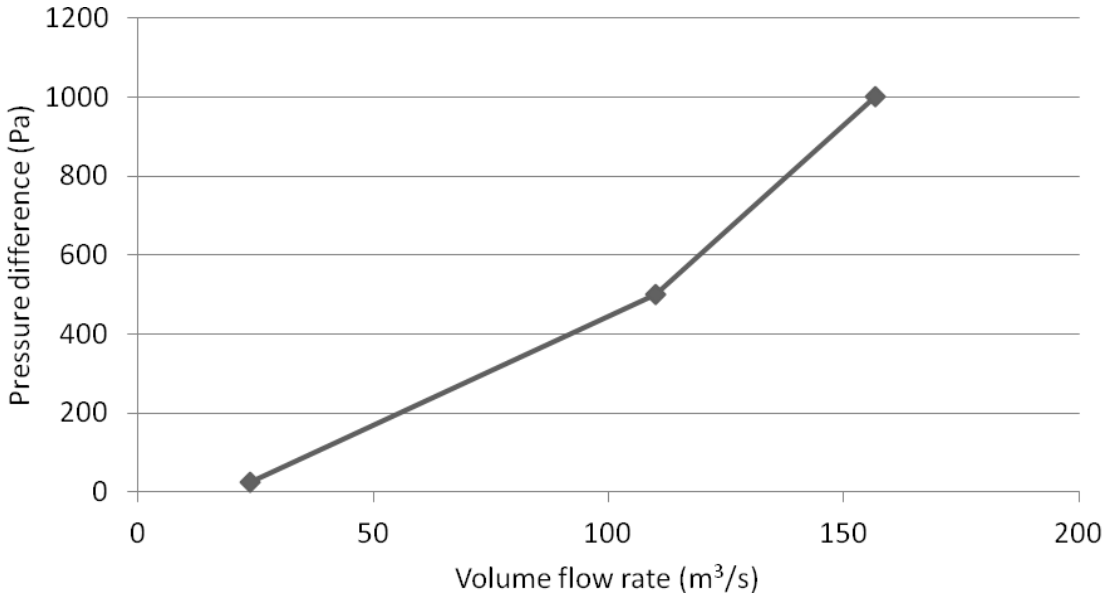

Figure 134: Pressure characteristic curve used as the porous material resistance in the CFD model. The linear effect comes from the porous resistance *k* from Chapter 2 instead of the Atkinson's resistance R, which is a squared law. More points would reduce the errors that this could potentially cause.

The characteristics of air are also needed for simulation and are summarized below. They are a standard in the materials database of the Fluid Flow Code.

11.1.4 Air properties

Path: Gases Pre-Defined

Specific heat ratio (Cp/Cv): 1.399

Molecular mass: 0.0290 kg/mol

The dynamic viscosity is plotted in Figure 135. This is a standard definition used by Dassault Systèmes.

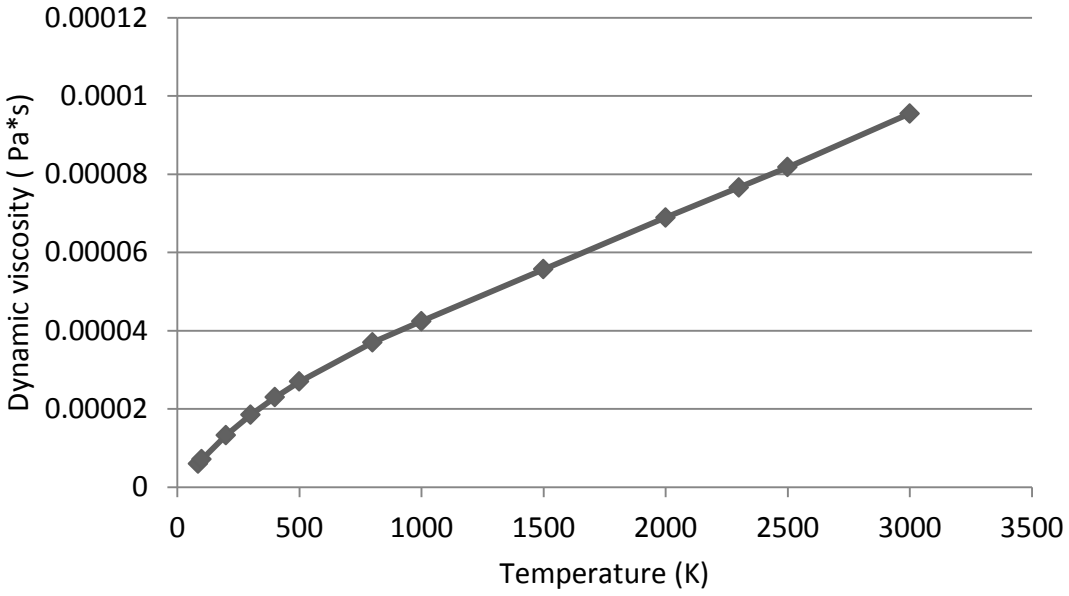

Figure 135: Dynamic viscosity as assigned default configuration for air

The specific heat coefficient as a function of temperature is plotted in Figure 136. As with all of the properties of air, this is a standard definition.

Specific heat (Cp)

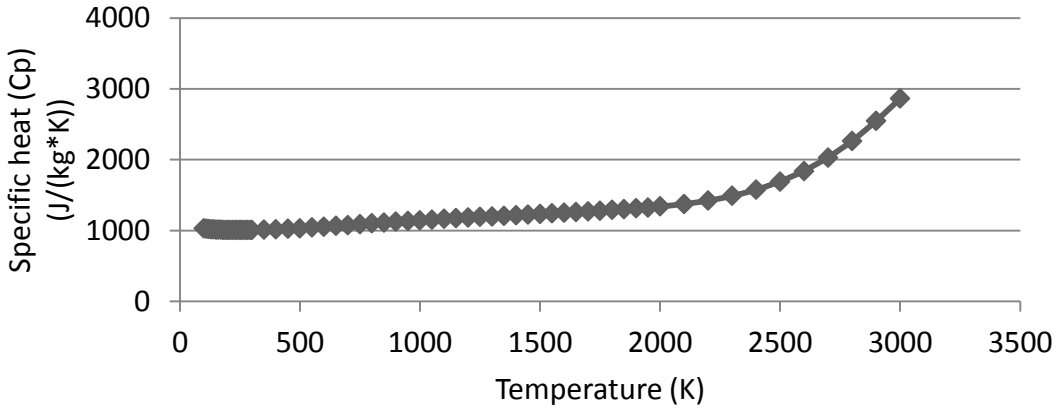

Figure 136: Specific heat as assigned default configuration for air

The air thermal conductivity is plotted in Figure 137.

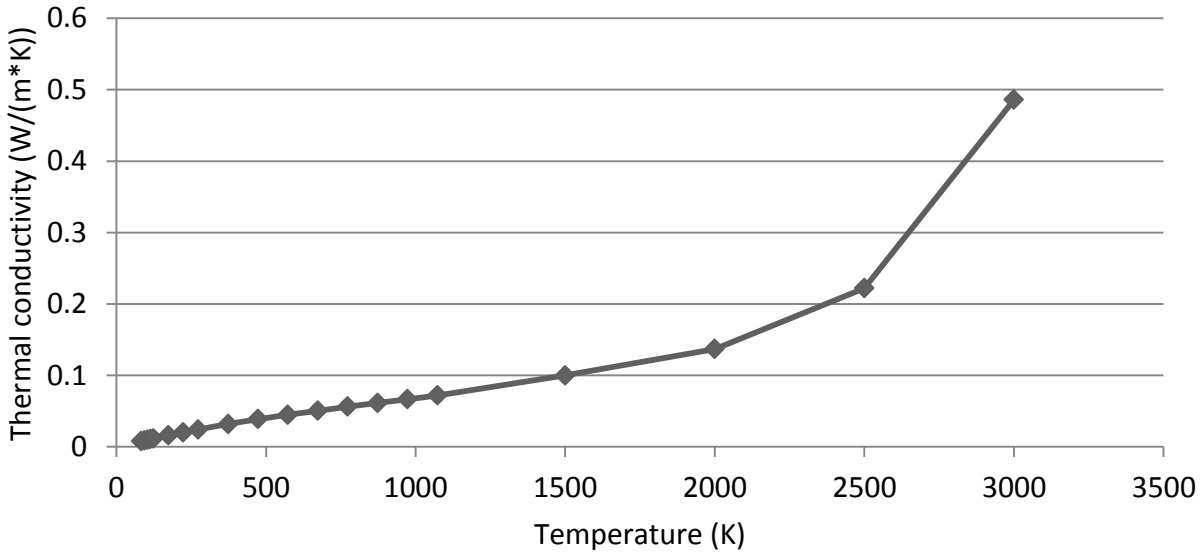

Figure 137: Thermal conductivity as assigned default configuration for air

11.1.5 Internal flow model properties and values

The following section consists of the CFD geometric properties assigned to the CFD model. The mesh conditions were set at a resolution level of 7 to mimic as best possible, the same mesh sizing as the PSM which derived the flow characteristics. All of the characteristics in the next sections are referred to in Chapter 2.4

11.1.6 Initial mesh settings

Automatic initial mesh: On

Result resolution level: 7

Advanced narrow channel refinement: Off (This reduces the number of the smallest cells caused by small juts in the walls of the NHEA. This function being off prevents millions of cells being generated)

Refinement in solid region: Off (There are no calculations of temperature being used)

In Figure 138, a full mesh display of the thermal reservoir CFD model is shown. The smallest cells are closest to the boundary conditions, while the larger, less refined cells are in areas where the solver tolerance factors (ie: minimum gap size) deem them not needing refinement, such as in the middle of the porous medium. The mesh is set at its highest resolution level for this model.

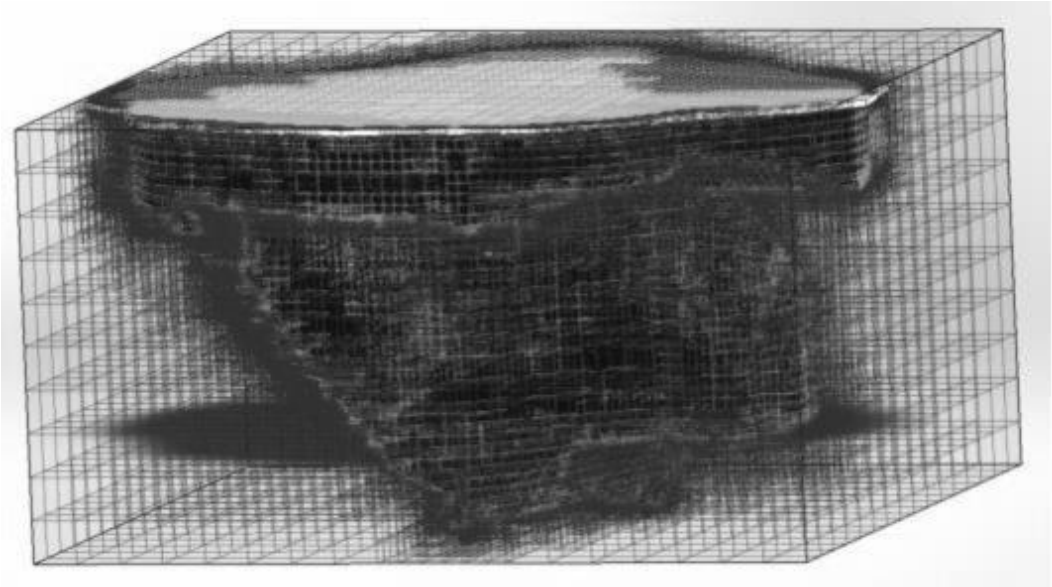

Figure 138: Mesh display of the NHEA CFD model. Dark black cells are solid, the medium colored cells are liquid or porous material and light cells are partial cells or both. The largest cells range from around 20m to the smallest cells which are less than a meter.

11.1.7 Calculation mesh

The calculation mesh settings show how the refinement of the cells was executed. The original mesh configuration is given in Table 44 and then the resulting refinements lead to the final amount of cells and their nature in Table 45.

Table 44: Basic mesh dimensions

Number of cells in X	18
Number of cells in Y	16
Number of cells in Z	10

Table 45: Number of cells used in the model

Total cells	138295
Fluid cells	25688
Solid cells	45485
Partial cells	67122
Irregular cells	0
Trimmed cells	0

11.1.8 Geometry resolution

The immersed boundary conditions were set to automatic in this model according to the APD requirements of Chapter 2.4. They were evaluated on components such as the trench boundary geometry and the air to rock surface interface.

Evaluation of minimum gap size: Automatic

Evaluation of minimum wall thickness: Automatic

11.1.9 Computational domain

The computational domain of the porous media and in general fluid domain (including air) space is shown in Table 46. These measurements do not include the outside solid shell of the model, which is necessary to enclose the fluid domain requirement of the CFD solver.

Table 46: Size of the internal porous medium not including the outside shell of the model

X min	-432.726 m
X max	428.307 m
Y min	-368.402 m
Y max	403.398 m
Z min	-277.066 m
Z max	188.553 m

11.1.10 Physical features

The physical features element of the CFD model inputs deal with the outer solid shell properties and the flow characterisation numerical techniques available to the code. There was no humidity, temperature effects, humidity or roughness applied in this model. The lists of options for operation of the solver are:

Heat conduction in solids: Off

Time dependent: Off (This is a steady state solution only)

Gravitational effects: On (9.81 m/s^2 in the vertical direction)

Flow type: Laminar and turbulent

High Mach number flow: Off

Humidity: Off

Default roughness: 0 micrometer

11.1.11 Initial model variable conditions

The global parameters of the k epsilon model for turbulence, initial vector properties of the internal fluid, and the initial thermodynamic parameters were designated and are shown in Table 47. The model was a steady state model with the top boundary being an environmental pressure boundary at an absolute pressure, while the flow rate boundaries that the model converged to, taken from the VnetPC simulations described earlier. The initial temperature of the model was set to 20°C. The turbulence and intensity scales for the $k-\varepsilon$ turbulence model were set to the default values recommended for the flow regime from the CFD tool.

Table 47: Global parameters needed to be set for the initial CFD conditions

Thermodynamic parameters	Static Pressure: 97000.00 Pa Temperature: 293.20 K
Velocity parameters	Velocity vector Velocity in X direction: 0 m/s Velocity in Y direction: 0 m/s Velocity in Z direction: 0 m/s
Turbulence parameters	Turbulence intensity and length Intensity: 2.00 % Length: 5.077 m

11.1.12 Boundary condition values

All 30 trenches and the environmental boundary condition needed to have flow rate or absolute pressure values assigned to them. The atmospheric conditions are applied to the environmental boundary conditions are shown in Table 48.

Table 48: Initial conditions for the large environmental boundary condition at the surface of the thermal reservoir. The surface pressure was taken from the physical experiment during the time when the fan pressure was largest to also fit the ventilation code model simulation.

Type	Environment Pressure
Coordinate system	Face Coordinate System
Reference axis	X
Thermodynamic parameters	Environment pressure: 97000.00 Pa Temperature: 293.20 K
Turbulence parameters	Turbulence intensity and length Intensity: 2.00 % Length: 5.077 m
Boundary layer parameters	Boundary layer type: Turbulent

In general, the format is similar for all of the outlet conditions (air leaving the reservoir), as demonstrated by the example shown in Table 49. The flow rate for this trench is 18.72 m^3/s.

Table 49: Outlet volume airflow boundary condition for the 800 Level trench compared with the physical experiment

Type	Outlet Volume Flow
Coordinate system	Face Coordinate System
Reference axis	X
Flow parameters	Flow vectors direction: Normal to face Volume flow rate normal to face: 18.72 m^3/s

11.1.13 Flow simulation results

The CFD model took approximately 8 hrs for a full cycle of meshing and to converge to a steady state solution. The expected result for pressure difference from the surface to the 800 Level is 2.45kPa for observation described in Chapter 10. The pressure difference that was calculated by the CFD code for the 800 Level was 2.495 kPa. This is a difference of 50Pa and is a very good agreement for the extremely complicated structure, size and flow conditions. A potential error related to the thermal properties may explain the 50Pa. As was shown in the Chapter 10 physical experiment, a pressure difference of up to 300 Pa may be due to the particular thermal conditions within the NHEA. In Table 50, the overall solution results for pressure in the CFD simulation are presented. The pressure "goals" all represent the absolute pressures predicted by the CFD simulation. Each "goal" represents a different slusher trench within Block 2 where a flow rate was assigned. The particular values of interest for this discussion are the environmental or surface boundary condition and the 800 Level or the underground station. The absolute pressure values are shown as having a difference of 2495.29 Pa from the surface measurement of 97011.27 Pa to 99506.57 Pa underground.

Table 50: Flow Simulation CFD results

Relative Pressure Difference (Pa)	Goal Name	Absolute Value (Pa)
-1427.1841	Trench 2.6.2N	98438.4619
-1577.5838	Trench 2.6.1N	98588.8616
-1582.9490	Trench 2.6.1S	98594.2268
-1817.0048	Trench 2.7.1N	98828.2826
-1887.1541	Trench 2.8.1N	98898.4319
-1888.3074	Trench 2.8.1S	98899.5852
-2015.8799	Trench 2.8.0S	99027.1577
-2022.5099	Trench 2.8.0N	99033.7877
-2233.9017	Trench 2.9.1N	99245.1795
-2497.4109	Trench 2.10.0N	99508.6887
-2495.2945	Trench 2.10.0S	99506.5723
-2985.0884	Trench 2.12.1N	99996.3662
-3091.6539	Trench 2.13.1N	100102.9317
-3167.9004	Trench 2.13.0S	100179.1783
-3179.2813	Trench 2.13.0N	100190.5591
-3240.5879	Trench 2.14.1N	100251.8658
-3206.0004	Trench 2.14.1S	100217.2782
-3350.4908	Trench 2.15.2S	100361.7686
-3474.6116	Trench 2.15.1S	100485.8895
-3480.9356	Trench 2.15.1N	100492.2134
-3605.5720	Trench 2.15.0N	100616.8498
-3607.1075	Trench 2.15.0S	100618.3853
-3781.5091	Trench 2.16.1S	100792.7869
-3804.4196	Trench 2.16.1N	100815.6974
0	Surface	97011.2777

In Table 51, the flow rate results are displayed along with a calculation of resistance for each trench that was sensed. These flow rates were confirmed as the results of the ventilation software inputs into the model. The resistances are only for this one configuration of the CFD code, and due to different flow conditions and volume of rock that is utilized. These values would change for different configurations of the air flow control doors.

Table 51: Flow rate results from CFD model

Resistance of flow rate locations (Ns^2m^8)	Goal Name	Unit	Value (m^3/s)
-2.9948	Trench 2.6.2N	(m^3/s)	-21.8300
-4.5017	Trench 2.6.1N	(m^3/s)	-18.7200
-4.5170	Trench 2.6.1S	(m^3/s)	-18.7200
-393.0772	Trench 2.7.1N	(m^3/s)	-2.1500
-755.9483	Trench 2.8.1N	(m^3/s)	-1.5800
-5.3883	Trench 2.8.1S	(m^3/s)	-18.7200
-12.0577	Trench 2.8.0S	(m^3/s)	-12.9300
-3901.4440	Trench 2.8.0N	(m^3/s)	-0.7200
-53.5301	Trench 2.9.1N	(m^3/s)	-6.4600
-7.1265	Trench 2.10.0N	(m^3/s)	-18.7200
-7.1204	Trench 2.10.0S	(m^3/s)	-18.7200
-117.9833	Trench 2.12.1N	(m^3/s)	-5.0300
-115.6669	Trench 2.13.1N	(m^3/s)	-5.1700
-31.3645	Trench 2.13.0S	(m^3/s)	-10.0500
-171.1489	Trench 2.13.0N	(m^3/s)	-4.3100
-62.8599	Trench 2.14.1N	(m^3/s)	-7.1800
-9.1485	Trench 2.14.1S	(m^3/s)	-18.7200
-45.0913	Trench 2.15.2S	(m^3/s)	-8.6200
-137.3313	Trench 2.15.1S	(m^3/s)	-5.0300
-753.0408	Trench 2.15.1N	(m^3/s)	-2.1500
-572.3032	Trench 2.15.0N	(m^3/s)	-2.5100
-109.4800	Trench 2.15.0S	(m^3/s)	-5.7400
-1.7909	Trench 2.16.1S	(m^3/s)	-45.9500
-10.8561	Trench 2.16.1N	(m^3/s)	-18.7200
0	Surface (Block 2 Sum)	(m^3/s)	281.6202
	VG Av Velocity 1	(m/s)	0.0049
	Equation Goal 1	[Pa]	2495.2945

In Figure 139, all of the horizons or trenches monitored for pressure in the CFD code are shown. The 800 Level (at an absolute pressure value of 99500 Pa) does have some distance between horizons vertically, and therefore, there is no doubt that the correct level was being monitored. A minimum difference of 300Pa is between this level and the next horizon above or below.

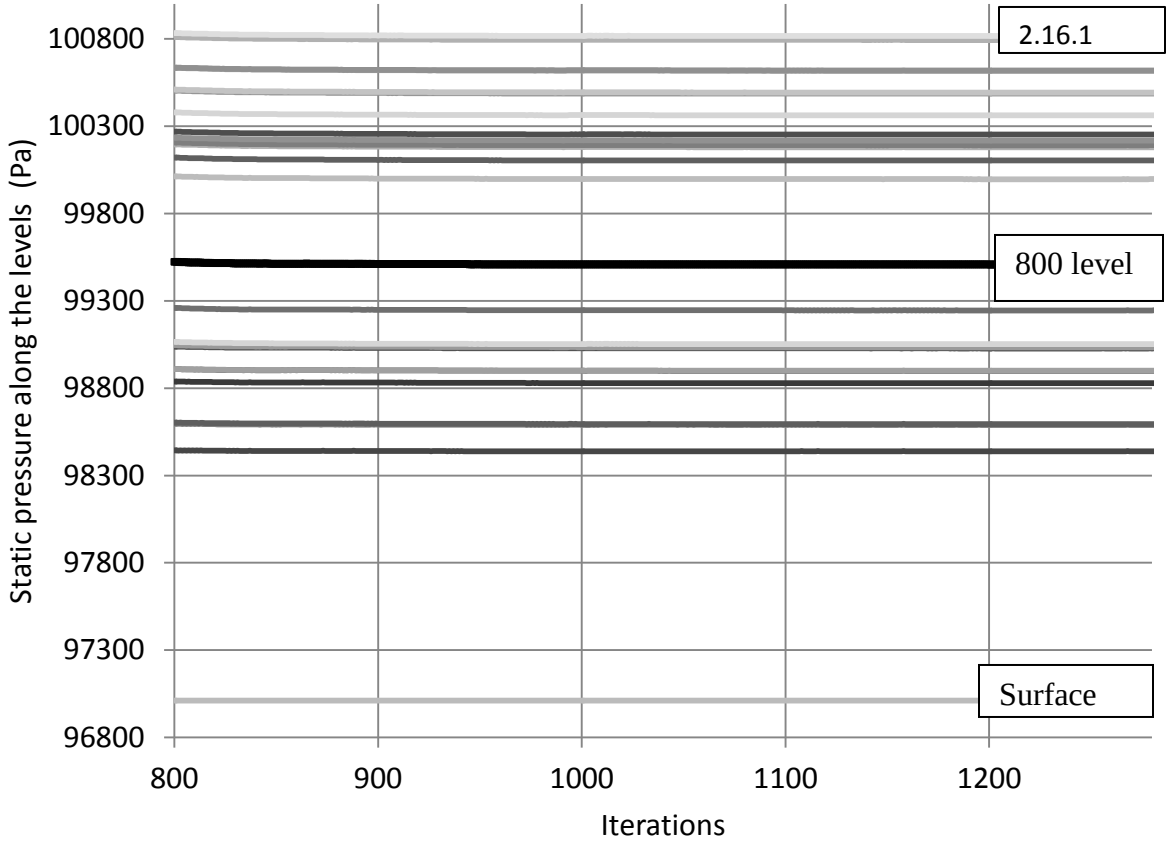

Figure 139: Total pressure monitored during CFD simulation for the various elevation horizons. The monitored 800 level curve is at 99700 Pa (highlighted black) while the surface was at 97000 Pa. The levels are ordered in reverse to Table 61 from the top to the bottom.

In general, the results of this configuration of the CFD NHEA turned out well. To test the potential for geometry error by the uniform distribution, a sensitivity analysis was conducted.

11.1.14 Sensitivity of results

Since the true rock distribution of the thermal reservoir is unknown, a test of the methodology of this thesis involving PSMs was conducted to see if it could provide insight on the potential composition. First, a self-similar scaling of the original PSM used in the NHEA CFD simulation was tested for scaling properties. This means the material properties of the individual PSM were scaled directly by a scale factor then re-inputted into the NHEA model, which was again simulated. In Figure 140, the plot of the PSM resistance vs volume is shown. In terms of diameter sizes of the spheres, they ranged from an average of 0.129m through to 1290m, which is a physical impossibility. This is the same method for testing the power law relationship in Chapter 9.

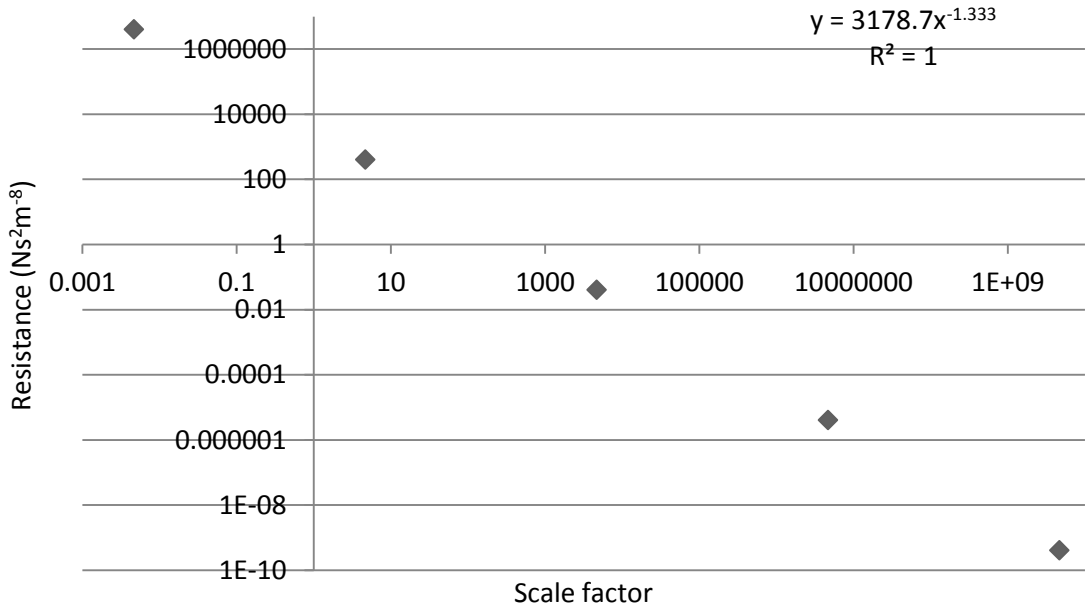

Figure 140: PSM direct scaling results for resistance of the material used for the equivalent continuum pit CFD model on a log-log plot

In Table 52, the pressure difference across the reservoir is plotted against the length of the PSM used in this synthetic experiment. The 0.162m length sample means that the original PSM was scaled down 100 times while the 1620m length sample means the PSM was scaled up 100 times. When the PSM was scaled down 100 times, the resistance curve was too high for the NHEA model. The behaviour and direction of flow was reversed in nature (even with the natural compression of air) and totally against the known behaviour. When this level increased to about the approximate length of sample of 16.2m, the pressure drop balanced out at 2490 kPa and showed a consistency all the way up the remaining scaling curves as seen in Figure 141.

Table 52: Sensitivity of the pressure difference from the surface to the 800 Level for different scaled values of the PSM

Pit Absolute Pressure difference (Pa)	Length of sample (m)
1638.72	0.162
2388.72	1.62
2490.72	16.2
2500.89	162
2501.92	1620

As a result of this simulation and the testing of the scaling properties of PSMs on a large media problem, it is possible to obtain potentially reasonable values from the PSM techniques. Unfortunately, since the true reservoir porous media rock distribution is not known, only a hypothesis can be made from these simulations since the pressure and flow rate characteristics have been seen to be to a fair degree accurate. This hypothesis is that the average rock diameter is between 0.129m to 1.29m.

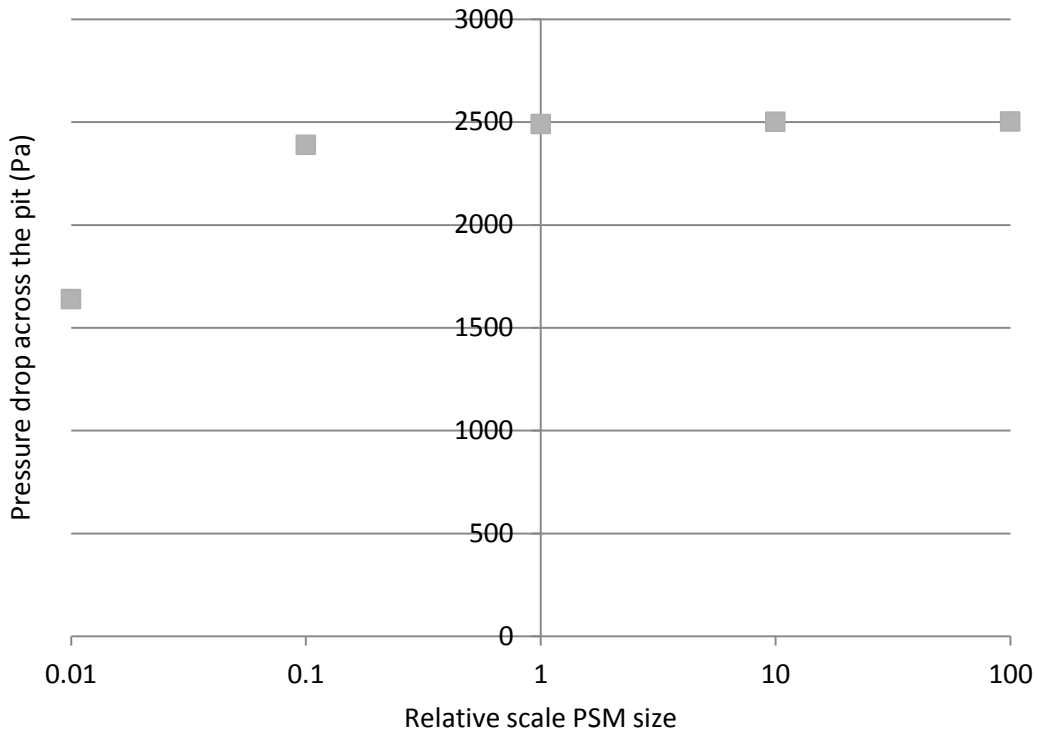

Figure 141: Pressure drop across the pit vs PSM scale model size. The relative PSM scale is on a log plot of the axis. The hypothesised true distribution of the NHEA is predicted at 0.3 times the original PSM.

11.2 CFD Application of the porous media model

Since the values of the physical experiment and the CFD model showed agreement, several parameters and behaviours of interest could now be examined. Some of these parameters include the following control mechanisms:

1. Pressure throughout the NHEA volume – The pressure distribution within the NHEA is of interest due to the fact that it can be related back to the fan pressures required to operate the system. The natural compression of the air is taken into account and if the flow trajectories are plotted with the pressure values, it may be possible to accurately predict the exact pressure

characteristics of each trench. An example of the pressure distribution throughout a section of the NHEA is shown in Figure 142. The top line in the figure is a cross-section of the surface interface between the air and rock.

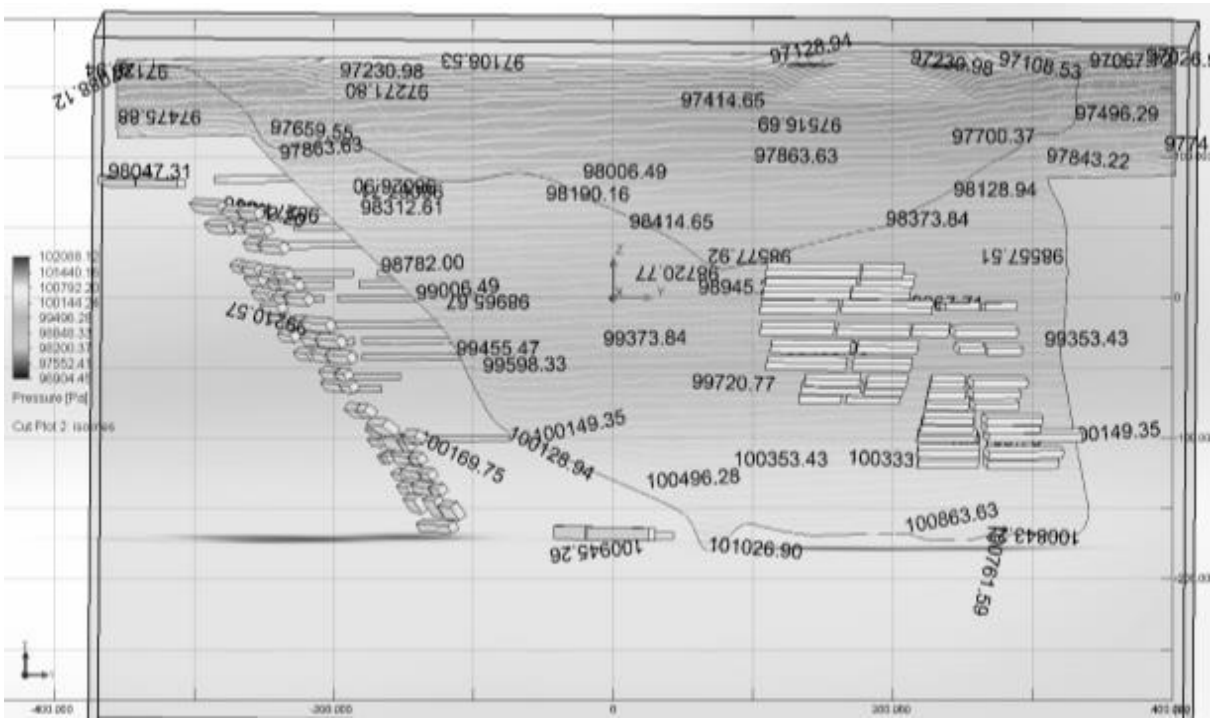

Figure 142: Pressure distribution within the reservoir simulation.

2. Velocity vectors and contour plots – The velocity contours of the NHEA can help identify potential areas of high and low heat exchange by the use of, or more importantly the non-utilisation, of the porous media. The areas of the lowest velocities show that there is not much airflow through those volumes while at the same time areas of high flow can be seen. In Figure 143, a plot of the velocity vector field is shown. The sizes of the velocity vectors indicate the relative magnitude and direction of flow. While this is only one section, the entire three dimensional object can provide great value in this analysis for potential modifications of this surface or inlet of the porous media. From the figure below, the surface influence can be seen by the almost direct vertical vector field over the upper level trenches. This is because the air always

chooses the path of least resistance. In terms of the surface, this means the shortest possible distance through the porous media.

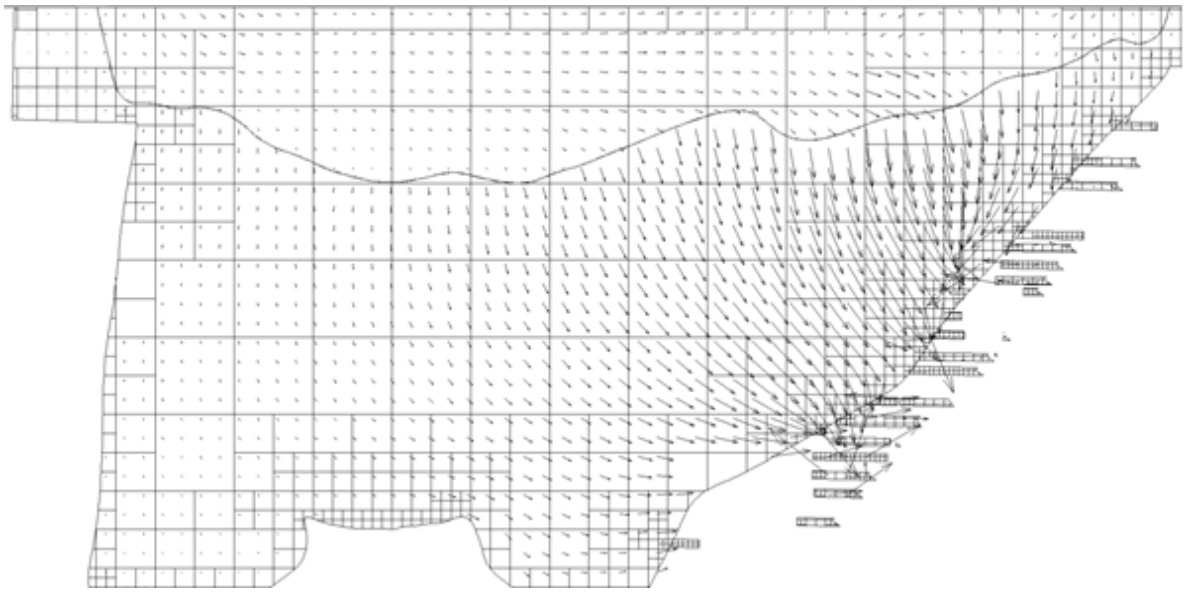

Figure 143: Velocity vector plot of the reservoir simulation. The largest vectors have a velocity of 1.2 cm/s

3. Trajectories – The trajectories are important for analysis of the reservoir for information about the length, and path, of the airflow. Also, the volumes of airflow from each specific trench can be obtained by using the string translation or tortuosity calculation from Chapter 7. Volumetric analysis of how much volume each trench utilizes can become crucial to future interpretations of the operating system. Also, when the complete system is simulated, overall efficiency of the thermal mass may become interpretable, and maximised, with a trench selection state operation procedure. Figure 144 shows a demonstration of these results graphically. If the flow rate lengths are calculated for this structure, they may be used in the evaluation of heat exchange either for sections, or as a whole. This is due to temperature and pressure profiles that can also be gathered from these results.

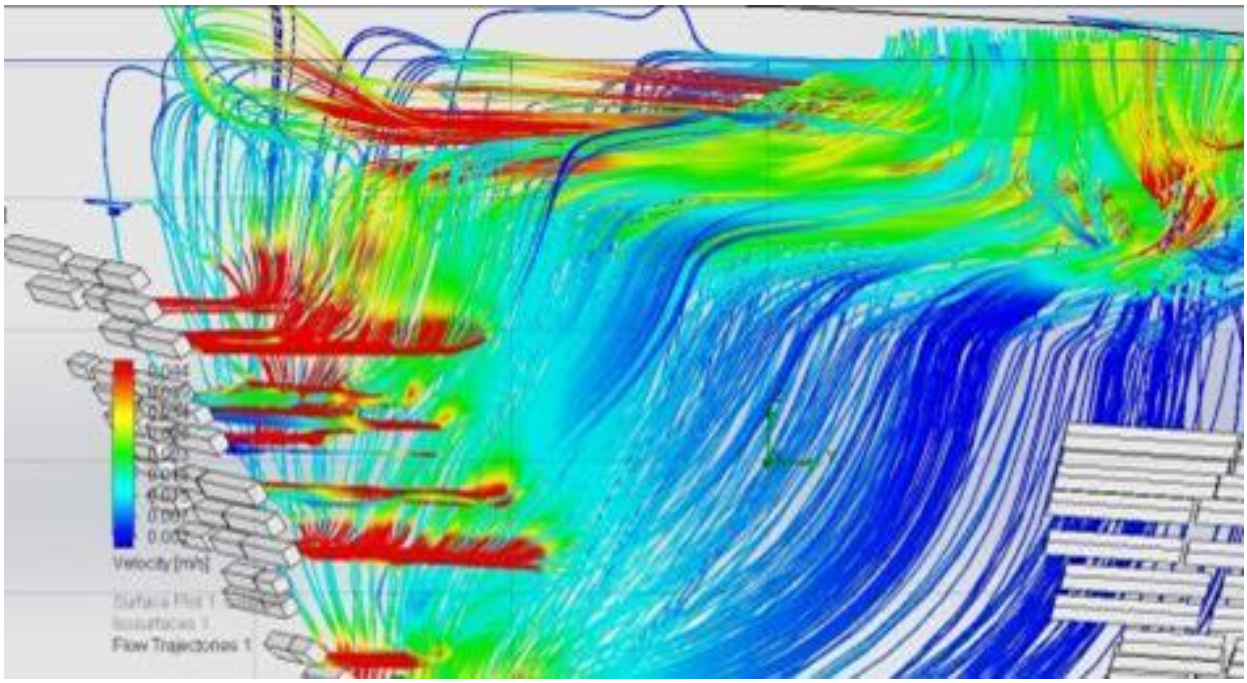

Figure 144: Flow trajectories from the trenches sensed in this verification procedure. The view is from behind Block 2, which means that airflow is moving from right to left. The influence of the surface of the model can be seen by the flattening of the flow trajectories just above the top trench modelled on the left hand side. The darker colors are areas of higher velocity of the airflow, which is about 0.01 m/s.

4. Non–obvious complex behaviour – Due to the complex geometry of the NHEA shell, along with the fact that there is a non-uniform surface between the air and porous media, irregular distribution behaviour issues of airflow and pressure that can be examined interactively only form. One of the things that can be looked at in detail is how the slope of the air to porous media surface influences the intake of air into the center horizons of the thermal reservoir, as seen in Figure 145. In Figure 146, other behaviour caused by interactions between the geometry of the shell and the porous medium, such as swirls, are evident; air can actually be drawn back from other trenches. Finally, since the true particle size distribution of rocks inside this pit is unknown, a multiple combinations of material properties of the porous medium can be defined within this CFD model to investigate and improve the calibration process.

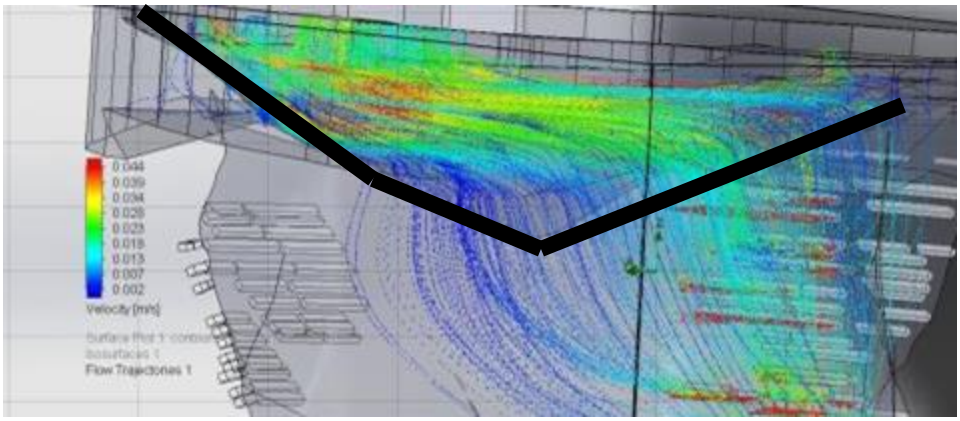

Figure 145: Overlay of the surface geometry with the airflow trajectories. The shape of the surface of the reservoir (highlighted in black) has a substantial influence on how the air moves through the porous media or more specifically the direction and angle of attack that the airflow chooses to enter the porous media with the constraint of the geometry of the shell.

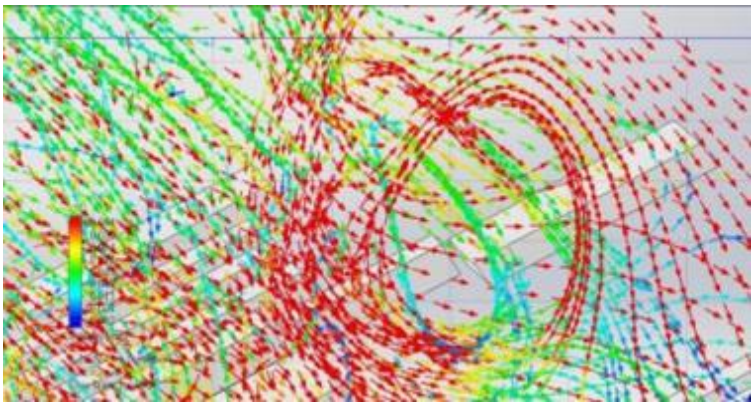

Figure 146: Observed behaviour of airflow inside the CFD simulation. This swirl effect is caused by the geometry of the shell of the porous media. This swirl draws flow from several trench horizons.

11.2.1 Discussion

The results from the CFD model and the physical experimentation agreed with a good level of accuracy with a total difference of 50Pa between the CFD code and physical data. Due to the true distribution of the rock internal to the thermal reservoir not being known, a sensitivity analysis was done to see the effects of the potential distribution average rock size. The PSM technique

came up with a hypothesis of 0.3 times the magnitude of the original PSM, which had an average diameter of 1.2m. The rationale for this is the 50Pa difference going to almost 0 between the CFD model and physical data. This hypothesis cannot be proven at this time. It may also be that the distribution chosen was fair for analysis, and it is the rock temperatures that cause the 50Pa difference.

The large scale porous media problem introduced within this chapter leads to the use of the entire methodology of this thesis. The field data was collected in a fashion that abides by the concepts of the constant head pressure test. The CFD model was designed from the geometry taken from mine design software that was inputted by surveys of the area over time. Calibration of the CFD model was done using the techniques from Chapter 9 for terms of scaling, to bolster the Flow Simulation tool scaling calculation using the porous resistance *k*. With the model calibrated, pressure and velocity fields, flow trajectories for volume evaluations and non-obvious airflow behaviour patterns due to the complex geometry and outlet environment could then be examined, showing the full capabilities of the technique.

By further testing using the CFD model, potential design changes can start to be evaluated in a way that has never previously been possible. For instance, the geometric effect of the outer shell and air to surface interface can be detailed. The assessment of operational conditions can also be profiled, since there are 96 trenches that can be optimised for temperature performance to the collection level, which then gets sent down to depth at the site. While these techniques have not yet been fully developed, concepts such as hydraulic tomography first developed by Vesselinov *et al.* (2001) and then refined by Sharmeen *et al.* (2012) use inversion techniques to solve for

thermal properties of water in rock fractures. If this technique is linked with the trajectory combinations that the PSM provide, the data may be used to help refine the characteristics of the porosity, porous media resistance, potential rock distribution and thermal heat exchange coefficients.

In general, indications are that the PSM methodology can be used to reverse engineer a porous media problem, even though it has many unknowns. By doing so, it may be possible to state that the PSM technique can be used to forward engineer a thermal reservoir and potentially other porous media problems under the condition that the rocks under analysis do not move with the airflow.

12 Thesis application, contributions, questions, and further work

12.1 Application of PSM to other problems

The following section is a summary of the PSM technique, highlighting some of the strengths and weaknesses for general application use. To begin, the vertical format of the PSM technique is shown in Figure 147.

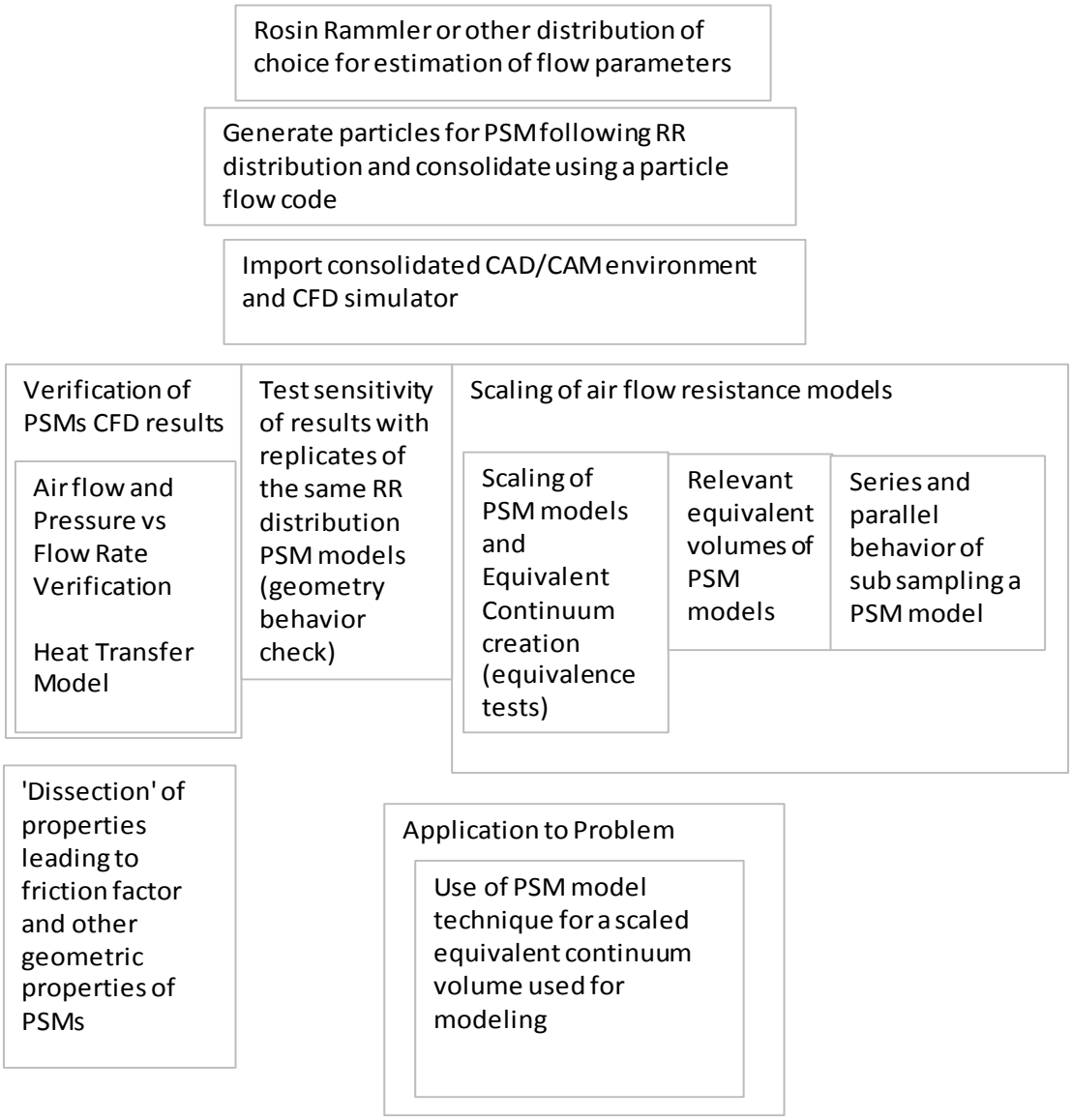

Figure 147: Summary of the PSM technique and this thesis

The context of the application of the technique will be as general as possible, but emphasis will be placed on whether or not the application is new in nature, meaning not all parameters have been decided, or pre-existing, meaning some constraints may be already in place or properties are known. The largest difference caused by this classification is the material characterisation, which has several effects on analysis.

1. Rosin Rammler or other distribution of choice for PSM analysis- For any application involving porous media, the choice of distribution of rocks/soils fragments is a key factor that will affect the air flow resistance and heat transfer characteristics. If the problem is new and forward engineering is possible, then many of the difficulties of this thesis are overcome. The thermal reservoir problem of Chapter 11 was an old problem, where characteristics of the rock type, and the size along with shape parameters of the internal distribution were unknown. The choice to approximate the distribution of the NHEA with a uniform distribution was the only alternative, but it did allow the one parameter of porosity to be utilized. It was shown that porosity could represent different distributions of different sizes, which is a weakness of just using porosity as a control variable. For completion of the work, a comprehensive campaign tracing the spread factor of the Rosin Rammler distribution from 0.5 to 2 should be undertaken for future applications. This spread of the distribution can be examined for direct relationships between the Rosin Rammler distribution and the resistance values of airflow. Also, the determination of the equivalence between a Rosin Rammler distribution and a uniform distribution should be assessed in terms of the ‘low level’ geometric parameters such as cross-sectional area and perimeter, in future work.

2. Different shapes of particles used in PSM analysis – Different sizes and shapes of the particles used in a PSM should also be examined for differences between them and the spheres chosen as the base of this thesis. Different angularity and sphericity may be tested and 'geometrically dissected' (in a CAD / CAM software tool, as in this work) for their comparison. The anisotropic behaviours of porous media could then be examined.

3. Importation of the Rosin Rammler distribution into the Fluid Flow Code - In the fluid flow code, a 'calculation barrier' begins to form at about 1500 spheres, which is why there were no PSMs with more than this number of spheres in this thesis. At this level, the importation process is the factor that slows down, or crashes, the program, due to limits of how many objects can be written to the CAD/CAM software. To truly represent the Rosin Rammler distribution at the lower levels of the shape factor range $0.5 < n < 0.75$, more than 3000 spheres need to be imported to represent the larger spread of the distribution (see PDF and CDF graphs in Chapter 2). To characterize this range can become an important baseline in the future uses of PSMs. Scaling laws can then be used for completion of a table of Rosin Rammler values vs air flow resistance for a requested volume of rock to be represented. A more comprehensive relationship linking the Rosin Rammler distribution and PSM resistance should then result.

Large number of spheres for sub-sampling- The maximum limits of what is capable of being imported or simulated for the PSM technique need to be tested to see how large a sample can still maintain the characteristics of scaling shown in Chapter 9. This knowledge can show other users where the barriers of the different CAD/CAM software are.

4. Verification of the CFD codes – When the PSM technique is applied to a novel application area, code verification exercises should be undertaken, such as the following:

Verification of other CFD tools – If a different CFD tool is used, a verification process should be done to confirm the accuracy of the code relative to physical results.

Verification of another fluid – When dealing with a new application of PSM, simulations assess the effects of the material properties of either water or a gas other than air should be undertaken for further verification of the CFD tool chosen.

Icing and latent heat transfer – The PSM geometry technique should be imported into different fluid flow codes, which can handle phase changes to air/water/ice in a PSM, if phase change is known to be important.

5. Tests of sensitivity to the Rosin Rammler distribution – For any new or old application where the PSM technique is being utilized, it is recommended that a sensitivity analysis should be conducted. Although it has been shown that the results should be close for air flow resistance, a proper estimation of what the potential differences are should be at least examined.

6. Scaling properties of PSMs – Even though flow simulation tool have their own scaling properties for the porous resistance as described in Chapter 2.4, PSM volumes used to define the characteristics of air flow may need to be examined in the future. The Atkinson's friction factor

proved independent in this thesis, which enables the following two techniques to be more appropriate for property scaling purposes, in comparison to the self-similar scaling used herein.

Establish and adopt a power law relationship – There was evidence presented in this thesis for a power law relation between the volume of a sample and its resistance. How and why the coefficients behave the way they do is a question that is most likely based on geometric parameters and should be examined in the future.

Series and parallel behaviour PSM combinations for scaling – Combining PSMs in series and parallel produces results for air flow resistance consistent with expectations for varying scale. The PSM technique has the advantage that the 'units' combined can have complex internal structure.

7. Geometric dissection of PSMs –The 'geometric dissection' process undertaken upon the CAD/CAM assemblies suggests that the flow simulation tools may be unnecessary since the pressure loss and flow rates can be determined by substitution in the Atkinson's equation, if the geometric properties are established. The exception is the tortuosity which is a factor that needs flow simulation to assess flow path lengths. The drawback of the technique, at this time, is the fidelity of the geometric breakdown. Corrections in the technique need to be implemented if, during the dissection, more than 10,000 CAD/CAM objects are created; on the highly specified computer used in this work, there was just insufficient RAM to accommodate all the new objects. One 'work around' for this is progressive separation of the PSM files into sub-files for analysis and collection of data from the components. However, it was shown that rather fewer

dissection slices (around 4) than the number used in this work may be all that is required estimation of the Atkinson's resistance, but it is recommended that at least 30 samples be taken for statistical purposes.

This information stated above should lead to the ability to apply the PSM technique to different porous media applications.

12.2 Questions posed during this thesis

The following section summarizes a series of questions that have been investigated within this thesis. Following this, an examination of the overall theme questions of the thesis will be presented.

Q1. Can one take Rosin Rammler parameters to characterize a synthetic ensemble that may be imported into a CFD environment so that airflow resistance curves can be produced?

The consolidated particle flow code results were then imported to the CAD/CAM code using commands from the Flow Simulation tool API, which enabled a physical 3D PDM to be printed out at 1:1 scale. Following this, the CAD/CAM model was then able to be placed into the CFD flow simulation software for air flow resistance testing, and the physical model physically tested to verify the CFD simulation results.

Q2. If the process of importation into the CFD environment is possible, then what characteristics can be obtained from the results of these CFD models?

Parameter values possible to estimate from the PSM in the CAD/CAM environment are profiled in Chapter 3. The main parameters required from the PSM are the pressure and the flow rates entering and leaving the model. Other heat exchange parameters such as the Prandtl number can be evaluated but were not considered in this thesis, but may be useful in other application areas.

Q3. How could airflow resistance curves from synthetic ensembles presented in Chapter 3 be experimentally verified?

Consideration of question 3 led to modifications of the wind tunnel apparatus to match the CFD model environment. Converging inlet and diverging outlet ducts were placed into the wind tunnel to match the exact sample containment box, identical in both the physical and CFD environment, without inducing additional turbulence into the air flow system. The flow rate was measured at the duct inlet, and the pressure drop across the sample was then measured via static pressure tappings and observed with both a barometeric standard and a micromanometer. The experiment was a variation of the constant head pressure test. Within the CFD environment the results benefitted from simulated observations free from experimental noise.

Q4. If an experiment was devised to complete the experimental verification, can the entire experiment also be characterized to compare with all of the data gathered from the experiment?

The laboratory data was then also used to characterize the wind tunnel, to ensure accuracy of the information gathered from it, which was shown in Chapter 4 through Bernoulli and shock loss calculations.

Q5. Do the experimental airflow resistance curves agree with those determined from CFD modelling?

Through the comparison of the CFD to the physical experiment results, there is sufficient evidence to say there is good agreement between the two. The main consideration for error is that the physical experiment was subject to observational errors introduce by the precision of the instrumentation used and natural phenomena that may have introduced 'noise' into observations, such as vibrations of the fan and wind tunnel. The CFD environment is a noiseless one and any errors can really only be associated with omission or commission of appropriate air flow physics in the model. Practically, the main source of error appeared to be associated with the resolution of the hot wire anemometer used for air velocity observations in the physical experiment.

Q6. How sensitive are the CFD results that lead to airflow resistance curves to varying instances of synthetic ensembles that share the same Rosin Rammler distribution?

CFD experiments of five PSMs each sharing the same Rosin Rammler distribution parameters led to the resolution of this question. They are generally close at about a 4% difference in flow rate for the same pressure drop, when one of the five samples was removed from the comparison set due to differences in the simulated particle consolidation process. The simulated observations

led to similar values of air flow resistance, these being closer with fine meshing compared with coarse meshing. Less than a 10% difference in air flow resistance was generally seen between the coarse and fine PSM meshing settings.

Q7. Can the resistance curves determined from CFD modelling permit any further physical interpretation of porous media characteristics to be inferred?

Some parameters which are traditionally difficult, if not impossible to estimate, such as the tortuosity of the porous media, and the low-level geometric properties of hydraulic radii and diameters were shown to be calculable. Beyond those characteristics, the porosity, fluid-solid interface surface area and finally Atkinson's resistance and friction factors can be determined from 'geometric dissection' of PSMs.

Q8. Having characterized porous media air flow resistances, do CFD simulations of PSMs produce reliable heat transfer behaviour?

As a continuation of the fluid flow resistance experiments, the flow rate and pressure measurements were tested in the same way as previously performed, but the starting temperature of the physical PSM was depressed initially, in comparison to the starting air flow temperature. The transient temperatures of the PSM solid portion and the air in interstitial spaces were monitored as the warmer air was passed through the same, both '*in silica*' and *in-situ*. Comparison of physical and simulated temperature transients exhibited good agreement, and this behaviour was repeatable for the physical tests. More specifically, for the experiments

conducted, the degree of agreement of simulated and physical observations for two of the three internal sensors showed a very high degree of accuracy and repeatability. While the third had some error, it still was well within the experimental limits tested. The reason for these differences was attributed to due to leftover of the breakaway support (a remnant of the PSM manufacturing process). The sensor error was still shown to be reasonable for it matched the profile of the average temperature in the section of sensor corridor in which the thermistor was placed.

Q9. How do airflow resistance curves change with the scale of the problem considered?
The airflow resistance curves presented in Chapter 9 do seem to follow consistent scaling laws. Three distinct approaches to development of scaling laws were investigated; all three produced scaling curves of the same form, but were developed with different basis. For the self-similar scaling methodology proposed, a key point is that two distinct PSMs of the same porosity can have substantially different values of air flow resistance due to the different particle sizes tested. The third method developed, that of establishing the air flow resistance of a PSM as a basic resistance element with defined bulk dimensions and then considering series and parallel combinations of this basic resistance element to scale up to much larger bulk dimensions, is thought to be the best approach of the three investigated. Rather than relying on empirical fitting of air flow resistance values from samples of different scales, the series / parallel combination methodology appears to have a physical, rather than empirical, basis for air flow resistance scaling.

Q10. Can an Equivalent Continuum proxy for airflow resistance replace a PSM CFD representation?

It was shown that with PSMs replaced by an equivalent continuum, a value of almost the same for resistance (99%) can be found as in Chapter 9.

Q11. If there is a relation between volume of the sample vs the resistance, can it be used to predicted the resistance at particular requested sample values?

A technique by plotting the resistances vs bulk volume shows that power law relationships can occur. This was tested with a sub sample of a chosen volume, and the resulting resistances were in line with the power law scaling approximation. A key requirement of the methodology development in this thesis was that there be a firm rationale for scaling results of air flow resistance experiment of porous media, obtained at laboratory scales, to dimensions equivalent to the smallest finite volume element used in CFD models of large (~1km^3) bodies of broken rock (such as that presented in Chapter 11). This can be used to find the representative elemental volume of choice for use in mesh sizes of a larger porous media problem.

Q12. When airflow resistance curves of PSMs are considered as resistance branches in a ventilation network, do series and parallel resistance equivalence rules still hold?

The results of Chapter 9 show that the air flow resistance values of PSM sub-samples applied within series and parallel branch resistance formulae do lead to accurate estimates of the air flow resistance values observed for the larger PSM bodies from whence the sub-samples were taken.

Q13. Can application of the overall methodology developed, components of which have been previously justified, be demonstrated?

The material presented in Chapter 11 demonstrates the overall methodology for air flow and heat exchange modeling of large bodies of broken rock developed within this thesis.

The field data was collected for the porous media problem explored followed the principles of the constant head pressure test, albeit at ~1km^3 scale. The CFD model of the large scale broken rock body was created using its geometry defined in mine design software, in turn developed from surveys of the area. Properties used in the large scale broken rock body problem were defined using the PSM air flow resistance establishment method and scaled up to the smallest finite volume element of the large scale model using the techniques developed in Chapter 9. Using the CFD tool to model the large scale body permits pressure and velocity fields, and flow trajectories to be estimated. Non-obvious, complex flow and heat transfer behaviour patterns emerge in the results of these simulations, principally due to the complex geometry of the body and the air flow outlet manifold.

The overall theme questions of this thesis include:

1. Does determination of geometric parameters for the discontinuous porous medium lead to improvements in accuracy, precision, or computational efficiency in modelling and understanding flow and heat transfer for real-world applications involving broken rocks and disturbed soils (e.g. ice stopes, geothermal energy, permafrost thaws)?

This question can only be answered by progressing through the entire material of this thesis. The complete methodology of the PSM technique was applied to take an assumed porosity of a large scale problem and create an initial PSM discontinuum model that uses all of the low level parameters as seen in the geometric dissection Chapter 7. This model was tested by both the self-similar scaling and test volume vs resistance curves explained in Chapter 9. A series of equivalent continuum model materials were made out of these results. A sensitivity analysis was conducted on the entire thermal reservoir model using these various materials, and then was compared for insights on their accuracy by comparing the information with physical data.

This type of analysis before the PSM approach developed could not be performed, so “yes” is the answer to whether or not improved understanding about flow and heat transfer has been obtained. A second developed understanding porous media is that the air flow resistance of a material can be different even with the same porosity. A third understanding developed is that a reliable air flow resistance scaling procedure emerges from treating the PSM derived air flow resistances as branch resistances in mine ventilation air flow networks and applying branch series and parallel combination formulae. Such an approach has not been reported previously due to the relative complexity of the problem. In terms of computational efficiency of calculation, not unexpectedly, the PSM as a base is slower in nature computationally than its equivalent

continuum representation and this is due to the detail and complexity of the geometry that PSMs contain.

2. Which of the approaches explored leads to the best characterization of flow and heat transfer phenomena in these materials?

If the data is collected in with detail commensurate with green or brown field developments, then an equivalent continuum model is the more reasonable approach to porous media modelling. The problem with this is that the data that needs to be collected includes the air flow resistance of the porous medium, which can be extremely complicated to do. The PSM approach allows for the rubbing length of flow, rubbing area of the flow, the porosity, and ultimately the porous air flow resistance to be estimated.

3. Can the PSM be used to calibrate large scale equivalent continuum models to reduce computational time and increase accuracy for problems of a spatial scale of relevance to the mining industry, which may be in the tens to thousands of meters?

As can be seen from the discourse of Chapter 11, the PSM approach appears to lead to property estimates being made, with a meaningful basis, to so that models of large scale mining problems can be calibrated. While further work on the large scale applications should be performed, the initial results of this thesis indicate that the approach taken is promising..

12.3 Contributions of this thesis

The contributions of this thesis can be summarised as follows:

1. PSM CFD simulation and verification with a physical wind tunnel and manufacture of PSM 3D printed ensemble – The manufacturing of a complex 3D discontinuum porous media model in a direct one to one scale model is a first in the field. While wind tunnels have verified CFD codes for many individual spheres and airfoils, a porous media consisting of 500 spheres with a complex internal structure has not been verified in both flow and thermal physical experiments in the fashion undertaken in this work.

2. Air flow performance – This thesis contains the method and results of the verification CFD code portion compared with the physical wind tunnel experiment. Typical verifications can deal with either pressure or flow rate, but the approach taken with the PSM was in the form of Atkinson's resistance and friction factor. This was confirmed with the sampling campaigns in Chapter 9.

3. CFD mesh sensitivity and repeatability for Rosin Rammler distributed solids – The contribution here is testing the PSM discontinuum models for repeatability in regards to geometry created through the Rosin Rammler distribution. One Rosin Rammler distribution was consolidated in 5 ways, and it was shown that there are similar airflow resistance characteristics even though the geometry of each of the PSM were distinct.

4. PSM derived estimates of Atkinson's resistance – This contribution is the geometric interrogation of the PSM to find high precision estimates perimeters lengths, cross-sectional areas, and true flow path length (also known as the tortuosity), as they appear in Atkinson's equation for air flow *branch* resistance.

5. Heat transfer performance of PSMs – In this component of the thesis, the contribution is the comparison of sets of thermal parameters of the PSM CFD models with a physical wind tunnel temperature transients. The results are compared with the 1:1 scale CFD PSM and are a first for complex models of porous media to be verified in this way.

6. An original idea supported by the work reported in this thesis is that elemental volumes of broken rock bodies can be treated as air flow resistance branches as they appear in mine ventilation networks. If they can be considered as air flow branches, then series and parallel combinations of the air flow resistances of these elements then lead to estimates of air flow resistance of porous media bodies of much larger scale. The work reported in verifying such an approach led to consistent, and accurate estimates of air flow resistance at larger scales.

7. Modelling an approximately 1 km^3 thermal regenerator – The contribution here was the PSM technique for obtaining air flow resistance parameters of the porous medium, led to predictions of overall behaviour from CFD simulations that are consistent with site observations.

12.4 Conclusions

With time, it is believed that the PSM technique could become a used as a proxy technique to apply to porous media, due to the findings of this thesis.

The three fundamental ways of characterising porous media air flow and heat transfer behaviour were investigated and tested in this thesis.

1. Verification of a physical wind tunnel experiment for air flow and heat exchange – The method of creation and testing of the PSM with the physical wind tunnel provides confidence in the CFD tool for use in modelling applications of complex broken rocks or soils where the particle sizes follow the Rosin Rammler distribution.

2. Geometric dissection – if PSMs can be established that produce air flow resistance behaviour consistent with experimental results, the PSM can be 'geometrically interrogated' in the CAD/CAM environment to establish estimates of parameters important in fluid flow and heat transfer behaviour. For example, the CAD/CAM can readily return the surface area between solid and fluid across which heat transfer occurs.

3. Kirchoff laws apply to porous media resistances – The series and parallel branch resistance formulae are a direct corollary of application of Kirchoff's laws for network flow. The strongest method for scaling air flow resistance properties, beyond straightforward empirical, curve fitting technique, was shown to be through the applications of Kirchoff's Laws verified through comparison of the resistance of the larger bodies with the CFD code, as shown in Chapter 9.

Taken together, these three measures for characterizing the behaviour of bodies of broken rock will lead to improved understanding of how air flows through them, and how heat can be stored and removed from them, so that novel engineering applications, for the mining industry and beyond, can be explored.

13 References

Ababou , R *et al.* 1994. Continuum Modelling Of Coupled Thermo-Hydro-Mechanical Processes in Fractured Rock. In: *CMWR'94, 10th International Conference on Computational Methods in Water Resources*, Heidlberg, Germany, July 19-22, 1994. A.Peters et al (eds.), Kluwer Academic Publishers, Netherlands, pp.651-658

Acuña, E, Tousignant, A., Bilal, N., Fava, L., Goforth, D., O'Connor,D., Allen, C., 2010. A combined ventilation and thermodynamic model for dry surfaces to predict and optimize the NHEA cooling and heating capacity for Creighton mine. In: *13th United States/North American Mine Ventilation Symposium, 2010*. Hardcastle & McKinnon (Eds.)

Alfredsson, H, 2010. *Solving stiff systems of ODEs in CFD applications Developing and evaluating the Stiff ODE Suite* , Master of Science Thesis, Department of Chemical and Biological Engineering Division of Chemical Reaction Engineering. Chalmers University of Technology, Göteborg, Sweden, 2010

ANSYS Inc., 2010. *What is Computational Fluid Dynamics (CFD)*. [online] Available at <http://www.fluent.com/solutions/whatcfd.htm> [Accessed 6 September, 2010]

Arenson, L.U., Sego, D.C., and Newman, G. 2006. The use of a convective heat flow model in road designs for northern regions. In: *Climate Change Technology Conference*. Ottawa, Ontario, Canada. 10-12 May, 2006. doi: 10.1109/EICCCC.2006.277276

ASTM 2006. Standard Test Method for Sieve Analysis of Fine and Coarse Aggregates Active Standard (C136-06). In: *ASTM Annual Book of Standards, American Society for Testing and Materials,* West Conshohocken, Pa., doi: 10.1520/C0136-06

ASTM. 2006b. Standard test method for permeability of granular soils (constant head) (D2434). In: *ASTM Annual Book of Standards, American Society for Testing and Materials*, West Conshohocken, Pa. doi: 10.1520/D2434-68R06

ASTM 2008. Standard Test Method for Determining Transmissivity and Storage Coefficient of Low-Permeability Rocks by In Situ Measurements Using the Constant Head Injection Test Active Standard (D4630). In: *ASTM Annual Book of Standards, American Society for Testing and Materials,* West Conshohocken, Pa. doi: 10.1520/D4630-96R08

ASTM. 2010. Standard test method for measurement of hydraulic conductivity of saturated porous materials using a flexible wall permeameter (D5084). In: *ASTM Annual Book of Standards, American Society for Testing and Materials*, West Conshohocken, Pa. doi: 10.1520/D5084-10

ASTM. 2007. Standard test method for measurement of hydraulic conductivity of porous materials using a rigid-wall, compaction-mold permeameter (D5856). In: *ASTM Annual Book of Standards, American Society for Testing and Materials,* West Conshohocken, Pa. doi: 10.1520/D5856-95R07

Asus website, 2013. *ASUS G74Sx Specifications.* [online] Available at <http://www.asus.com/ROG_ROG/G74SX/ > [Accessed May 1, 2013]

Aubertin, M., Chapuis, R.P., Bussière, B., and Aachib, M. 1993. Propriétés des résidus miniers utilizés comme matériaux de recouvrement pour limiter le DMA. In: *Proceedings of the Geoconfine 93,* A.A. Balkema, Rotterdam, pp. 299–308.

Aubertin, M., Bussière, B., and Chapuis, R.P. 1996. Hydraulic conductivity of homogenized tailings from hard rock mines. *Canadian Geotechnical Journal, 33*: pp 470–482.

Auer, L.H, Rosenberg, N.D, Birdsell, K.H, Whitney, E.M, 1996. The effect of barometric pumping on contaminant transport. *Journal of Contaminant Hydrology 24*: pp 145-166.

Bear, J, 1972. *Dynamics of Fluids In Porous Media, Volume 1*. American Elsevier Publishing Company.

Blowes, D, Moncur, M, Smith, L,Sego, D, Bennet, J, Garvie, A, Linklater, C, Gould, G, Reinson, 2006. Construction Of Two Large-Scale Waste Rock Piles In A Continuous Permafrost Region. In: *7th International Conference on Acid Rock Drainage ICARD – Abstracts March 26-30.*

Brown, P.L., Crawford, J., Irannejad, P., Miskelly, P.C., Noël, M.M., Pantelis, G., Plotnikoff, W.W., Sinclair, D.J., and Stepanyants, Y.A. 2001. *SULFIDOX: Version 1.1. A tool for modelling the temporal and spatial behaviour of heaps containing sulfidic minerals.* ANSTO Technical Report, ANSTO/ED/TN01-03.

Bouffard, S. C., Dixon, D. G., 2001 Investigative study into the hydrodynamics of heap leaching processes. *Metallurgical and Materials Transaction* 32, pp. 763–776

Bussière, B. 1993. *Évaluation des propriétés hydrogéologiques des résidus miniers utilizés comme barrières de recouvrement*. Master's thesis, École Polytechnique, Montréal, Que., 171 pages.

Canadian Tire website 2013. *Mastercraft Deluxe Digital Multimeter*. [online] Available at <http://answers.canadiantire.ca/answers/9045/product/0520055P/mastercraft-mastercraft-deluxe-digital-volt-meter-questions-answers/questions.htm> [Accessed 10 February 2013]

Carman, P.C, 1937. Fluid flow through granular beds. *Transactions, Institution of Chemical Engineers, London, 15*: pp. 150-166.

Chapuis, R.P., and Aubertin, M. 2003. Predicting the coefficient of permeability of soils using the Kozeny–Carman equation. *Technical Report EPM-RT-2003–03*, École Polytechnique, Montréal, Quebec.

Compass website, 2013. *Tdyn CFD+HT* [online] Available at <http://www.compassis.com/compass/en/Productos/Tdyn> [Accessed 20 June 2013]

Comsol 2014, *COMSOL Multiphysics Software* [online] Available at <http://www.comsol.com/> [Accessed February 25 2014]

Cunningham, C.V.B., 1983. The Kuz–Ram model for prediction of fragmentation from blasting. In: R. Holmberg & A Rustan (eds), *Proceedings of First International Symposium on Rock Fragmentation by Blasting, Luleå Sweden*, pp. 439–454.

Cunningham, C.V.B., 1987. Fragmentation estimations and the Kuz–Ram model – four years on. In: W. Fourney (ed.), *Proceedings of Second International Symposium on Rock Fragmentation by Blasting, Keystone, Colorado*, pp. 475–487.

Cunningham, C.V.B., 2000. The effect of timing precision on control of blasting effects. In: R. Holmberg (ed.), *Explosives & Blasting Technique: Munich–Rotterdam: Balkema.* pp. 123–128.

Cunningham, C.V.B., 2005. The Kuz-Ram fragmentation model – 20 years on. In: R Holberg (ed.), *Brighton Conference Proceedings 2005, Brighton, England*. pp. 201-210.

Darcy H.,1856. *Détermination des lois d'écoulement de l'eau à travers le sable*, (In appendix - Note D - of Les fontaines publiques de la ville de Dijon

Dassault Systèmes Systèmes *SolidWorks Corp., 2012*. [online] Available at <http://www.solidworks.com/sw/products/cfd-flow-analysis-software.htm> [Accessed 13 November 2012]

Dassault Systèmes Systemes website, 2013. *SolidWorks Flow Simulation.* [online] Available at <http://www.3ds.com/products/solidworks/> [Accessed 10 January 2013]

Dimension Printing website, 2013. *Dimension printing*. [online] Available at <http://www.dimensionprinting.com/3d-printers/printing-productspecs1200series.aspx> [Accessed 10 January 2013]

Doucet, C , 1995. *The Effect of Geology on Fragmentation in Small Development Headings,* thesis submitted to the faculty of graduate studies in the Department of Mining and Metallurgical Engineering McGiII University, Montreal, 1995

Envers, P, Controlled Air Through Efficient System at Inco. *Canadian Mining Journal*, July 1986, pp. 12-14.

Fava, L, Millar, D, Anderson, B, Schafrik, S, 2011. Modelling of the Natural Heat Exchange Area for Operation Decision Support. In: *14th US/North American Mine Ventilation Symposium*, Utah, United States, 17-20 June 2012

Fluent, Inc. 2010. *Fluent for Catia 5.0 Brochure*. [online] Available at <http://www.ansys.com/assets/brochures/Fluent_for_Catia-5.0_12.pdf > [Accessed 6 September 2010]

Fluorotherm Products Website, 2013. *FEP General Properties*. [online] Available at < http://fluorotherm.com/Properties-FEP.asp> [Accessed 10 February 2013]

Fracman Software, 2010. *MAFIC Software Information.* [online] Available at <http://fracman.golder.com/software/mafic.asp> [Accessed 6 September 2010]

Fréchet, M, 1927. Sur la loi de probabilité de l'écart maximum, In: *Annales de la Société Polonaise de Mathematique, Cracovie* volume 6, pp. 93–116.

Geomore Website, 2013. *Oil On My* Shoes (Sedimentary Rocks) [online] Available at < http://www.geomore.com/sedimentary-rocks/> [Accessed 23 December, 2013]

GeoSlope International Ltd. 2006. *Software Validation Test Plan and Report for GEOSTUDIO™ VADOSE/w 2007 VERSION 7.11* [online] Available at <http://pbadupws.nrc.gov/docs/ML0823/ML082390631.pdf > [Accessed January 11, 2012]

Goering, D.J., 2003. Passively cooled railway embankments for use in permafrost areas. *Journal of Cold Regions Engineering*, 17(3): pp. 119-133.

Goering, D.J., and Kumar, P., 1996. Winter-time convection in open-graded embankments. *Cold Regions Science and Technology*, 24(1)*:* pp. 57-74.

Goering, D.J. 2002. Convective Cooling in Open Rock Embankments. In: *Proceedings, 11th International Conference on Cold Regions Engineering, Anchorage, AK* : pp. 629–644

González-Tello,P, Camacho F, Vicaria, J.M,González, P.A, 2008. A modified Nukiyama-Tanasawa distribution function and a Rosin Rammler model for the particle-size-distribution analysis, *Powder Technology, vol. 186,* nr. 3, 2008, pp. 278-281

Golder Associates, Consulting Geotechnical Engineers, 1980. *A study to determine ventilation and refrigeration requirement and costs in deep Canadian mines*. Unpublished report

Hamm, V, Sabet, B.B., 2010. Modelling of fluid flow and heat transfer to assess the geothermal potential of a flooded coal mine in Lorraine, France. *Geothermics 39* (2010): pp 177–186

Hardcastle, S.G, Kocsis, C, Li, G, Hortin, K, 2008. Analyzing ventilation requirements and the

utilization efficiency of the Kidd Creek mine ventilation system. In: Wallace (ed), *12th U.S./North American Mine Ventilation Symposium 2008,* Reno, Nevada, U.S.A., June 9-11, 2008. pp 27-36

Hartman, H.L and Mutmansky, J.M, 1986. *Introductory Mining Engineering*, John Wiley & Sons

Hewlett-Packard website, 2013. *HP-520 Hewlett-Packard Specifications* [online] Available at <http://www8.hp.com/h20195/v2/GetDocument.aspx?docname=c04140587> [Accessed 1 July 2013]

Holm, A, Blodgett, L, Jennejohn, D, Gawell, K, 2010. *Geothermal Energy: International Market Update.* [online] Available at <http://www.geoenergy.org/pdf/reports/GEA_International_Market_Report_Final_May_2010.pdf> [Accessed 20 September 2010]

Holman, J.P., 1997. *Heat Transfer*. 8th ed., McGraw-Hill, New York, 1997.

Hrennikoff, A, 1941. Solution of Problems of Elasticity by the Frame-Work Method. *ASME Journal of Applied Mechanics Volume* 8, A619–A715.

Idelchik, I.E.,1986. *Handbook of Hydraulic Resistance*. 2nd ed., Hemisphere, New York, 1986

Incropera, F P., DeWitt, D P., 2006. *Fundamentals of Heat and Mass Transfer* (6th Edition) Wiley. pp. 490-515.

Itasca International Inc., 2013. *Overview of PFC3D.* [online] Available at <http://www.itascacg.com/pfc3d/overview.php > [Accessed 7 November 2012]

Itasca Houston, 2014. *Petroleum Geomechanical Software* [online] Available at <http://www.itascahouston.com/petro_software.html> [Accessed 10 January 2014]

Johnson, O.S., 2006. Thermo- and psychrometric properties of intake air passing through fragmented strata. In: *Proc. 11th U.S./North American Mine Ventilation Symposium*, Taylor & Francis Group Plc. pp 29- 34

Jong, E.C, Luxbacher, K.D, 2010, Application of Schlieren techniques for improved understanding of underground mine ventilation. In: *13th United States/North American Mine Ventilation Symposium, 2010*. Hardcastle & McKinnon (Eds.) pp. 53-57

Kalitzin, G., and Iaccarino, G., 2002. Turbulence Modelling in an Immersed-Boundary RANS-Method, *Center for Turbulence Research Annual Research Briefs*, Stanford University, California, pp. 415 – 426

Khajeh , E, Maijer, D, 2011. Permeability of Dual-Structured Porous Media. *The Open Transport Phenomena Journal*, 2011, vol 3, pp. 56-61.

Klassen, R, Arenson, L, Sego, D, Bigga, K, 2007. *Heat Convection Modelling In Waste Rock Piles.* [online] Available at <http://bgcengineering.com/publications/list?filter0=**ALL**&filter1=0030> [Accessed 20 November 2010]

Kojovic, T, Michaux, S, Mackenzie, M, 1995. "Impact of blast Fragmentation on crushing and screening operations in Quarrying", In: *Procedures from Explo'95 Conference, publication series no 6/95 Carlton, VIC,* AusIMM, 1995, pp. 437-444

Kocsis, C, 2009. *New Ventilation Design Criteria for Underground Metal Mines Based Upon the Life-Cycle Airflow Demand Schedule*, thesis submitted to the faculty of graduate studies in the Department of Mining Engineering University of British Columbia, Vancouver, 2009

Kozeny, J, 1927. *Ueber kapillare Leitung des Wassers im Boden*. Sitzungsber Akadamie. Wissenschaften., Wien, 136(2a): pp. 271-306

Kuo, E Y and Ritchie, A I M, 1999. The impact of convection on the overall oxidation rate in sulfidic waste rock dumps In: *Proceedings Mining and the Environment II*, 1999 (Eds: D. Goldsack, N. Belzile, P. Yearwood and G. Hall), pp 211-220.

Kuznecov, N. V., 1980, The Petersson conjecture for cusp forms of weight zero and the Linnik conjecture. Sums of Kloosterman sums, *Matematicheskii Sbornik, Novaya Seriya* 111(153) (3), pp. 334–383

L'Écuyer, M., Chapuis, R.P., and Aubertin, M., 1992. Propriétés hydro-géotechniques des résidus miniers de Solbec et Cupra, Québec. In: *Proceedings of the 45th Canadian Geotechnical Conference*, Toronto, Ont., pp. 79.1–11

Laboratory of Ecohydrology, 2013. *Chapter 8 Field and Laboratory Tests* [online] Available at <http://echo2.epfl.ch/VICAIRE/mod_3/chapt_8/main.htm> [Accessed 20 June 2013]

Lai, Y.M., Li, J.J., Niu, F.J., and Yu, W.B. 2003a. Nonlinear thermal analysis for Qing-Tibet railway embankments in cold regions. *Journal of Cold Regions Engineering*, 17(4): pp 171-184.

Lai, Y.M., Zhang, L.X., Zhang, S.J., and Mi, L. 2003b. Cooling effect of ripped-stone embankments on Qing-Tibet railway under climatic warming. *Chinese Science Bulletin*, 48(6): pp 598-604.

Latham, J-P, Maerz, N, Noy, M Schleifier, J, Tose, S, (2003). A blind comparison between results of four image analysis systems using a photo-library of piles of sieved fragments. *International Journal Fragmentation by Blasting*, vol 7, pp 105-132

Launder, B.E. and Spalding, D.B., 1972. *Lectures in Mathematical Models of Turbulence*. Academic Press, London, England.

Launder, B. E. and Spalding, D. B. The Numerical Computation of Turbulent Flows. *Computer Methods in Applied Mechanics and Engineering*, Vol. 3, 1974, pp. 269-289

Layne Christensen Company, 2010. *Aquarius Project – Artificial Ground Freezing.* [online] Available at <http://www.groundfreezing.com/aquarius_project.html> [Accessed 7 September 2010]

Leea, S.H, Kima, H.J, Sakaib, E. Daimonb, M, 2003. Effect of particle size distribution of fly ash–cement system on the fluidity of cement pastes. *Cement and Concrete Research* 33 (2003) pp. 763–768

Lefebvre, R and Gelinas, P, 1995. Numerical modelling of AMD production in waste rock dumps. In: *Proceedings Mining and the Environment 1995*, pp 869-878.

Lefebvre, R, 1994. *Characterization and modelling of acid mine drainage in waste rock pile*, PhD Thesis, Laval University, Quebec (in French).

Lefebvre, R, 1995. Modelling acid mine drainage in waste rock dumps. In: *Proceedings of the TOUGH Worskhop '95*, (Ed: K. Pruess), pp. 239-244.

Lefebvre, R, Hockley, D, Smolensky, J, and Gelinas, P, 2001a. Multiphase transfer processes in waste rock piles producing acid mine drainage 1: Conceptual model and system characterization, *Journal of Contaminant Hydrology*, 52: pp. 137-164.

Lefebvre, R, Hockley, D, Smolensky, J, and Lamontagne, A, 2001b. Multiphase transfer processes in waste rock piles producing acid mine drainage 2: Applications of numerical simulation, *Journal of Contaminant Hydrology*, 52: pp 165-186.

Lefebvre, R., Lamontagne, A, Wels, C., and Robertson, A, MacG, 2002. ARD Production and Water Vapor Transport at the Questa Mine. In: *Proceedings of the Ninth International Conference on Tailings and Mine Waste, Tailings and Mine Waste '02*, pp. 479-488.

Linklater, C.M., Sinclair, D.L., and Brown, P.L. 2005. Coupled chemistry and transport modelling of sulfidic waste rock dumps at the Aitik mine site Sweden. In: *23rd Annual Meetings of the American Society of Mining and Reclamation* 3134 Montavesta Rd. Lexington, KY 40502, March 26-30, 2006 pp. 275-293

Lundberg, S., (1961).Tappning, transport och krossning av skivrasberg på 320 m avv. i KUJ. Delutredning: Siktanalys av skivrasberg [Drawing, transportation and crushing of caving material at level 320 m in the Kiruna underground mine. Interim report: fragment size distribution of material from caving] (Unpublished report 116-1071a). Kiruna, Sweden: LKAB.

Maerz, N.H. Palangio, T.C. Palangio, T.W. Elsey, K. , 2007. Optical sizing analysis of blasted rock: lessons learned. *In: Vienna Conference Proceedings 2007*, P. Moser *et al.* 2007 European Federation of Explosives Engineers, ISBN 978-0-9550290-1-1, pp 75- 82.

Mašín , D, 2003. Application of the fractal fragmentation model to the fill of natural shear zones. In: *Fractals in Geotechnical Engineering. Kolymbas (ed.),* Logos, Berlin; pp. 57-65

Massachusetts Institute of Technology, 2010. *The Reynolds Analogy.* [online] Available at <http://web.mit.edu/16.unified/www/FALL/thermodynamics/notes/node122.html> [Accessed 21 September 2010]

Matbase database website, 2013. *ABS 430 Material Properties.* [online] Available at <http://www.matbase.com/material/polymers/commodity/abs.general.pupose/properties> [Accessed 10 June 2012]

McPherson, M J., 1986. The analysis and simulation of heat flow into underground airways. *International Journal of Mining and Geological Engineering,* pp. 165-196

McPherson, M J., 2007. "Subsurface Ventilation and Environmental Engineering". Springer

Mejeoumov, G.G, 2007, *Improved cement quality and grinding efficiency by means of closed mill circuit modelling*. Thesis submitted to the Office of Graduate Studies of Texas A&M University, December 2007

Microsoft Excel Website, 2013. *Microsoft Excel Software* [online] Available at <http://office.microsoft.com/en-ca/excel/> [Accessed 1 June 2013]

Montecinos, C., Wallace Jr., K, 2010. Equivalent roughness for pressure drop calculations in mine ventilation. In: *13th United States/North American Mine Ventilation Symposium, 2010*. Hardcastle & McKinnon (Eds.) pp 225-230

Monzon, M. 1998. *Étude en laboratoire des propriétés hydrogéo techniques des résidus miniers utilizés comme barrière de recouvrement*. Mémoire de M.Sc.A., Ecole Polytechnique, Montréal, Que.

Muralikrishna A, k, Shenoy, U.V, 2000. Heat Exchanger design targets for minimum area and cost. *Institute of Chemical Engineers, Vol 78, Part A,* March 2000, pp 161-167

MVS Engineering website, 2012. *VnetPC* [online] Available at <http://www.mvsengineering.com/index.php/downloads/software> [Accessed 12 December 2012]

Nichol, C., Smith, L., and R. Beckie. 2005. Field scale experiments of unsaturated flow and solute transport in a heterogeneous porous medium. *Water Resources Research volume 41*. pp. 275-293.

NGI Laboratories, 2014. *Discrete Element Method* [online] Available at <http://www.ngi.no/en/Contentboxes-and-structures/Reference-Projects/Reference-projects/Discrete-Element-Method-DEM/> [Accessed 5 April 2014]

Objectivity website, 2012. *Objectivity Paraview Geo* [online] Available at <http://paraviewgeo.objectivity.ca/> [Accessed 1 May 2012]

Oda, M., 1986. An equivalent continuum model for coupled stress and fluid flow analysis in jointed rock masses, *Water Resources Research Vol 22*, pp. 1845- 1856

Ofoegbu, G.I., Read, R.S., Ferrante, F., 2013. *Bulking factor of rock for underground openings. U.S. Nuclear Regulatory Commission Contract NRC 02-07-006 contract report* [online] Available at: http://pbadupws.nrc.gov/docs/ML0807/ML080700314.pdf. [Accessed 28 May 2013]

Omega website, 2013. *Thermistor Products*. [online] Available at <http://www.omega.com/prodinfo/thermistor.html> [Accessed 10 February 2013]

Outal , S, Jeulin , D, Schleifer , J, 2008. A New Method For Estimating The 3D Size-Distribution Curve Of Fragmented Rocks Out Of 2D Images, *Image Analysis & Stereology* 2008; vol 27:pp. 97-105

Pantelis, G and Ritchie, A I M, 1991. Macroscopic transport mechanisms as rate-limiting factor in dump leaching of pyritic ores. *Applied Mathematical Modelling*, vol 15: pp. 136-143.

Pantelis, G, 1993. *FIDHELM: Description of model and users guide*. Australian Nuclear Science and Technology Organisation Report ANSTO/M123.

Papakonstantinou, K.A., Kiranoudis, C.T., Markatos, N.C., 2000. Numerical simulation of airflow field in single-sided ventilated buildings. *Energy and Buildings 33 (2000)*, pp. 41-48

Paroscientific, Inc website, 2012. *Digiquartz Model 745 High Accuracy Precision Standard*. [online] Available at < http://www.paroscientific.com/model745.htm> [Accessed 10 May, 2012]

Partyka, 2003. ENGR 3327 Ventilation Course Notes. Laurentian University Press.

Poetsch, F.H, 1863. F.H. Poetsch patent for a freezing process to the Abteufung (Shaft Sinking) of pits in the Bergbouter (Mining Industry)

Rockfield, 2013. *ELFEN Software* [online] Available at <http://www.rockfield.co.uk/software> [Accessed 23 January 2013]

Rogers, G and Mayhew, Y, 1992. *Engineering Thermodynamics: Work and Heat Transfer.* 4th edition, USA: Prentice Hall PTR

Rosin, P.; Rammler, E., 1933. The Laws Governing the Fineness of Powdered Coal, *Journal of the Institute of Fuel* Volume 7: pp. 29–36.

Rutherford, J.G, 1960. Heating Mine Supply Air. *Precambrian*, Col. 33, pp 17-23

Schlichting, H., 1959. *Entstehung der Turbulenz*. Springer 1959.

Schlichting, H.,1979. *Boundary Layer Theory*. 7th ed., McGraw –Hill, New York, 1979

Shen, C, Mckinzie, B, Arbabi, S, 2010. A Reservoir Simulation Model for Ground Freezing Process. Presented at the *SPE Annual Technical Conference and Exhibition* held in Florence, Italy, 19–22 September 2010. [online] Available at <http://www.spe.org/atce/2010/pages/schedule/tech_program/documents/spe1324181.pdf> [Accessed 20 November 2010]

Sharmeen, R, Illman.W.A, Berg, S.J, Ye, T.J, Park, Y, Sudicky, E.A and Andos, K., 2012. Transient hydraulic tomography in a fractured dolostone: Laboratory rock block experiments. *Water Resources Research, Volume. 4.* doi:10.1029/2012WR012216 pp. 1-20

Siddiqui, F.I, Ali Shah, S.M, Behan, J.K, 2009. Measurement of Size Distribution of Blasted Rock Using Digital Image Processing Journal of King Abduaziz University., Vol. 20 No. 2, pp. 81-93

Smith, L. and R. Beckie. 2003. Hydrologic and geochemical transport processes in mine waste rock, Ch 3. p. 51-72. In Jambor, J.L., Blowes, D.W, Ritchie, A.I.M. (eds.), *Environmental Aspects of Mine Wastes. Mineral Association Canada Short Course Vol. 31*. St. Louis, Missouri. [online] Available at <http://www.asmr.us/Publications/Conference Proceedings/2006/> [Accessed 21 November 2010]

Sobieski , W, Zhang , Q, Liu, C, 2012. Predicting Tortuosity for Airflow Through Porous Beds Consisting of Randomly Packed Spherical Particles. *Transport in Porous Media* (2012) vol 93: pp. 431–451

Strelec, S, Gazdek, M, Mesec, J Određivanje, 2011. Blasting design for obtaining desired fragmentation. *Određivanje bušačko-minerskih parametara za dobivanje željene fragmentacije, Tehnički vjesnik* 18, 1(2011), pp. 79-86

Stachulak, J.S., 1991. Ventilation Strategy and Unique Air Conditioning at Inco Limited, *CIM Bulletin, Vol. 84, No. 950*, pp. 41-55.

Sun, B.X., Xu, X.Z., Lai, Y.M., and Fang, M.X., 2005. Evaluation of fractured rock layer heights in ballast railway embankment based on cooling effect of natural convection in cold regions. *Cold Regions Science and Technology*, 42(2): pp 120-144.

Sylvestre, M J-G, December, 1999. *Heating And Ventilation Study Of INCO'S Creighton Mine*, Department of Mining and Metallurgical Engineering McGill University, Montreal, Master's thesis

Tasdemir, A, Tasdemir, T, 2009. A Comparative Study on PSD Models for Chromite Ores Comminuted by Different Devices. *Particle and Particle System Characteristics* 26 (2009) pp. 69–79.

Tidwell, V, 2006. Air Permeability Measurements In Porous Media. *Gas Transport in Porous Media,* C. Ho and S. Webb (eds.) pp. 273–278.

TSI Inc. website, 2014. *DP-Calc Micromanometer 8705.* [online] Available at <http://www.tsi.com/dp-calc-micromanometer-8705/> [Accessed 2 February, 2014]

Vale - Various personal correspondence (2010-2014)

Van Driest, E.R., 1956. On Turbulent Flow Near a Wall. *Journal of the Aeronautical Sciences*, Vol. 23, No. 10, p. 1007 – 1011.

Vesselinov, V., S. P. Neuman, and W. A. Illman, 2001, Three-dimensional numerical inversion of pneumatic cross-hole tests in unsaturated fractured tuff 2. Equivalent parameters, high-resolution stochastic imaging and scale effects, *Water Resources. Research., 37(*12), pp. 3019–3041.

Wagner, K., Smith, L., and R. Beckie. 2006. Hydrogeochemical characterization of effluent from mine waste rock, Cluff Lake Saskatchewan. In: *7th ICARD Proceedings, International Mine Water Association.* pp. 2207 – 2217

Weibull, W., 1951. A statistical distribution function of wide applicability, *ASME Journal of Applied Mechanics* Volume 18. pp. 293–297.

Wels, C, Lefebvre, R, Robertson, A, 2003. *Control of Airflow in Waste Rock Dumps* [online] Available at <http://www.infomine.com/publications/docs/EBook% 2003%20Air%20in%20Dumps.pdf> [Accessed 20 November 2010]

Western Miner, Volume 55 #7, July 1982

White, F.M., 1994. *Fluid Mechanics*. 3rd ed., McGraw-Hill, New York, 1994

Wilcox, D.C., 1994. *Turbulence Modelling for CFD*. DCW Industries.

Wipware Software, 2013. *Wipware Software* [online] Available at <http://wipware.com/products-services/> [Accessed 20 January, 2013]

Yanshin, B.I, 1965. Hydrodynamic Characteristics of Pipeline Valves and Elements. Convergent Sections, Divergent Sections, and Valves. *Mashinostroenie*, Moscow, 1965

Yimsiri, S., Soga, K. (2010). DEM analysis of soil fabric effects on behaviour of sand. *Geotechnique* 60, No. 6, pp. 483–495

Yu, W.B., Lai, Y.M., Zhang, X.F., Zhang, S.J., and Xiao, J.Z. 2004. Laboratory investigation on cooling effect of coarse rock layer and fine rock layer in permafrost regions. *Cold Regions Science and Technology*, 38(1): pp. 31-42.

Zeghal , M, El Shamy, U, 2008. Liquefaction of saturated loose and cemented granular soils. *Powder Technology*, 184, 2, pp**.** 254-265

14 Appendix

The following is the translate macro to import spheres from a text file consisting of x,y,z and a scaling factor from a base sphere constructed at the origin:

```
'Sidney's Data Input File Points – Pre-condition (One sphere must be made on the origin)
Dim swApp As Object
Dim currentDoc As Object
Dim boolstatus As Boolean
Dim longstatus As Long, longwarnings As Long
Sub main()
   UserForm1.Show
End Sub

‘Command button code (operating code)

Private Sub CancelButton_Click()
   End
End Sub

‘Second method of the user command button

Private Sub CommandButton1_Click()

Dim swApp As Object
```

```
Dim currentDoc As Object
Const swDocPART = 1
Const swDocASSEMBLY = 2
Dim fileName As String
Dim nextline As String
Dim trimmed As String
Dim xVal, yVal, zVal, sVal As Double
Dim CommaLoc1, CommaLoc2, CommaLoc3 As Long
Dim point As Object

   Const errorString = "You must have a part file open to use this feature."
   Set swApp = CreateObject("SldWorks.Application")
   Set currentDoc = swApp.ActiveDoc
   If currentDoc Is Nothing Then
      swApp.SendMsgToUser (errorString)
      End
   End If
   If (currentDoc.GetType = swDocPART) Then

      ' Commented Out currentDoc.Insert3DSketch

      fileName = Me.fileName.Value
      Open fileName For Input As #1 ' Open file.
```

```
    Line Input #1, nextline 'Read line into variable.
    Do While Not (nextline = "-END-") ' Loop until -END- is found.

        Values = Split(nextline, ",")
        xVal = Val(Trim(Values(0)))
        yVal = Val(Trim(Values(1)))
        zVal = Val(Trim(Values(2)))
        sVal = Val(Trim(Values(3)))

       ' Commented Out  Set point = currentDoc.CreatePoint2(xVal, yVal, zVal)
'Editing This Macro Here
        Set Part = swApp.ActiveDoc
        boolstatus = Part.Extension.SelectByID2("Revolve1", "SOLIDBODY", 0, 0, 0, False, 0,
Nothing, 0)
        Part.FeatureManager.HideBodies
        boolstatus = Part.Extension.SelectByID2("MySketch", "SKETCH", 0, 0, 0, False, 0,
Nothing, 0)
        Part.BlankSketch
        Set Part = swApp.ActiveDoc
        boolstatus = Part.Extension.SelectByID2("Point5@MySketch", "EXTSKETCHPOINT",
0, 0, 0, True, 0, Nothing, 0)
        boolstatus = Part.Extension.SelectByID2("Point5@MySketch", "EXTSKETCHPOINT",
0, 0, 0, True, 0, Nothing, 0)
```

```
        'boolstatus = Part.Extension.SelectByID2("Point22@3DSketch1",
"EXTSKETCHPOINT", 0.1, 0.1, 0.1, True, 0, Nothing, 0)
        'boolstatus = Part.Extension.SelectByID2("Revolve1", "SOLIDBODY", 0, 0, 0, True, 0,
Nothing, 0)
   boolstatus = Part.Extension.SelectByID2("Revolve1", "SOLIDBODY", 0, 0, 0, False, 1,
Nothing, 0)
Dim myFeature As Object
Set myFeature = Part.FeatureManager.InsertMoveCopyBody2(0, 0, 0, 0, 0, 0, 0, 0, 0, 0, True, 1)
boolstatus = Part.Extension.SelectByID2("", "SOLIDBODY", 1.99536165092695E-03,
2.7944277350116E-03, 3.63451585707253E-03, True, 0, Nothing, 0)
Set myFeature = Part.FeatureManager.InsertScale(0, True, sVal, sVal, sVal)
boolstatus = Part.Extension.SelectByID2("", "SOLIDBODY", 0, 0, 0, True, 1, Nothing, 0)
Set myFeature = Part.FeatureManager.InsertMoveCopyBody2(xVal, yVal, zVal, 0, 0, 0, 0, 0, 0,
0, False, 1)
boolstatus = Part.Extension.SelectByID2("", "SOLIDBODY", 0, 0, 0, True, 1, Nothing, 0)
        Part.FeatureManager.HideBodies
' Selection Process Old
      "Part.ClearSelection2 True
      "boolstatus = Part.Extension.SelectByID2("Point5@MySketch", "EXTSKETCHPOINT", 0,
0, 0, False, 2, Nothing, 0)
      "boolstatus = Part.Extension.SelectByID2("Point5@MySketch", "EXTSKETCHPOINT", 0,
0, 0, True, 4, Nothing, 0)
```

```
        "boolstatus = Part.Extension.SelectByID2("Point22@3DSketch1", "EXTSKETCHPOINT",
0.1, 0.1, 0.1, True, 8, Nothing, 0)
        "boolstatus = Part.Extension.SelectByID2("Revolve1", "SOLIDBODY", 0, 0, 0, True, 1,
Nothing, 0)
'Scaling Part Old
        "Set myFeature = Part.FeatureManager.InsertMoveCopyBody2(xVal, yVal, zVal, 0, 0, 0, 0,
0, 0, 0, True, 1)
        "Set myFeature = Part.FeatureManager.InsertScale(0, True, 2, 2, 2)
            Line Input #1, nextline
        Loop
        Close #1  ' Close file.
    Else 'must be a drawing
       swApp.SendMsgToUser (errorString)
    End If
    End
End Sub
Private Sub fileName_Change()
End Sub
Private Sub UserForm_Click()


End Sub
```